Optical Fiber Based Sensors for Harsh Environments

by

Mohamed Ashraf Saad Zaghloul Mohamed Bayoumy

B.Eng., Faculty of Engineering, Cairo University, 2009

M.Sc., Faculty of Engineering, Cairo University, 2012

Submitted to the Graduate Faculty of
Swanson School of Engineering in partial fulfillment
of the requirements for the degree of
Doctor of Philosophy

University of Pittsburgh

2019

UNIVERSITY OF PITTSBURGH

Swanson School of Engineering

This dissertation was presented

by

Mohamed Ashraf Saad Zaghloul Mohamed Bayoumy

It was defended on

July 18, 2019

and approved by

Mahmoud El-Nokali, Ph.D., Associate Professor
Department of Electrical and Computer Engineering

Guangyong Li, Ph.D., Associate Professor
Department of Electrical and Computer Engineering

Feng Xiong, Ph.D., Assistant Professor
Department of Electrical and Computer Engineering

Paul Ohodnicki, Ph.D., Material Scientist / Technical Lead
National Energy Technology Laboratory

Dissertation Director: Kevin Peng Chen, Ph.D., Professor
Department of Electrical and Computer Engineering

Optical Fiber Based Sensors for Harsh Environments

Mohamed Ashraf Saad Zaghloul Mohamed Bayoumy, Ph.D.

University of Pittsburgh, 2019

The primary objective of this study is to develop optical fiber-based sensors that are capable of operating in extreme conditions. Silica-based optical fibers are well known for their resilience to harsh environments. Whether they are integrated into distributed sensing schemes or as point sensors, optical fibers offer low-costs, highly accurate sensing platforms for various physical quantities.

In this dissertation, state-of–the-art Al-doped radiation sensitive optical fibers for distributed ionizing radiation measurements are presented for the first time. This optical fiber sensor, coupled with a Rayleigh scattering-based optical frequency domain reflectometry (OFDR) scheme, was used to monitor and quantitate ionizing gamma radiation from a ^{60}Co radioactive isotope.

An alternative multi-core optical fiber was deployed to simultaneously monitor two different parameters. The dual-core fiber has been fabricated with two distinct optical cores to allow for differences between the cores' temperature and strain coefficients. With such differences, temperature and strain changes were discriminated using a Brillouin scattering time domain analyzer (B-OTDA).

Ultrafast lasers are commonly used to inscribe thermally stable nanostructures on optical fibers' cores. IR laser-induced structures inscribed on low-loss, radiation-hard silica fibers were used to develop point and distributed sensors for in-pile nuclear reactor measurements. The sensors were subjected to, arguably the most challenging of artificial environments, with temperatures above 600°C, and high neutron fluxes at levels above 1.2×10^{14} n/s/cm^2. The sensors were also used to monitor the temperature distribution inside of a solid oxide fuel cell (SOFC). The information obtained from the operational SOFC can be used to prolong its lifetime and increase its efficiency.

Lastly, additive manufacturing embedding of optical fibers into metallic parts were attempted. A nickel-iron alloy, Invar-36, was investigated as a coating material for silica. The coefficient of thermal expansion (CTE) of Invar-36 can be carefully engineered to be close to that of silica. With a reduced CTE mismatch at the glass-metal interface, problems of adhesion and delamination can be deterred to extreme conditions. The proposed sensor designs and implementations would allow monitoring complex structures, and harsh environments like in SOFCs, gas turbines, robotics, or in high performance machinery, with minimal invasiveness.

Table of Contents

List of Tables

List of Figures

Preface

This research was supported in part by an appointment to the National Energy Technology Laboratory Research Participation Program, sponsored by the U.S. Department of Energy and administered by the Oak Ridge Institute for Science and Education.

To Hana and Lina.

1.0 Introduction to Optical Fiber Sensors

Silica-based optical fibers have been ubiquitously present, in the last three decades, in various optical schemes to allow for distributed, or point sensing of a multitude of physical quantities. One unique trait of optical fibers is, when coupled with an interrogation scheme, their ability to perform distributed measurements and provide spatial profiles of the quantity measured. An unmodified fiber can be used to perform spatially continuous measurement along the fiber with high spatial resolutions.

One distributed sensing scheme is the Rayleigh-based optical backscattering reflectometry technique, which has been successfully deployed in various distributed sensing scenarios for monitoring temperature, strain, and concentration of certain gas species. This method combines the high resolution (0.1 mm) of the interrogation technique with the merits of deploying optical fibers as distributed sensors; like low attenuation on signal transmission, a 0.2 dB/km for conventional germanosilicate single mode fibers at 1550 nm operation; signal multiplexing, and proven resilience to electromagnetic interference [1], offering a great solution for distributed sensing problems. This renders optical fiber-based sensors superior their electronic counter-parts.

Another distributed sensing scheme is based on Brillouin scattering. Using an optical time-domain analyzing scheme, the spatial distribution of temperature and/or strain can be determined, albeit with a lower spatial resolution, but can be utilized for longer distance applications (~kilometers). The distributed fiber sensors that can withstand harsh environments are particularly useful for energy applications from fossil fuel, to renewable energy, and to nuclear energy.

Ultrafast, femtosecond lasers are frequently used to introduce refractive index changes, or nanometric defects on optical fiber cores. These laser-induced refractive index changes can be generated with spatial continuity to develop distributed sensors, or periodically to develop a point sensor; or a fiber Bragg grating (FBG). The laser-induced defects are considered as enhancements where the laser-treated fiber core sections usually function as temperature sensors with higher thermal stability [2].

Optical fiber-based sensors have demonstrated very low intrusiveness to the structures or environments they are monitoring. Additionally, optical fibers endure harsh environments and additive manufacturing processes of high temperatures, tensile strains, and/or ionizing radiation levels that makes it possible for optical fiber-based sensors to appear in numerous domestic, industrial, and military applications, as we will be discussed in the following sections.

1.1 Optical fibers for ionizing radiation detection and quantitation using Rayleigh OFDR interrogation scheme

The safe and efficient operation of nuclear power systems relies on gathering a multitude of information by sensing networks crossing the entire nuclear power system during both normal and distressed operation scenarios. As a sensing-technology, well-suited for harsh environments, optical fiber sensors are primary candidates for nuclear energy applications to collect information at both component and system levels. Using multiplexing techniques, point sensors such as fiber Bragg gratings have been used to monitor physical parameters such as temperature and strain for radioactive environments. Various distributed sensing schemes are also being explored for the nuclear energy industry.

Akin to photosensitivity of optical fibers under various laser irradiations, ionized nuclear radiation could induce irreversible changes in optical fibers. Several studies have shed light on radiation effects on optical fibers. It has been established that the predominant effect of radiation on optical fibers is the creation of color centers, which is responsible for both radiation-induced attenuation (RIA) and formation of new photo luminescence centers [1, 3]. Other radiation effects include density changes leading to changes in the index of refraction, polymer alteration including strength degradation and embrittlement, and bonding configuration changes [4, 5].

The sensitivity of optical fibers to nuclear radiation has often been regarded as a vulnerability. Most of the research effort for several decades has been focusing on studying the ionizing radiation’s adverse effect on optical fibers, and the development of optical fibers that exhibit traits of high resilience to nuclear radiation in various physical sensor scenarios [4-10]. These efforts have yielded several fiber products that are useful for various radiation environments.

On the other hand, optical fiber sensitivity to radiation can be explored from an opposite perspective. The radiation-induced optical property changes provide a means to detect radiation. This, combined with distributed fiber sensing schemes such as Rayleigh scattering optical frequency domain reflectometry (Rayleigh OFDR), provide an excellent technique to measure radiation with high spatial resolution of up to 1 cm per measurement along the entire optical fiber using one fiber, and one fiber feedthrough.

In chapter 2, we propose the use of radiation sensitive optical fibers for distributed radiation measurements. Special fibers that are sensitive to gamma radiation as low as 1 Gy and that can withstand total dosages in excess of 10,000 Gy are studied for high-spatial resolution radiation sensing. As a low-cost sensing platform, the radiation-sensitive optical fibers can be readily embedded in construction materials such as concrete or components such as steam pipes and electrical cables in new or existing nuclear energy systems. This enables ubiquitous deployment of distributed radiation sensors for a large number of scenarios. The high spatial resolution radiation detection will improve situational awareness to quantify the severities of problems in distress situations. During normal operations, the irreversible changes and degradation of components, structures, and systems under radiation can be correlated with distributed and accumulated radiation dosages measured by the optical fibers [11, 12]. This will enable better prediction of the operation lifetime and a cost-effective maintenance schedule.

1.2 Specialty optical fibers for simultaneous detection of temperature and strain using BOTDA interrogation scheme

Brillouin optical time domain analysis (BOTDA) is the sensing of temperature and strain changes along an optical fiber by measuring the frequency shift changes of Brillouin backscattering. As compared to other sensing modalities (e.g. Rayleigh- and Raman-based), BOTDA is not strictly power dependent and can be used over distances as long as 100 km. BOTDA may be used to monitor the operation and structural integrity of oil and gas pipelines and wells, electrical power lines, and transportation infrastructure (e.g. bridges, railroads, highways) [13, 14].

Because frequency shift changes are a linear combination of temperature and strain changes, their discrimination is a challenge [15-17]. Temperature and strain can be discriminated by solving a system of linear equations that comprise measurements of frequency shift changes from two spatial channels (spatial channels 1 and 2). The spatial channels are subjected to the same temperature and strain changes yet have different temperature and strain coefficients. For example, two single mode optical fibers can be used [18].

However, because they occupy different claddings, they may not experience the same temperature and strain changes. Also, two spatial modes of a multimode optical fiber can be used

[19-21]. However, because they occupy the same core, the multimode optical fiber may not be fabricated such that the coefficients are sufficiently different.

Recently, it was demonstrated that two cores of a multicore optical fiber can be used [22, 23]. This contrasts the use of two single mode optical fibers and two spatial modes of a multimode optical fiber. Because the cores occupy the same cladding, they may experience the same temperature and strain changes. And, because the cores are separate, the multicore optical fiber may be fabricated such that the coefficients are sufficiently different. In general, the ability of spatial channels to discriminate temperature from strain is quantified by error amplification factors which are a measure of the coefficients' differences [24]. For multicore optical fibers, temperature (strain) error amplification factors greater than 12.05°C/MHz (253.77 μϵ/MHz) were demonstrated. Therefore, it may be of interest to fabricate a multicore optical fiber such that the error amplification factors are less.

In chapter 3, a multicore optical fiber that has two distinct cores is fabricated. The differences between the cores' temperature and strain coefficients are such that temperature (strain) changes can be discriminated with error amplification factors of 4.57°C/MHz (69.11 μϵ/MHz), being 2.63 (3.67) times less than previously demonstrated. As proof of principal, using the multicore optical fiber and a commercial BOTDA, the temperature (strain) changes of a thermally expanding metal cylinder are discriminated with an error of 0.24% (3.7%).

1.3 Fiber Bragg gratings for monitoring temperature changes inside nuclear reactor cores

Nuclear reactors are reliable and low-cost, carbon free energy sources to supplement intermittent renewable energy production tied to the electric grid. To ensure operational safety, multiple-level redundancies are built into nuclear reactors. These fail-safe designs of nuclear power systems often lead to prolonged construction periods and higher construction and operational costs. An alternative approach to ensure operational safety is through better sensing and control schemes. High spatial resolution and multi-modal information gathering sensors through the nuclear power system could have potentials to reduce design redundancy, and subsequently overall cost of the nuclear power systems. Thus, development and implementation of radiation-hardened advanced sensors in reactor cores is a major theme for the development of next generation nuclear power systems.

Reactor cores are arguably the most challenging of artificial environments. High temperatures (up to 800°C) and strong neutron fluxes at levels of 1×10^{14} /s/cm^2 essentially put most of sensor devices out of operation. Currently, thermocouple temperature sensors are probably the only reliable measurement devices for in-core applications. Since the 1990s, researchers have being exploring the use of optical fiber sensors for in-core monitoring for nuclear power systems [25]. Well known for their resilience in harsh environments [26], fiber Bragg grating (FBG) sensors and distributed fiber sensors can perform multiple simultaneous measurements including temperature, strain, pressure, water levels, and chemical sensing with high spatial resolutions. This makes FBG sensors attractive sensing devices for nuclear energy applications.

Study of the behavior of various types of FBGs in ionizing radiation environment has spanned for over two decades [27]. Probably the most comprehensive studies are from Fernandez and Gusarov et al., which reported their experiments on FBG sensors in harsh nuclear core environments at the BR1 and BR2 reactors (SCK.CEN) from 1999 to 2008. In 2002, they reported the use of FBGs in various optical fibers, especially photosensitive fibers and telecommunications fibers for on-line temperature monitoring in low neutron flux (~10^{11} n/s/cm^2) and high neutron flux (~10^{14} n/s/cm^2) environments. Moderate gamma irradiation was also presented in those studies [28, 29]. FBG sensors reported in these studies were irradiated at low temperature from 10 to 80°C, while FBGs endured various radiation doses up to 160 MGy of gamma radiation and a total fast neutron fluence (> 1 MeV) up to 1.47×10^{17} n/cm^2.

After comparative studies using a thermocouple sensor as a reference, it was reported that FBG sensors can measure temperature in those environments with a 3°C accuracy. Studies carried out by Fernandez and Gusarov et al. reveal that both optical fiber materials and FBG sensor fabrication process have great impacts on performance of FBG under these harsh conditions [30-34]. Fielder et al. [35] also claimed an 87% survival rate of FBG sensors in neutron/gamma radiation studies, where FBG fabricated in Ge-doped and B/Ge co-doped fibers endured 1012 hours of fast neutron flux (1×10^{13} n/s/cm^2) irradiation with accumulated neutron fluence of ~5×10^{19} n/cm^2, and γ-irradiation of 2×10^3 MGy.

Recently, Remy et al. [36] used FBG sensors to measure the longitudinal compaction effect on pure silica core and F-doped core samples exposed to fast neutron fluences of ~4.76×10^{19} n/cm^2 at 291°C by measuring the radiation-induced length changes, namely the longitudinal length shortening of the fiber samples.

In chapter 4, we report in-core studies of FBG sensors at radiation levels and operating temperatures similar to those occurring inside commercial nuclear reactors. FBG irradiation tests were performed at >600°C with fast neutron fluxes above 1.2×10^{14} n/s/cm^2 for a 55 day continuous irradiations with 5.7×10^{20} n/cm^2 accumulated dose, at least a 10-fold higher dose than previously reported. To evaluate the potential capability of the fiber sensors to monitor reactor anomalies, multiple events were implemented during the irradiation to create abrupt changes of reactor temperatures and neutron powers. FBG responses to these abnormal conditions were characterized to assess thermal-optic properties of FBGs at different stages of irradiation and their temporal response during abrupt temperature changes. Experimental results presented in chapter 4 provide a quantitative evaluation of FBG performance in commercial reactor cores. It also provides cues on how to mitigate FBG property drifts in reactor cores in order to improve both reliability and accuracy of FBG sensors for in-core applications.

1.4 Distributed ultrafast laser-enhanced optical fiber sensors for monitoring in-pile and internal solid oxide fuel cells environments

Ultrafast lasers are widely used to write structures onto optical fiber cores. The effect of focusing a IR light onto a fiber core is a change of the refractive index of the silica-based core. The refractive index changes are due to the formation of nanostructures on the fiber core. These structures can form an FBG when inscribed periodically using a plane-by-plane laser on core translation; or using an interference pattern from a phase mask, or an interferometry scheme. The refractive index changes can also be made with spatial continuity to comprise a continuous nanostructure. These artificially laser-induced nanogratings can function as distributed sensors.

The nanostructures induce transmission losses to the optical signal and enhance the Rayleigh backscattered signal, hence can be coupled with Rayleigh interrogation schemes. Moreover, they exhibit higher thermal stability compared to the intrinsic, non-artificial sites on the fiber core. The nanostructured section of the fiber core is less vulnerable to temperature variations, whereas natural thermal processes easily alters intrinsic scattering sites in non-artificial fiber cores. In chapter 5, a novel method of laser processing is harnessed to fabricate thermally stable, optical fiber-based, distributed sensors. The distributed sensors were used to monitor temperature changes inside an operational nuclear reactor core. Also in chapter 5, a detailed presentation of an array of Rayleigh-enhanced fibers that were used to measure temperature changes inside a solid oxide fuel cell (SOFC). The first successful in situ measurement of a high-temperature operational SOFC to this date.

1.5 Embedding optical fibers into metallic parts using additive manufacturing

In the last two decades, considerable research endeavors were conducted to embed fiber optics into metallic structures driven by the need for sensors to withstand harsh environments. Fiber optic sensors have low weight and offer very little intrusiveness which allow them to be shielded from the hostile environment without disrupting the host structure.

These formed smart structures with in situ sensing capabilities demonstrated proper ways of inspecting system integrity using non-destructive testing, and monitoring the subsurface changes in temperature and strain [37]. Moreover, the extended functionality of these “smart” parts allow for optimal asset management [38]; a longer and more reliable operation with real-time feedback in the event of mechanical instability and/or structural failure, replacing the need for visual inspection [39, 40].

Silica-based optical fibers can deploy various sensing techniques like FBGs, Fabry-Perot (F-P) etalon, or simply a strand of optical fiber connected to a proper frequency domain interrogation technique like Rayleigh or Raman Reflectometers, or a time domain interrogation technique like Brillouin Scattering Reflectometer or Analyzer.

There are numerous potential applications for embedded strain sensors. They can be used to measure the strain field in layered materials, or as pressure sensors, or to monitor the accumulation of residual strains during layered manufacturing. They can be deployed in complex structures, harsh environments like in gas turbines, robotics, or in high performance machinery [39].

The difference in the coefficient of thermal expansion (CTE) between the host metallic part and the silica-based optical fiber constitutes primarily a challenge for embedding optical fibers into metallic parts. It is also an obstacle in the way of internal monitoring of high temperature metals using fiber sensors, under operational conditions. For operation at high temperatures, the sensing component would suffer from the internal tensile stresses [41] arising from the mismatch in CTE that would compromise the bonding between silica glass and surrounding metal [38]. The axial components from stresses transfer to the glass-metal interface, and ultimately cause slippage of different parts and delamination, when these stresses overcome the adhesion. Breakage(s) of the fiber sensor can also occur if the glass-metal interface does not clear the fiber at all points of contact, creating shear stresses that often break the glass fiber.

Different adhesion mechanisms have been demonstrated in various literatures, as discussed below, but the delamination problem remains as adhesion breaks down at a certain point during operation at high temperatures. Increasing interface adhesion and methods for reducing the stresses associated with CTE mismatch between the embedded optical fiber sensor and the metallic part are key challenges that must be overcome for deployment in the highest possible temperatures of operation.

In chapter 6, a new embedding process is studied. A metallization and embedding technique using composite metal alloy, with carefully crafted CTE, to better manage the CTE mismatch between metal components and optical fiber. A conventional single mode optical fiber is firstly metalized with a keying layer (tungsten or chromium), electro-coated with Invar-36 alloy, and embedded in stainless steel parts. The choice of encapsulation with an Invar buffer is anticipated to deter delamination to more extreme temperatures. The targeted Invar-36 alloy composition would have a CTE (1.2 ppm/K) that is close to (approximately 2 times) that of silica glass, while the discrepancy in CTE between Invar-36 and stainless steel would be overcome by strong adhesion between the two metals, hence achieving distributed sensors with higher sensing ranges.

2.0 High Spatial Resolution Radiation Detection using Distributed Fiber Sensing Technique

Optical fibers have been used to monitor ionizing gamma, neutron, or mixed, gamma and neutron, radiation. Previous studies reported in literature are mostly based on radiation-induced quenching of optical fluorescence in rare-earth doped fiber [42]. However, these radiation sensing schemes are only suitable for point measurements and cannot provide distributed measurements with high spatial resolutions.

In this chapter, we present our study on using optical fibers and distributed fiber-sensing schemes to perform real-time distributed gamma-ray radiation sensing with high spatial resolution. The radiation induced optical property changes of a state-of-art, ionizing radiation sensitive, Al-doped fibers were studied using cobalt-60 gamma-ray sources. The distributed optical loss of the fiber was characterized using Rayleigh backscattering optical frequency domain reflectometry (Rayleigh OFDR). The optical loss of the un-protected specialty fiber under various gamma dose rates remains linear up to 100 grays (Gy). Using the gamma radiation-sensitive fiber, the localized optical losses measured by Rayleigh OFDR were mapped to the accumulated gamma radiation dosage with 1 cm spatial resolution, effectively quantitating the ionizing radiation field around the radioactive isotope.

The study was extended further to explore the potential for multi-functional distributed fiber sensor by integrating distributed fiber temperature and gamma ionizing radiation sensors in electrical cables for multi-functional measurements to improve the safety of nuclear power systems at both the component and system levels. The radiation-sensitive distributed fiber sensor and one radiation-hard conventional telecommunications fiber were deployed in an electrical cable, and tested for radiation, and temperature sensing. As sensors that can be readily embedded in a wide variety of materials and structures, radiation-sensitive fibers can be low-cost and highly flexible tool to gauge the performance degradation and longevity of materials and components used in nuclear power systems.

2.1 Experiments on the Radiation-Sensitive Fibers

2.1.1 Experimental setup

Aluminum doped single mode fibers from Corning Incorporated [43] were used for distributed radiation measurements for its increased sensitivity to gamma radiation [11]. Aluminum is a common dopant that is used extensively to raise refractive indices of fiber cores especially in erbium-doped optical fibers. Systematic radiation studies have revealed that radiation induced attenuation (RIA) of Al- and Er- co-doped fibers depends on aluminum concentrations [44, 45]. RIAs of Al- and Er-co-doped fibers follow linear relationship with Al concentrations [46]. This trait makes Al-doped fibers useful devices for distributed radiation sensing. The sensitivity and dynamic ranges of the distributed radiation sensors can be potentially tuned by the Al dopant concentration.

The preform of the Al-doped fiber was fabricated through an outside vapor deposition (OVD) process. The aluminum concentration in the fiber core is 4.8% to achieve a refractive index contrast $\Delta n=0.3\%$ between the core and the cladding for single-mode guiding at 1550 nm. The OVD process allows the fabrication of fibers with single-mode fiber cores co-doped by both aluminum and germanium. The concentration of aluminum can be adjusted and reduced through addition of germanium dopants to maintain the required refractive index contrast between the fiber core and cladding (Δn=0.3%) for the single-mode operation in the telecom window [47].

To achieve high spatial resolution interrogation, the Rayleigh backscattering OFDR distributed fiber sensing scheme was used to interrogate sensing fibers to achieve high spatial resolution. An Optical Backscattering Reflectometer (Luna Innovations® OBR4600) was used to measure the backscattering profile of the Al-doped fibers. The radiation tests were run in the Westinghouse Research Facility (Churchill, PA) using a bundle of ^{60}Co gamma radiation rods. Eight ^{60}Co rods were inserted in an aluminum holder as the gamma radiation source for the experiment, shown in figure 1(a). A single mode aluminum doped fiber (fiber under test or FUT in figure 1(b)) was wrapped around an acrylic cylinder that has an outer diameter of 14.5 cm and a height of 30.48 cm. The fiber was carefully wound into a helical structure with an average pitch or ring spacing of 9.5 mm, and it was held in position by an adhesive tape at every loop as shown in figure 1(b).

In total, an 11.4 m long Al-doped FUT was wrapped on the surface of the cylinder for radiation measurements. One end of the FUT was connected to the Rayleigh OFDR interrogation system through fusion splicing to an angled physical contact (APC) patch cable from the top end of the acrylic cylinder as depicted in figure 1(b). The other end of the fiber was left loose and laid on the table of the hot cell after tying it into several knots with small radii for light to leak out the sharp bends, to prevent the back-reflection of the fiber end.

A simplified diagram of the OBR instrument is schematically shown in figure 1c, which can be used to explain the essence of the operational principles of the OFDR instrument. A highly coherent continuous wave (CW) tunable laser source (TLS) is coupled through a fiber coupler (FC) into the reference with the length L and the FUT. The reflections from Rayleigh backscattered signal in the test arm and the reference arm are coupled back through the same fiber coupler and mixed at the photodetector (PD). As the TLS's wavelength linearly sweep from λ_0-$\Delta\lambda/2$ to $\lambda_0+\Delta\lambda/2$, locations and amplitudes of Rayleigh backscattering signal along the fiber can be retrieved through a fast Fourier transform (FFT) algorithm. The detailed description of the instrument can be found in [12, 48].

The dosimetry calibration measurement was performed using optically stimulated luminescence (OSL). The OSL dosimeters (nanoDot model dosimeter by Laudauer Inc.) used are effective for doses in the linear range, which extends from 0.05 mGy to 100 Gy. Crude estimates of the dose rate were used to determine the duration of the dosimetry runs such that the OSL dosimeters were neither overexposed nor underexposed. Seven dosimeters were positioned on the cylinder as shown in figure 1(b). Four were distributed with equal spacing about the cylinder's exterior at the same elevation from the cylinder bottom, and this elevation was measured as the shortest Euclidean distance measured from the cylinder's surface to the midpoint of the radioactive source and was expected to be the point of highest exposure to radiation. The other three were positioned on the cylinder's exterior, each at a different elevation. The dosimeter positions were carefully noted by stressing the fiber at all the marked dosimeter locations and using the OBR distributed strain sensor to determine the strained positions on the fiber length.

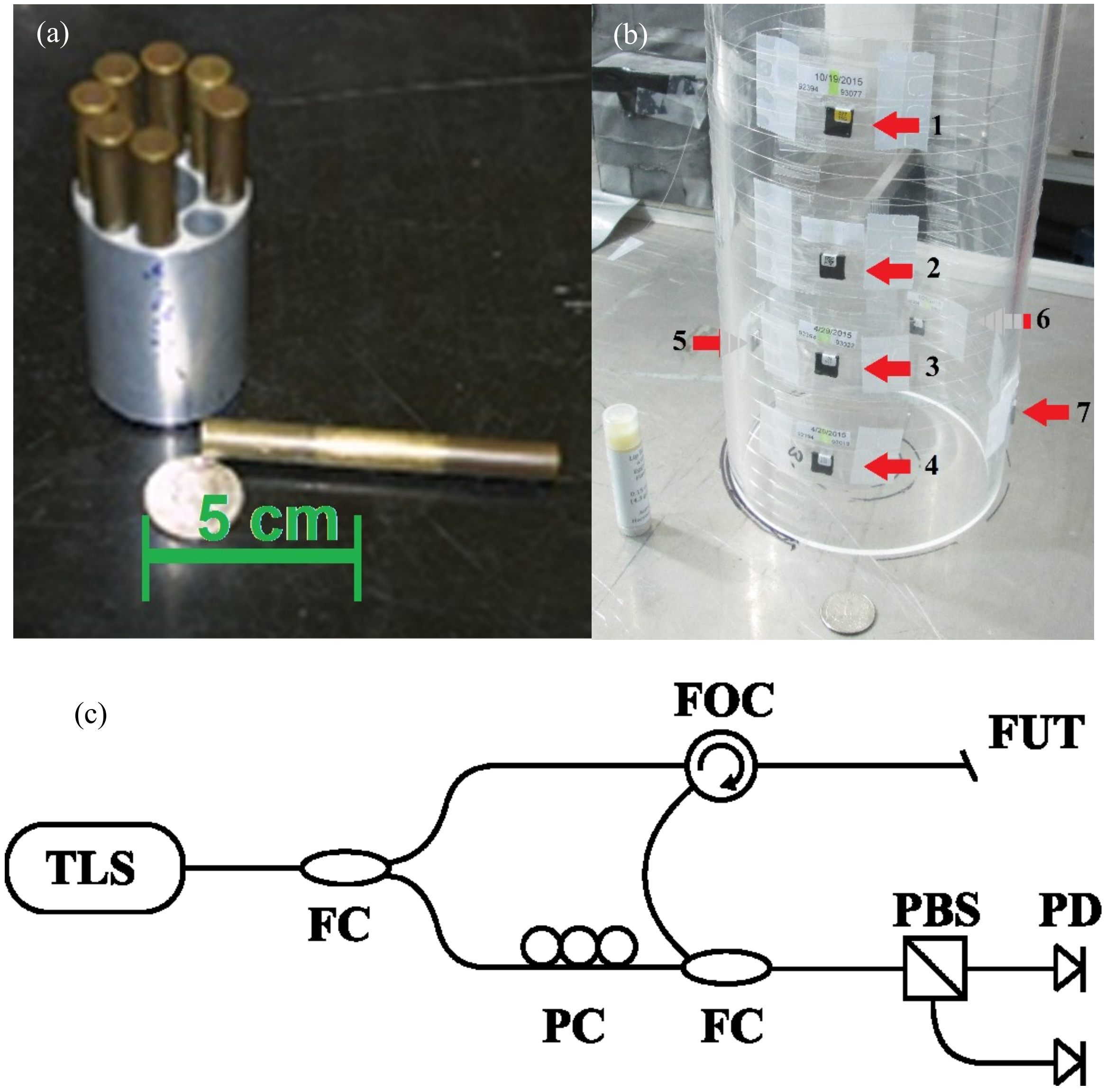

Figure 1 (a) A photograph of the gamma radiation source bundle that constitutes of eight ^{60}Co radioactive isotope rods placed inside of an encasing Al holder. (b) A photograph of the acrylic cylinder with Al doped FUT wound around it in a helical structure, and the OSL dosimeters placed at seven different locations on the cylinder are pointed at with red arrows. (c) A simple schematic illustrating the Rayleigh-based OFDR interrogator used and connected to the FUT on the cylinder in (b). The system comprises a tunable laser source (TLS), fiber coupler (FC), polarization controller (PC), fiber optic circulator (FOC), polarizing beam splitter (PBS), and a photodetector (PD) [49] © 2017 IEEE.

Dosimetry measurements were performed in parallel to accurately determine the radiation dosages experienced at different sections of the fiber tested. The fiber was tested using the OBR distributed strain measurement function, again to distinguish the part of the FUT that constitutes the helical structure from the rest of the fiber length. The cylinder with the FUT was positioned inside a hot cell at the Westinghouse radiation testing facility, and the fiber was carefully laid through the chamber's radiation secured hatch to be connected to the OBR right outside the hot cell. Since the RIA is highly dependent on temperature changes [50, 51], the hot cell temperature was controlled to maintain a 21.6 ±1 °C temperature throughout the whole run to prevent variation of RIA due to temperature.

Other factors affecting the optical signal transmission on the fiber like humidity (that can affect the hydrogen content through OH absorption), and bending losses, were also maintained unchanged. It is imperative here that the parameters concerned, which influence the RIA are only the total dose and dose rate dependence.

Radiation testing commenced by placing the ^{60}Co gamma radiation source coaxially inside the cylinder using a pair of mechanically controlled manipulators. Rayleigh backscattering profiles were continuously acquired once the radiation source was in position. The maximum spatial resolution of the OFDR instrument was set as 38 μm while the TLS scanned wavelengths from 1545.86 nm to 1588.72 nm. After an initial irradiation of three minutes, the radiation source was removed and the dosimeters were collected to calibrate the radiation intensity. Once all dosimeters were retrieved, the source was then placed back again position to resume radiation. The Rayleigh backscattering profile of the fiber wrapped on the cylinder was monitored with 60 seconds intervals. Measurements continued until the entire section of the fiber wrapped on the cylinder significantly degraded and the optical backscattering reflectometer could no longer determine the reflected optical signal on the entire length of the wound fiber due to radiation induced attenuation of the backscattered signal.

2.1.2 Data analysis and discussion of the results

To process the measured data, the amplitude of the optical signal (dB/mm) along the fiber length was recorded from the OFDR instrument with 38 µm spatial resolution. Two hundred and fifty adjacent data points were averaged to reach 1 cm spatial resolution. The cumulative intensity of the optical signal along was the average of these 250 points. Figure 2(a) shows the cumulative intensity along the FUT for gamma-ray exposures of 4, 5, 7, and 9 minutes. The localized losses are shown in figure 2(b). Each curve is obtained from the absolute value of the derivative of the corresponding smoothed cumulative optical signal amplitude presented in figure 2(a). The losses along the fiber systematically increase at all points on the fiber length due to the exposure to gamma ionizing radiation.

The localized losses peak at the locations closest to the radiation source, and reveal the source's radiation profile. It was determined that the OSL dosimeters closest to the ^{60}Co source measured doses in the range of 20 to 30 Gy, well within the linear response region of the OSL dosimeters. The accuracy of the nanoDot model dosimeter is specified by the vendor (Landauer, Inc.) to be ±10%. These measured doses and the known duration of the dosimetry run enable the calculation of dose rates experienced by the fiber at the location of the dosimeters, or the dosage as a function of time with 10% accuracy.

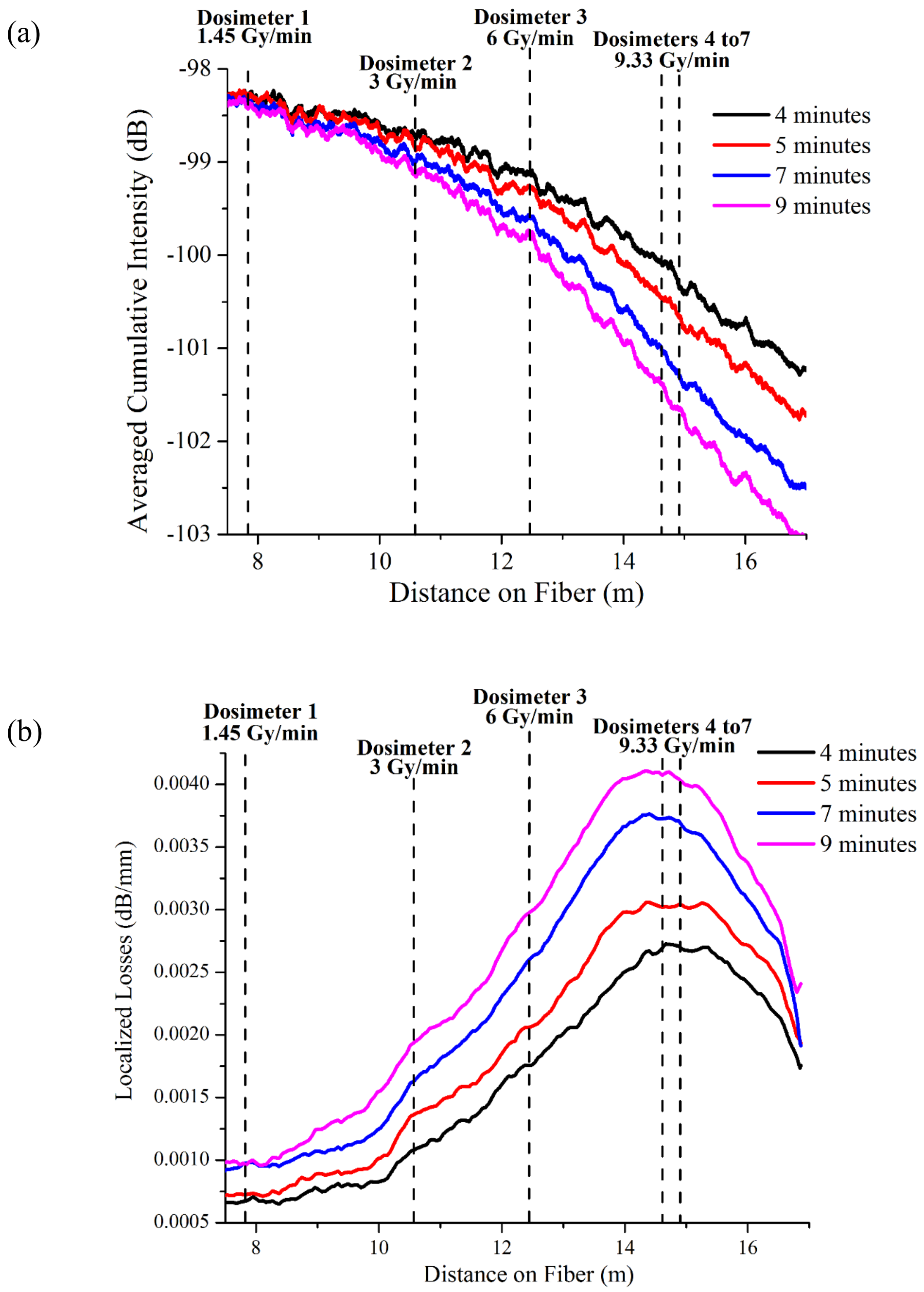

Figure 2 (a) Cumulative intensity at different spatial points on the fiber, for gamma radiation exposures at 4, 5, 7, and 9 minutes. The curves were averaged for every adjacent 250 points. (b) Spatially localized losses along the length of the fiber wrapped around the cylinder obtained from applying the MATLAB algorithm to the four cumulative intensities in (a). The dosimeter locations and measured dose rates are marked on the curves. The curve annotated 9 minutes marks the last measurement obtained in the linear range before the non-linear variation of RIA appeared first at the section closest to the radiation source [49] © 2017 IEEE.

Figure 2(b) presents localized loss along the fiber at four different exposure times of 4, 5, 7, and 9 minutes. The locations of dosimeters are also labelled in the figure, where gamma dose rates were measured by OSL dosimeters. The dose rates for the four dosimeters placed at the same elevation were averaged, while the rest of the dosimeters revealed the dosage rate variation with elevation measured from the bottom of the cylinder.

The localized RIA profiles measured by the Rayleigh OFDR instruments provide means of distributed sensing of gamma radiation dosage with high spatial resolution. To explore the applicability of the Al-doped fibers for gamma radiation measurement, the localized RIA as a function of accumulated dosages is studied at four locations with dosimeter calibrations. These results are presented in figure 3(a-d).

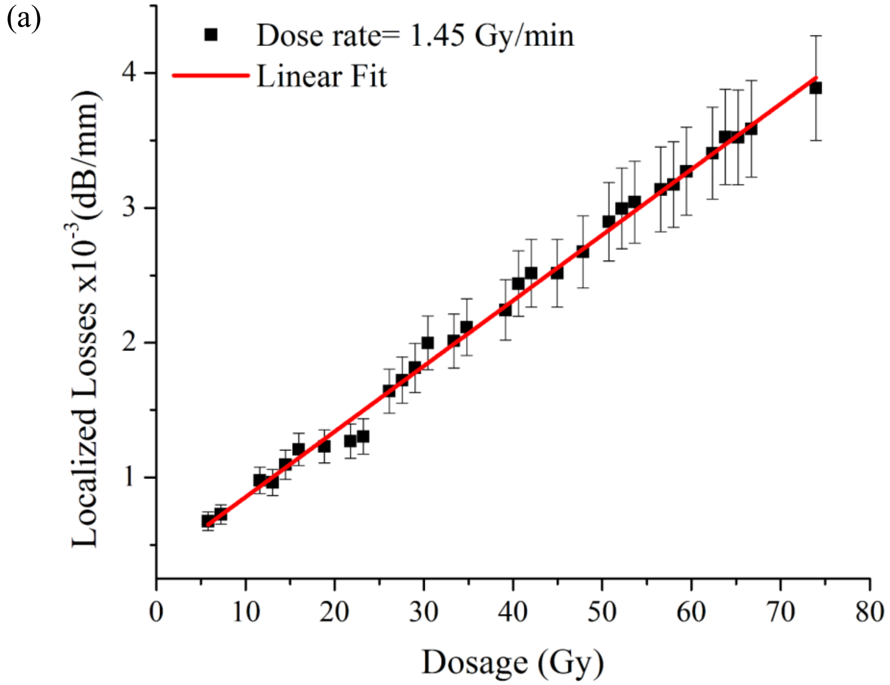
(a)
Dose rate= 1.45 Gy/min
Linear Fit
Localized Losses x10^-3(dB/mm)
1
2
3
4
0
10
20
30
40
50
60
70
80
Dosage (Gy)

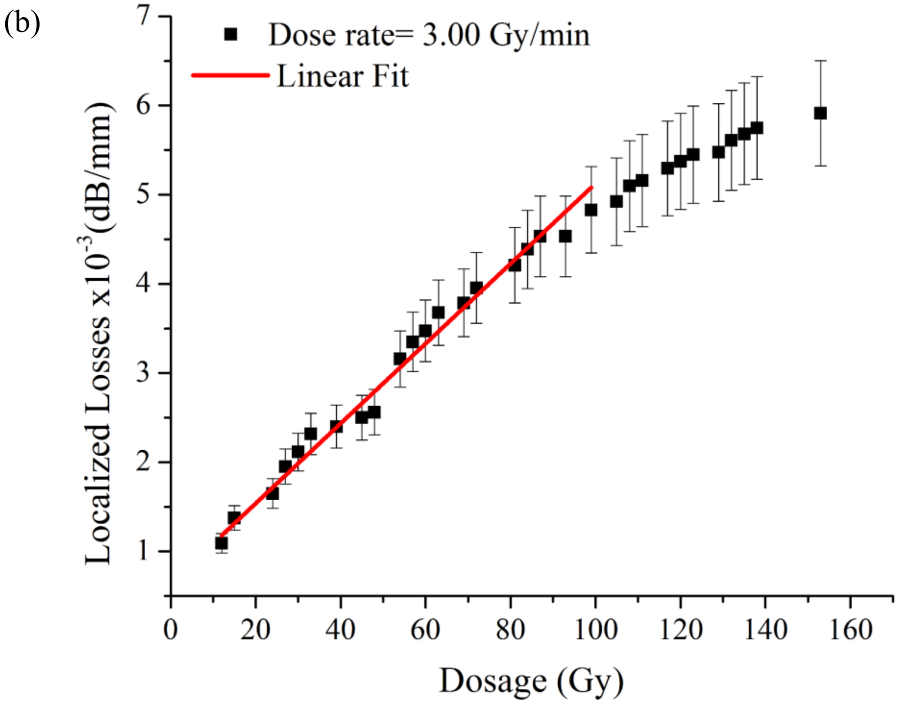
(b)
Dose rate= 3.00 Gy/min
Linear Fit
Localized Losses x10^-3(dB/mm)
1
2
3
4
5
6
7
0
20
40
60
80
100
120
140
160
Dosage (Gy)

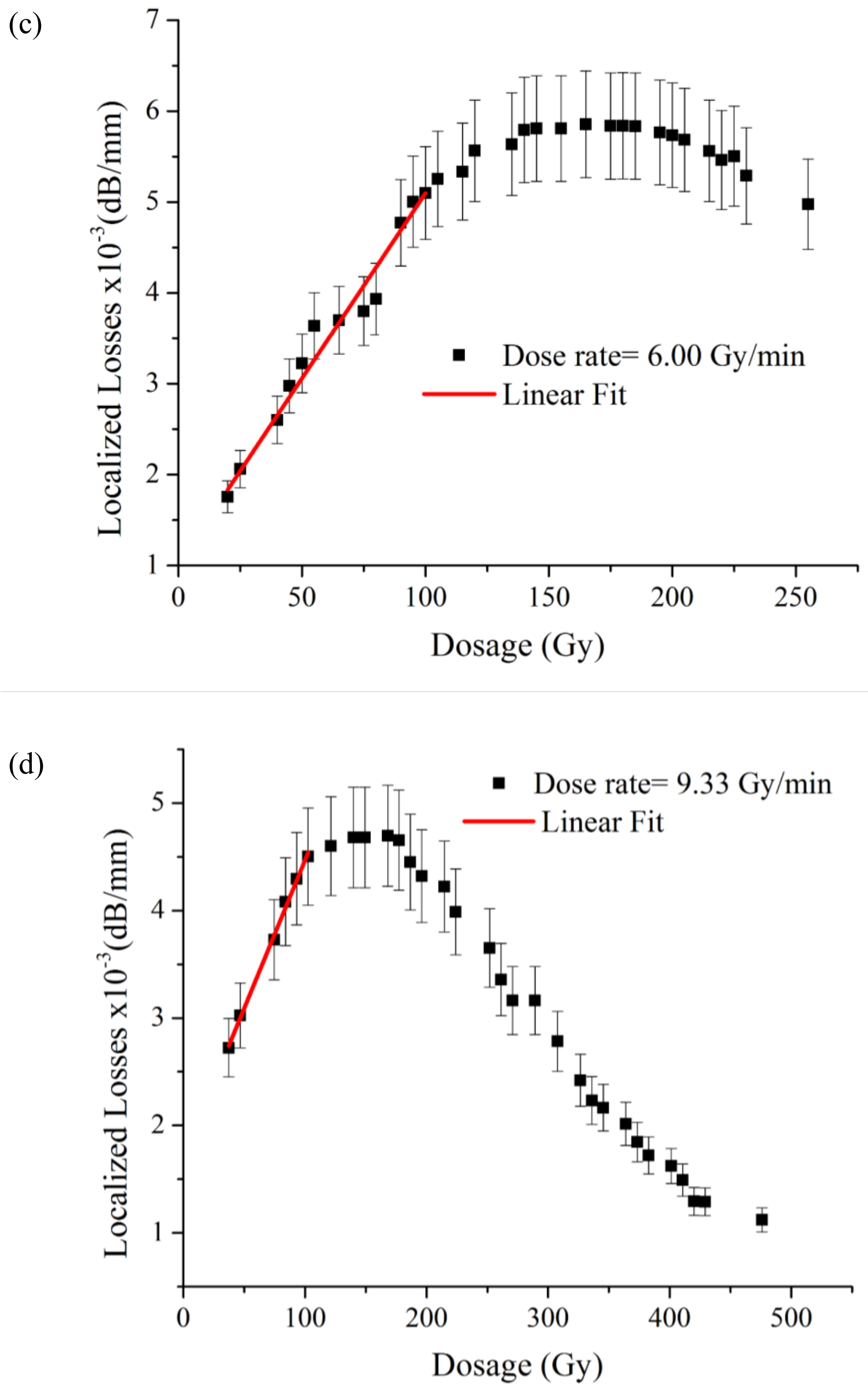

Figure 3 Radiation induced localized losses plotted against gamma radiation dosage for the dosimeters designated as (a) 1, (b) 2, (c) 3, and (d) 4 to 7. The errors bars reflect the 10 % uncertainty due to the OSL dosimeters. The plots were linearly fitted in the linear range (< 100 Gy) and the fitting specifications and results reported in table 1 [49] © 2017 IEEE.

At all locations, while dose rate calibrations are available, localized RIAs grow with accumulated dosage when the accumulated dosage is less than 130 Gy. When the accumulated dose is less than 100 Gy, the localized radiation induced optical losses follow linear relationships with total dosages as shown in figures 3(a-d). The linear fits are also shown in the figures. The slopes and intercepts of the linear fits for the four dose rates calibrated by the OSL dosimeters are also summarized in table 1. At low dose rates of 1.45, 3, 6 Gy/min, respectively, the linear fits were carried out using accumulated dosage between 5.8 and 100 Gy. The linear fit for 9.33 Gy/min was performed using accumulated dosage between 37.33 and 102.67 Gy. All linear fit yields excellent R-squared fitting confidence greater than 96.9 % as presented in table 1.

However, the longer exposure with accumulated dosage above 130 Gy leads to saturation of localized RIA and further reduction of localized RIA. This is consistent with several prior irradiation studies of RIA growth kinetics on other fibers using ^{60}Co gamma ray sources [1, 52, 53]. This can be related to competition between the radiation-induced defect generation, which leads to increase of RIA, and the radiation-induced defect bleaching that tends to reduce the RIA.

The RIA saturation at both higher dose rate and accumulated dosage shown in figures 3(b-d) also highlight the limitation of the simple linear calibration of the Al-doped fiber currently used for these studies. When the dose rate reaches 9.33 Gy/min, the linear slope decrease to 0.00028 dB/mm/Gy, which is significantly lower than those at 6 Gy/min or lower. In all dose rates, RIA starts to saturate at 130 Gy and beyond. When the growth kinetics of localized RIA does not grow with the accumulated dosage, it becomes difficult to use fiber as a radiation sensor. This saturation effect limits the maximal accumulated dosage that can be effectively measured by the optical fibers.

Table 1 Slopes of the linear region at different radiation dosage rates with their corresponding standard error and intercepts.

Dosimeter Designation	Dosimeter Elevation (mm)	Dosage Rate (Gy/min)	Calibration Slope $\times 10^{-5}$ (dB/mm/Gy)	Standard Error in Slope $\times 10^{-7}$ (dB/mm/Gy)	Ordinate Intercept $\times 10^{-4}$ (dB/mm)	Linear Fitting Range (Gy)	R-squared
1	208	1.45	4.86	8.16	3.68	5.80-73.95	0.99163
2	149	3.00	4.48	12.47	6.40	12.00-99.00	0.98550
3	108	6.00	4.08	22.92	10.20	20.00-100.00	0.96925
4- 7	55	9.33	2.75	6.72	17.10	37.33-102.67	0.99703

It is worth to note that the saturation effect depends on type of fibers used for measurements [50, 51], which can be adjusted by controlling the dopant species and concentrations in fiber cores during the fiber manufacturing process. Given that the Al-doped fiber is far more sensitive than other optical fibers to the gamma radiation, the reduction of aluminum dopant concentration (currently at 4.8 wt %) could yield distributed radiation fiber sensors with larger linear ranges in terms of both dose rates and accumulated dosages. Within the linear calibration ranges of the fiber as presented in figure 3, it is possible to relate localized RIA data measured by the fiber to the localized accumulative radiation dosage. The vast amount of data provided by the distributed optical loss measurements as both functions of fiber length and irradiation time (e.g., figure 2) can potentially yield far more detailed radiation measurements than conventional dosimeters.

To explore this potential, localized losses as functions of accumulated dosages at four dose rates shown in figure 3 are plotted in one figure with accumulated dosages from 5.8 Gy to 100 Gy as shown in figure 4. All these data are fitted together using one linear function. Despite system error at the high dose rate of 9.33 Gy/min, a single linear fit can be used to relate radiation dosage to the localized RIA measured by the Rayleigh OFDR instrument as depicted in figure 4 as:

$$\text{RIA (dB/mm)} = (4.81\times10^{-5})\times\text{Dose (Gy)} + 4.33\times10^{-4}\ \text{(dB/mm)}. \qquad (2\text{-}1)$$

The R-squared confidence of the linear fit is 97.4%. Using this linear relationship, the accumulated dosage can be correlated using the localized RIA measurements with an average error of 5.5% for dose rates of 1.45, 3, and 6 Gy/min. At the dose rate of 9.33 Gy/min, the average error is higher at 12.4% due to saturation effects as presented in figure 3(d).

Fitting results shown in figure 4 suggests that, within an accumulated dosage of 100 Gy and with a maximum dose rate of 9.33 Gy/min, the accumulated dose rate can be measured by the distributed fiber sensor with measurement accuracies comparable with OSL dosimeters (10%) but with far better spatial resolution of 1 cm.

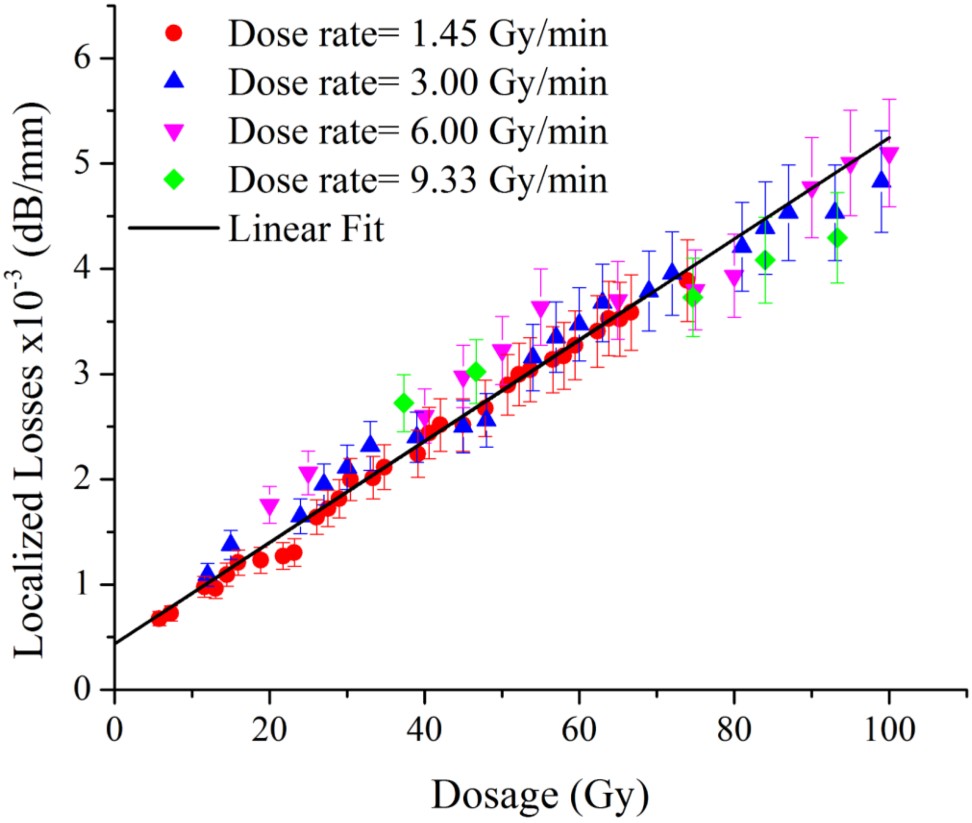

Figure 4 All data in the linear range of operation of the Al-doped fiber sensor, at the four dose rates, linearly fitted together [49] © 2017 IEEE.

Using the current calibration configuration shown in figure 1(b) as an example; since optical losses of every 1 cm section of the fiber were recorded as a function of time, and the localized dose rate in the calibration configuration shown in figure 1(b) can be calculated based on the geometric distance between the location of the fiber and that of the source, hundreds of calibration curves can be generated using one irradiation configuration (e.g., figure 1(b)). This information could yield a far more accurate distributed irradiation sensor for an unknown source and other fiber deployment configurations.

Figure 5 explores the potential to use Al-doped fiber as a distributed fiber sensor to perform high spatial resolution radiation detection and monitoring. The accumulated radiation dosage profile at the cylindrical surface was calculated using the linear fit calibration of figure 4. Using a computer algorithm implemented in MATLAB, the localized RIA along the fiber was converted to a surface mapping of radiation dosage received on the cylindrical surface. The reconstructed radiation fields in 3D format for 4, 5, 7 and 9 min of gamma-ray radiation exposures are presented in figure 5(a). The radiation source is located at the center of the bottom of the cylinder. Within the maximum irradiation time of 9 minutes, the entire fiber response to the gamma radiation remains in the linear range including the locations where the maximum dose rate occur (9.33 Gy/min). The localized RIA vs the elevation of the cylinder is presented in figure 5(b) at constant azimuth. The peak of the localized RIA moves to higher elevation at longer exposure time. This is probably due to the saturation effect while lower dose rate leads to larger saturation dosage. This is also depicted by figures 3(b-d).

The 3D mapping of accumulated dosage received by the cylinder surface where the fiber was wrapped depicts the influence of radiation on the cylinder by a gamma source located at the bottom of the cylinder. The area of the cylinder that received the most irradiation is at the same elevation where the center of the gamma source is located. The distribution of accumulated radiation dosage on the cylinder surface is also approximately symmetric along the z-axis (height) with respect to the center of the radiation source bundle. The gradual drop of the accumulated dosage on the cylinder surface from the peak dosage is also consistent with the dosage distribution per the geometrical configuration of the source.

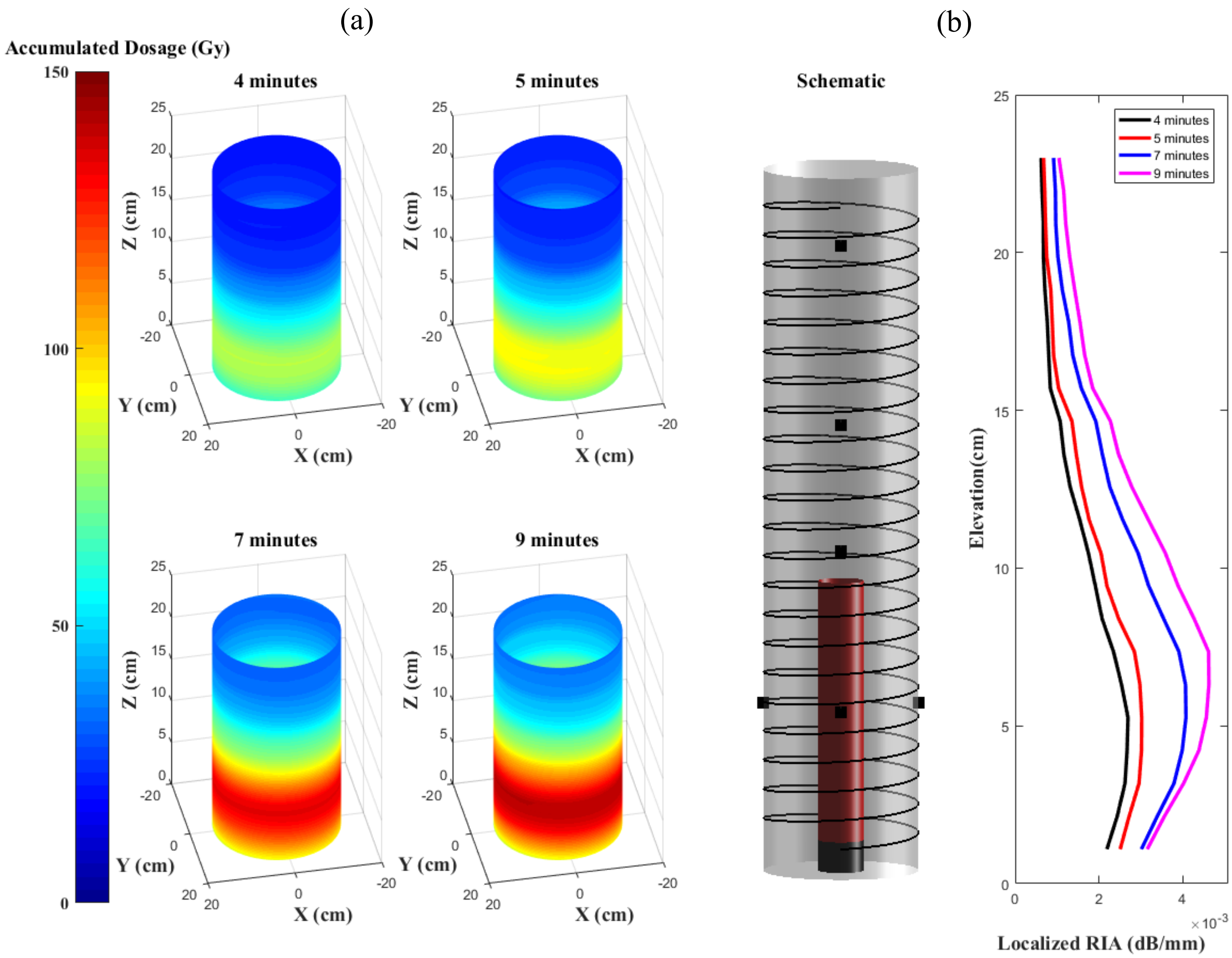

Figure 5 (a) A 3D construction of the schematic of the experimental setting with the radiation source and dosimeters located inside and outside the cylinder, respectively. The 3D radiation profile on the cylindrical surface constructed by mapping the localized radiation induced attenuation on the fiber to their respective locations in the constructed geometry. The region exhibiting the highest losses is the one closest to the source, and the reconstructed profile successfully points out the location of the gamma radiation source and its radiation profile. (b) The curves to the right show how radiation induced attenuation vary with different elevations at a constant azimuth, peaking at the region of highest radiation dose rate [49] © 2017 IEEE.

As a sensor that can be easily embedded in a wide variety of materials, structures, and components used in nuclear industry, the high spatial resolution measurement of radiation provided by the distributed fiber sensors can offer a unique tool to gauge the performance and longevity of nuclear components under prolonged radiation. In the next section, we will explore this potential.

2.2 Electrical Cable with Built-in Radiation Sensing Capabilities

Sensor networks used in nuclear energy systems must withstand harsh environments and perform proper measurements during both normal operation and in harsh post-accident situations for long periods of time. Meanwhile, the deployment of sensor networks should not significantly increase engineering complexities and costs for new and existing nuclear power systems, which are already very expensive.

The availability of optical fibers as distributed radiation sensing platforms offers a significant advantage for sensor deployment. In this section, we propose to use electrical cables, which are ubiquitously deployed in nuclear power systems, as platforms for housing distributed optical fiber sensors. Fiber sensor-embedded electrical cables have been developed for strain and temperature measurements for electrical power transmission lines. The incorporation of distributed fiber gamma radiation sensors will significantly enhance the functionality of electrical cables, not only as devices for power and signal transmissions, but also as smart components to perform a wide array of measurements including sensing for ionizing radiation, to improve the safety of nuclear power systems. From another perspective, the integration of distributed fiber radiation sensors can also be used to gauge the aging of low and medium power, instrumentation, and control cables under prolonged radiation use in the nuclear industry.

2.2.1 Experimental setup

The fiber-embedded cable prototype used in this section to demonstrate proof-of-concept was composed of a 3 m long flexible polyvinylchloride (PVC) conduit as shown in figure 6. The conduit is 2.26 cm in diameter and can tolerate radiation for up to 100 kGy. It was tightly packed with two harsh environment electrical cables and an Ethernet cable to resemble the multi-functional cable used in nuclear systems. Also packed inside the conduit, two types of optical fibers sheathed with high temperature, chemical resistant polytetrafluoroethylene (PTFE) tubing sleeves. First was the radiation-hard, Ge-doped, conventional telecommunications optical fiber (Corning's SMF 28e+), to be used primarily to obtain temperature measurements inside the hot cell. Secondly, the radiation-sensitive, Al-doped optical fiber, described in the section 2.1.1, to detect and quantitate ionizing gamma radiation. Both fibers were fusion spliced together at one end of the cable. From the other end, the SMF28 was fused to a fiber patch cable to be connected to the OBR via an APC connector. Thus both temperature and radiation can be monitored using one interrogator.

Figure 6 A photograph of the multi-purpose electrical cable fitted with single mode Al-doped and single mode telecommunications fibers (pointed out by red arrows), for real-time monitoring of radiation effects and temperature changes, respectively [49] © 2017 IEEE.

The cable was placed in the hot cell, constituting a spatial configuration of three straight and orthogonal sections, and secured into position using duct tape as shown in figure 7. A mocked-up radiation source in the figure shows the relative location of the source bundle and the cable, while the black arrows point out the locations where the dosimeters were placed. Ice packs were placed on several parts of the cable to distinguish these selected regions of the cable prior to gamma exposure, using the distributed temperature measurements. These included the point closest to the radiation source and five other points all chosen for the positioning of the dosimeters. Subsequently, the seven dosimeters were positioned in their selected places. Two dosimeters were placed at the location on the cable closest to the radiation source (i.e., shortest Euclidean distance), one in front of and the other at the back of the cable. Dosimetry tests were started by briefly placing the radiation source onto its properly marked location, then removing it after seven minutes to collect the dosimeters before over exposure to the radiation. Then radiation exposure was resumed for 7 hours, where measurements and real time monitoring of reflective losses and temperature changes on both fiber lengths inside the cable were carried out simultaneously using the OBR. These results are shown in figure 8.

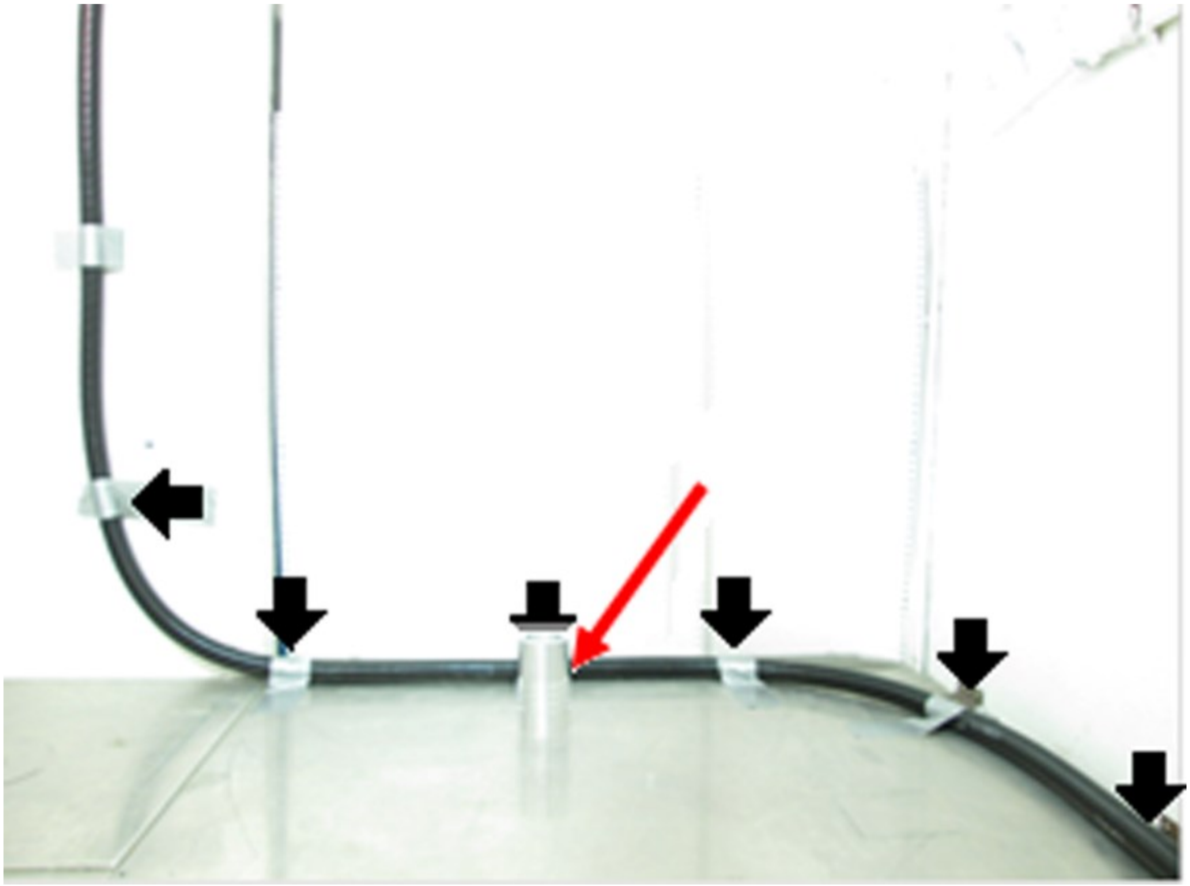

Figure 7 A photograph of the experimental setting arrangement, where the multi-purpose cable was positioned in three orthogonal directions to monitor the gamma-ray radiation emission from the radioactive ^{60}Co isotope source bundle (modelled here using a mocked-up aluminum cylinder pointed out by the red arrow) inside the hot cell at Westinghouse research facility, where the dosimeters were positioned at the locations indicated by the black arrows [49] © 2017 IEEE.

2.2.2 Data analysis and discussion of the results

Figure 8(a) shows the 1D spatial distribution of the localized losses on the section of the Al-doped fiber in the cable. The region closest in proximity to the radiation source developed the highest losses, pointing out the location of the source. By mapping the radiation dose rate spatial profile obtained from the dosimetry to the localized losses spatial profile, the localized losses indicated the dosages experienced by the fiber, which is a quantitative measurement in the linear region of the fiber's response to radiation. The radiation-induced temperature measurement errors are shown in figure 8(b). Given that the temperature of the hot cell is controlled within 1°C, the temperature changes measured by both standard Ge-doped telecommunications fiber and Al-doped fiber are within the temperature fluctuation ranges of the environment. Although the gamma irradiation induces significant loss in Al-doped fiber around the vicinity of the source, the distributed temperature measured by the Al-doped fiber is within 1°C.

Figure 9 illustrates the radiation dosage incurred along the entire electrical cable after four minutes of exposure to gamma radiation. The spatially resolved radiation dosages along the electrical cable were inferred from the localized RIA measurement using the embedded optical fiber sensors. Embedded optical fibers in electrical cables not only provide a feasible way to monitor radiation-induced ageing of electrical cables, but it also provides a ubiquitous sensing solution to perform other high-resolution measurements such as temperature and other measures pertaining to safety of nuclear power systems.

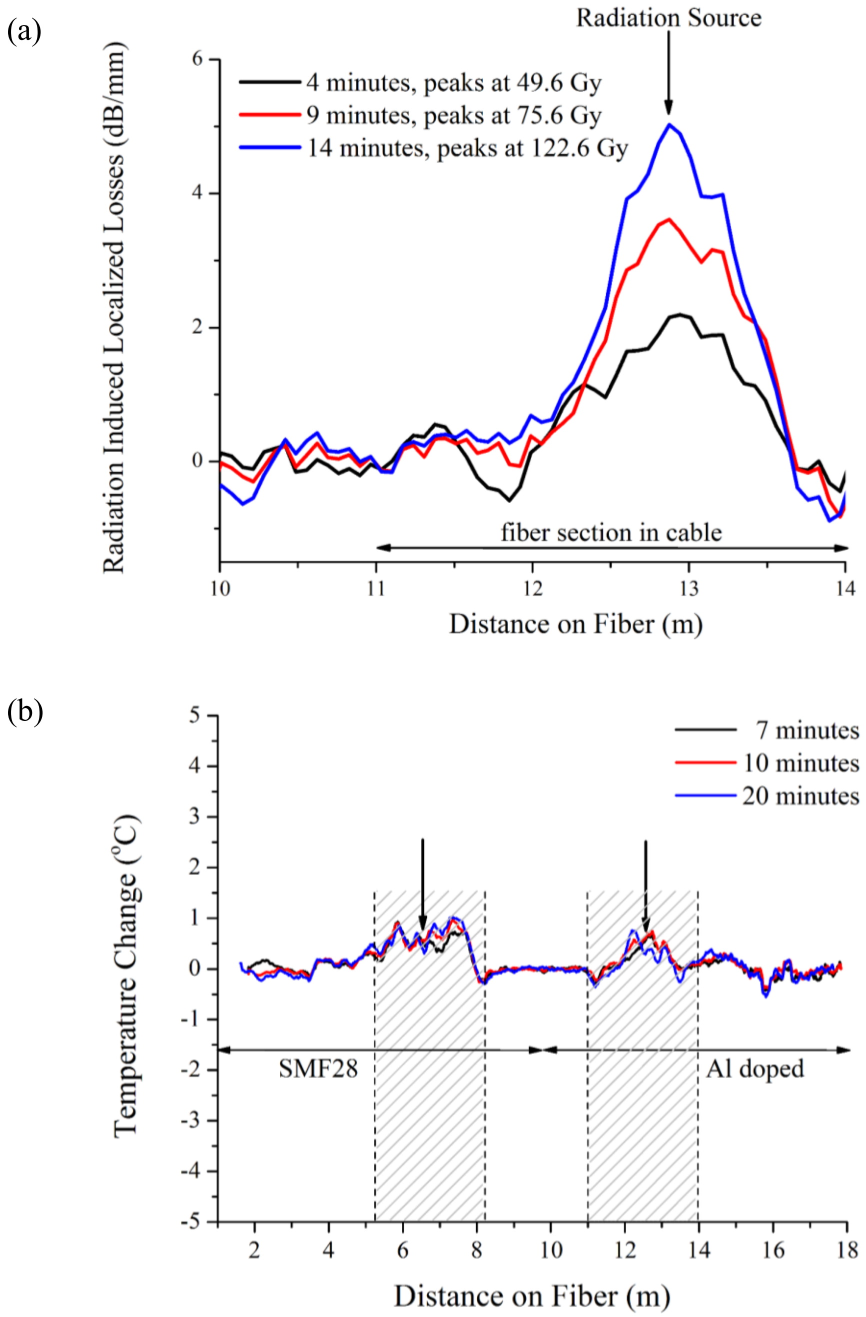

Figure 8 (a) Radiation induced localized losses on the single mode Al doped fiber within the cable. The arrow points at the localized losses peaks at the location closest to the radiation source. (b) Fiber degradation shown as temperature changes on the two fibers inside the cable with the arrows pointing at the locations on the sample closest to the ^{60}Co radiation source. Even the stressed regions of the fiber showed minor fluctuations (< ±1°C). Stresses here are expected to be mainly due to the PTFE tubing reaction to ionizing radiation [49] © 2017 IEEE.

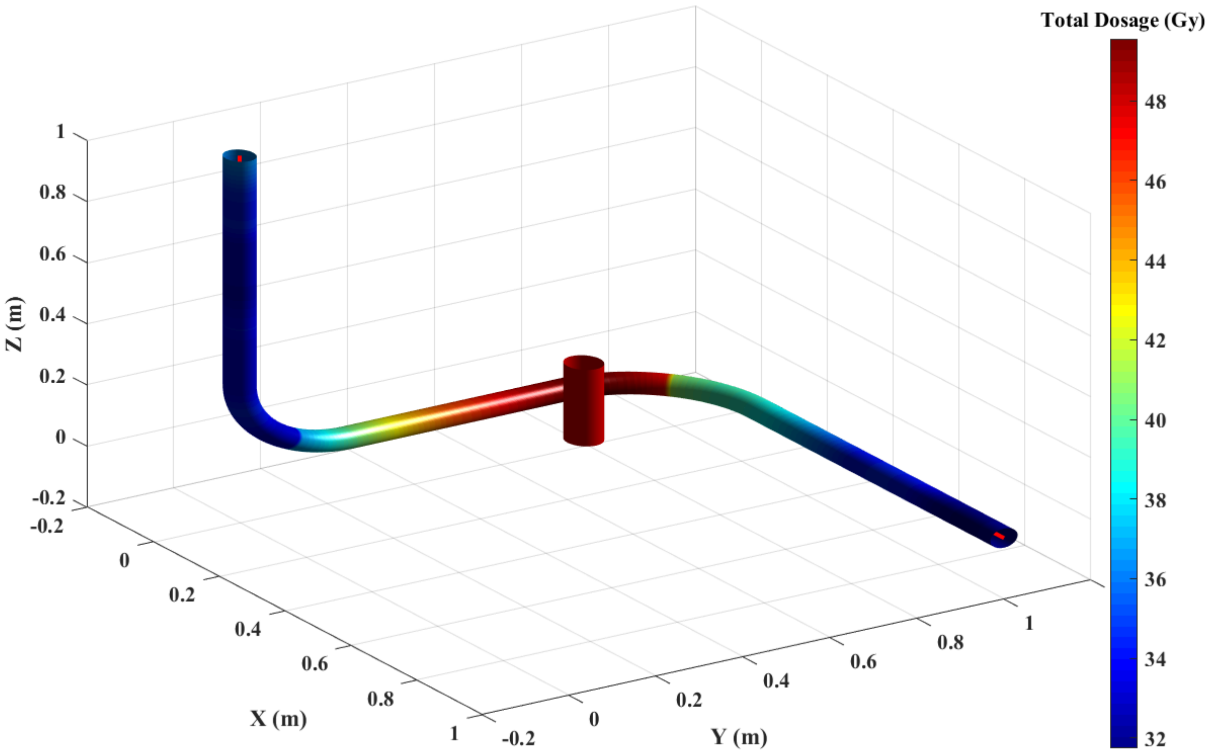

Figure 9 A 2D construction of the radiation effect on the single mode Al doped fiber is provided after 4-minute exposure to gamma rays. By measuring the localized RIA, the location and intensity of the radiation source can be determined for qualitatively detecting ionizing radiation and its position, and quantitatively detecting the radiation intensity and dose rates. The color bar shows the recording of the accumulated dosage experienced by the fiber inside the cable [49] © 2017 IEEE.

2.3 Discussion and Conclusions

This chapter explored the perspectives on the use of optical fibers and distributed fiber sensing schemes to perform real-time radiation measurements with high spatial resolution. Apart from conventional optical fiber sensing approaches for radiation measurement, this method utilizes the sensitivity of aluminum-doped fiber to radiation as a means to detect radiation dosage. A

Rayleigh OFDR distributed sensing scheme was used here to spatially resolve the locations of radiation-induced losses with 1 cm spatial resolution. As a sensor that can be readily embedded in a wide variety of materials and structures, radiation-sensitive fibers can be a low-cost and highly flexible tool to monitor radiation for many applications for nuclear power systems. Using electrical cables as a ubiquitous sensor platform, this chapter explored the potential of distributed fiber sensing by integrating distributed fiber temperature and radiation sensors in electrical cables for multi-functional measurements across the entire length of the electrical cable to improve the safety of nuclear power systems at both the component and system levels. By selecting optical fibers with different level of radiation tolerances, the fiber sensor in electrical cables can be used to detect radiation leak or monitor electrical-cable degradation under the radiation with high spatial resolutions.

In general, using radiation-induced attenuation as a means to measure radiation dosage may not be a viable means for repeated measurements (i.e., irreversible). However, given that radiation-induced damages in most materials and components is not reversible, the distributed optical fiber radiation sensors presented in this chapter provide a practical embedding solution to gauge the performance degradation and longevity of materials and components used in nuclear power systems. As demonstrated, the distributed fiber radiation sensors can also be readily combined with other distributed sensors using radiation-resilient fibers for temperature and strain measurements. This will provide an integrated solution to monitor degradation of components and materials in radiation environments and correlate it to radiation dosages.

3.0 Discrimination of Temperature and Strain in Brillouin Optical Time Domain Analysis using a Multicore Optical Fiber

A multicore optical fiber that has two distinct cores is fabricated by Corning® [54]. The two cores were mismatched during fabrication to produce dissimilar Brillouin resonant frequencies that can be used to sense for two physical quantities, simultaneously, namely the temperature and strain spatial distributions on the optical fiber. This chapter presents a study of using multicore fibers as distributed sensors, for temperature and strains in a BOTDA scheme.

3.1 Theory

In BOTDA, the frequency shift changes are a linear combination of temperature and strain changes. Temperature and strain changes can be discriminated by solving a system of linear equations that comprise measurements of frequency shift changes from two spatial channels (spatial channels 1 and 2). The spatial channels are subjected to the same temperature and strain changes yet have different and temperature and strain coefficients. In matrix form, where the coefficients comprise a matrix, the system of linear equations is given by [12]:

$$\begin{bmatrix} \Delta\nu_1 + \delta\nu \\ \Delta\nu_2 + \delta\nu \end{bmatrix} = \begin{bmatrix} c_{T,1} & c_{\epsilon,1} \\ c_{T,2} & c_{\epsilon,2} \end{bmatrix} \begin{bmatrix} \Delta T \\ \Delta\epsilon \end{bmatrix}. \tag{3-1}$$

$\Delta\nu_1$ and $\Delta\nu_2$ are the measured frequency shifts changes of spatial channels 1 and 2, respectively. $\delta\nu$ is the measurement error of $\Delta\nu_1$ and $\Delta\nu_2$. It is assumed that $\delta\nu$ is the same for $\Delta\nu_1$ and $\Delta\nu_2$

because it is assumed that $\Delta\nu_1$ and $\Delta\nu_2$ are measured in the same manner $c_{T,1}$ and $c_{\epsilon,1}$ ($c_{T,2}$ and $c_{\epsilon,2}$) are the temperature and strain coefficients, respectively, of spatial channel 1 (spatial channel 2). ΔT and $\Delta\epsilon$ are the temperature and strain changes, respectively, experienced by spatial channels 1 and 2. $c_{T,1}$ and $c_{T,2}$ ($c_{\epsilon,1}$ and $c_{\epsilon,2}$) can be experimentally determined by measuring $\Delta\nu_1$ and $\Delta\nu_2$ while varying ΔT ($\Delta\epsilon$) and keeping $\Delta\epsilon$ (ΔT) constant. Effectively, $c_{T,1}$, $c_{T,2}$, $c_{\epsilon,1}$, and $c_{\epsilon,2}$ are the slopes of best fit lines of the measurements. It is assumed that the measurement errors of $c_{T,1}$, $c_{T,2}$, $c_{\epsilon,1}$, and $c_{\epsilon,2}$ are negligible. ΔT and $\Delta\epsilon$ can be solved for by multiplying both sides of equation 3-1 by the inverse of the matrix. It can be shown that the resulting error of ΔT and $\Delta\epsilon$ are given, respectively, by the equations [24]:

$$\delta T = \delta\nu \frac{\sqrt{(c_{\epsilon,2})^2 + (c_{\epsilon,1})^2}}{c_{T,1}c_{\epsilon,2} - c_{\epsilon,1}c_{T,2}} \tag{3-2}$$

and,

$$\delta\epsilon = \delta\nu \frac{\sqrt{(c_{T,2})^2 + (c_{T,1})^2}}{c_{T,1}c_{\epsilon,2} - c_{\epsilon,1}c_{T,2}}. \tag{3-3}$$

Note that equations 3-2 and 3-3 were calculated in accordance with error propagation, i.e., all terms that comprise $\delta\nu$ were added in quadrature. As can be seen, $c_{T,1}$, $c_{T,2}$, $c_{\epsilon,1}$, and $c_{\epsilon,2}$, make up factors that multiplicatively increase, or amplify, $\delta\nu$. These factors are referred to here as temperature and strain error amplification factors, respectively, i.e. $\delta T/\delta\nu$ and $\delta\epsilon/\delta\nu$, respectively. Effectively, $\delta T/\delta\nu$ and $\delta\epsilon/\delta\nu$ are a measure of the difference between $c_{T,1}$, $c_{T,2}$, $c_{\epsilon,1}$, and $c_{\epsilon,2}$. The ability of the spatial channels to discriminate ΔT and $\Delta\epsilon$ is quantified by $\delta T/\delta v$ and $\delta\epsilon/\delta v$, respectively.

3.2 Experiment

3.2.1 Multicore optical fiber

A multicore optical fiber that had two cores (core 1 and 2) was fabricated. Details regarding the transmission characteristics of cores 1 and 2 can be found in references [55, 56]. The transmission characteristics of cores 1 and 2 were comparable to that of a standard single mode optical fiber. Figure 10(a) shows the multicore optical fiber's cross section. It had a 125 μm diameter cladding. Cores 1 and 2 served as spatial channels 1 and 2, respectively. Cores 1 and 2 had radii of 4.25 μm and 4.4 μm, respectively, and were separated by 54.5 μm. Cores 1 and 2 were Ge doped, had step index profiles and, had deltas of 0.46 % and 0.34 %, respectively. Figure 10(b) shows a theoretical calculation of the difference between the frequency shifts of cores 1 and 2 as a function of the difference between their deltas when one of the cores had a delta of 0.34 %. The frequency shifts from cores 1 and 2 were measured using a commercial BOTDA. The commercial BOTDA is described below. Figure 10(c) shows the measured frequency shifts which were 10.73 GHz and 10.85 GHz, respectively. Using different core compositions, fiber cores' responses to temperature and strain (i.e. $c_{T,1}$, $c_{T,2}$, $c_{\epsilon,1}$, and $c_{\epsilon,2}$) were also sufficiently different.

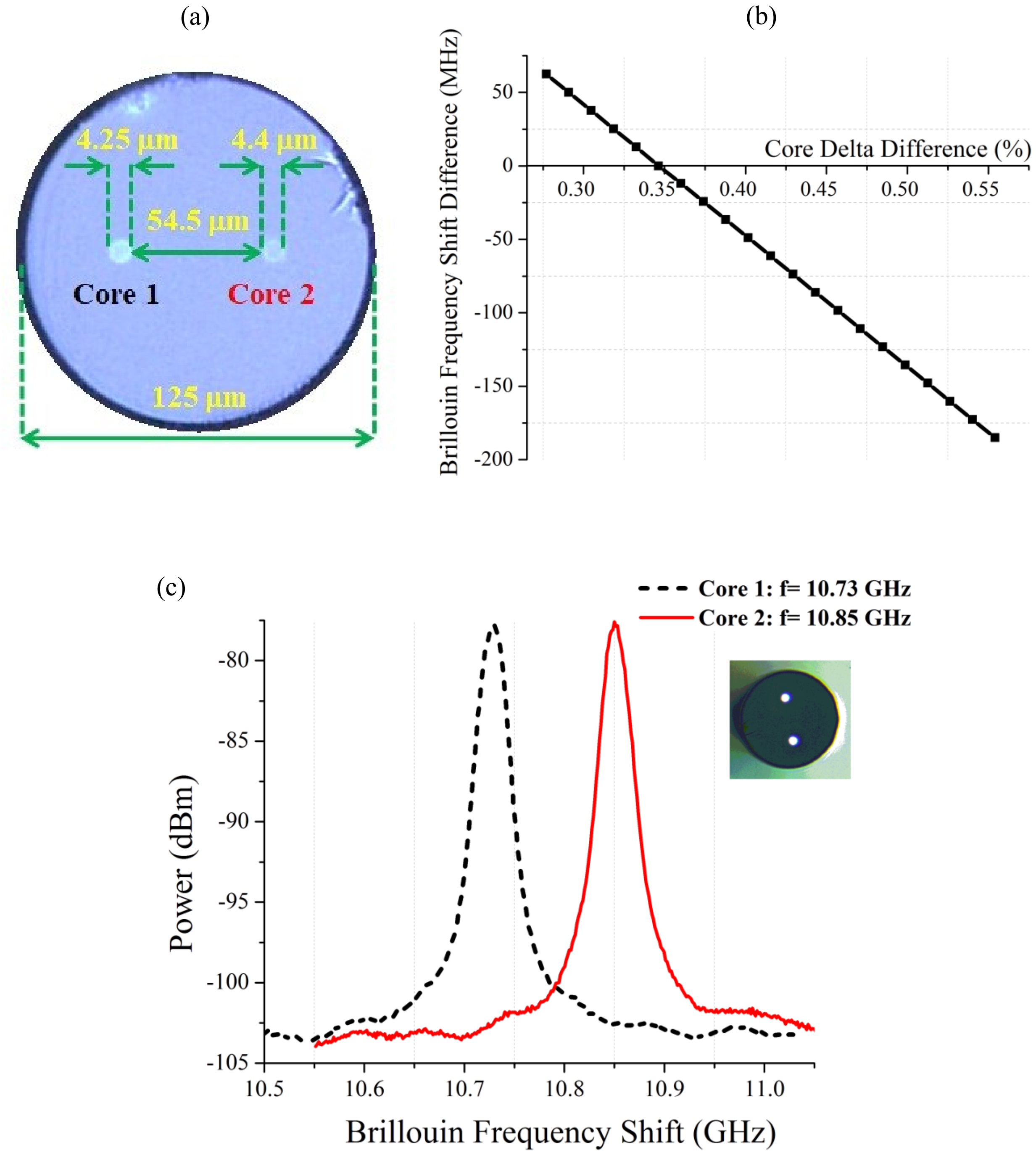

Figure 10 (a) A microscopic image of the cross section of multicore optical fiber that has two cores (cores 1 and 2). (b) A plot of the theoretical calculation of the difference between the frequency shifts of cores 1 and 2 as a function of the difference between their deltas as described in the text. (c) Measured frequency shifts of cores 1 and 2 as described in the text. Reprinted with permission [57] © 2018 MDPI.

3.2.2 Commercial Brillouin optical time domain analyzer

In the experiments, $\Delta\nu_1$ and $\Delta\nu_2$ were measured using a commercial BOTDA (OZ Optics®). A light pulse (1550 nm) was launched into cores 1 or 2 at one end of the multicore optical fiber and continuous wave light was launched into cores 1 or 2, respectively, at the other end (i.e. they counter propagated). The light pulse created spontaneous Brillouin back-scattering as it propagated. The frequency difference between the light pulse and the continuous wave light could be varied from 10.5 GHz to 11.0 GHz. Due to stimulated Brillouin scattering, there was power amplification (gain) when the frequency shift of the spontaneous Brillouin back-scattering was equal to the frequency difference between the light pulse and the continuous wave light. $\Delta\nu_1$ and $\Delta\nu_2$ were measured by measuring that power amplification (i.e. the Brillouin gain spectrum). The spatial resolution of the commercial BOTDA was 1 m. The lengths of the multicore optical fibers used in the experiments were 20 m. $\Delta\nu_1$ and $\Delta\nu_2$ were measured by measuring a frequency shift every 1 m over 20 m and then averaging. $\delta\nu$ of the commercial BOTDA depended on many factors, such as, launched power, optical fiber length, and measurement time. In the experiments, $\delta\nu$ was ~0.64 MHz.

The commercial BOTDA had two channels (channels 1 and 2). $\Delta\nu_1$ and $\Delta\nu_2$ were measured simultaneously by connecting cores 1 and 2 to channels 1 and 2. Cores 1 and 2 were connected to channels 1 and 2, respectively, via fusion splicing of a single mode optical fiber. However, due to size, one single mode optical fiber could be spliced to one core at a time. Therefore, two multicore optical fibers were used: one single mode optical fiber was spliced to core 1 of one multicore optical fiber and another single mode optical fiber was spliced to core 2 of another multicore optical fiber.

3.2.3 Experimental determination of $c_{T,1}$ and $c_{T,2}$

$c_{T,1}$ and $c_{T,2}$ were experimentally determined by measuring $\Delta\nu_1$ and $\Delta\nu_2$, while varying ΔT, and keeping $\Delta\epsilon$ constant. Effectively, $c_{T,1}$ and $c_{T,2}$ are the slopes of best fit lines of the measurements. The 20 m lengths of the two multicore optical fibers were loosely coiled and placed in an oven. Note that loose coiling ensured that $\Delta\epsilon$ was constant. ΔT was varied by varying the temperature of the oven. The temperature of the oven was varied from 35°C to 95°C in increments of 5°C. A thermocouple was also placed in the oven. The thermocouple was used to measure the temperature of the oven. For each increment, $\Delta\nu_1$ and $\Delta\nu_2$ were measured using the commercial BOTDA. $\Delta\nu_1$ and $\Delta\nu_2$ were plotted as a function of ΔT. Figure 11(a) shows the plots. $c_{T,1}$ and $c_{T,2}$ were determined by calculating the best fit lines of the plots. Figure 11(a) also shows the plots of the best fit lines. The determined value of $c_{T,1}$ ($c_{T,2}$) is shown in the first (second) row of table 2. The measurement errors of $c_{T,1}$ and $c_{T,2}$ were 0.02456 MHz/°C and 0.01456 MHz/°C, respectively.

3.2.4 Experimental determination of $c_{\epsilon,1}$ and $c_{\epsilon,2}$

$c_{\epsilon,1}$ and $c_{\epsilon,2}$ were experimentally determined by measuring $\Delta\nu_1$ and $\Delta\nu_2$ while varying $\Delta\epsilon$ and keeping ΔT constant. Effectively, $c_{\epsilon,1}$ and $c_{\epsilon,2}$ are the slopes of best fit lines of the measurements. The two 20 m lengths of the multicore optical fiber were wound between two posts that were separated by 10 m. The position of one post was fixed and the position of the other post was varied by a motor controlled stage (Thorlabs®). The motor controlled stage had 0.1 μm and 8 μm position resolution and repeatability, respectively. The setup is depicted in figure 11(b). $\Delta\epsilon$ was varied by varying the position of the motor controlled stage which stretched the two 20 m lengths of the multicore optical fiber. $\Delta\epsilon$ was varied from 0 $\mu\epsilon$ to 400 $\mu\epsilon$ in various increments.

The determination of the increments is described below. For each increment, $\Delta\nu_1$ and $\Delta\nu_2$ were measured using the commercial BOTDA. $\Delta\nu_1$ and $\Delta\nu_2$ were plotted as a function of $\Delta\epsilon$. Figure 11(c) shows the plots. $c_{\epsilon,1}$ and $c_{\epsilon,2}$ were determined by calculating the best fit lines of the plots. Figure 11(c) also shows plots of the best fit lines. The determined values of $c_{\epsilon,1}$ ($c_{\epsilon,2}$) is shown in the third (fourth) row of table 2. The measurement errors of $c_{\epsilon,1}$ and $c_{\epsilon,2}$ were 0.00282 μϵ/MHz and 0.00313 μϵ MHz, respectively.

The increments were determined via calibration with a standard single mode optical fiber whose strain coefficient was known (Corning® SMF-28®). During the experiment, the standard single mode optical fiber was also wound between the two posts. When the position of the motor controlled stage was varied, the frequency shift from the standard single mode optical fiber was measured using the commercial BOTDA. The increment was determined by using the known strain coefficient and the measured Brillouin frequency shift to calculate $\Delta\epsilon$.

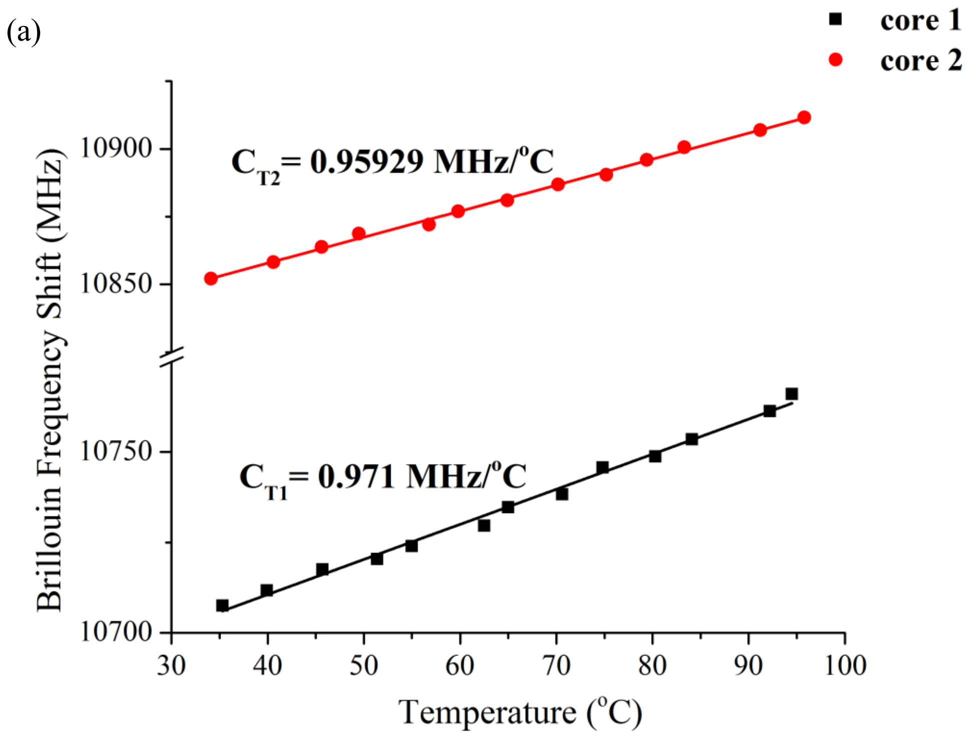

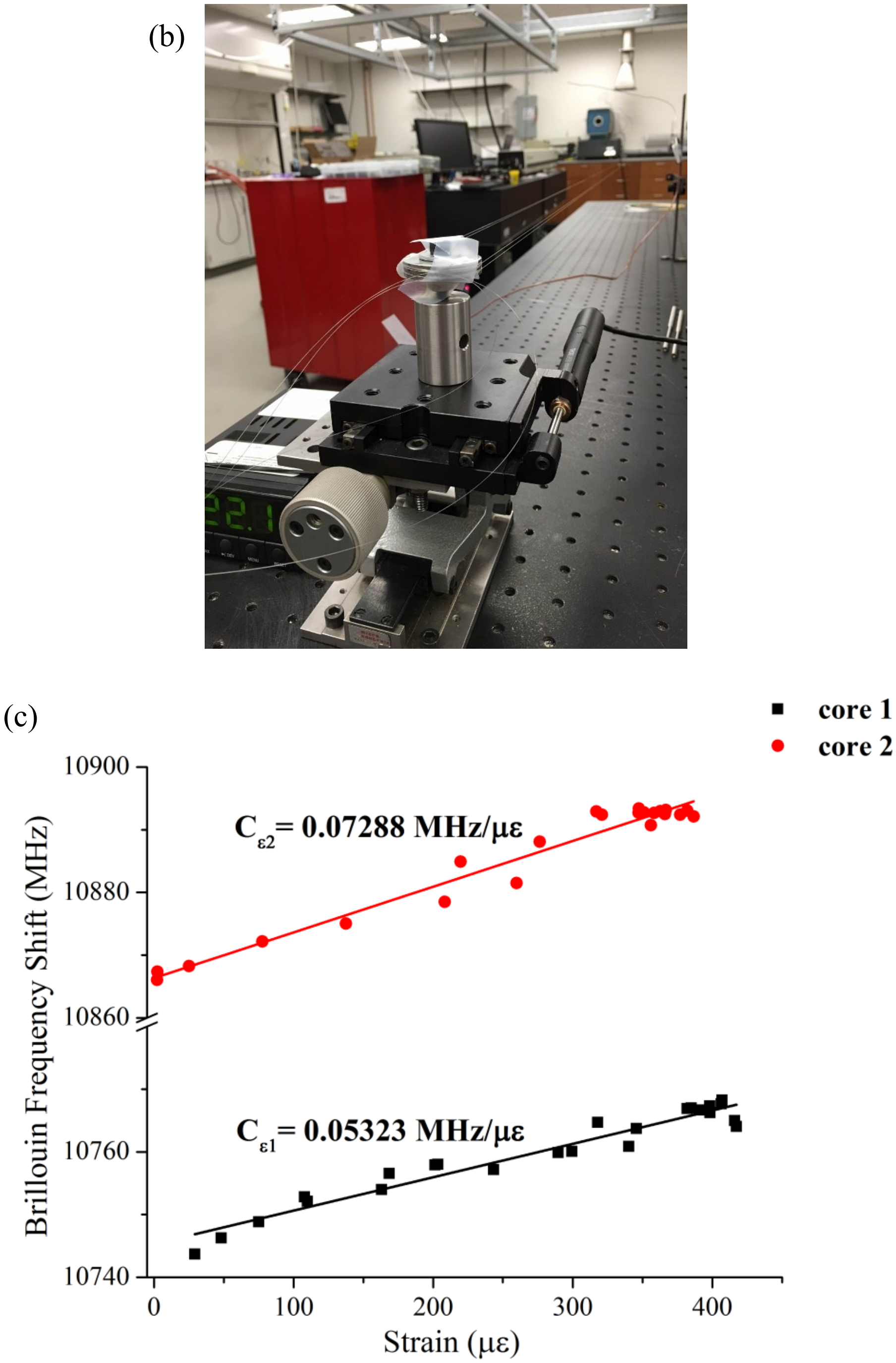

Figure 11 (a) Photograph of the experimental setup used to determine the strain coefficients. (b) Experimental determination of temperature coefficients ($c_{T,1}$ and $c_{T,2}$). Plots and best fit lines of $\Delta\nu_1$ and $\Delta\nu_2$ as a function of ΔT as described in the text. (c) Experimental Determination of strain coefficients ($c_{\epsilon,1}$ and $c_{\epsilon,2}$). Plots and best fit lines of $\Delta\nu_1$ and $\Delta\nu_2$ as a function of $\Delta\epsilon$ as described in the text. Reprinted with permission [57] © 2018 MDPI.

3.2.5 Comparison with references [23] and [24] results

Using the experimentally determined values of $c_{T,1}$, $c_{T,2}$, $c_{\epsilon,1}$, and $c_{\epsilon,2}$, $\delta T/\delta v$ and $\delta\epsilon/\delta v$ were calculated according to equations 3-2 and 3-3, respectively. $\delta T/\delta v$ and $\delta\epsilon/\delta v$ are shown in the first column of table 2: $\delta T/\delta v = 4.57$°C/MHz and $\delta\epsilon/\delta v = 69.11$ μϵ/MHz. These values were compared to those of references [23] and [24]. $c_{T,1}$, $c_{T,2}$, $c_{\epsilon,1}$, and $c_{\epsilon,2}$, reported in references [23] and [24] are shown in the second and third columns, respectively, of table 2. Using them, $\delta T/\delta v$ and $\delta\epsilon/\delta v$ were calculated according to equations 3-2 and 3-3, respectively. $\delta T/\delta v$ and $\delta\epsilon/\delta v$ for references [23] and [24] are shown in the second and third columns, respectively, of table 2. For reference [23], $\delta T/\delta v = 12.05$°C/MHz and $\delta\epsilon/\delta v = 253.77$ μϵ/MHz. For reference [24], $\delta T/\delta v = 13.25$°C/MHz and $\delta\epsilon/\delta v = 299.18$ μϵ/MHz. Here, $\delta T/\delta v$ and $\delta\epsilon/\delta v$ are 2.63 times and 3.67 times less, respectively, than that of references [23]. Here, $\delta T/\delta v$ and $\delta\epsilon/\delta v$ are 2.90 times and 4.33 times less, respectively, than that of references [24].

Table 2 Temperature and strain coefficients $c_{T,1}$, $c_{T,2}$, $c_{\epsilon,1}$, and $c_{\epsilon,2}$ and error amplification factors ($\delta T/\delta v$ and $\delta\epsilon/\delta v$); (first column) in this study; (second column) reference [23]; (third column) reference [24], as described in the text.

	This study	Reference [23]	Reference [24]
$c_{T,1}$ [MHz/°C]	0.9710	1.0300	1.1500
$c_{T,2}$ [MHz/°C]	0.9593	1.0800	1.0500
$c_{\epsilon,1}$ [MHz/μϵ]	0.0532	0.0517	0.0486
$c_{\epsilon,2}$ [MHz/μϵ]	0.0729	0.0485	0.0489
$\delta T/\delta v$ [°C/MHz]	4.57	12.05	13.25
$\delta\epsilon/\delta v$ [μϵ/MHz]	69.11	253.77	299.18

3.2.6 Proof of principle

As proof of principle and to verify the improved accuracy for both temperature and strain measurements, ΔT and Δϵ of a thermal expansion of a hollow metal cylinder were sensed using the two-core fiber. The metal cylinder is made of aluminum alloy 6063-T5. The diameter of the cylinder is 12 cm with a wall thickness of 3 mm. Two-core fibers with length of 20 meters were tightly wound around the metal cylinder, which is shown in Figure 12(a). Cores 1 and 2 of the two-core fiber were probed by the commercial BOTDA via APC patch cables that were fusion spliced to the samples. The metal cylinder was placed in an oven. At elevated temperatures, the expansion of the metal cylinder will exert strain on the fiber given the larger thermal expansion coefficient of aluminum alloy and that of silica fiber. Given the well-known material properties of the aluminum alloy and the simple geometry, the strain induced on the fiber can be precisely determined.

The temperature of the oven was changed from the ambient temperature to 90°C in increments of approximately 5°C. For each increment, $\Delta\nu_1$ and $\Delta\nu_2$ were measured using the commercial BOTDA. A thermocouple was placed in the oven to verify the temperature changes of the metal cylinder. The strain changes of the metal cylinder due to thermal expansion were calculated using a finite element analysis (FEA) method (COMSOL). The Brillouin frequency shifts vs temperature along the 20 m section of the fiber of core 1 is presented in figure 12(b). The measurement was acquired with 1 m spatial resolution and been 5 point-averaged to yield smooth profile.

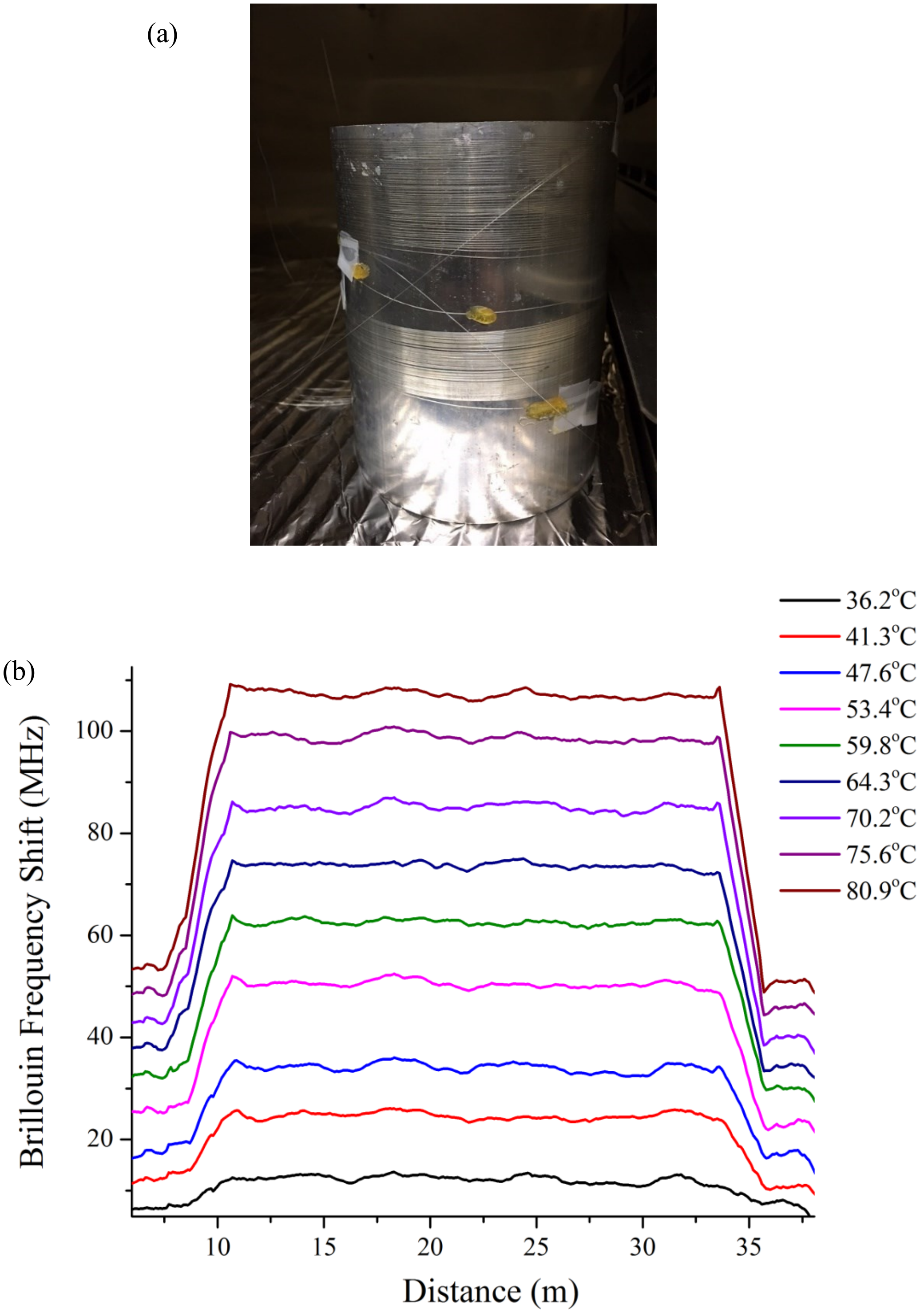

Figure 12 (a) Photograph of the Al cylinder inside the furnace with the dual core samples wound around the cylinder. (b) Brillouin frequency shift of one sample at different temperature and strains caused by metallic cylinder expansion. Reprinted with permission [57] © 2018 MDPI.

For each measurement, temperature and strain measured by the two-core fibers were calculated using the matrix formulate (equation 3-1) from the measured Brillouin frequency shifts $\Delta\nu_1$ and $\Delta\nu_2$ from core 1 and core 2. These results are graphically presented in figure 13, while fiber measured temperature and strain are plotted against temperature measured by the thermal-coupler and FEA simulation.

Slopes of linear fits of the temperature and strain calibration figure presented in figure 13 yields 0.24% system error for temperature measurements and 3.7% system error for strain measurements. To better illustrate the measurement accuracy at different temperature and strain ranges, experimental data presented in figure 13 is also presented in table 3, while dual-core fiber measured temperature and strains are compared with calibration measurements and calculations from temperatures ranges between 36.1°C to 81.3°C. On averages, the two-core fiber yielded 1.7 % measurement error of temperatures and 10.7% average error for strain measurements. The large measurement errors are mostly contributed those measurements performed at lower temperatures of below 50°C with lower thermal expansion induced strains. At higher temperature above 50°C, the average measurement errors reduces to 0.45% and 5.3%, respectively.

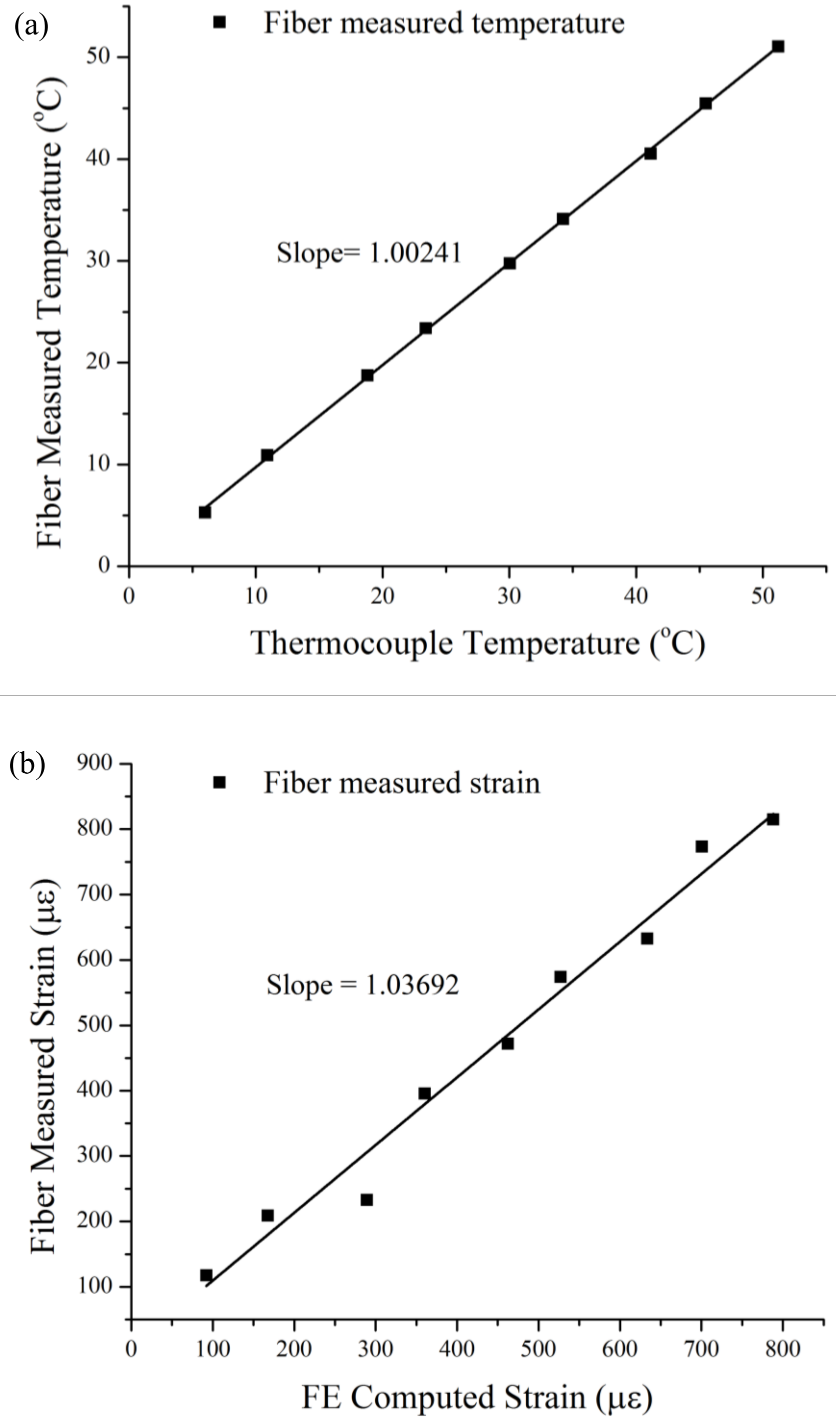

Figure 13 Linear fitting of (a) dual core-measured temperature versus the thermocouple temperature, and (b) dual core-measured strain versus the finite element computed strain. The system errors can be calculated as the deviation of the slopes from unity. Reprinted with permission [57] © 2018 MDPI.

Table 3 (First column) Temperature of metal cylinder as measured by the thermocouple; (second column) temperature of metal cylinder as measured using the multicore optical fibers; (third column) strain exerted by metal cylinder as determined by FE simulation; (fourth column) strain exerted by metal cylinder as measured using the multicore optical fibers, as described in the text.

Temperature [°C] (Thermocouple)	Temperature [°C] (Multicore optical fiber)	Strain [μϵ] (FE analysis)	Strain [μϵ] (Multicore optical fiber)
36.10	35.39	92.37	117.51
41.00	41.01	167.80	208.72
48.90	48.85	289.41	233.07
53.50	53.49	360.22	395.28
60.15	59.87	462.59	471.80
64.35	64.21	527.25	574.16
71.25	70.63	633.47	632.45
75.60	75.57	700.43	773.47
81.30	81.16	788.18	815.03

3.3 Conclusion

In conclusion to chapter 3, a multicore optical fiber that had two cores was fabricated. The differences between the cores' temperature and strain coefficients were such that temperature (strain) changes could be discriminated with error amplification factors of 4.57°C/MHz (69.11 μϵ/MHz), being 2.63 (3.67) times less than previously demonstrated. As proof of principle, using the multicore optical fiber and a commercial BOTDA, the temperature (strain) changes of a thermally expanding metal cylinder were discriminated with an average error of 0.24 % (3.7 %).

Here, it was assumed that the measurement errors of $c_{T,1}$, $c_{T,2}$, $c_{\epsilon,1}$, and $c_{\epsilon,2}$ were negligible. A theoretical analysis of error amplification factors that is more complete than equations 3-1 to 3-3 should account for non-negligible measurement errors of $c_{T,1}$, $c_{T,2}$, $c_{\epsilon,1}$, and $c_{\epsilon,2}$ [24]. However, the measurement errors of $c_{T,1}$, $c_{T,2}$, $c_{\epsilon,1}$, and $c_{\epsilon,2}$, reported here and in references [23] and [24] were a few percent. When using a multicore optical fiber for BOTDA, strain due to bending must be taken into account [23]. However, here, it was assumed that strain due to bending was uniform over the length of the multicore optical fiber and negligible.

Here, temperature and strain resolutions are not reported. Reporting of strain and temperature resolutions may be considered arbitrary because, temperature and strain resolutions depend on many experimental factors, such as, launched optical signal power, optical fiber length, and measurement time. Because different works utilize differing experimental factors, temperature and strain resolutions may not be comparable. In contrast, error amplification factors are comparable because, for a given set of experimental factors, error amplification factors quantify the difference between the abilities of two multicore optical fibers to discriminate temperature form strain. It may be of interest to investigate the use of other types of multimode and multicore optical fibers to discriminate temperature and strain in BOTDA, e.g., those with elliptical cores [58-61].

4.0 Radiation Resilient Fiber Bragg Gratings in Random Air-Hole Fibers for Sensing Applications in Nuclear Reactor Cores

In this chapter, we report in-core studies of FBG sensors at radiation levels and operational temperatures similar to commercial nuclear reactors. FBG irradiation tests were performed at >600°C with fast neutron fluxes above 1.2×10^{14} n/s/cm^2 for a 55-day continuous irradiations with 5.7×10^{20} n/cm^2 accumulated dosage. This is at least 10-folded higher than any other previous studies. To evaluate potentials of fiber sensors' capability to monitor reactor anomalies, multiple events were implemented during the irradiation to create abrupt changes of reactor temperatures and neutron powers. FBG responses to these abnormal conditions were characterized to assess thermal-optic properties of FBGs at different stages of irradiation and their temporal response during abrupt temperature changes. The experimental results presented in this chapter provide quantitative evaluation of FBG performance in commercial reactor cores. It also provides cue on how to mitigate FBG property drifts in reactor cores to improve both reliability and accuracy of FBG sensors for in-core applications

4.1 Fiber Selection, FBG Fabrication, and Neutron Testing Setup

4.1.1 Selection of radiation-hard fibers

The in-core radiation experiments reported in this chapter were carried out in the MIT nuclear research reactor. Given the limited space for sensor insertion, two different types of optical fibers were selected for the experiment. The optical fibers were selected based on previous literature studies on radiation-hardened fibers under both gamma and neutron irradiation. They were also selected based on the cost of fibers for potential large scale deployment. These two fibers include pure-silica random air-line (Corning RAL®) fibers and pure silica core, F-doped cladding single-mode fibers (Corning Vascade®). According to Morana et al. [62], F-doped single mode fibers exhibited the lowest radiation-induced attenuation (RIA) at 1550 nm operation, in a study where fs-FBGs inscribed on F-doped, pure-silica core, and Ge-doped fibers were exposed to an accumulated gamma dose of 1 MGy. However, upon exposure to radiation, F-doped fibers had shown a slightly larger Bragg wavelength shift (BWS) towards the blue (-0.03 pm/kGy for F-doped) compared to pure silica core fibers (-0.02 pm/kGy for pure silica core). Ge-doped fibers exhibited by far the largest radiation-induced BWS by approximately 2 orders of magnitude, which is undesirable for harsh environment sensing.

The pure silica core fibers are commonly known to have low susceptibility to RIA and hence are the most radiation resistant fibers, especially in operation in near IR range [63]. The entire RAL fiber is made of a single fused silica material with identical thermal expansion coefficient in both fiber core and cladding regions. Both fiber core and cladding also have similar responses under both neutron/gamma radiation. Thus, it is conceivable that the fiber will have even better resilience under radiation exposure. Comparing with other radiation hardened pure silica fibers such as photonic crystal fiber [64], which is also ideally suited for FBG inscription [26], RAL can be manufactured at much lower cost.

The RAL fiber was fabricated by Corning® using the outside vapor deposition (OVD) process. A pure silica core cane was inserted into a silica soot blank made with the OVD process to form a preform. The preform was consolidated in a consolidation furnace at a pressurized nitrogen atmosphere around 1450 °C to form a glass cladding containing air bubbles. The preform was then drawn into fiber. During the draw process, the air bubbles were stretched into thin elongated airlines. The optical confinement of the guided mode within the fiber was achieved by the surrounding random air-hole structures with a lower average refractive index. Comparing with other air-hole microstructural fibers, RAL fibers can be made at much lower cost. Figure 14(a) shows a scanning electron microscope (SEM) cross-section photo of the random-hole fiber, where the 8 μm diameter fiber core is surrounded by a random air-hole ring 45 μm in diameter to provide optical confinement. Figure 14(b) shows detailed air-hole distributions in the fiber cladding. Size of air-hole ranges from 15 nm to 1 μm. The size and distribution of the air-hole can be controlled by the nitrogen pressure during the fiber preform consolidation process.

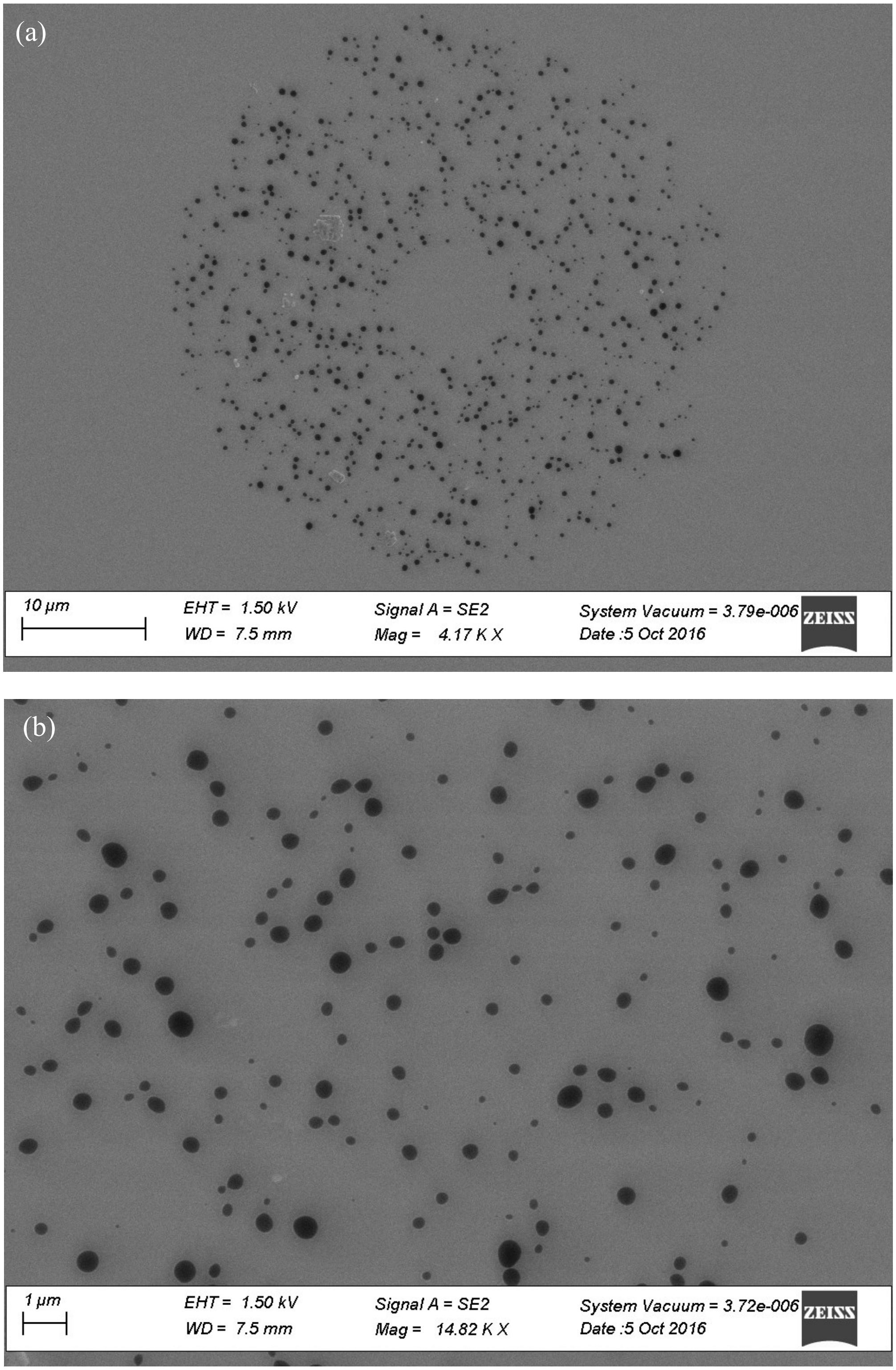

Figure 14 (a) An SEM image of the pure-silica core random air-line cladded optical fiber of 125 µm diameter. (b) A detailed SEM image of the RAL fiber cladding riddled with air structures with sizes varying from ~15 nm to ~1 µm. Reprinted with permission [65] © 2018 OSA.

4.1.2 FBG fabrication methods

The FBG inscription on the RAL fibers has proved to be a challenging process [66]. RAL fiber is a micro-structured optical fiber that consists if an array of air holes unsystematically distributed along the fiber axis, in the cladding region, around the unstructured- pure silica- core of the fiber. These air structures in the cladding strongly scatter the laser beam during the process of FBG inscription [66]. But since the traditional FBG inscription using UV light is not possible for micro-structured fibers [67], along with pure-silica core fluorine-doped (Vascade®) fibers [68], the use of femtosecond IR laser becomes the right choice to inscribe type II-IR FBGs on these types of fibers to make effective and enduring sensors for harsh environments [26].

4.1.2.1 Phase mask inscription method

To fabricate the Bragg grating in the RAL fiber, a Ti:sapphire regenerative amplifier operating at a central wavelength of $\lambda = 800$ nm was used. The fs-beam diameter was ~7 mm at the $1/e^2$ level. The full width at half maximum (FWHM) transform-limited width of the pulses was ~80 fs, as measured using non-collinear auto-correlation. However, the pulses were pre-chirped to 500 fs in order to facilitate Type II-IR grating formation [69] and the associated nano-grating formation [70]. The pulse repetition rate was kept at 5 Hz. The linearly polarized laser pulses were focused into the fiber core using a 12 mm focal length plano-convex acylindrical lens after passing through a silica phase mask, which has a 3.21 µm pitch. The fiber was positioned approximately 300 µm away from the phase mask along the beam propagation direction. The acylindrical lens was dithered ± 10 µm at 0.1 Hz with a piezo actuator in order to scan the beam across the fiber core. The resulting grating structure produced a high-order resonance at ~ 1525 nm in the telecom band as shown in figure 15(a).

As a result of the non-uniform existence of the air structures in the cladding, an order of magnitude reduction of photoluminescence of the focused beam on the core was obtained as compared to unstructured portion of silica around the cladding. This resulted in appearance of ±1 diffracted orders with angles 48.3° measured from the normal to the phase mask and fiber axis that cause an increase in path length through the fiber cladding. To improve the FBG inscription process, a larger pitched (3.17 μm) phase mask was used to achieve a ±1 diffraction orders with smaller angles (14.4°), hence minimizing the optical path through the structured cladding. Figure 15(b) shows the effect femtosecond laser on the cladding air-microstructures.

These type-II FBGs inscribed using the phase mask inscription method, have proven thermal stability for temperatures up to 800°C for at least 125 hours [66]. While type II-IR FBGs inscribed on SMF-28 have shown higher thermal stability at temperatures up to 1150°C, and an easier inscription process, the remarkable resilience of RAL fibers to ionizing radiation damage makes it worthwhile to endure the highly demanding FBG inscription process.

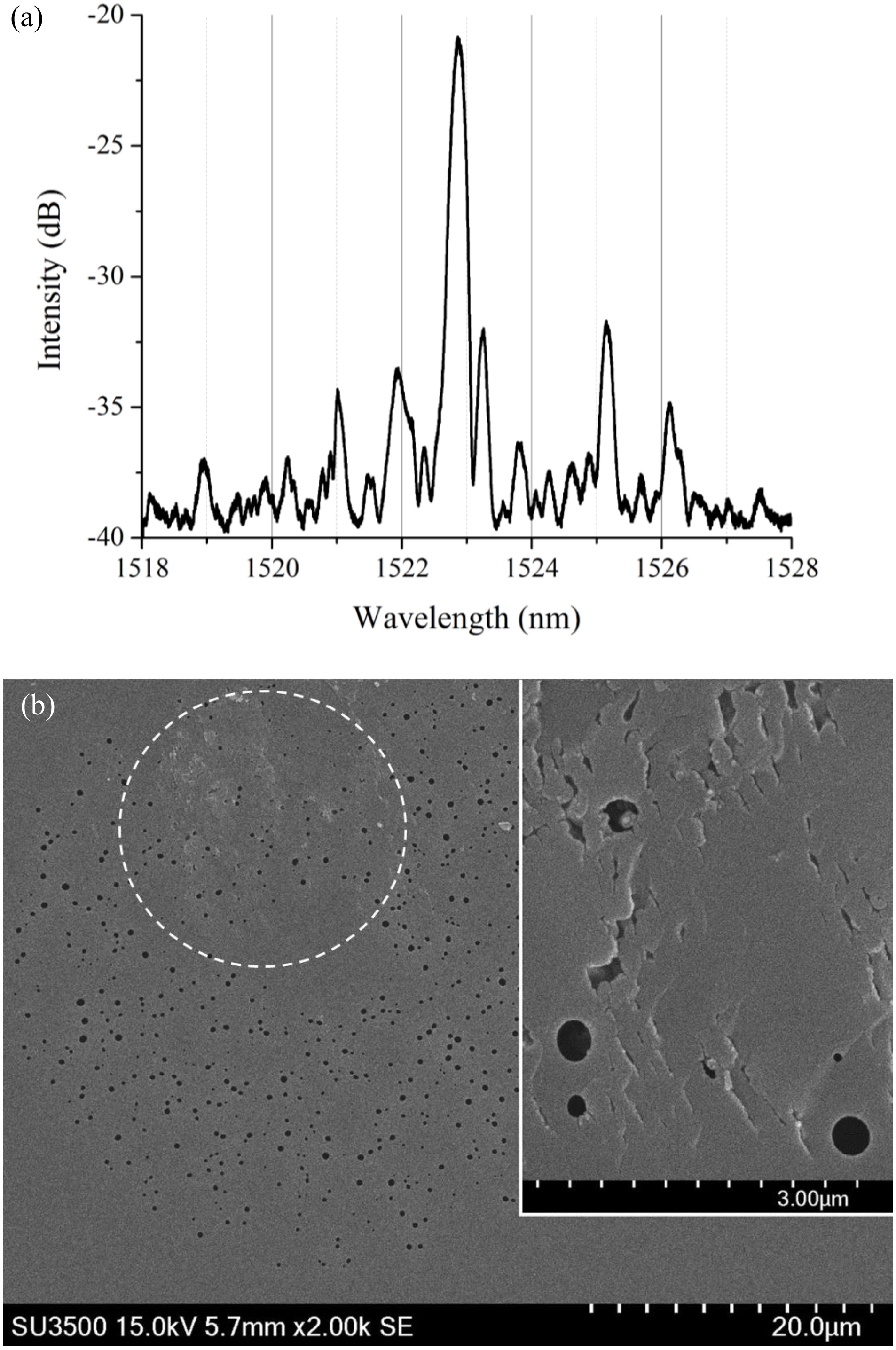

Figure 15 (a) Phase mask incribed FBG reflection profile at room temperature before exposure to neutron flux. Reprinted with permission [65] © 2018 OSA. (b) Cross-sectional microscopic image of the pure silica-core, random-airline cladding showing the effect of the femtosecond IR laser on the RAL cladding as air the structures collapsed as elaborated in the inset figure [66] © 2018 IEEE.

4.1.2.2 Plane-by-plane inscription method

Another low cost FBG fabrication method was attempted as described in [71, 72]; utilizing an ultrafast laser that is focused on the fiber core then is translated perpendicularly to fiber axis, intermittently affecting the silica fibers' core index. The FBGs and random fiber gratings (RFGs) were fabricated plane-by-plane by using a Ti:Sapphire regeneratively amplified femtosecond infrared (fs-IR) laser (Spitfire®, Coherent®). The laser beam was focused on the fiber by a microscope objective (50 ×/0.6, Nikon®) while the fiber was translated along an air bearing stage (Aerotech®) with a positional accuracy of ±10 nm. A long focal length cylindrical lens was added to the laser beam path with its focal point positioned at the same location as that of the microscope objective so that a plane of index modification could be produced in the fiber by a single pulse. The fs-IR laser operates at the wavelength of 800 nm and with pulse durations of 120 fs. Pulse energy incident on the fiber was 2.2 μJ.

The FBG spectra of the FBG fabricated on samples of RAL fibers and radiation-hard pure-silica fibers are shown in figures 15 (a-b). Some difficulties arose on FBG fabrication on RAL owing to the dispersive nature of the micro-structured cladding. Firstly, it was not possible to see the core, which made it difficult to align the center of the fiber core on the objective focus. Secondly, the random air lines are not perfectly parallel to the fiber axis throughout the whole length of the sample, so that laser radiation on the fiber core was not uniform when the laser beam is scanned along the fiber which makes this method better suited for FBG fabrication rather than continuous inscription of enhanced Rayleigh structures. The effect of air-line structures dispersion is clear on the spectra shown in figures 16(a-b). The FBGs fabricated using the plane-by-plane method were later tested inside the MIT nuclear reactor, but the irradiation test results are not presented in this dissertation.

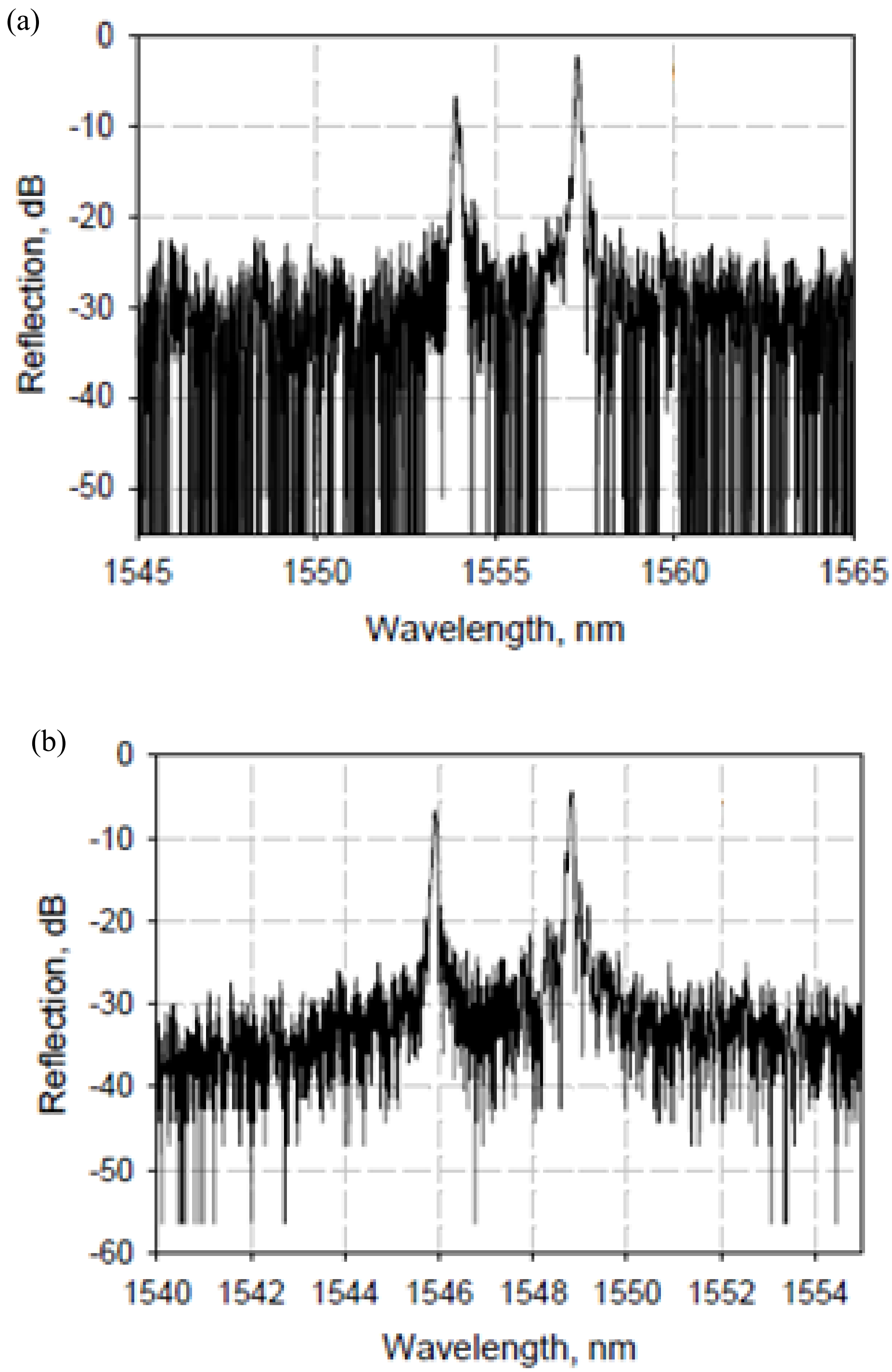

Figure 16 Plane-by-plane inscribed FBG spectra inscribed on (a) RAL fibers, and (b) pure-silica fibers. Distortion caused by the air filled micro-structures, in the cladding of a RAL fiber, during the FBG inscription is evident on the reflection spectrum.

4.1.3 FBG sensor installment inside of neutron reactor core

FBGs were inscribed using phase mask method in 25 m section of fibers. The locations of the FBGs are approximately 3.5 cm from one end of the fibers. The sensor section of the fiber was slipped into a 6 m long 316-stainless steel tubing with an outer diameter of 1.59 mm (one-sixteenth of an inch), and a wall thickness of 0.25 mm (0.010”) for protection and mechanical support of the sample as it descends into the reactor core. The rest of the fiber, which was not subject to any radiation outside the reactor, was sheathed with polyvinylchloride (PVC) tubing. One end of the stainless-steel tube was sealed by welding in argon gas ambient, while the other end of the stainless steel tube was left open to allow the fiber to be fusion spliced to an APC patch cable to connect with an FBG interrogation system. The FBG interrogation system comprised a TUNICS T100S-HP tunable laser and a CT400 optical switch (both from Yenista Optics®) with four interrogation channels. FBG spectra were recorded every 20 seconds as wavelengths of the tunable laser were swept in the range from 1440 nm to 1640 nm with a wavelength resolution of 2 pm.

The in-core experiment was carried out at the MIT Research Reactor (MITR). The MITR is a 6 MW light water-cooled, heavy water-reflected reactor with in-core positions for flow loops and instrumented experiment facilities. The core design provides a high power density with a neutron flux and spectrum similar to that of a typical light water power reactor. The MITR operates 24/7 with 10-week cycles; typically in-core experiments will operate under steady-state conditions for the duration of each cycle. The fibers are irradiated in the MITR’s In-Core Sample Assembly (ICSA) facility. The ICSA consists of a dry, pressurized (inert-gas filled) grade 2 titanium thimble that extends from the bottom of the reactor core to the top of the reactor primary core tank, and permits simplified installation of instrumented experiments desiring temperatures up to 900 °C. The experiment capsule and instrumentation leads are all contained within this thimble and are routed at the top through pressure fittings and out of the reactor biological shielding. The heating in this facility is supplied entirely by nuclear heating of the materials under neutron and gamma irradiation, with some fine control available by manipulating the ratio of helium to neon in the facility cover gas. The temperature is actively monitored by multiple thermocouples within the core and feeds back into the gas control system, generally permitting ±2°C stability during the cycle. Local temperatures are set by the reactor power, materials, and geometry of the heat transfer pathway – the ultimate heatsink is the 50 °C reactor primary coolant flowing at the exterior of the ICSA thimble.

Figures 17(a-b) show a photo and 3D schematic sketch of the test capsule which is placed inside the ICSA thimble. It consists of a graphite sample holder in a 20.5 cm long grade 2 titanium cylinder cup. Stainless tubes containing various fiber sensors are inserted in 4 holes drilled into the graphite sample holder as shown in figure 17(a). Three K-type 1/16" thermocouple temperature sensors with Inconel sheaths (from Omega®) were also inserted into the graphite sample holder to perform temperature measurements at three different locations inside the capsule. The locations of the thermocouples are -18 cm, -12.5 cm, and -5 cm from the center of the titanium cup. The titanium cup, which was placed on a grade 2 titanium pedestal or spacer, was positioned in the middle section of the reactor core to receive the maximum neutron flux. Figure 17(c) shows the ICSA thimble descending into the reactor core as photographed from the reactor opening.

The neutron flux profile in the reactor core at 5.6 MW, where the test capsule was located, is shown in figure 17(d). The test capsule, which is depicted in the figure using a grey bar, is placed in the region with the maximum fast neutron flux, which are in excess of 1.2×10^{14} n/s/cm^2 for fast neutrons with >0.1 MeV kinetic energy and 0.6×10^{14} n/s/cm^2 for fast neutrons with >1 MeV kinetic energy.

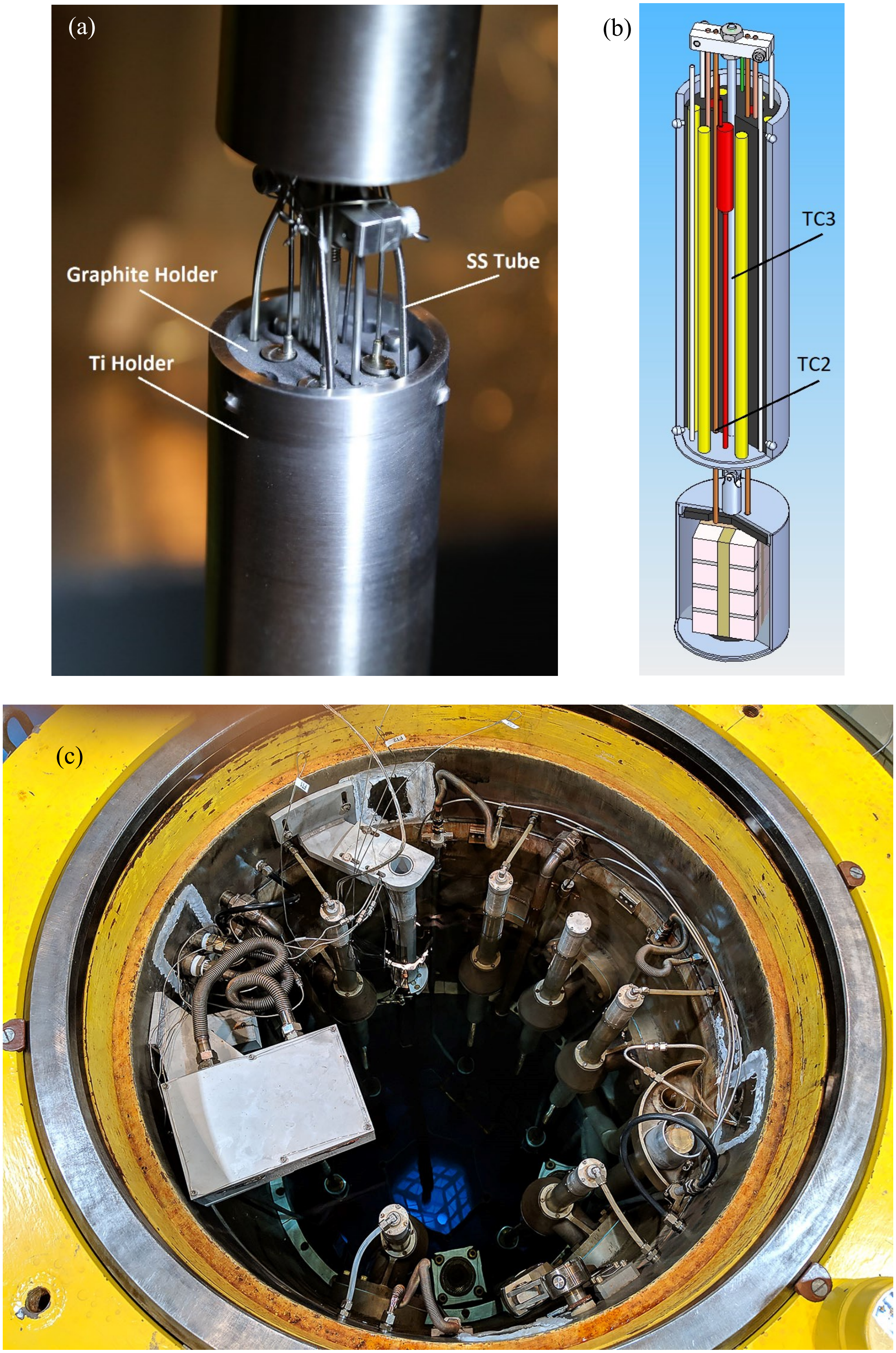
(a)
Graphite Holder
SS Tube
Ti Holder
(b)
TC3
TC2
(c)

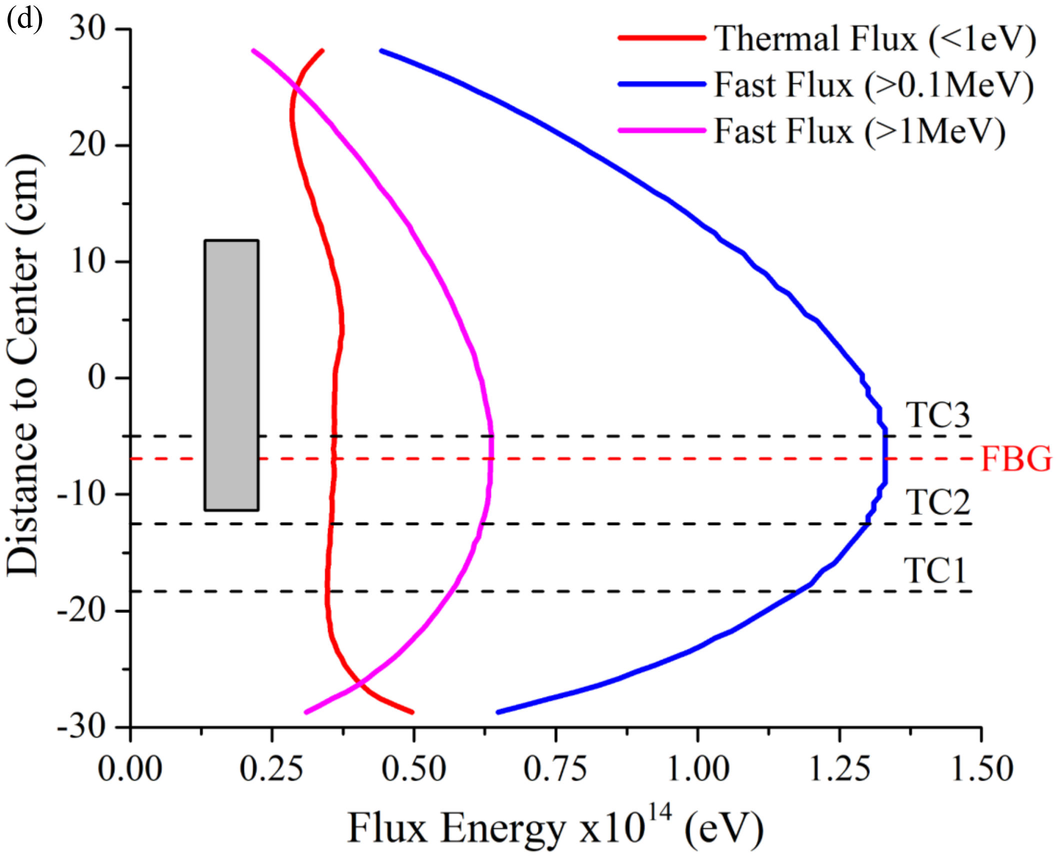

Figure 17 (a) A photograph of stainless-steel tubes with fiber sensor samples and thermocouples inside, inserted into the capsule to be lowered into the reactor core. (b) A 3D schematic of the sample holder capsule that shows the positions of the fiber samples and thermocouples. (c) A photograph of the MIT Neutron reactor from above showing the grade-2 Ti ICSA thimble, a vessel for test samples, extending from the reactor top to the reactor core at the bottom. (d) The neutron fluxes are also plotted to show their spatial profiles relative to the center of the capsule. The latter is represented on the figure by a grey rectangle. The locations of the FBG and thermocouples in the capsule are also marked on the figure. Reprinted with permission [65] © 2018 OSA.

4.2 Results and Discussion

When the experiment commenced, the capsule temperature was raised by 50 °C from the room temperature at the first day allowing a test of the response of the sensors before exposure to neutron flux and to confirm that the sensors were safely inserted inside the nuclear reactor core. The reactor power was then steady at 5.62 MW over a period of 3 days with the capsule reaching a final temperature of 622 °C with a combination of nuclear heating and helium/neon regulation. figure 18(a) shows the FBG spectra every 5 days during the test. To simulate FBG sensor behaviors during various reactor anomaly scenarios, several events were staged to assess the response of the FBG after durations of exposure to neutron flux. The reactor power and the capsule temperature measured by TC3 is presented in figure 18(b) (upper figure). Reactor power was reduced to 4 MW and 0 MW at Day 18 and Day 33, respectively. A small neutron power reduction also occurred at Day 42. The temperature and neutron power was then increased at various rates.

FBG spectra were measured from wavelength sweeps by the tunable laser from 1440 nm to 1660 nm with 2 pm resolution. The FBG peak wavelength and intensity amplitude, measured from peak to baseline, were recorded every 20 seconds. The overall radiation effect on the FBG wavelength and strength is shown in figure 18(b) (lower figure). Although reactor anomalies impact the FBG performance, the overall trend of the radiation effect is to cause a blue shift of the FBG resonant wavelength. At constant temperatures (622 °C) and neutron flux (5.6 MW), the FBG wavelength drifts slowly towards shorter wavelength, with an average wavelength drift rate of 0.0961 nm/day. The FBG wavelength drifts appear to be linear to the accumulated neutron flux. Over the test period of 60 days, FBG wavelength shifted 4.47 nm towards the shorter wavelength. This is consistent with previous observation of radiation induced compaction and creation of color centers induced refractive index changes of silica fiber under neutron, gamma, and x-ray radiation.

While a red Bragg wavelength shift (BWS) occurs when FBGs experience a rise in irradiation dose, a blue BWS or drift occurs slowly at constant or no irradiation (annealing) conditions [27]. Although FBGs behavior can be qualitatively explained, the lack of models that accounts fully for the underlying physics governing the behavior of various types of FBGs in radiation environments remains a problem [27, 28].

The radiation also weakened the FBG strength. On average, during the first 30 days of radiation, the FBG amplitude dropped by 0.125 dB/day, which is plotted together with the FBG wavelength shifts in figure 18(b) (lower figure). The reduction of FBG strength can be a combined effect of radiation-induced loss that occurred with the fiber itself and the degradation of the FBG under intense irradiation. However, the reduction of FBG strength appears to saturate as the test progressed. Overall, the FBG strength drops by 6 dB over a period of 60-day of active irradiation.

Due to three simulated anomaly interrupts of reactor operations at Days 18, 33, 41 and 55, reactor temperatures and neutron flux were varied to 4 MW, 0.1 MW, 5.59 MW and 0 MW from the targeted 5.6 MW steady states. Behaviors of FBG were also influenced by these interrupts. Results are presented in figures 19(a-d). The interrupts of the reactor operation have impact on both FBG wavelength and FBG strength. The continuous irradiation of FBG from Day 6 to Day 18 produced 1.2 nm FBG wavelength blue-shift from 1527.27 nm to 1526.08 nm. The FBG shift follow a linear relationship with the accumulated neutron dose or irradiation time. This amounts to an FBG linear shift rate of -0.0958 nm/day. This wavelength shift rate remains largely consistent without significant saturation. During the subsequent constant irradiation periods between Day 22 and Day 31, Day 38 and Day 41, and Day 42 and Day 55, FBG wavelengths shift rates are measured to be -0.0900 nm/day, -0.0975 nm/day, and -0.1012 nm/day, respectively. FBG wavelength shifts were not characterized during the nuclear power interrupts. This is because the power profiles during the interrupts are complex and relatively short. The relative steady FBG wavelength shift summarized in table 4 suggests that it could come from a single underlying mechanism, if the mechanism is a complex one. A linear and steady FBG wavelength drift might be mitigated or calibrated on-the-fly to improve the FBG measurement accuracy for static measurement applications (e.g. temperature or strain). For example, a temperature insensitive in-fiber interferometer might be used to calibrate radiation-induced refractive index (RII) change.

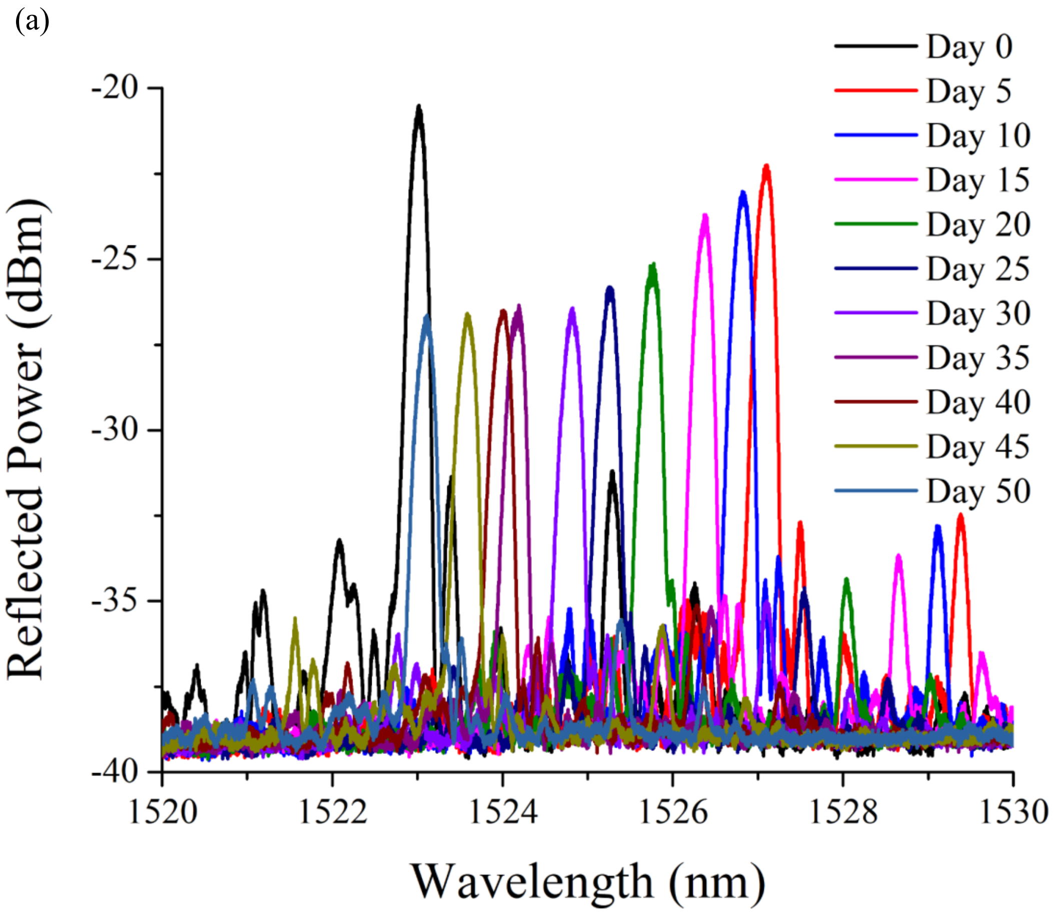

(b)

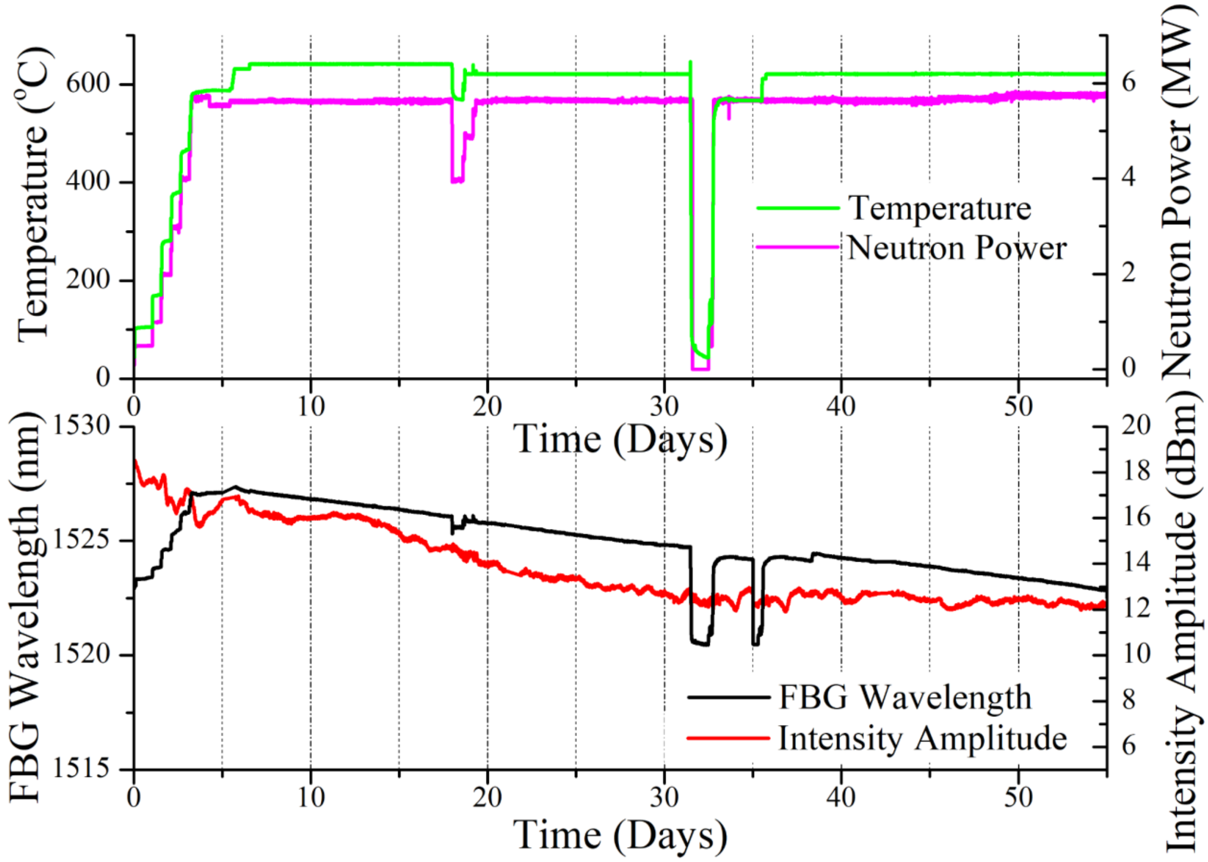

Figure 18 (a) FBG peak wavelength systematic shift due to neutron flux induced index changes (RII) at constant temperature. The intensity peaks also slightly drops due to the effect of RIA. (b) The in-core temperature and neutron power for the events staged in the first 55 days of nuclear reactor operation, and the FBG response in the form of wavelength and intensity amplitude shifts. Reprinted with permission [65] © 2018 OSA.

On the other hand, irradiation-induced FBG peak reduction show strong signs of saturation. During the first period of steady radiation between Day 6 and Day 18, FBG peak reduced by 2 dB with a -0.136 dB/day decay rate. The FBG peak decayed at a lower rate during the second period of steady radiation between Day 22 and Day 31 at -0.113 dB/day. The decay rates show strong saturation after 38 days with -0.04 dB/day and -0.023 dB/day during the last two steady irradiation periods, respectively. Intensity amplitudes of the FBG peaks are reduced by less than 0.6 dB between Day 38 and Day 55.

To evaluate FBG responses to reactor anomalies while temperature and neutron power levels experience abrupt changes, a number of events were staged on Day 18, 33, and 41. During these staged reactor anomalies, reactor power and temperature were raised and reduced at various steps for different periods of times, which creates opportunities to evaluate thermal optic properties of the FBG at various stages of neutron irradiations and different temperature and radiation flux conditions. Some of the transient responses of the FBGs are shown in figures 20(a-b). Results presented in figure 20(a) show a staged event while temperature and neutron power was fluctuated several times between 110-160 °C and 0.5-1 MW, respectively. This was designed to test the sensor responsivity of FBG sensors at low temperatures. The temperatures presented in figures 21(a-b) was measured by a thermocouple (TC3's location is depicted in figure 17(d)). Figure 21(b) shows the temporal responses of FBG sensors for another event while the reactor temperature was raised stepwise from 165 to 540 °C, and correspondingly the neutron power from 1 to 5.5 MW, while observing the FBG wavelength shift that mimics the change in the aforementioned parameters. The FBG wavelength responses to neutron power changes presented in figures 21(a-b) are compared with the thermocouple measurement results. If FBG wavelength shifts are directly and linearly related to reactor temperature changes under intense neutron flux, it is interesting to note that FBG wavelength has faster response times to reactor neutron power changes than those measured by the thermocouple devices. This is more pronouncedly illustrated in figure 21(b).

Given that thermocouples are the only temperature measurement devices within the reactor cores, it is not clear what is the cause of these different response times.

(a)

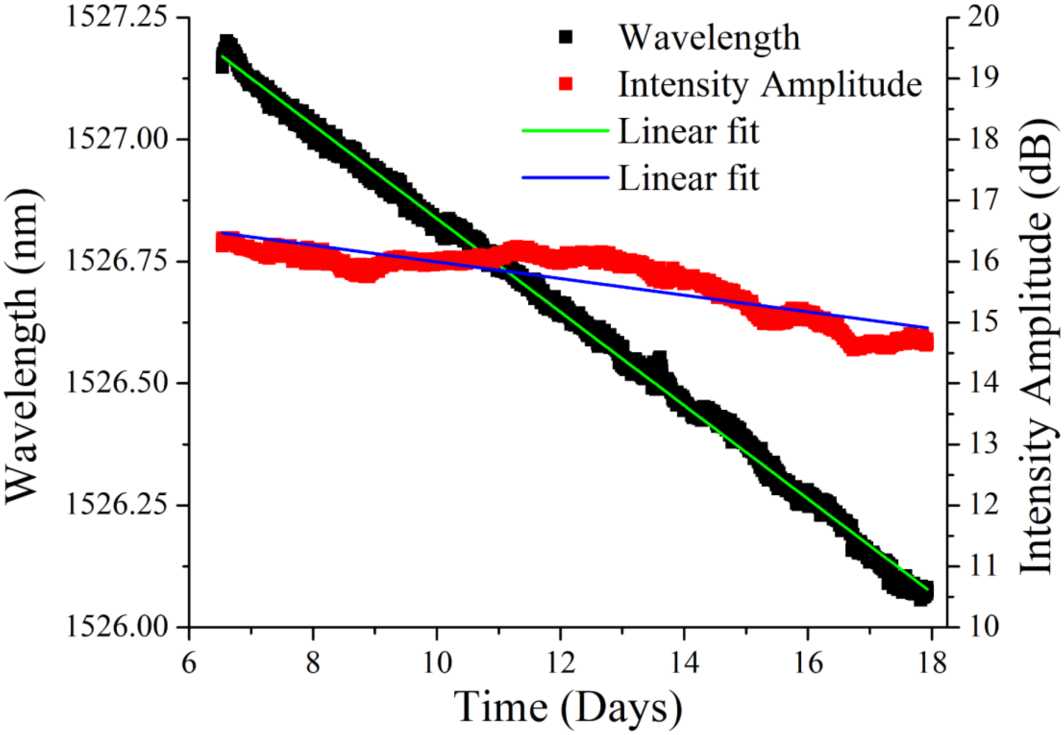
Wavelength
Intensity Amplitude
Linear fit
Linear fit
Wavelength (nm)
1527.25
1527.00
1526.75
1526.50
1526.25
1526.00
Intensity Amplitude (dB)
20
19
18
17
16
15
14
13
12
11
10
6
8
10
12
14
16
18
Time (Days)

(b)

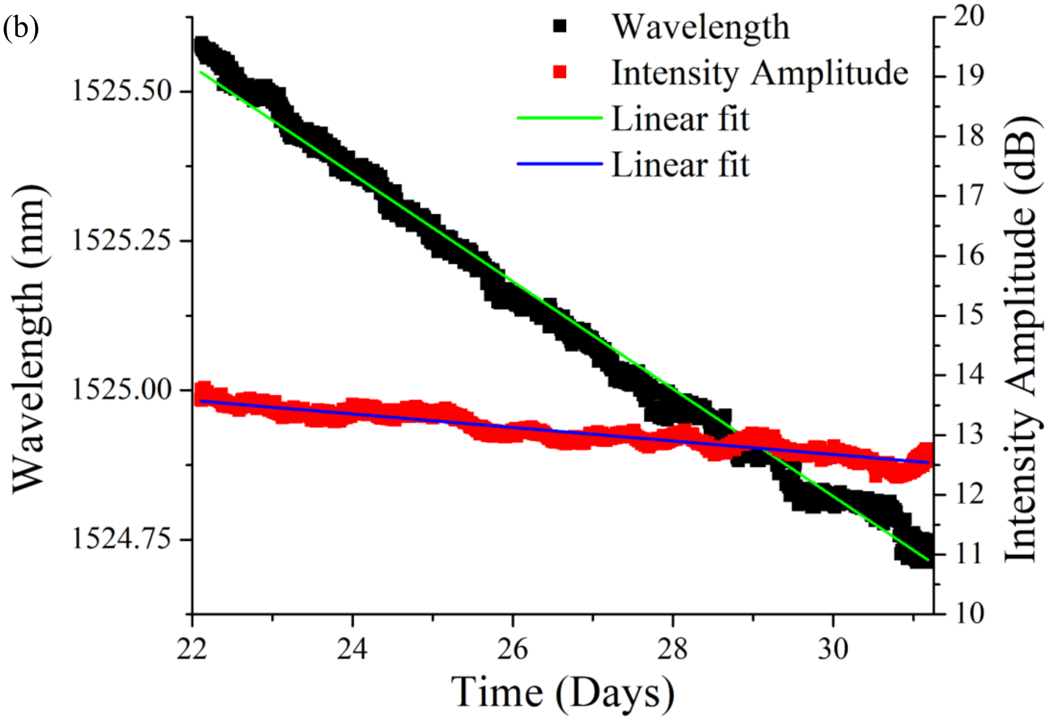
Wavelength
Intensity Amplitude
Linear fit
Linear fit
Wavelength (nm)
1525.50
1525.25
1525.00
1524.75
Intensity Amplitude (dB)
20
19
18
17
16
15
14
13
12
11
10
22
24
26
28
30
Time (Days)

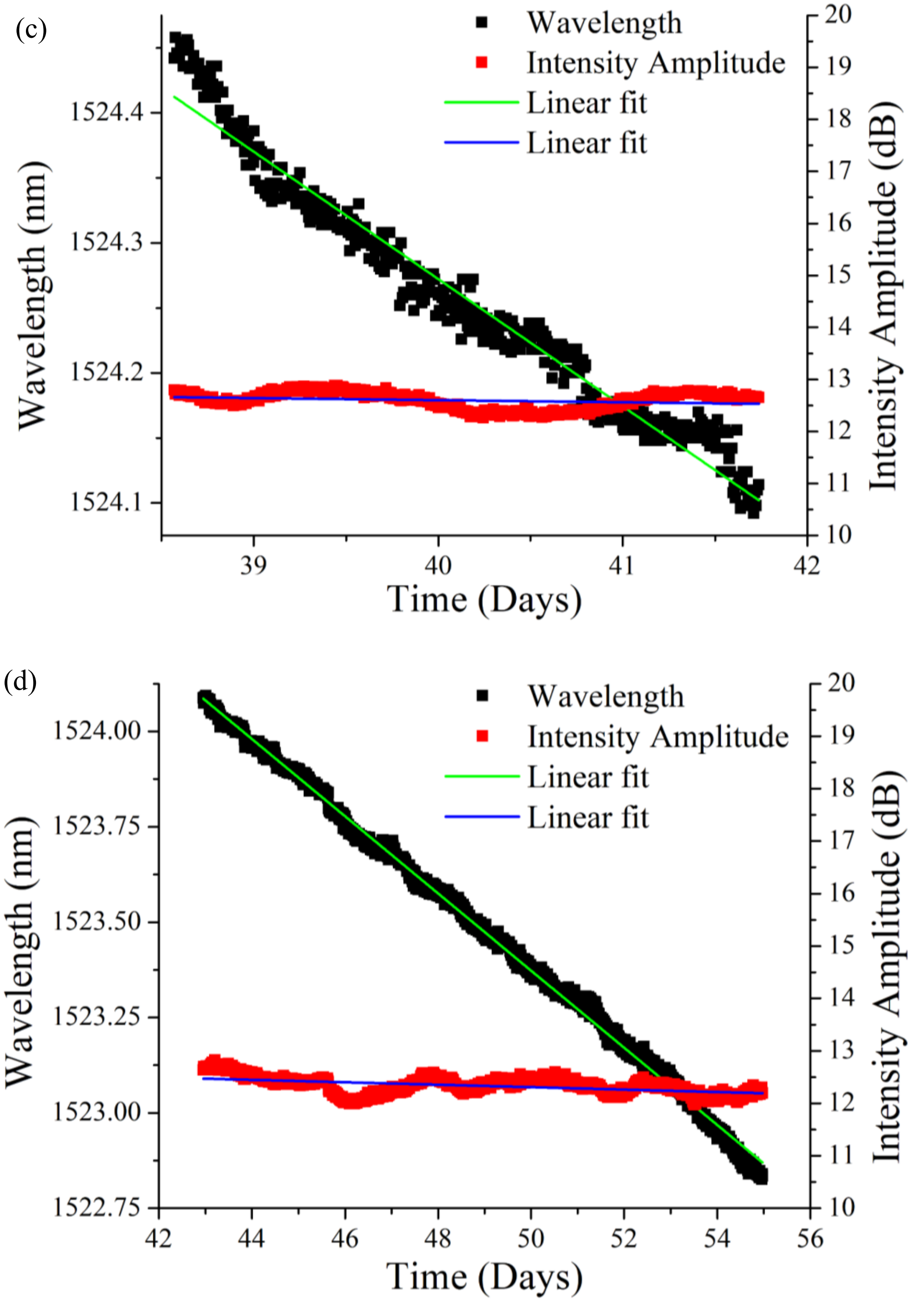

Figure 19 . FBG peak wavelength systematic shift due to neutron flux induced index changes (RII) at constant temperature. The intensity peaks also slightly drops due to the effect of RIA. Reprinted with permission [65] © 2018 OSA.

Table 4 Linear fit characteristics, Wavelength drift with neutron flux at constant temperature.

Time period (Days)	Neutron Power (MW)	Temperature (°C)	Wavelength Slope or Drift rate (nm/days)	Standard Error in Slope $\times 10^{-4}$ (nm/days)	R-square	Intensity Amplitude Slope or Drift rate (dB/days)	Standard Error in Slope $\times 10^{-3}$ (dB/days)	R-square
6.53-17.93	5.62	641.56	-0.09581	1.1666	0.9976	-0.13643	1.94	0.750
22.10-31.18	5.63	621.33	-0.08995	1.5232	0.9941	-0.11307	0.6715	0.932
38.58-41.74	5.64	621.51	-0.09746	8.6631	0.9653	-0.04033	8.18	0.048
42.87-54.97	5.70	621.50	-0.10116	1.2401	0.9974	-0.02324	0.98235	0.243

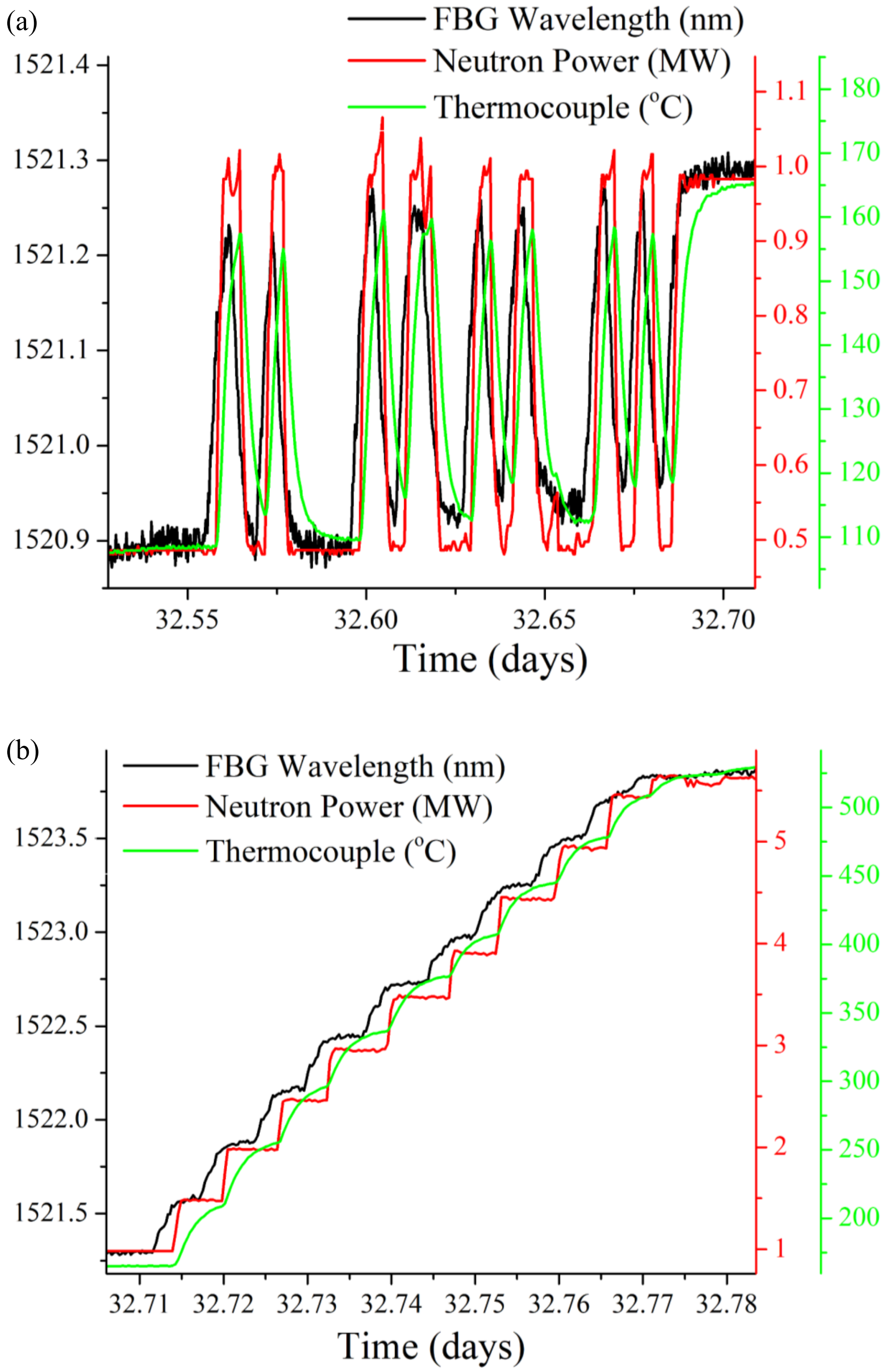

Figure 20 Different events (a) and (b) were staged by varying the neutron power and the temperature inside the reactor core, to study the response of the FBG point sensor noted as the FBG wavelength shifts. Reprinted with permission [65] © 2018 OSA.

To evaluate thermo-optical coefficients of the FBG at different stages of irradiation, the FBG wavelength and thermocouple measurements from four different temperature cycles in days 32, 33, and 55, were plotted in figures 21(a-d). All of the measurement data are linearly fitted to evaluate the FBG sensor's thermo-optic coefficient that would allow calibration of the sensor and conversion of FBG wavelength shifts to temperature readings. The wavelength changes were measured with respect to the initial wavelength at the start of each cycle, taken at constant temperature and neutron flux. The fitting specifications and results are also summarized in table 5. The results show a consistency in the temperature sensitivity coefficient with an uncertainty of 2.03 pm/°C.

(a)

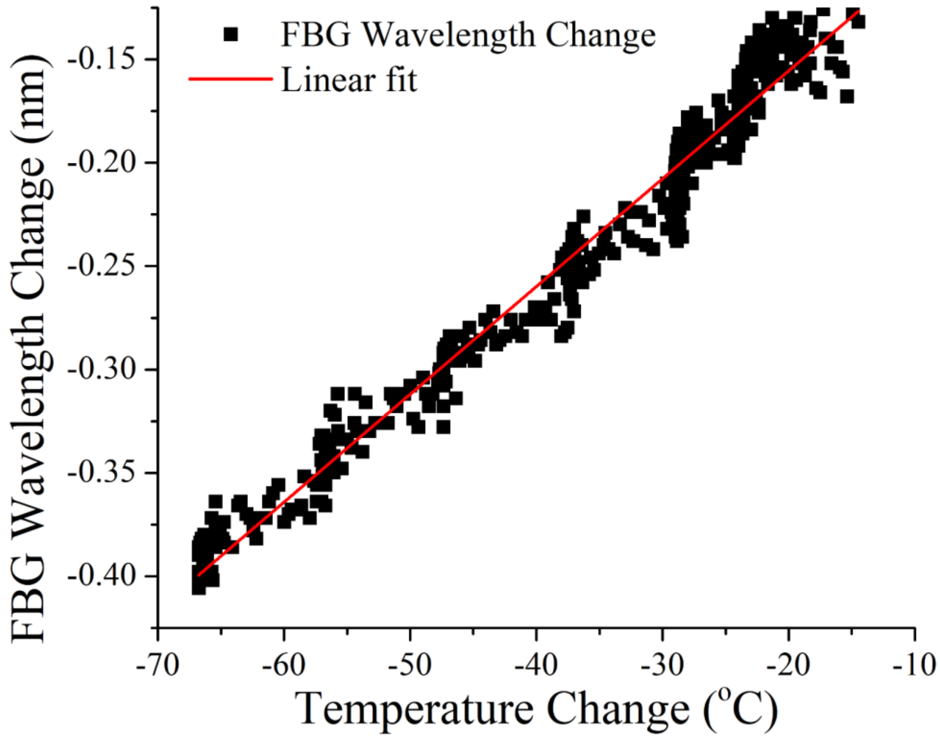

(b)

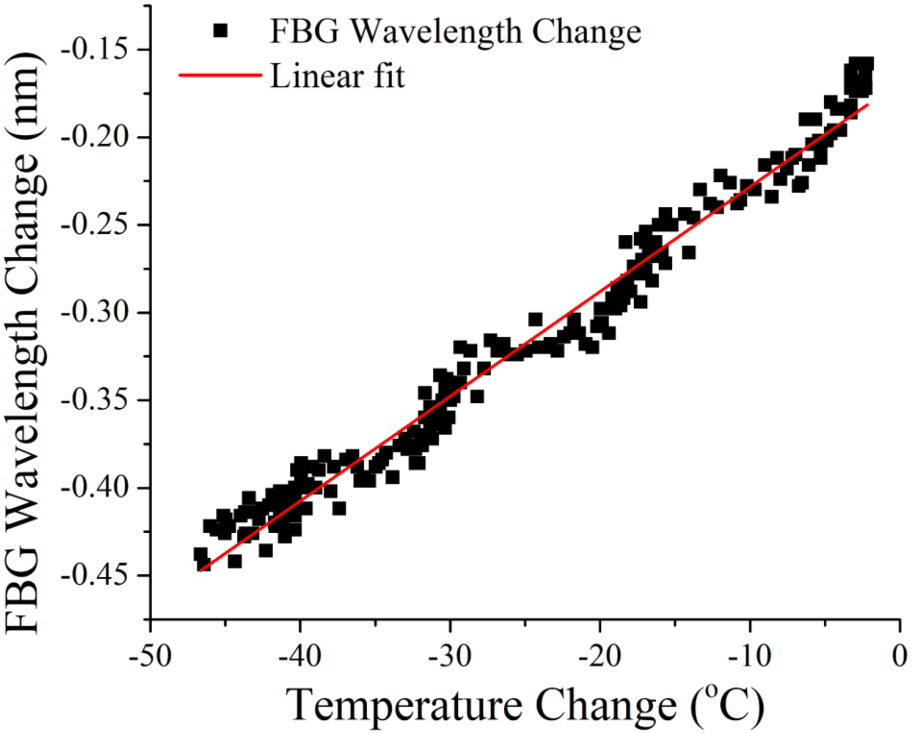
FBG Wavelength Change
Linear fit
FBG Wavelength Change (nm)
-0.15
-0.20
-0.25
-0.30
-0.35
-0.40
-0.45
-50
-40
-30
-20
-10
0
Temperature Change (^{o}C)

(c)

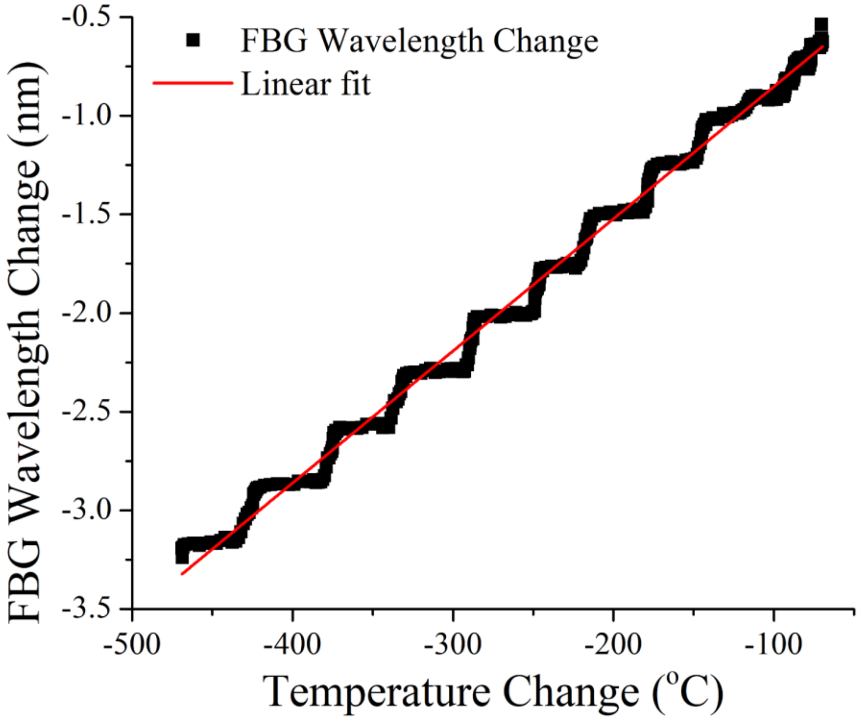
FBG Wavelength Change
Linear fit
FBG Wavelength Change (nm)
-0.5
-1.0
-1.5
-2.0
-2.5
-3.0
-3.5
-500
-400
-300
-200
-100
Temperature Change (^{o}C)

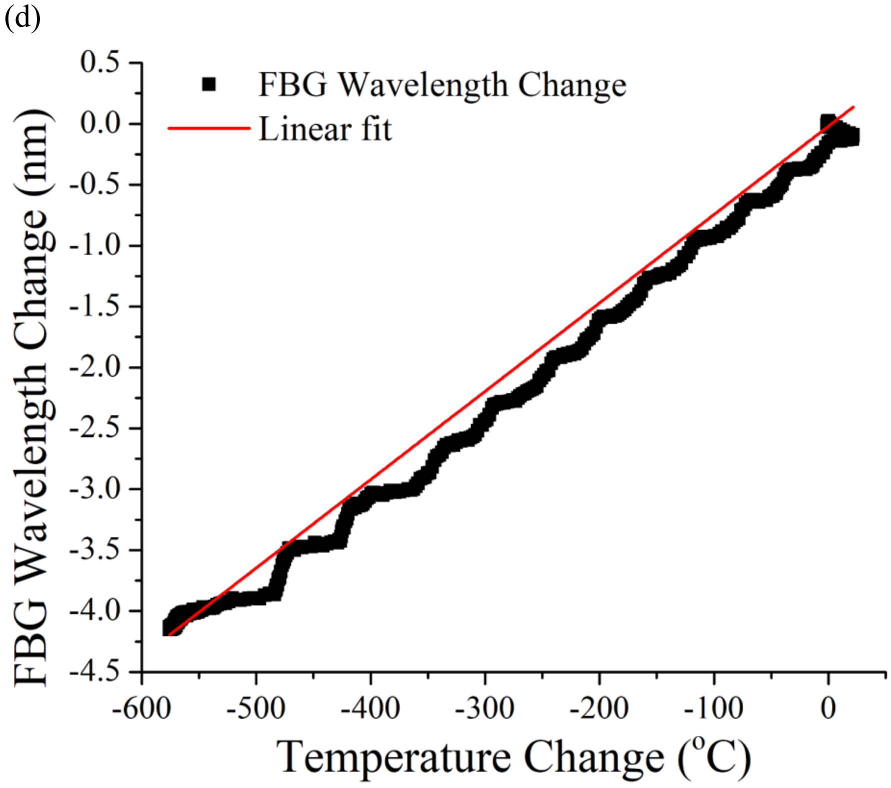

Figure 21 FBG wavelength shifts as plotted against temperature changes in four different temperature cycles. The results were linearly fitted to obtain the temperature sensitivity coefficient of the FBG sensor. Reprinted with permission [65] © 2018 OSA.

Table 5 Linear fit characteristics, Wavelength variation with temperature at constant neutron power.

Day	Temperature Sensitivity Coefficient α_T (pm/°C)	Standard Error in α_T $\times 10^{-2}$ (pm/°C)	R-square
32	7.25	0.64722	0.99787
33	6.70	1.29004	0.99542
55	5.22	3.88365	0.97184
55	5.97	6.11804	0.97734

4.3 FBG Sensor Prediction using LSTM Neural Networks

The present-day advancements in data science and machine learning methods can harness the novel-harsh environment-data obtained from the FBG point sensor inscribed on RAL fiber (described above), to develop early failure-detection systems based on artificial intelligence (AI). So far, such volume of measurements from nuclear reactor cores were not possible. Since the FBG sensor was able to survive harsh in-pile conditions, despite the wavelength drift, it was used to carry out static measurements of the reactor core temperatures. But most importantly it has generated 148786 spectra that can be used to train and build an AI system for prediction of the events forthcoming inside the nuclear reactor core. A Long-Short-Term Memory (LSTM) based neural network was developed for this purpose.

Recurrent Neural Networks (RNNs) are commonly used to represent spatiotemporal datasets with time dependency and/or space dependency between the previous and upcoming samples. For datasets with long time and/or spatial dependence(s) among its samples, a special type of RNNs is used in this case, which the LSTM networks [73]. The LSTM system predicts the behavior of the sensor at time step t, after training the system on the previous time steps t − 1, t – 2 … t − n. The predictive system used is composed of 15 hidden LSTM nodes and one dense layer connected to the output node. Each LSTM node in the network is carefully designed to capture long- and short-term dependency in a dataset; hence, the name Long-Short-Term Memory based networks.

Pre-processing was carried out to determine the FBG peak wavelengths and amplitudes for the recorded FBG spectra. The peak wavelengths and amplitudes measured with time were further smoothed to obtain a data set of 22580 points. The measurements were separated by one minute 30 seconds in the period between days 97 and 118 of irradiation, which is the longest period of irradiation with constant conditions of 642°C core temperature and reactor power of 5.7 MW (figure 22).

The dataset was first normalized between [-1, 1] before being fed to the system. Two thirds of the dataset were used in training the system for 10 complete training epochs, and the remaining one-third of the data were used in testing the system's accuracy. The results from the predictive system for FBG peak wavelengths and amplitudes are shown in figures 23(a) and (b), respectively. The LSTM system was able to detect the forth-coming behavior of the fiber sensor's peak wavelengths with an accuracy of 98.87%, and an accuracy of 96.10% for the sensor's amplitude, based on Root Mean Square Error (RMSE).

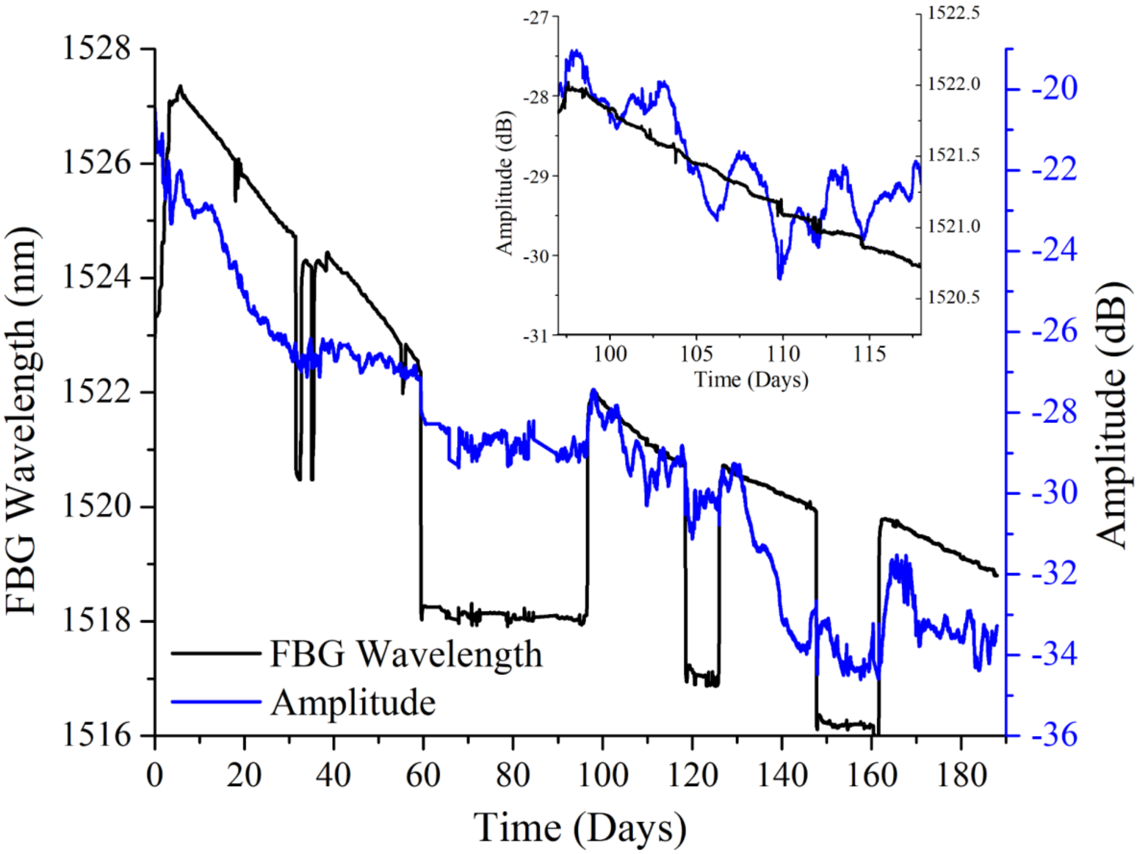

Figure 22 188 days of in-pile measurements obtained by the FBG point sensor on RAL fiber. The plotted peak wavelengths and amplitudes of the FBG spectra are smoothed every five adjacent points. The inset shows the peak wavelengths and amplitudes of the FBG spectra recorded in the period from day 97 to day 118 at 642°C and 5.7 MW of reactor power. This data presented in the inset was used to train the LSTM neutral network.

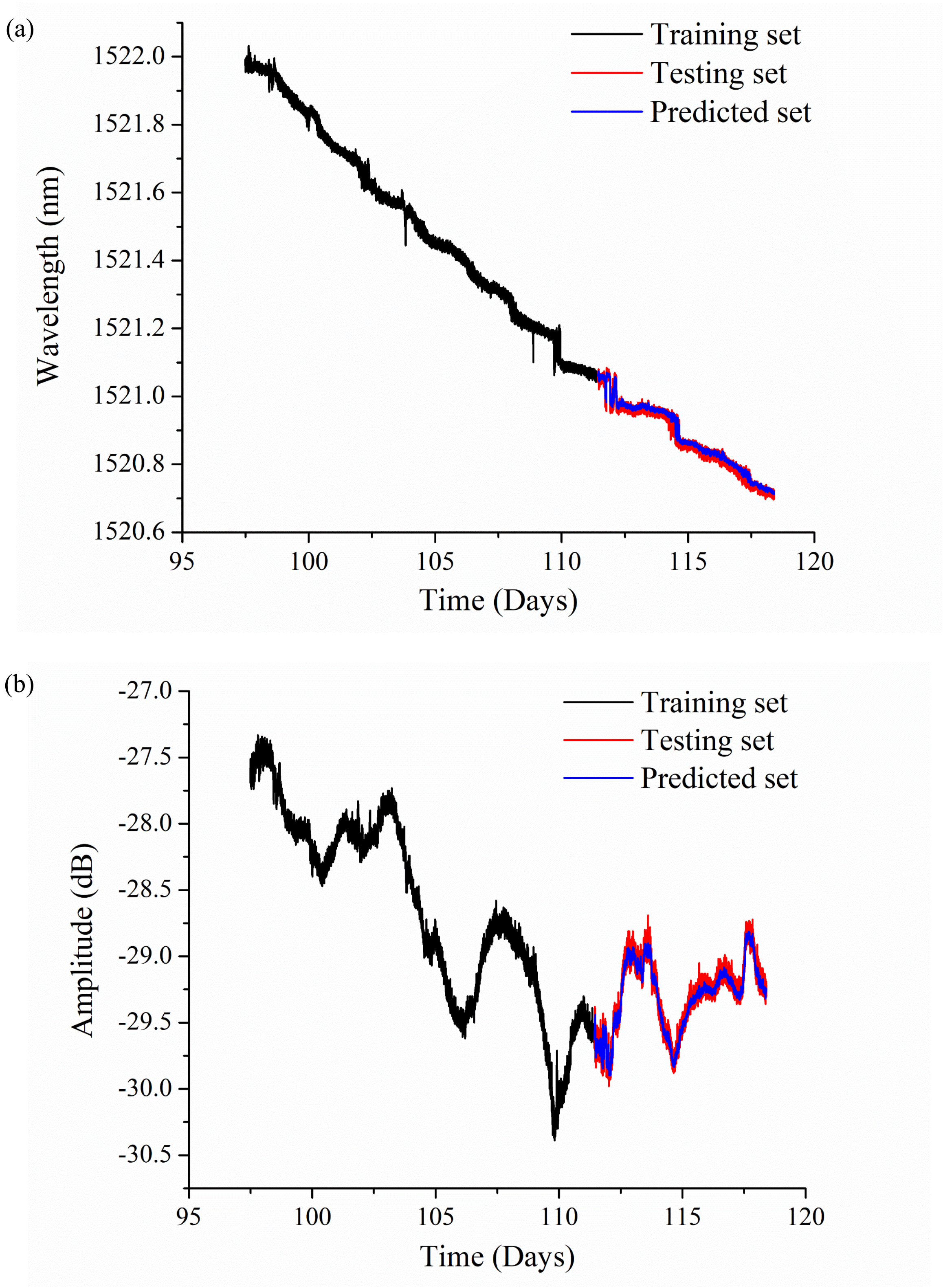

Figure 23 Neural network training, testing, and predicted data sets for FBG (a) peak wavelengths, and (b) amplitudes.

4.4 Summary and Conclusions

This chapter presented nuclear irradiation experimental results of temperature-stable FBG sensors fabricated by a femtosecond laser in pure silica random airline fibers, and the demonstrated prospects of developing AI systems for the task of predicting failures in nuclear reactor operation based on real-time measurements obtained by the fiber sensor. The results show that when appropriate fibers are chosen and suitable laser fabrication techniques are implemented, FBG sensors can be remarkably resilient devices in reactor cores under intense gamma and neutron irradiation at high temperatures. The FBG peak decay stabilizes after approximately 34 days of irradiation. However, the FBG wavelength shows a consistent drift toward shorter wavelength at almost constant linear rate of -0.1 nm/day. The reduction in grating strength is related to a reduction in the index modulation while the wavelength shift is due to a change in the average index of the glass under neutron irradiation. The use of FBGs for static measurement could be impacted by this linear FBG wavelength drift. A self-calibration method might be needed for FBG to perform static measurements such as absolute temperature measurements. Despite this drift, the FBG sensors can be used to perform quasi-static measurements while physical stimuli (e.g. temperature) variation occur in spans of 10 hours or shorter. This means that radiation-hardened FBGs such as those presented in this chapter could be used as multiplexible sensors for abnormal event monitoring, dynamic pressure, acoustic measurements…etc. Results presented in this chapter reveal that temperature-stable Type-II FBGs fabricated in radiation-hardened fibers could be used as sensors to perform in-pile measurements, to improve safety and efficiency of existing and next generation nuclear reactors.

An LSTM based neural network was developed for predicting the behavior of an optical sensor that monitors the environment inside of a research nuclear reactor core that mimics commercial nuclear reactors. The accuracy with which this neural network anticipates the reactor core events, is very high taking into consideration how sophisticated the dataset obtained from the fiber sensor was. This neural network, coupled with the FBG point sensor, can be applied in research, commercial, and military nuclear facilities to monitor the nuclear environment and issue early warnings for failures before disasters occur.

5.0 Ultrafast Laser Enhanced Optical for Distributed Sensing in Harsh Environments

Ultrafast lasers are well known for their use in writing FBGs on optical fiber cores [69]. Ultrafast lasers induce refractive index changes on silica-based fibers as a result of formation of self-ordered nano-gratings, as previously discussed in section 4.1.2. These induced changes proved very stable at high temperatures, therefore can function as point sensors [70, 74-76]. Moreover, the ultrafast formed FBGs proved superior to the ones produced by UV lasers in terms of temperature stability. However, the inscription process of an FBG, whether it employs phase masks, interferometric techniques, or direct-writes, requires a very high precision alignment to be able to form accurately the grating structure on the fiber core.

In this chapter, and using a similar methodology to the aforementioned FBG inscription process that utilizes ultrafast lasers, a more relaxed focusing geometry is used to continuously alter the refractive index of an optical fiber core; constituting a distributed fiber sensor. The continuous nanogratings formed in the fiber core enhance the Rayleigh scattering profile, and very much like the ultrafast written FBGs, the enhanced profiles are very stable at high temperatures and can be used to perform multi parameter measurements [77].

5.1 Formation of Ultrafast Laser- Induced Nanogratings in Optical Fiber Cores

The ultrafast laser-induced nanogratings are formed as a result of interference between the electric fields of the incident light and the plasmon-polariton wave from the randomness of surface inhomogeneity [78]. This interference results in a standing plasma wave [79, 80] that causes a periodic modulation of the electron plasma concentration, and permanent structural changes are induced in silica glass in the shape of a standing wave as shown in the SEM images in figure 24(a). The periodicity of the formed nanogratings is consistent with the 400 nm half wavelength of the formed standing wave in silica glass, i.e., 400/1.5 = 266.67 nm, as shown in figure 24(a) [78, 81-83]. The nanogratings width and height is dependent on the ultrafast laser energy deposited into the focal volume that in turn is determined by the laser's scanning speed [79, 84-86].

5.2 Distributed Fiber Sensors Point-by-Point Fabrication Method

A Coherent® MIRA-D Ti: sapphire seed oscillator and a RegA 9000 regenerative amplifier described in [2, 87] was used to inscribe the enhanced Rayleigh backscattering sections. A 20 cm section of the fiber's protective acrylic coating was removed; the bare fiber section was fixed on a fiber holder then a 200 nJ/pulse ultrafast laser of 300 fs pulse width (FWHM), and 800 nm, was focused on the center of the core of the fiber sample with a repetition rate of 250 kHz. The sample is mounted on a three-axis Aerotech® ABL2002 motion stage for focusing, and a rotary stage was used for lateral translation under the laser. The sample is translated in the lateral direction (axial of the fiber) of the fiber as the ultrafast laser continuously impacts the fiber core spatially point-by-point, hence the name of the fabrication method.

Oil-immersed objectives (80×) with a 1.25 numerical aperture (NA), and 1.518 refractive index was used to eliminate the effect of the spherical aberration of the fibers with cylindrical shapes. As for D-shaped fiber samples, those were fixed with their flat sides facing the laser beam, and a cylindrical telescope was used instead to shape the laser beam and control the shape of the focal volume. Enhanced structures were formed with lengths 12-13 cm, and featured a minimum of 40 dB boost in the Rayleigh backscattered signal and insertion loss of 0.15 dB/cm introduced by the laser irradiation-formed nanogratings. The laser scans the optical fiber core in the axial direction as shown in figure 24(b) with spatial continuity. The direction of light propagation is denoted by the propagation vector **k**, while the electric field **E** dictates the transverse dimension and direction of the nanogratings. The orientation of the nanostructures formed with respect to the induced standing plasma wave renders the enhancement of the Rayleigh profile polarization dependent. The optical fiber is connected to a commercial optical frequency domain reflectometer (OFDR) interrogator (Luna Innovations® OBR4600) described in section 2.1.1, to monitor the Rayleigh backscattering profiles during the laser irradiation process, as illustrated in a schematic of the ultrafast laser enhancing setup in figure 24(c).

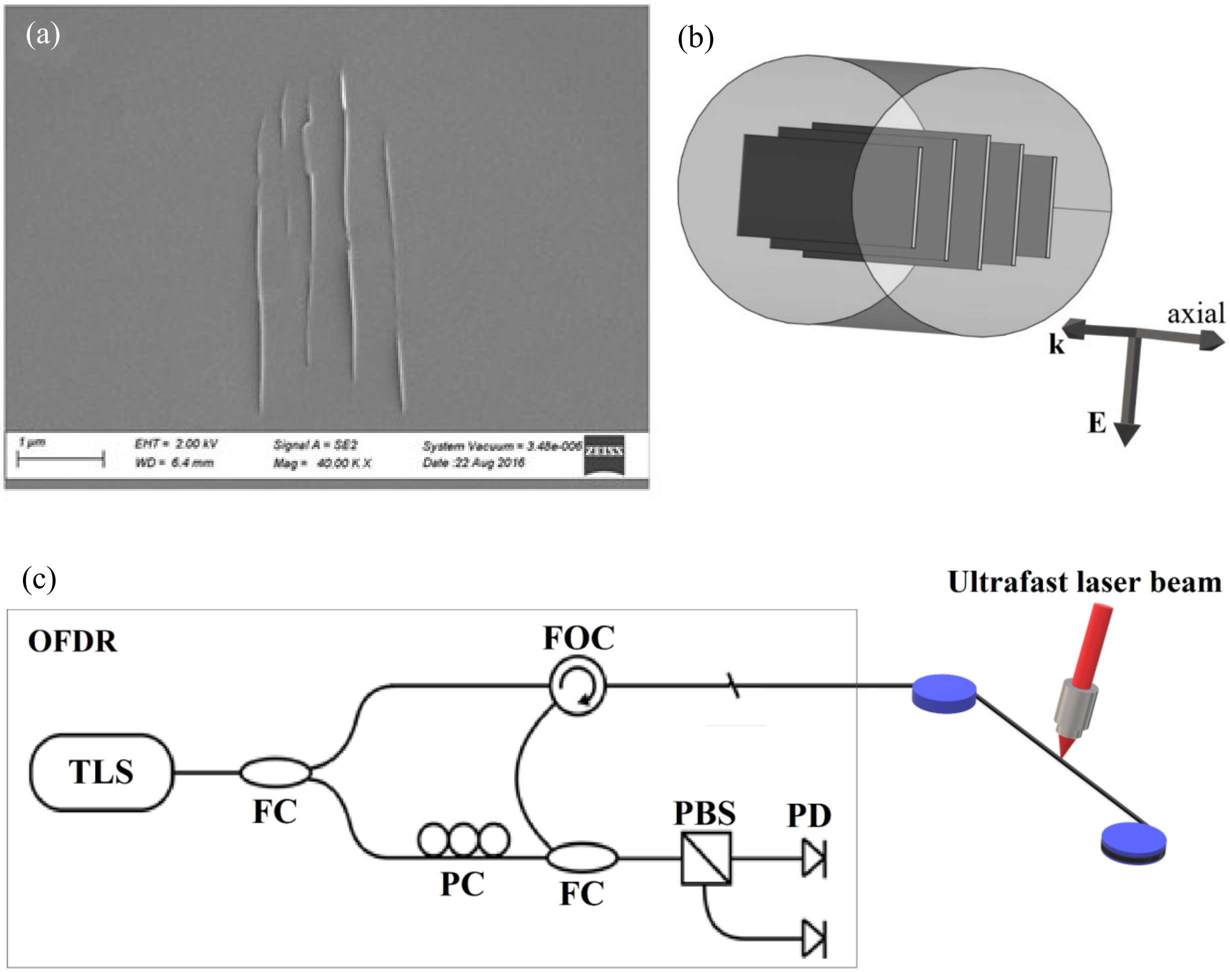

Figure 24 (a) An SEM image of nanogratings induced on a SMF-28® sample. Reprinted with permission [88] © 2017 Springer Nature. (b) An illustration of the nanogratings formed in a fiber core. The fiber core is scanned by ultrafast laser (normal to fiber core) in the direction of the fiber core (axial direction). The electric field magnitude detemines the size of the gratings, while the electric field direction determines the transverse orientation of formed gratings at the fiber cross-section. (c) The schematic of the ultrafast laser-induced nanogratings setup. An optical backscattering reflectomer is used view the enhanced Rayleigh profiles as the nanogratings are being inscribed on the fiber core.

5.3 Thermal Stability of Ultrafast Laser-Induced Nanostructures

The Rayleigh enhanced sections inscribed on Corning® SMF28e+® and Vascade® fibers were placed inside of a tube furnace and heated up to 800°C in controlled N_2 ambient. The temperature was stepped from room temperature up to 800°C in steps of 100°C, then kept at 800°C for 40 hours before stepping down to room temperature. Then faster heat cycling was performed raising temperature to 800°C then dropping to room temperature two times. The enhanced Rayleigh profiles at different heat cycling conditions are shown in figures 25(a-b). The Rayleigh appear stable for the enhanced section on Vascade®, while in SMF-28® the profile ultimately drops by ~15 dB at 800°C compared to the initial profile at room temperature as shown in figure 25(b) then becomes stable as well.

The temperature distributions were measured along the section of the distributed fiber sensor inside the oven at a 1 cm spatial resolution and the results are plotted in figures 26(a-b). Temperature changes of the furnace can only be measured by the ultrafast laser enhanced section on a fiber sample, whereas the sections on both sides of the laser-enhanced section failed to produce a valid temperature measurement for both samples on SMF-28® and Vascade® fibers. The spatial temperature distributions inside the furnace at 800°C show consistency after three heating cycles to 800°C, as shown in figures 27(a) and (b) for Vascade® and SMF-28® fiber samples, respectively. This consistency in temperature distribution measurements appears due to annealing of the laser-induced nanostructures that reach a constant state after a couple of heating cycles, and project constant Rayleigh profiles upon further heat treatment.

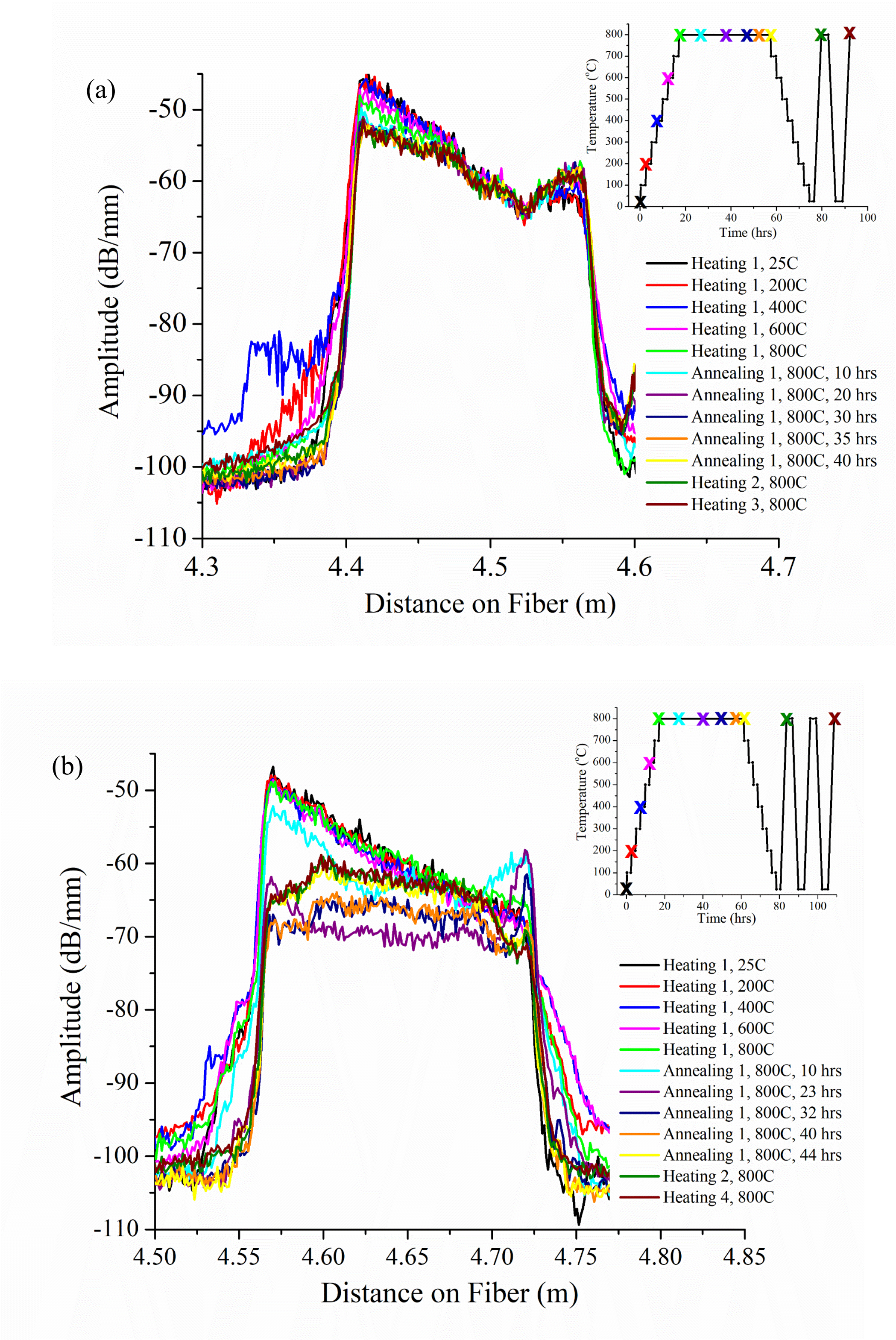

Figure 25 Ultrafast enhanced Rayleigh profiles at different temperature cycling conditions as shown in insets for (a) Vascade® and (b) SMF-28® fiber samples.

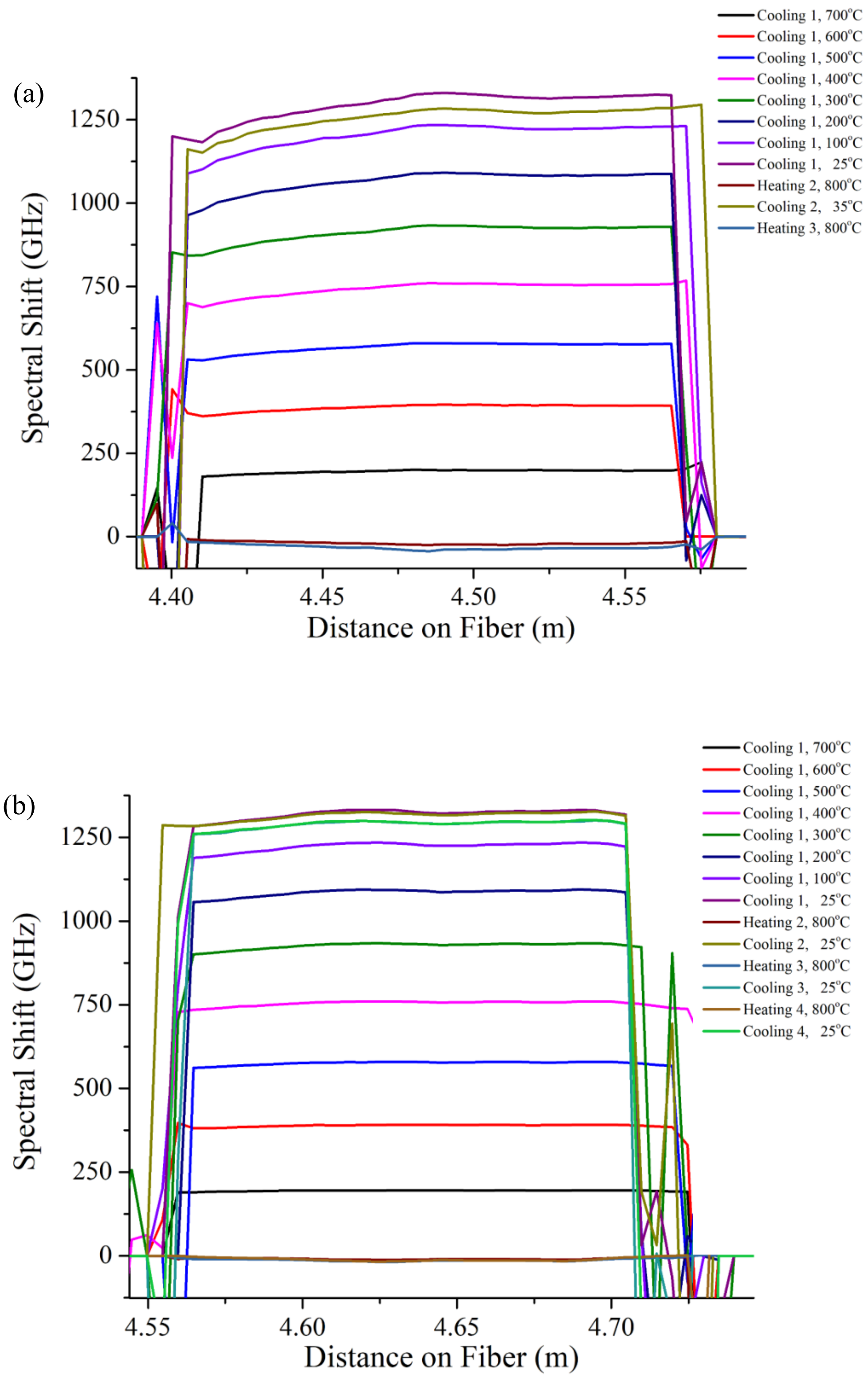

Figure 26 Spatial distributions of temperatures measured by the distributed (a) Vascade® and (b) SMF-28® fiber sensors at different temperature cycling conditions.

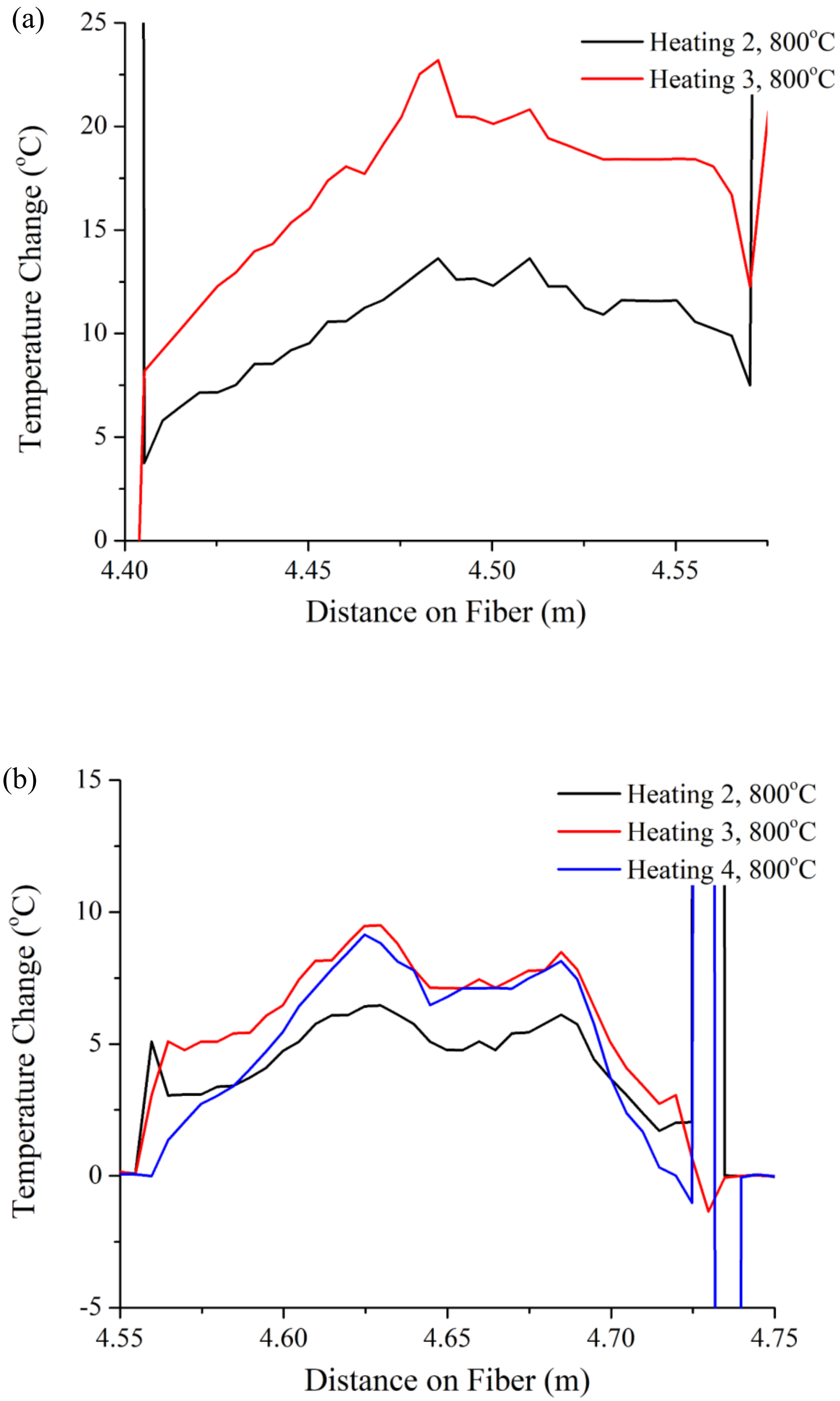

Figure 27 Spatial distributions of temperatures measured by the distributed (a) Vascade® and (b) SMF-28® fiber sensors for different heat treatments at 800°C.

5.4 Ultrafast Laser-Enhanced Distributed Sensors for Nuclear Reactor Core Sensing

The ionizing irradiation of the optical fiber distributed sensors was carried out at the MIT nuclear reactor in the setup described in chapter 4. The fiber samples were inserted inside of stainless steel tubes, which were placed inside a graphite holder in a grade 2 titanium capsule (figure 28(a)). The capsule was lowered to the neutron reactor core through an in-core sample assembly (ICSA) shown in figures 28(b) and (c).

5.4.1 Fiber selection for distributed in-pile reactor measurements

Three different types of fiber were used in this study: the ITU-T G.652.D (Corning® SMF28e+®), ITU-T G.654.C (Corning® Vascade EX1000®), and a specialty Corning® D-shaped fiber. Enhanced sections were continuously inscribed on the fiber cores for two SMF-28e+® and two Vascade® fibers and two D-fibers, with Rayleigh signal profiles shown in figures 29(a), (b) and (d). Two sensors were also fabricated on Vascade® fibers with intermittent enhancement of 1.7 mm sections at a pitch of 3.4 mm, shown in figure 29(c). Table 6 summarizes the information about the fabricated distributed sensors. The choice of optical fibers tested was governed by both cost effectiveness and reputation in resistance to ionizing radiation. As explained previously in section 4.1.1, that it has been established from literature studies that the Ge-doped SMF-28® [89], and the F-doped Vascade® [90] are radiation hardened fibers and would develop the lowest radiation induced attenuation (RIA) upon exposure to ionizing gamma and neutron radiations [63].

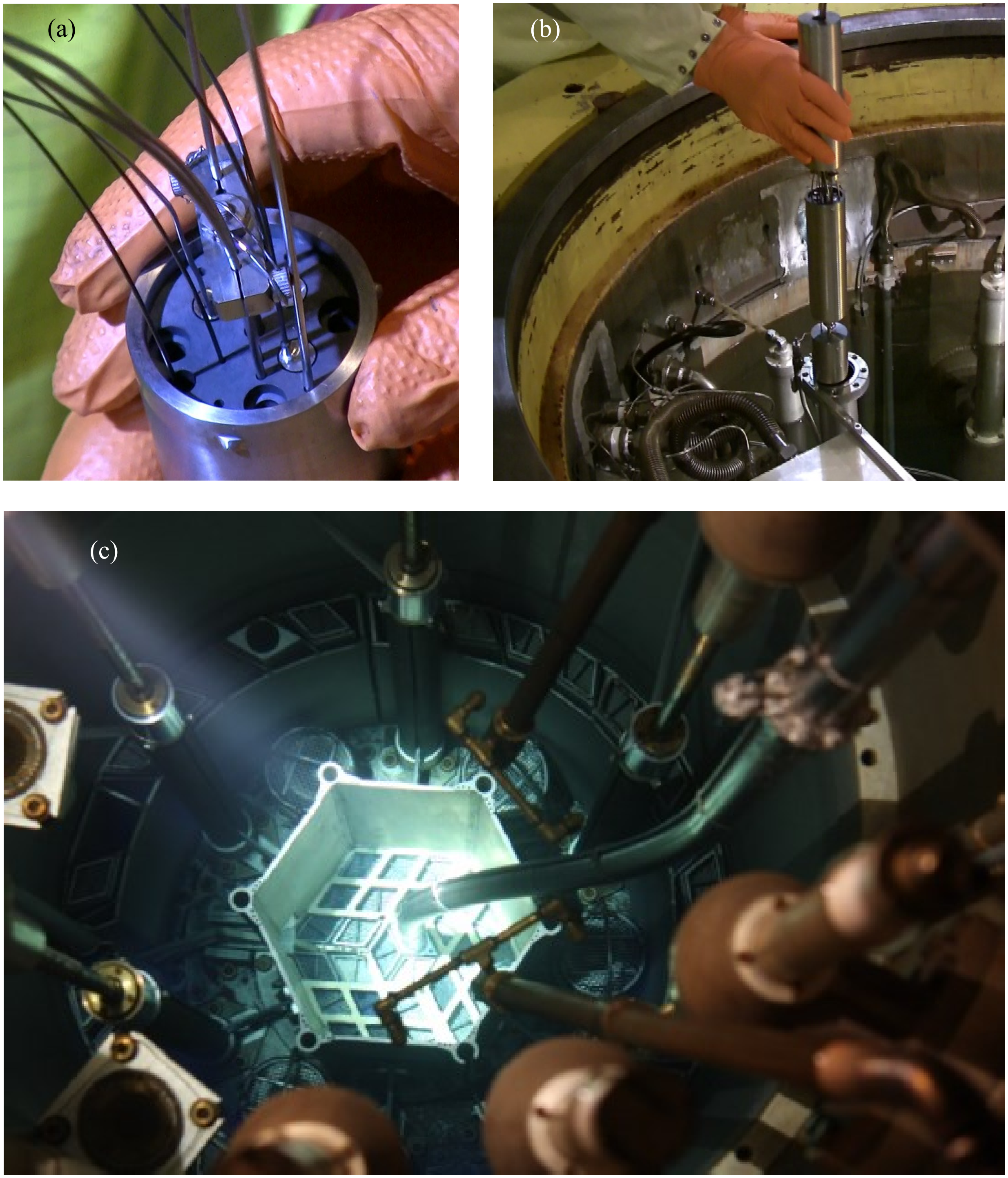

Figure 28 (a) Grade 2 Ti capsule with the stainless steel tubes and thermocouple leads inserted into a graphite sample holder. (b) In-core sample assembly (ICSA) at the MIT nuclear research reactor. (c) A photograph of ICSA thimble extending to the neutron reactor core ~3m below the reactor opening.

Moreover, there has been a difficulty in writing continuous temperature stable Rayleigh enhancing nanostructures on the micro-structured random airline (RAL) fibers' using the aforementioned point-by-point setup. This is owing to the unsystematic distribution of air holes array in the cladding region, around the unstructured- pure silica- core of the fiber. These air microstructures in the cladding strongly scatter the laser beam during the process of FBG inscription, and makes it difficult to focus the laser beam onto the pure-silica core of the RAL fiber as the laser translates in the axial direction of the sample [66].

It is worthy to note that until this point, there has not been much success in writing thermally stable, continuous, structures on microstructure-cladded RAL fiber cores that can withstand high temperatures. Using point-by-point inscription, the continuous samples inscribed on RAL fibers degraded quickly at 800°C in preliminary fiber selection tests. Later, plane-by-plane inscription method has been used as explained in section 4.1.2.2, to inscribe both FBGs and continuous nanostructures, the results of testing these are not reported here. Until this point, only by using the phase mask inscription method for FBGs, as explained in 4.1.2.1, the induced structures have proven thermal stability and resistance to neutron irradiation [65].

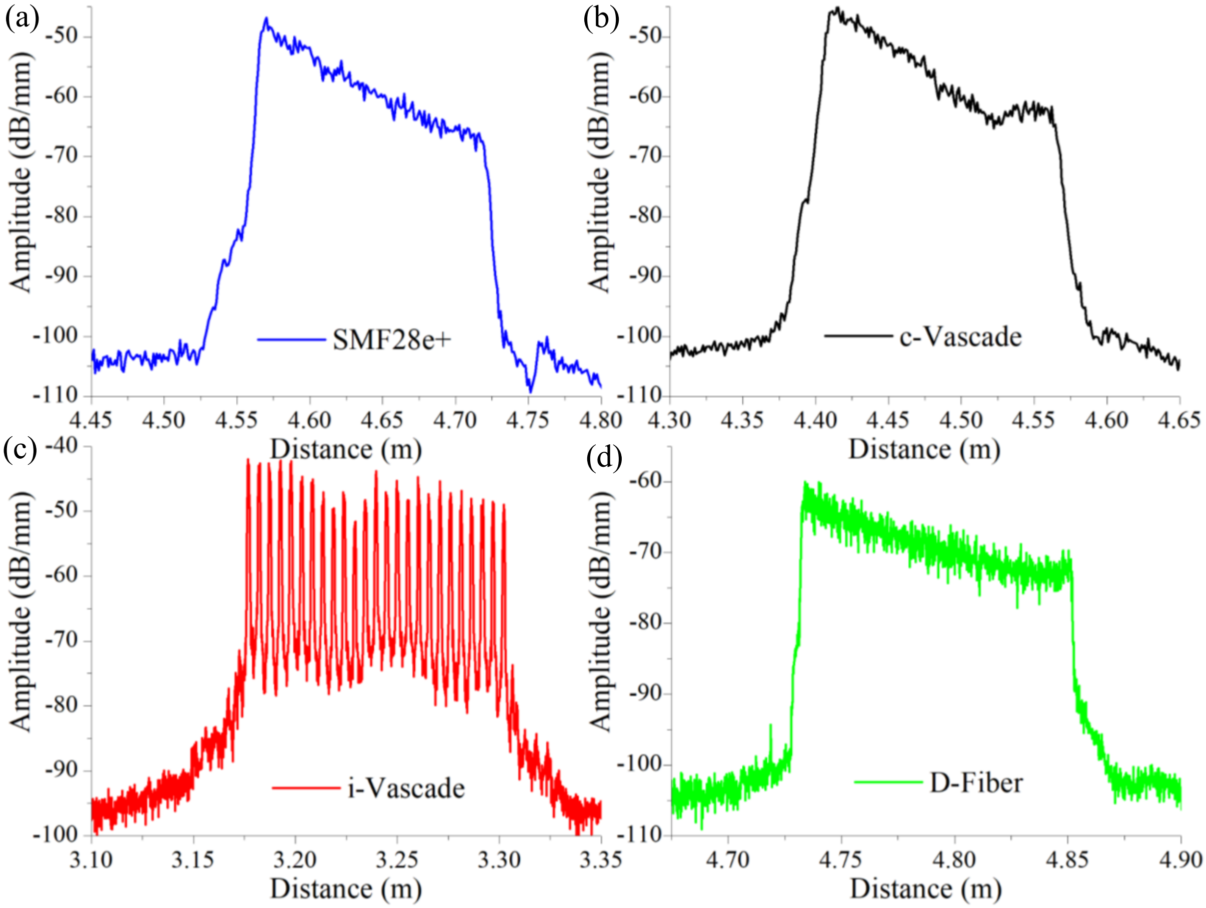

Figure 29 Ultrafast laser-enhanced Rayleigh profiles for samples (a) SMF-28e+®, (b) and (c) on Vascade® fibers, inscribed with spatial continuity and intermittently, respectively, and (c) on specialty D-shaped optical fibers.

Table 6 Summary of the ultrafast laser-enhanced spatially distributed sensor samples.

Sample ID	Commercial name	Fiber Standardization[1]	Core doping	Cladding doping	Enhanced structure
SMF-28®	SMF-28e+®	ITU-T G.652.D	Ge	Ge	Continuous
Vascade®	Vascade EX 1000®	ITU-T G.654.C	Pure-silica	F	Continuous (c-Vascade)
Vascade®	Vascade EX 1000®	ITU-T G.654.C	Pure-silica	F	Intermittent (i-Vascade)
D-fiber	D-fiber	Not standardized	Ge	Ge	Continuous

5.4.2 Distributed sensor deployment in neutron reactor core

The distributed fiber sensors were placed in the grade 2 Ti capsule (depicted in figure 30(a)), and the capsule lowered inside the ICSA thimble to the nuclear reactor core, and situated in a position where the Rayleigh-enhanced sections will experience the maximum neutron flux. Temperature fluctuation tests where initially executed to make sure that the fiber samples are in the correct position before the bombardment with neutron flux commenced. Figure 30(b) shows the temperature profile inside the reactor core as gaged by the distributed fiber sensors prior to the

---

[1] ITU-T is a division of the International Telecommunication Union (ITU) that coordinates telecommunication standardization.

reactor full operation. The 10 °C temperature differential between spatial locations inside the capsule agrees with a previous knowledge about the temperature profile of the capsule that was determined using thermocouples. The reactor was operated, and through a combination of nuclear heating and He/Ne regulation; the reactor power and temperature were raised over a period of three consecutive days to ultimately reach 5.62 MW at an in-core temperature of 622 °C. Events were simulated where the reactor power and in-core temperature were dropped then recovered over a period of time, and in some events cycled a few times, to gage the distributed sensors' responsivity to in-core environment changes and evaluate their overall performance as temperature sensors. Figure 30(c) shows all the reactor conditions for the 188 days neutron irradiation tests.

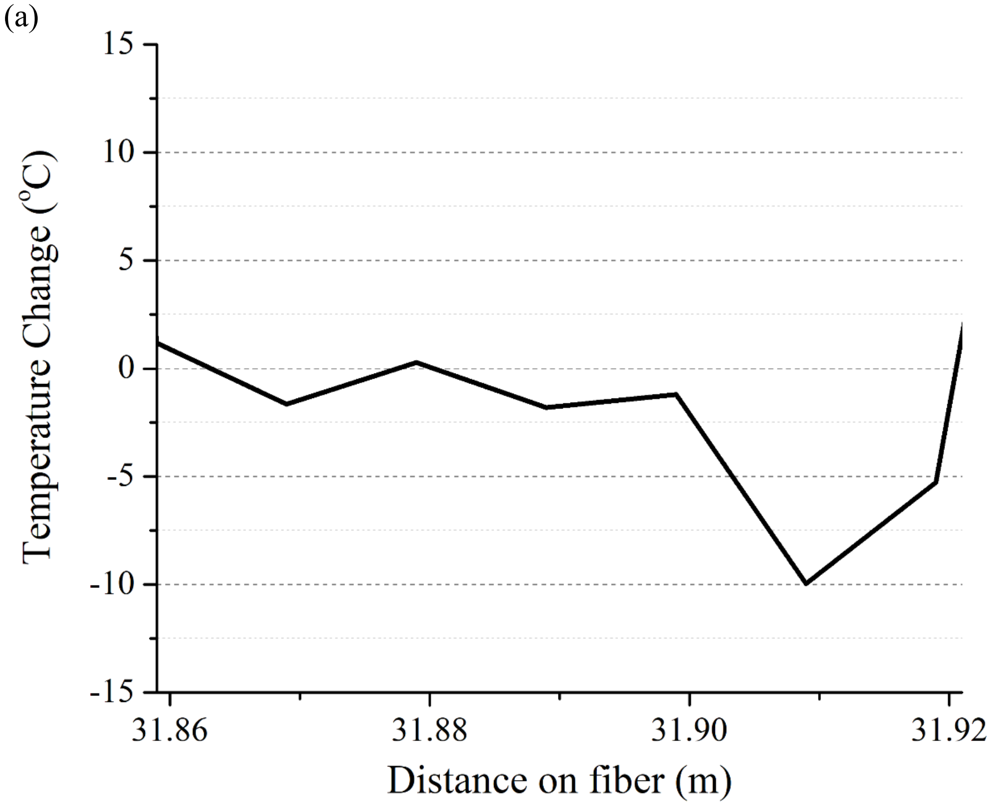

(b)

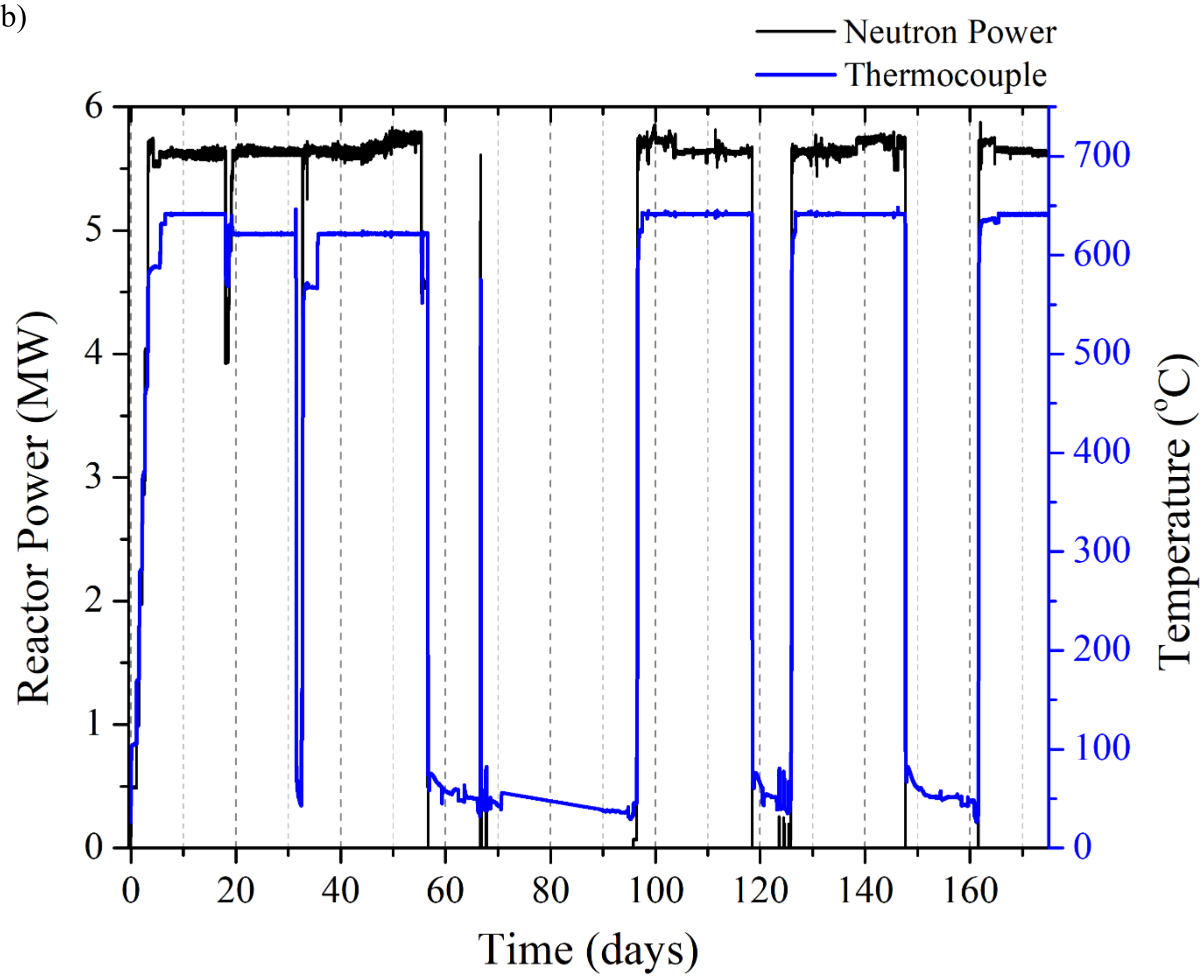

Figure 30 (a) Temperature distribution inside the capsule measured by the distributed sensor prior to neutron irradiation. (b) All the reactor conditions and staged events for the 188 days run of the MIT nuclear reactor for this experiment.

5.4.2.1 Neutron flux effects on Rayleigh enhanced spatial distributions

It was evident that radiation-induced refractive index (RII) changes have occurred from the ionizing effect of the neutron flux incident on the optical fiber samples for a significant amount of time. Figures 31(a-d) shows the temporal development of the backscattered Rayleigh signals from the laser-enhanced sections exposed to harsh environment inside of the nuclear reactor core. Figures 31(a) and (b) show the development of the continuous enhanced Rayleigh profiles of the samples on SMF-28® and Vascade®, respectively, were those samples still survived at Day 61 with an overall decay of 10 dB. The progression of the intermittent Vascade® sample, shown in figure 31(c), appeared to have totally decayed between Day 51 and Day 61. The enhanced section inscribed on the D-shaped fiber followed a rapid decay pattern, and was totally destructed after only one and a one-half day inside the reactor core (figure 31(d)).

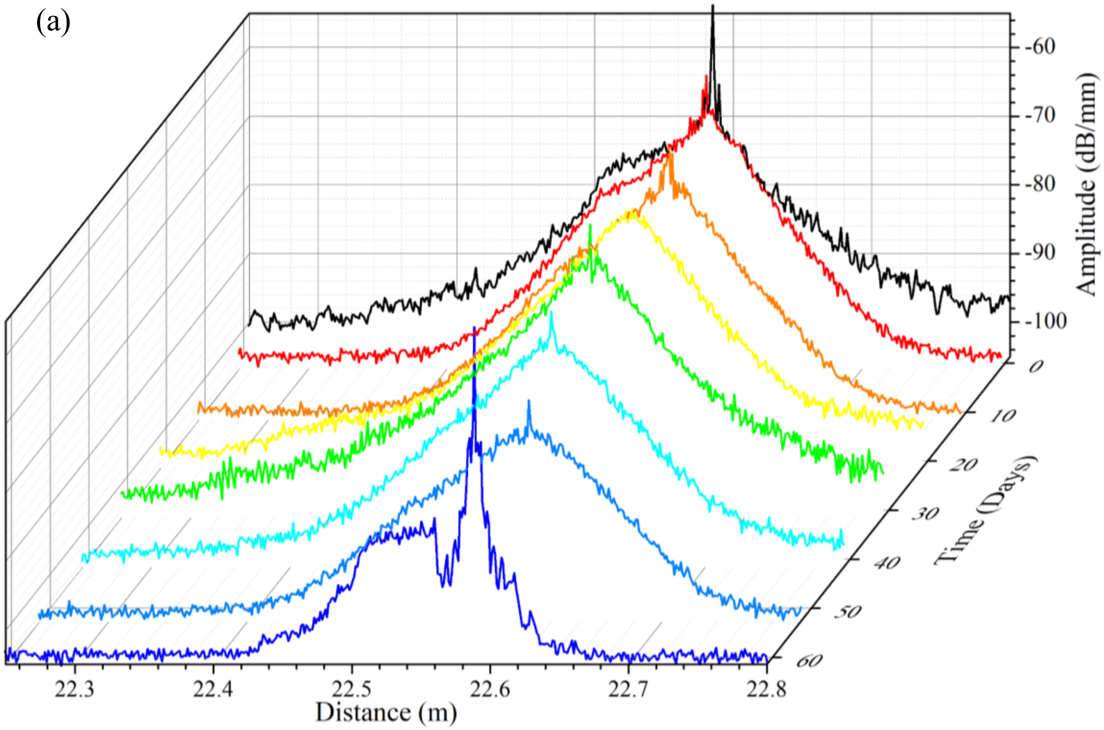
(a)
-60
-70
-80
-90
-100
Amplitude (dB/mm)
0
10
20
30
40
50
60
Time (Days)
22.3
22.4
22.5
22.6
22.7
22.8
Distance (m)

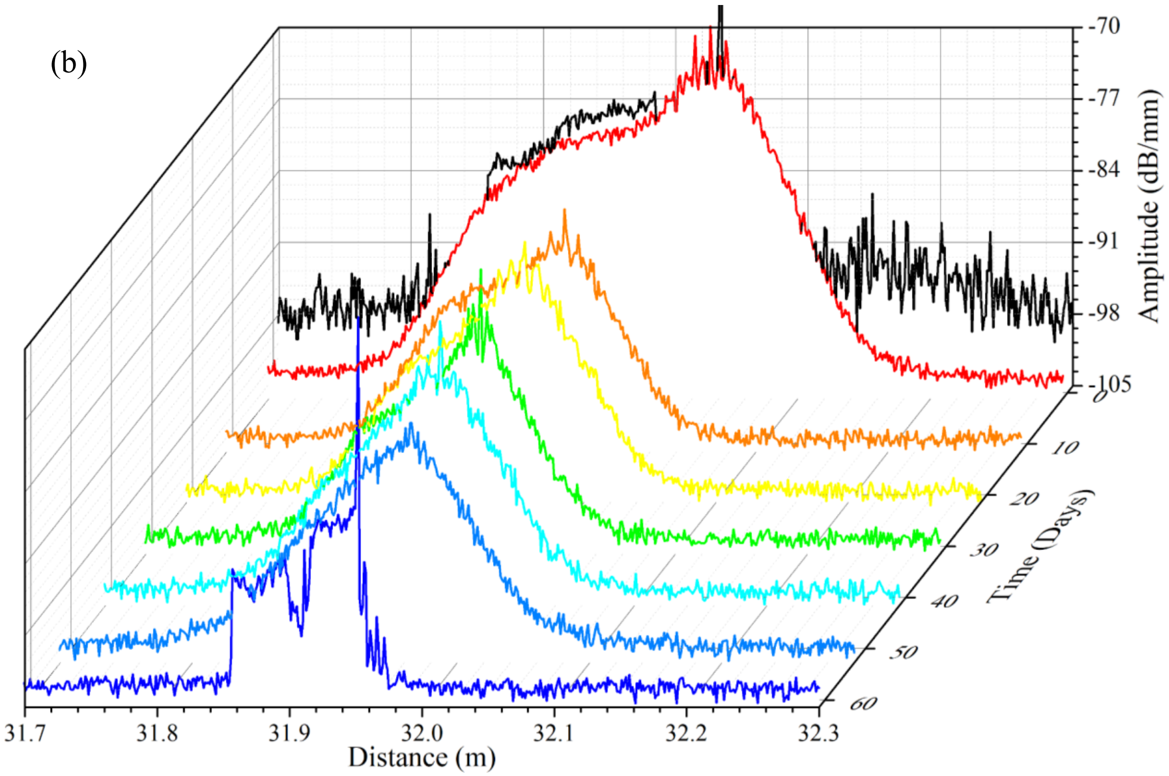
(b)
-70
-77
-84
-91
-98
-105
Amplitude (dB/mm)
0
10
20
30
40
50
60
Time (Days)
31.7
31.8
31.9
32.0
32.1
32.2
32.3
Distance (m)

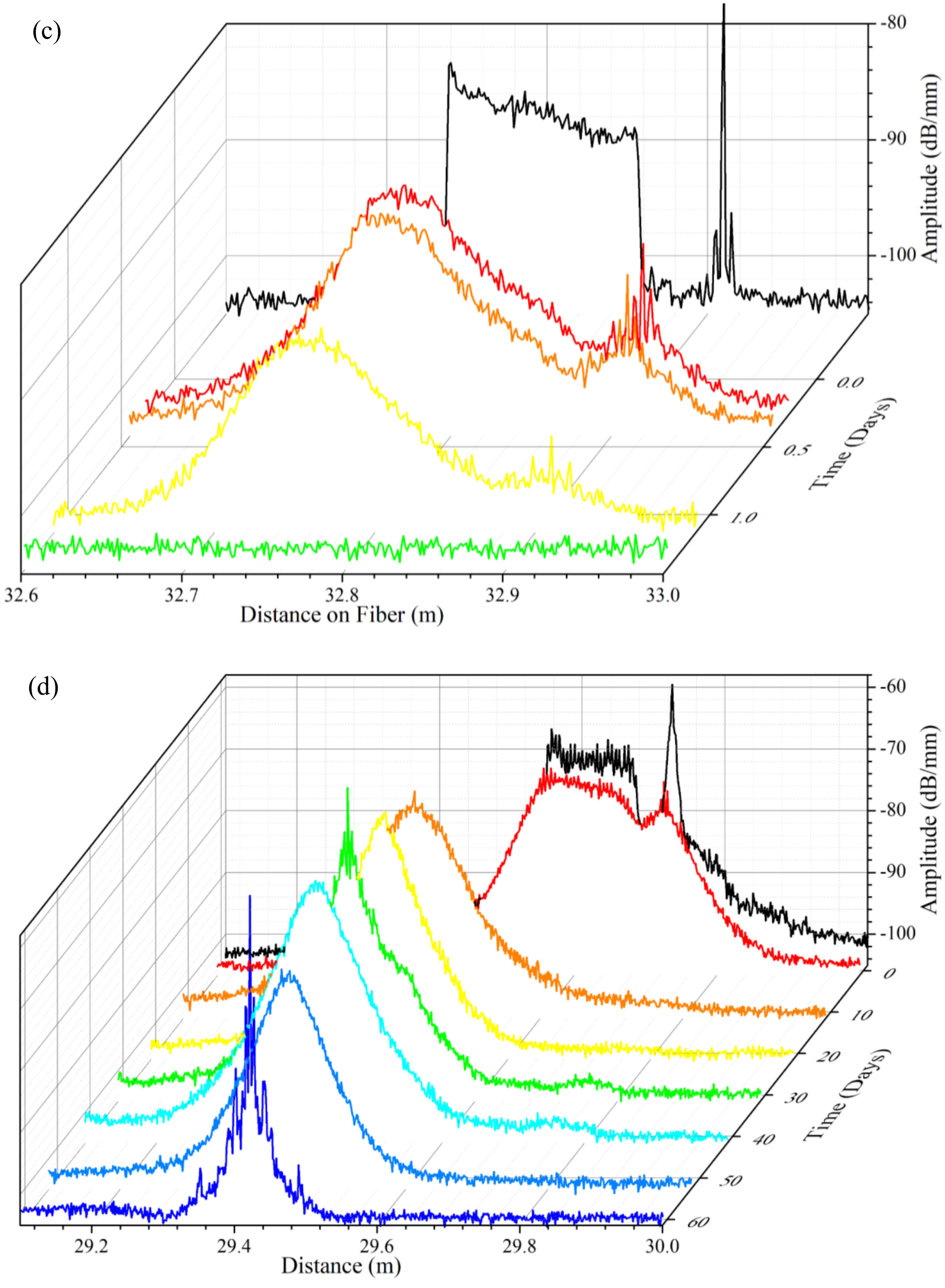

Figure 31 Rayleigh backscattered spatial profiles' devolution with exposure time to ionizing neutron radiation for ultrafast laser-inscribed samples on (a) SMF-28®, Vascade® both (b) continuously and (c) intermittently, and (d) D-fiber.

5.4.2.2 Distributed temperature profiles

The recorded data from the artificial events staged inside the nuclear reactor were processed to evaluate the performance of the samples as distributed temperature sensors inside the nuclear reactor cores. Only the enhanced sections continuously inscribed on Vascade® fibers (c-Vascade) samples were able to produce uniform spectral shift readings denoting the environmental changes inside the reactor core. That is to say, all other surviving samples of SMF-28® and i-Vascade have failed to produce a uniform spectral shift across the Rayleigh enhanced sections, and of course the rest of the fiber without laser-enhancements as well. Figures 32(a-c) show the Rayleigh spectral shifts as measured by a c-Vascade sample during events staged at three different periods of time with respect to references taken at the first day the respective event.

It is important to note that a reference can be maintained as long as the changes in the Rayleigh profile are not drastic due to RII changes. After the first 24 hours of neutron irradiation, the changes to the Rayleigh backscattered signal were drastic the reference had to be retaken. In the event from Day 16 to 18, the Rayleigh profile changes were slow, that is to say RII changes are saturating, which enabled the reference to be used for three days. The event in figure 32(c) at days 26 to 29, RII change rate is again slower allowing the reference to last for consecutive four days.

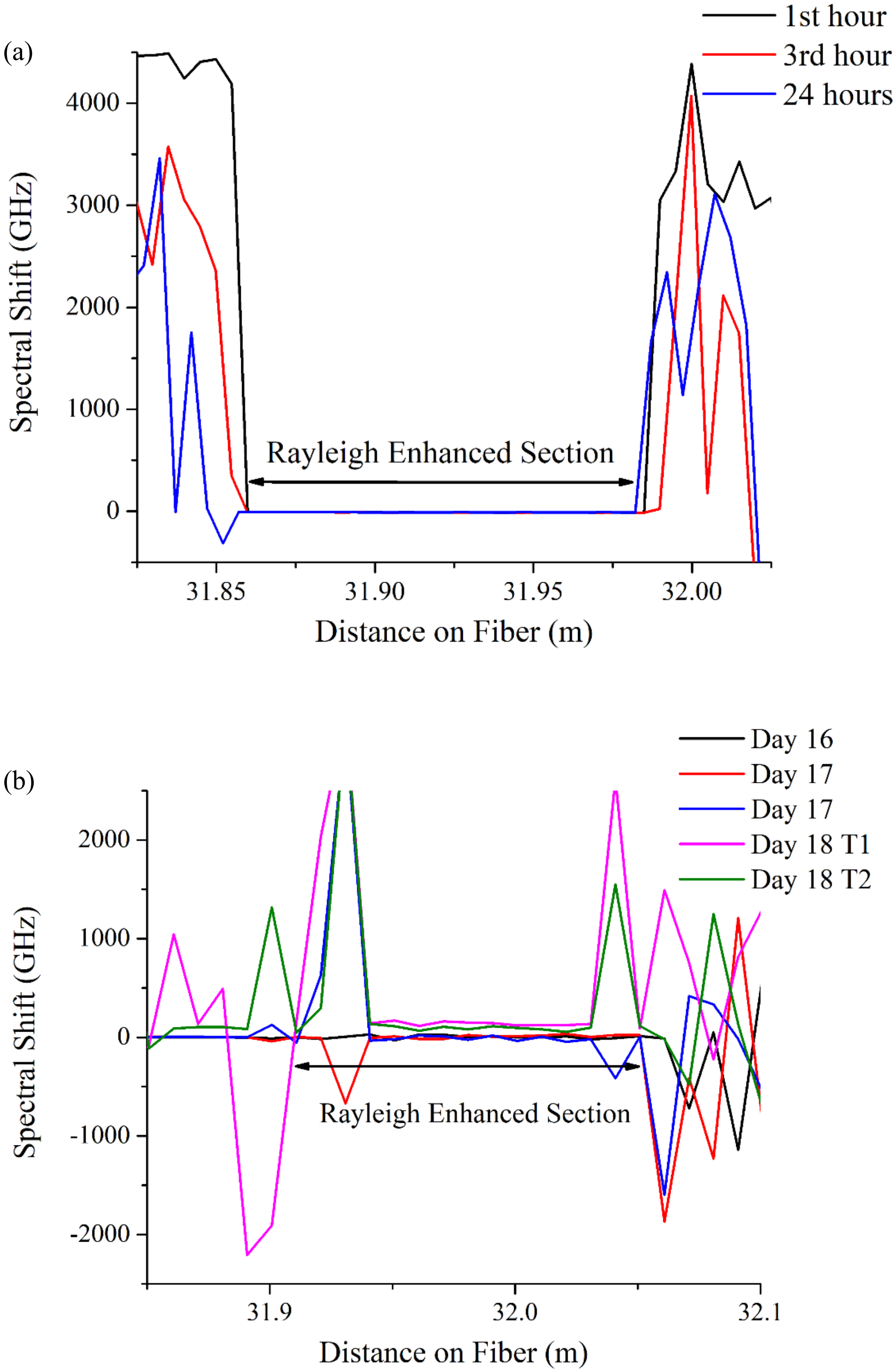
(a)
1st hour
3rd hour
24 hours
Spectral Shift (GHz)
4000
3000
2000
1000
0
Rayleigh Enhanced Section
31.85
31.90
31.95
32.00
Distance on Fiber (m)
(b)
Day 16
Day 17
Day 17
Day 18 T1
Day 18 T2
Spectral Shift (GHz)
2000
1000
0
-1000
-2000
Rayleigh Enhanced Section
31.9
32.0
32.1
Distance on Fiber (m)

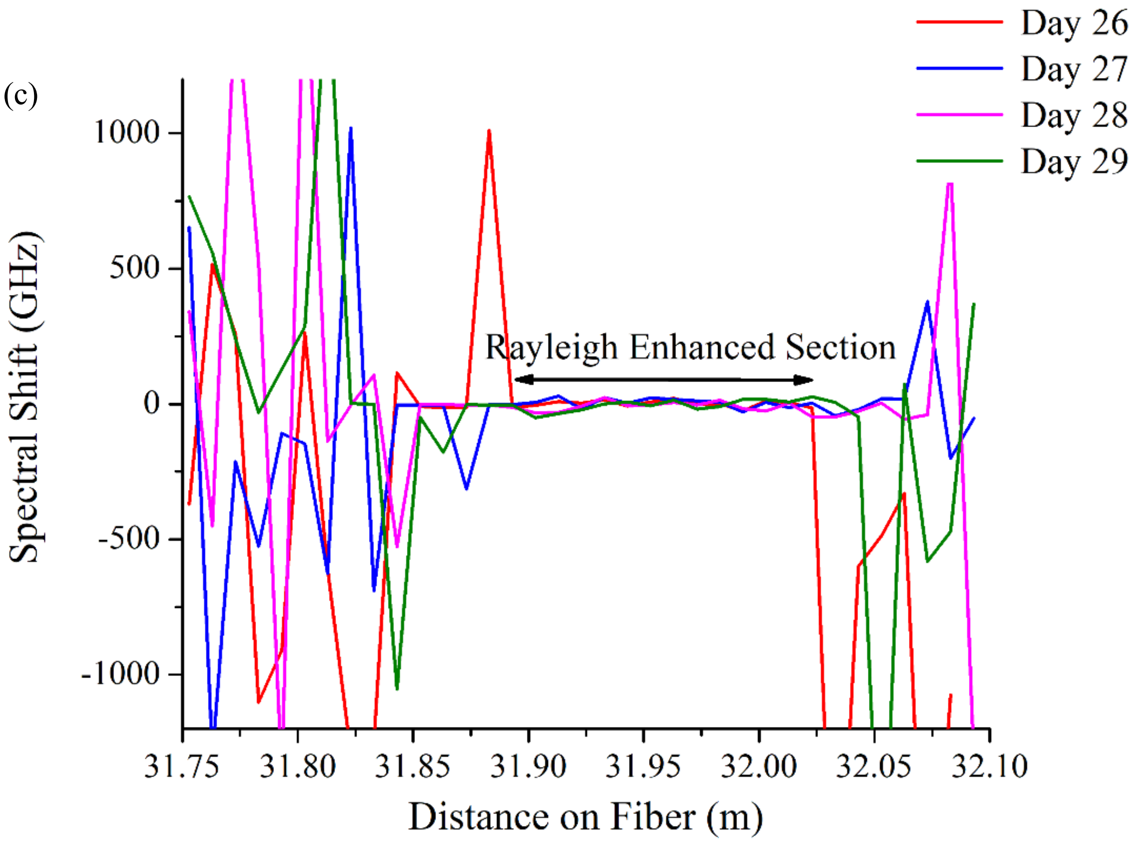

Figure 32 Spectral shifts spatial distributions measured by the distributed c-Vascade fiber sensor for (a) the first 24 hours, (b) day 16 to 18, and (c) day 26 to 29 of neutron irradiation.

5.4.2.3 Temperature cycling and the staged event on the 55th day of neutron irradiation

An in-core temperature cycle was staged on the 55th day of neutron irradiation, that featured stepping down the temperature first by 25°C and keeping the temperature stable for an hour to evaluate the sensor hysteresis then the temperature was lowered by 5°C and kept stable for 40 minutes to assess the sensor's maximal temperature resolution. Then four consecutive stepping down of core temperature by 10°C was performed, and at each time the temperature was kept constant for 20 minutes. This was carried out until the final drop in temperature was a total of

70°C, then the process was reversed to increase the temperature by the steps of 10°C, to reach the initial pre-event temperature after 4 hours and 40 minutes of temperature cycling.

The measured Rayleigh spectral shifts from the heat cycling event on day 55 was projected versus thermocouple measured temperatures to evaluate the Rayleigh thermo-optic coefficient as shown in figures 33(a-b). The data points were fitted linearly and the slopes obtained were the desired coefficients, which are expected to change with exposure time as the Rayleigh profile shifts due to RII. The r-squared figures obtained are quite indicative of the ability of the c-Vascade sample to function as a temperature sensor, at least for the period of the cycle test. The average spatial temperature change measured by the distributed sensor plotted against the temperature determined by the thermocouple closest to capsule center in figure 34 for c-Vascade (a) and i-Vascade (b) samples. The c-Vascade samples were closest in following the thermocouples readings of temperature changes, whereas the i-Vascade was significantly erroneous though it followed the same trend, as shown in figures 34(a) and (b), respectively. Again that may be due to the reference for i-Vascade expires sooner than that of the c-Vascade sample, such that re-referencing was needed during for same day measurements.

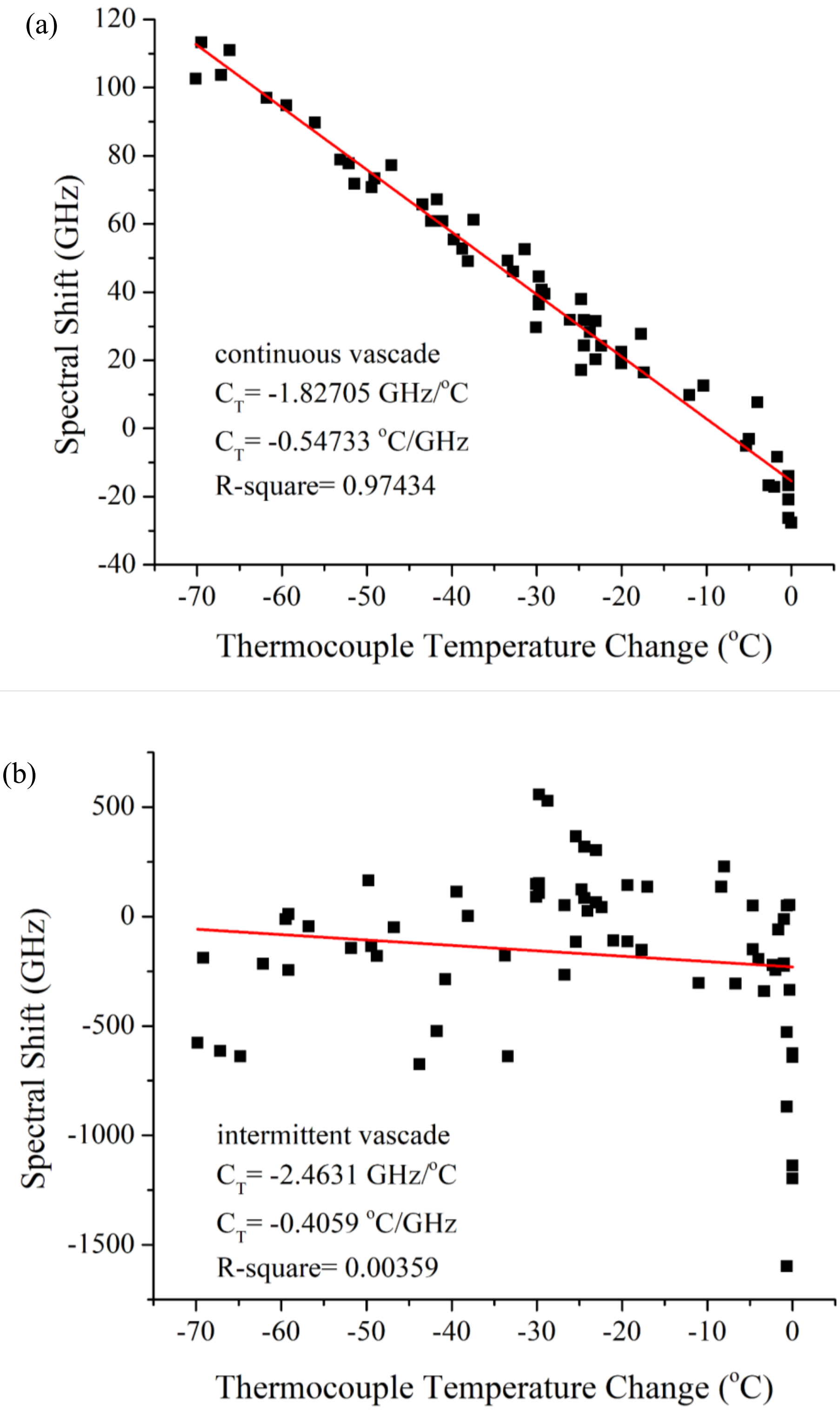

Figure 33 Spectral shifts for heat cycling on day 55 for (a) c-Vascade and (b) i-Vascade samples. Linear fitting is used to assess the Rayleigh thermo-optic coefficients of the samples.

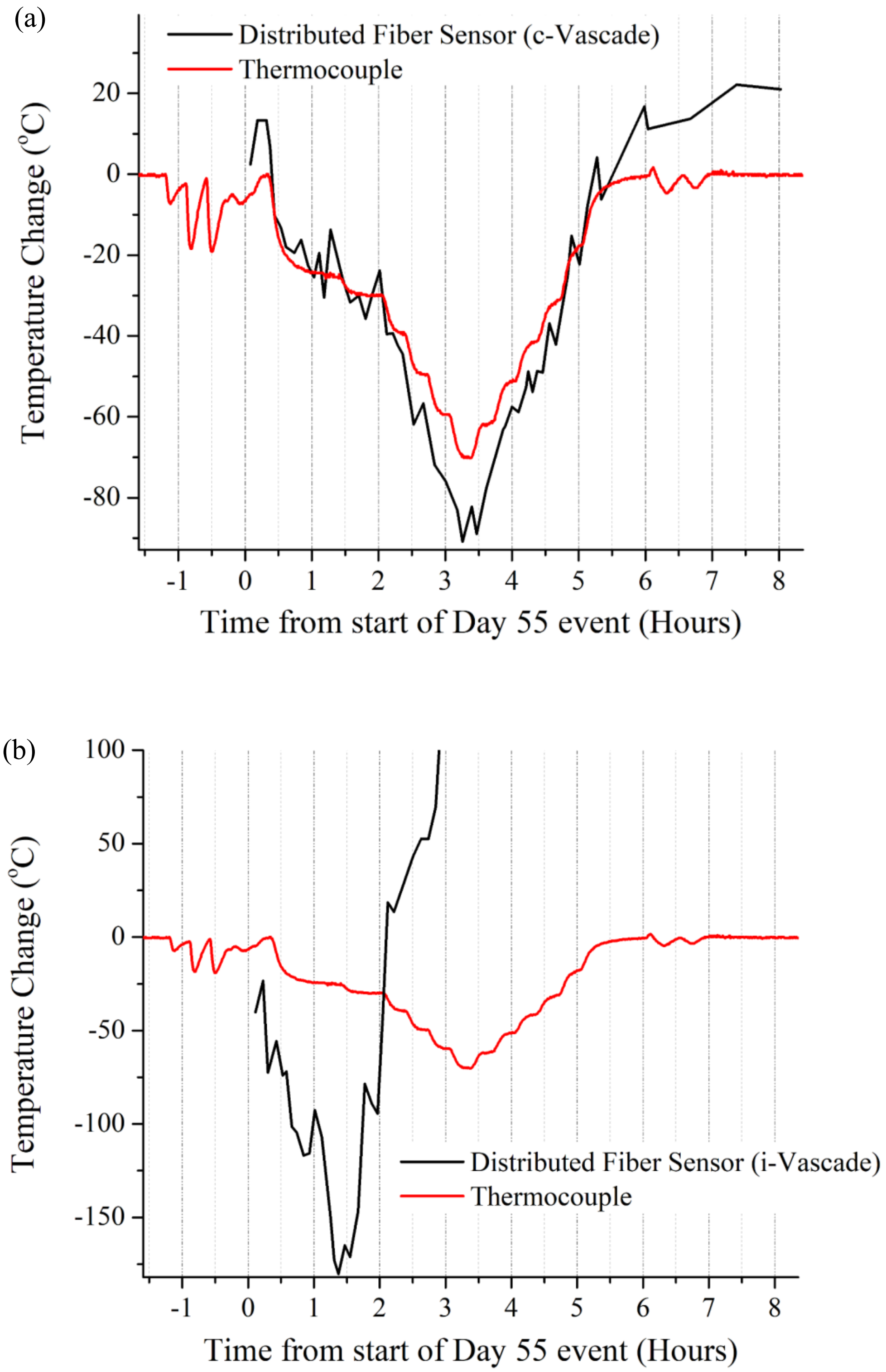

Figure 34 Heat cycle on day 55 as measured by the thermocouples and the distributed Rayleigh enhanced sensors on Vascade® fibers (a) continuously (c-Vascade), and (b) intermittently (i-Vascade).

5.4.2.4 Spectral shift quality of the Rayleigh distributions

The Rayleigh profiles' spectral shift quality (SSQ) was used to gauge the correlation between the measurements obtained at different temperatures during the heat-cycling event on day 55 and the reference taken at the start of the heat cycle. The SSQ is determined as:

$$\mathrm{SSQ} = \max\left(\text{cross correlation}\left(U_j(\nu), U_j(\nu-\Delta\nu_j)\right)\right) / \Sigma\, U_j(\nu)^2 \quad (5\text{-}1)$$

where $U_j(\nu)$ is the backscattered spectrum, at the fiber segment j and the optical frequency ν. $U_j(\nu-\Delta\nu_j)$ is the spectrum that experiences a shift in optical frequency $\Delta\nu_j$ generally due to change(s) in the fiber's temperature and/or strain. The summation in the denominator $\Sigma U_j(\nu)^2$ serves as a normalization, as the maximum expected value is the autocorrelation of the reference spectra. If the expected SSQ values are between 0 and 1, only when the values are above the threshold of 0.15 then the temperature and/or strain changes are in the measurable range [91].

The SSQ is shown at different times on day 55 for the c-Vascade and i-Vascade samples in figures 35(a) and (b), respectively. The results show that the c-Vascade samples have more consistent SSQ characteristics than the highly noisy profiles exhibited by the i-Vascade samples. The figures also emphasize the effect of Rayleigh enhancement in improving the SSQ, as only the Rayleigh enhanced sections of the fiber samples are above the 0.15 threshold.

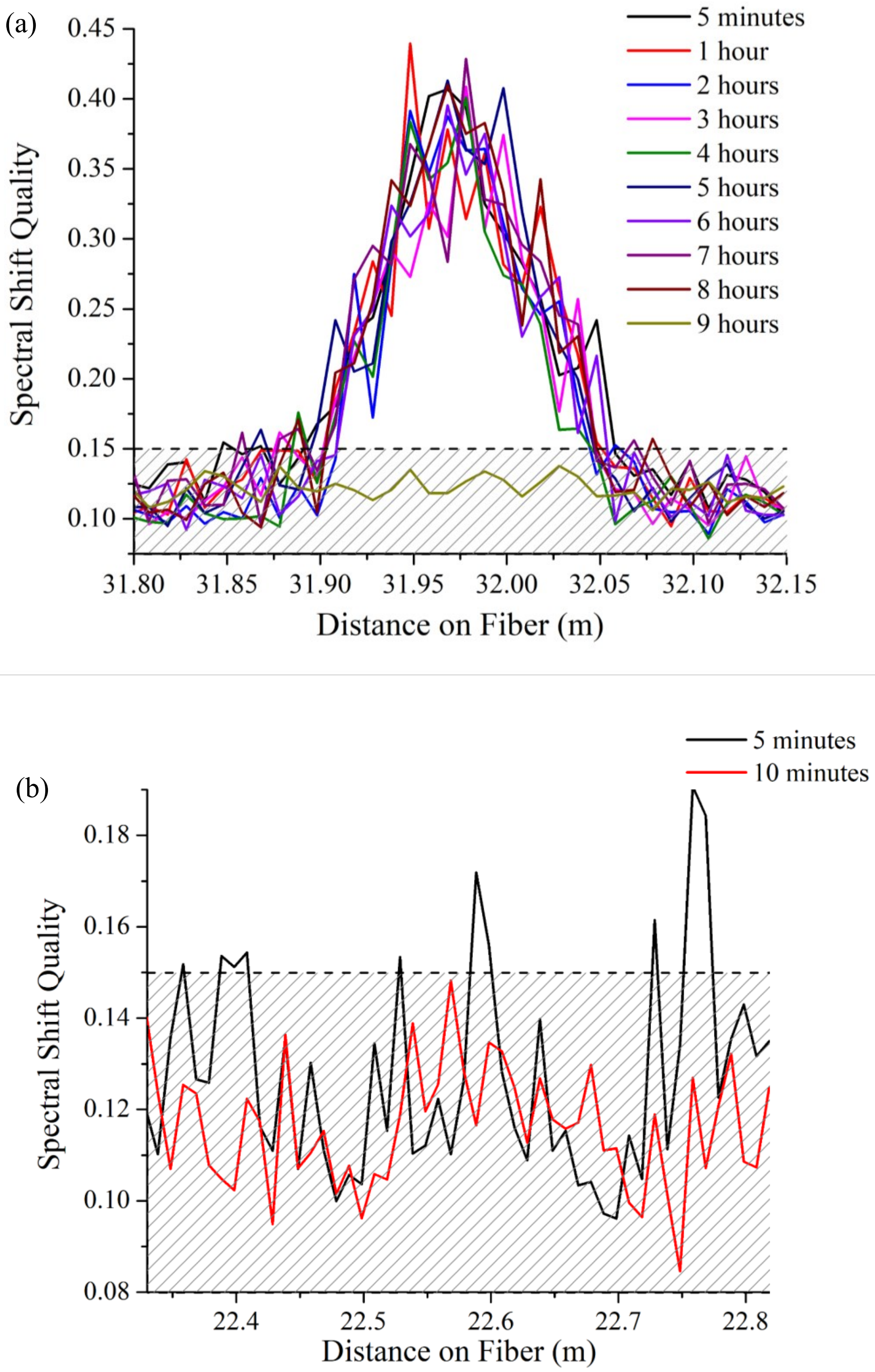

Figure 35 Rayleigh spectral shift quality calculated for the heat cycling event on the 55th day of irradiation, for the distributed Rayleigh enhanced sensors on Vascade® fibers (a) continuously (c-Vascade), and (b) intermittently (i-Vascade).

5.5 Ultrafast Laser-Enhanced Distributed Sensors for Solid-Oxide Fuel Cells

Solid-oxide fuel cells (SOFCs) are becoming more widely used in power-generation applications, but ultimately have yet to attain widespread industrial acceptance. The implementation of cleaner direct-energy conversion systems based on SOFC technology will ultimately only take place if the issues of cell degradation and system longevity are addressed. SOFC research in the past decade or more has focused largely on increasing operating efficiencies and prolonging the useful life of fuel cells and their constituent materials. Although there are not many large-scale SOFC systems in use today, some researchers predict that SOFCs will serve as core components in hybrid energy generation systems that make use of a fuel cell in combination with a gas turbine or other complimentary system for maximum efficiency [92]. Fortunately, we can observe a continuous trend in SOFC operating specifications towards higher efficiency and longer life, largely as a result of improvements in the materials and design of SOFCs.

Solid oxide fuel cells are notably the most efficient form of fuel-cell technology, because ceramic electrolyte materials offer significantly more ionic conduction than their liquid counterparts. To realize ionic conduction in common ceramic electrolytes like yttria-stabilized zirconia (YSZ), the electrolyte materials must be maintained at high temperatures – usually above 700°C and ranging as high as roughly 1000°C. Because SOFC systems operate in this high-temperature regime, their internal components are naturally subject to accelerated rates of degradation. Economic feasibility studies have shown that widespread adoption of SOFC technology could take place if the mean time to failure (MTTF) for cells is increased. There is still a significant requirement for improvements necessary for widespread industrial acceptance of these novel devices.

Numerous previous researchers have simulated and measured SOFC operating conditions, but the literature is still lacking detailed reports of SOFC internal operating temperatures and temperature features. This is because making measurements inside operating SOFC systems can be extremely challenging. In SOFCs, standard thermocouple measurements can be difficult. This is because thermocouples rely on a very small electrical voltage differential to derive local temperatures. In SOFC systems, large ambient electrical currents and much higher system voltages can skew thermocouple signals and produce erroneous readings. Long thermocouple wires are required to reach the high-value areas deep inside an SOFC stack, which additionally may introduce stray electro-magnetic interference and measurement errors. Access is generally also an issue, with each electrical feedthrough providing a potential failure point. This is why commercial SOFC systems generally provide a minimum amount of temperature sensors for production products. In the research arena, it is still difficult to instrument SOFC stacks given the harsh environment and mechanical wiring considerations. Therefore, the installation of even a few thermocouples for point measurements is considered novel and extensive [93].

In this section, a novel method for SOFC internal temperature measurement, which circumvents the traditional difficulties associated with electrical thermocouple type measurements, is presented. By using multiple fibers with ultrafast laser enhanced sections that function as thermally stable distributed sensors, the previously inaccessible temperature distributions in a harsh SOFC environment can be mapped. The proposed method provides more extensive distributed temperature information. This system can permit accurate internal SOFC temperature measurements, which will aid system designers and operators in increasing both the longevity and operating efficiency of an SOFC stack.

5.5.1 Fiber selection for distributed SOFC measurements

The Coherent® RegA 9000 Ti:sapphire laser and amplifier system (described in section 5.2) was used to fabricate 10 distributed optical fiber sensors. The fiber used were standard ITU-T G.652.D (Corning® SMF-28®) telecommunication optical fibers. The ultrafast laser was set to produce 800 nm, 270 fs laser pulses at 250 kHz repetition rate. The nanostructures were inscribed in the fiber core with the ultrafast laser set to 100 nJ pulse energy through a 100× oil immersion objective (NA 1.25) at a 2 um radius beam spot, and a writing speed of 1 mm/s over a length of 12 cm of each bare-fiber. The formation of nanogratings enhances the Rayleigh backscattering profile as explained before. The distributed fiber sensors are to be interrogated using the commercial OBR and based on OFDR technique, explained in section 2.1.1.

5.5.2 SOFC current-collector plate fabrication

SOFCs operating at high temperatures present extremely challenging measurement environments, even for robust silica optical fibers. Yan et al. previously reported extensively on the degradation characteristics of fused-silica optical fibers in similar harsh-environments [88]. One major concern was hydrogen darkening, where silica fibers absorb hydrogen, or more accurately suffer increases in their hydroxide base (-OH) content. When a fiber absorbs hydrogen, the signal-to-noise ratio (SNR) deteriorates and the interrogation technique becomes unreliable and fails completely. Both hydrogen and water produce similar loss effects, and both are abundant in a SOFC environment. Fortunately, the SOFC electrode design proposed here, can improve the backscattering stability for silica fibers used, as they are situated in channels separately from SOFC reaction sites.

The current-collector plates were 3D printed in an additive manufacturing (AM) process using EOS® 3D metal printer. The design schematics for the fabricated anode and cathode are shown in figures 36(a) and (b), respectively. The material of choice for SOFC electrode fabrication was Inconel-718, a Ni alloy that is widely known for its resistance to corrosion and oxidation. The plates were coated with a protective oxide coating, and heat-treated to prevent undesired reactions of interconnector material at oxidizing conditions, and prevent Cr evaporation. Figures 36(c) and (d) show photographs of the 3D printed Inconel electrode before and after ceramic coating, respectively. By 3D printing the current collector plates in Inconel-718, is was possible to include an array of micro-channels through which fibers could be inserted into to monitor the temperature changes of the SOFC electrodes, while keeping them away from the devastating effects of H_2, at high temperatures.

These channels were roughly 750 µm in diameter (508 µm after conductive ceramic coating), and 9.82 cm long. They spanned the entire length of the SOFC assembly, and were located approximately 0.8636 ± 0.0508 mm below the fuel (air) channels on the anode (cathode) side of the cell. This configuration permitted the installation of up to 10 optical fibers parallel to the fuel or airflow paths, with a minimum solid separation between the fiber and the hot gas path.

(a)

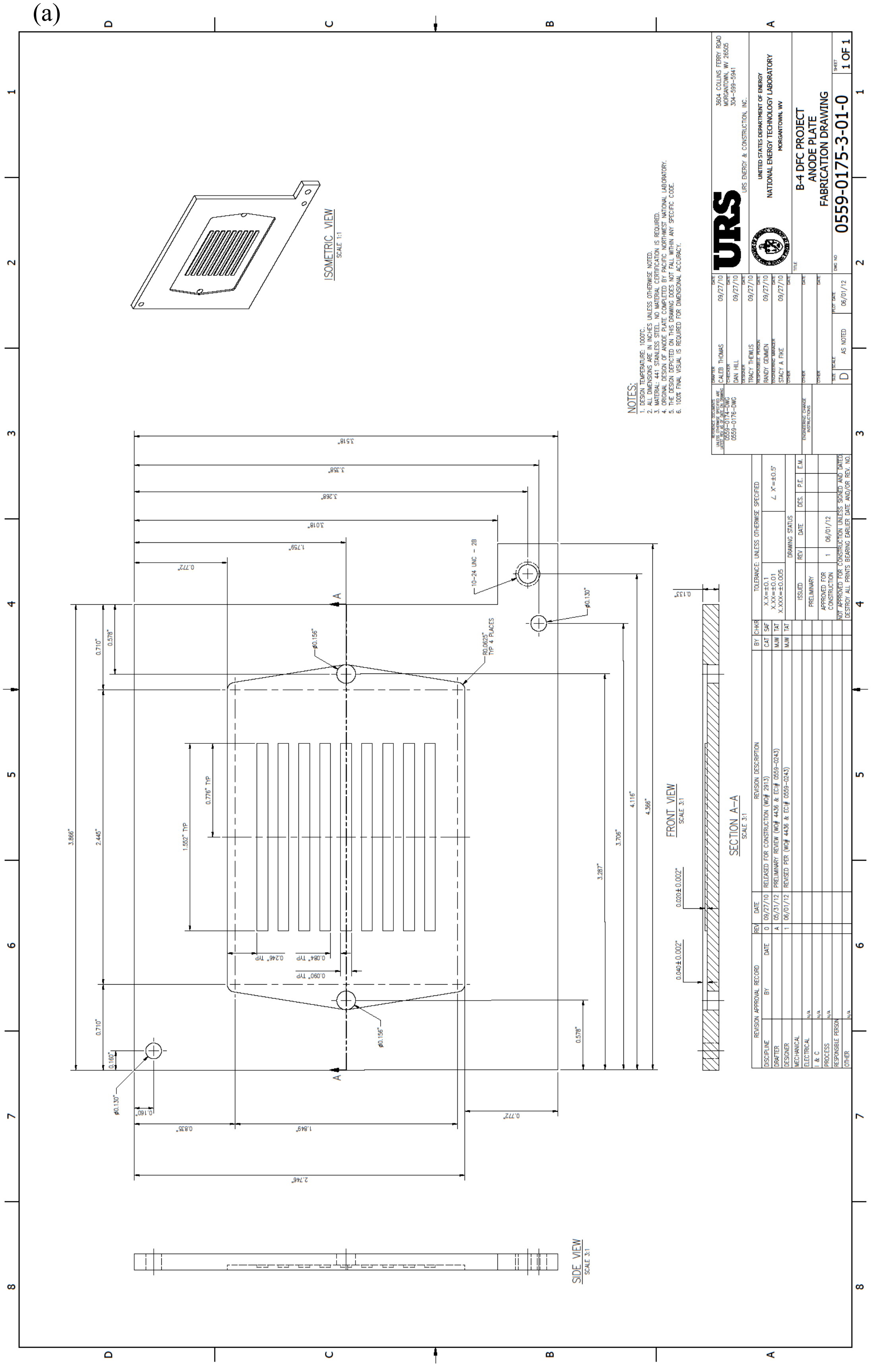
ISOMETRIC VIEW SCALE 1:1
FRONT VIEW SCALE 3:1
SECTION A-A SCALE 3:1
SIDE VIEW SCALE 3:1
NOTES:
1. DESIGN TEMPERATURE: 1000°C.
2. ALL DIMENSIONS ARE IN INCHES UNLESS OTHERWISE NOTED.
3. MATERIAL: 441 STAINLESS STEEL. NO MATERIAL CERTIFICATION IS REQUIRED.
4. ORIGINAL DESIGN OF ANODE PLATE COMPLETED BY PACIFIC NORTHWEST NATIONAL LABORATORY.
5. THE DESIGN DEPICTED ON THIS DRAWING DOES NOT FALL WITHIN ANY SPECIFIC CODE.
6. 100% FINAL VISUAL IS REQUIRED FOR DIMENSIONAL ACCURACY.
10-24 UNC - 2B
R0.0625" TYP 4 PLACES
ϕ0.156"
ϕ0.130"
0.020±0.002"
0.040±0.002"
URS ENERGY & CONSTRUCTION, INC.
3604 COLLINS FERRY ROAD MORGANTOWN, WV 26505 304-599-5941
UNITED STATES DEPARTMENT OF ENERGY
NATIONAL ENERGY TECHNOLOGY LABORATORY
MORGANTOWN, WV
B-4 DFC PROJECT
ANODE PLATE
FABRICATION DRAWING
0559-0175-3-01-0
SHEET 1 OF 1
SIZE D
SCALE AS NOTED
PLOT DATE 06/01/12
DRAFTER CALEB THOMAS 09/27/10
CHECKER DAN HILL 09/27/10
DESIGNER TRACY THEWLIS 09/27/10
RESPONSIBLE PERSON RANDY GEMMEN 09/27/10
ENGINEERING MANAGER STACY A FIKE 09/27/10
REFERENCE DOCUMENTS 0559-0174-DWG 0559-0176-DWG
TOLERANCE UNLESS OTHERWISE SPECIFIED X.X=±0.1 X.XX=±0.01 X.XXX=±0.005 ∠ X°=±0.5°
0 09/27/10 RELEASED FOR CONSTRUCTION (WO# 2913)
A 05/31/12 PRELIMINARY REVIEW (WO# 4436 & EC# 0559-0243)
1 06/01/12 REVISED PER (WO# 4436 & EC# 0559-0243)
NOT APPROVED FOR CONSTRUCTION UNLESS SIGNED AND DATED. DESTROY ALL PRINTS BEARING EARLIER DATE AND/OR REV. NO.

(b)

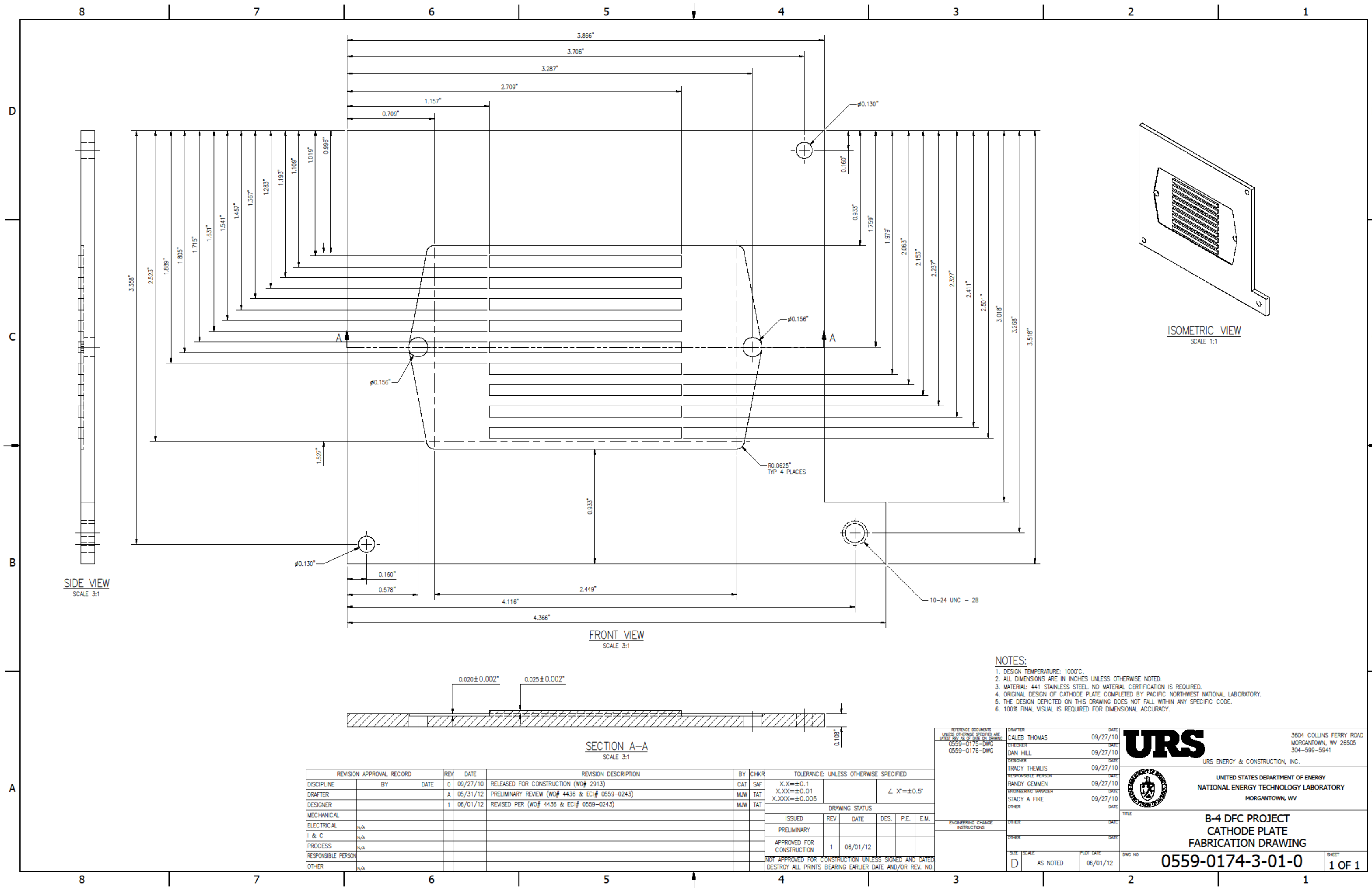

NOTES:
1. DESIGN TEMPERATURE: 1000°C.
2. ALL DIMENSIONS ARE IN INCHES UNLESS OTHERWISE NOTED.
3. MATERIAL: 441 STAINLESS STEEL. NO MATERIAL CERTIFICATION IS REQUIRED.
4. ORIGINAL DESIGN OF CATHODE PLATE COMPLETED BY PACIFIC NORTHWEST NATIONAL LABORATORY.
5. THE DESIGN DEPICTED ON THIS DRAWING DOES NOT FALL WITHIN ANY SPECIFIC CODE.
6. 100% FINAL VISUAL IS REQUIRED FOR DIMENSIONAL ACCURACY.

REVISION APPROVAL RECORD	BY	DATE
DISCIPLINE	BY	DATE
DRAFTER		
DESIGNER		
MECHANICAL		
ELECTRICAL	N/A	
I & C	N/A	
PROCESS	N/A	
RESPONSIBLE PERSON		
OTHER	N/A	

REV	DATE	REVISION DESCRIPTION	BY	CHKR
0	09/27/10	RELEASED FOR CONSTRUCTION (WO# 2913)	CAT	SAF
A	05/31/12	PRELIMINARY REVIEW (WO# 4436 & ECI# 0559-0243)	MJW	TAT
1	06/01/12	REVISED PER (WO# 4436 & ECI# 0559-0243)	MJW	TAT

TOLERANCE: UNLESS OTHERWISE SPECIFIED
X.X=±0.1
X.XX=±0.01
X.XXX=±0.005
∠ X°=±0.5°

DRAWING STATUS

ISSUED	REV	DATE	DES.	P.E.	E.M.
PRELIMINARY					
APPROVED FOR CONSTRUCTION	1	06/01/12			

NOT APPROVED FOR CONSTRUCTION UNLESS SIGNED AND DATED. DESTROY ALL PRINTS BEARING EARLIER DATE AND/OR REV. NO.

REFERENCE DOCUMENTS UNLESS OTHERWISE SPECIFIED ARE LATEST REV AS OF DATE ON DRAWING
0559-0175-DWG
0559-0176-DWG

ENGINEERING CHANGE INSTRUCTIONS

		DATE
DRAFTER	CALEB THOMAS	09/27/10
CHECKER	DAN HILL	09/27/10
DESIGNER	TRACY THEWLIS	09/27/10
RESPONSIBLE PERSON	RANDY GEMMEN	09/27/10
ENGINEERING MANAGER	STACY A FIKE	09/27/10
OTHER		
OTHER		
OTHER		

URS
3604 COLLINS FERRY ROAD
MORGANTOWN, WV 26505
304-599-5941
URS ENERGY & CONSTRUCTION, INC.

UNITED STATES DEPARTMENT OF ENERGY
NATIONAL ENERGY TECHNOLOGY LABORATORY
MORGANTOWN, WV

TITLE
B-4 DFC PROJECT
CATHODE PLATE
FABRICATION DRAWING

SIZE D
SCALE AS NOTED
PLOT DATE 06/01/12
DWG NO 0559-0174-3-01-0
SHEET 1 OF 1

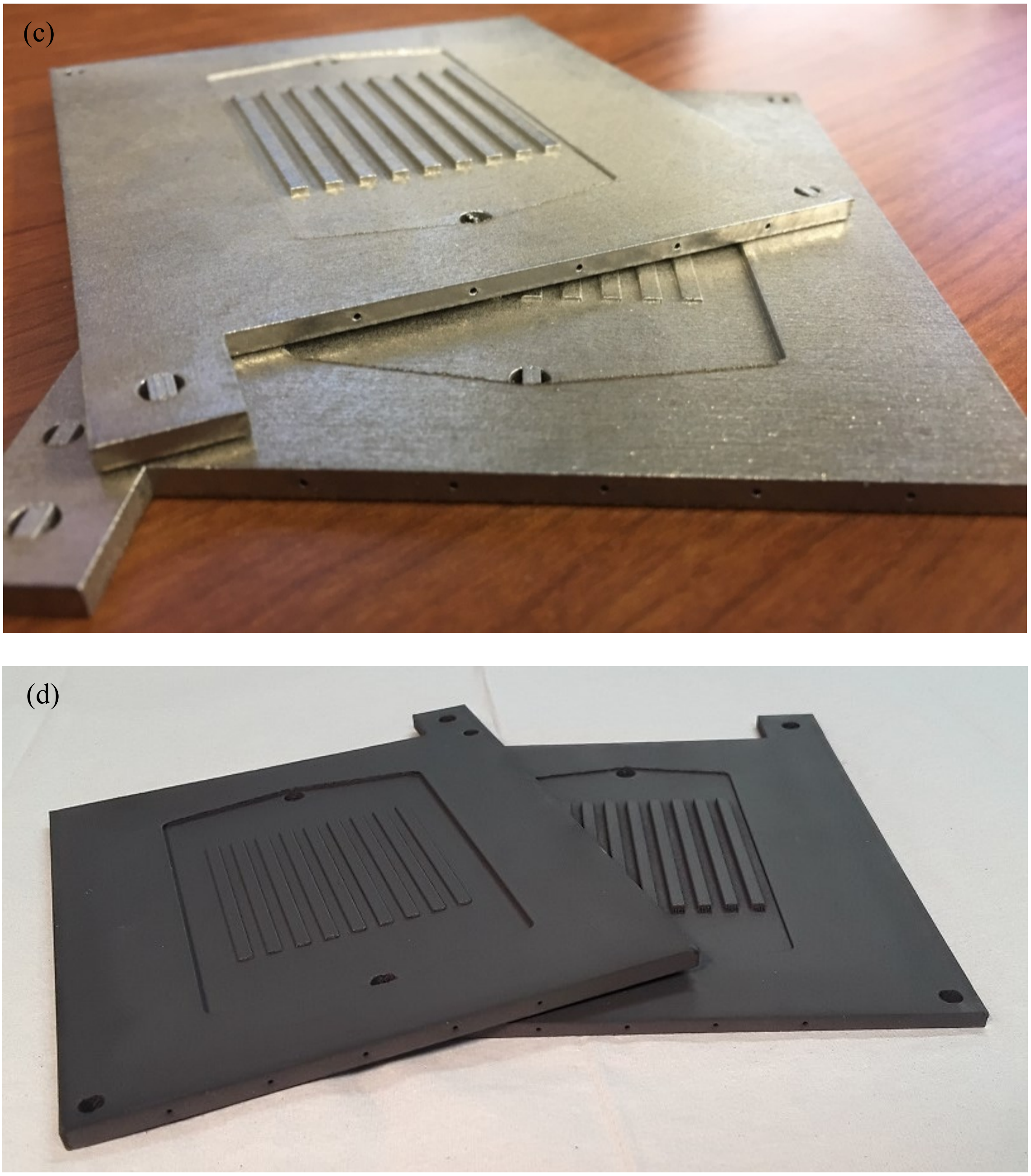

Figure 36 Design schematics with top, side and isometric views of the additively manufacture current-collector (a) anode, and (b) cathode plates. (c) A photograph of the 3D printed current-collector plates. Microstructured channels were carefully implemented during the AM process of electrode fabrication to allow for placement of the distributed fiber sensors apart from the paths of the hot reacting gases. (d) A photograph of the current-collector plates after uniform plating with ceramic, to prevent Cr leakage and prolonging the life-time of the current-collectors.

5.5.3 Distributed sensor deployment in SOFC system

To conduct the previously impossible internally distributed SOFC temperature measurements, a planar SOFC was designed and fabricated at the U.S. Department of Energy's National Energy Technology Laboratory fuel cell-testing facility in Morgantown, WV. The cell exhibits a YSZ electrolyte, a square (cross-section 5cm × 5cm) array of counter-flowing fuel and air channels, and 3D printed Inconel current-collector plates (figure 37(a)). After initial sealing and reduction of the SOFC, the system was cooled and all 10 fibers were threaded through fiber-channels in the current-collector plates. Five fiber sensors were inserted into the anode channels, and five were inserted into the cathode side, such that the 12 cm enhanced sections will contain the 9.82 cm long electrodes with a rough clearance of 1 cm left on both entrance and exit sides of the plates (figure 37(b)).

The SOFC system was next heated and connected to a digital load bank for measurement. Because this system utilizes a single cell rather than a large stack, it must be electrically heated for operation. Initially, the cell was heated up to 800°C under open-circuit conditions, and then Rayleigh reference spectrum was taken for the samples at the anode and cathode sides. This meant that all temperature measurements were referenced to the ambient high temperature, and that all subsequent measurements produced would indicate changes above or below the 800°C baseline. Although it is possible in some cases to measure absolute temperatures of this magnitude, it is observed to be much more reliable to record the reference at a stable high temperature, rather than at room temperature. Once the reference was complete, the cell was operated under various current loads, fuel conditions, and ambient temperatures. When varying fuel flow conditions, the fuel was first changed and the reference was re-taken to remove any gas-induced thermal transport effects, and permitting extraction of the current-induced temperature rise only.

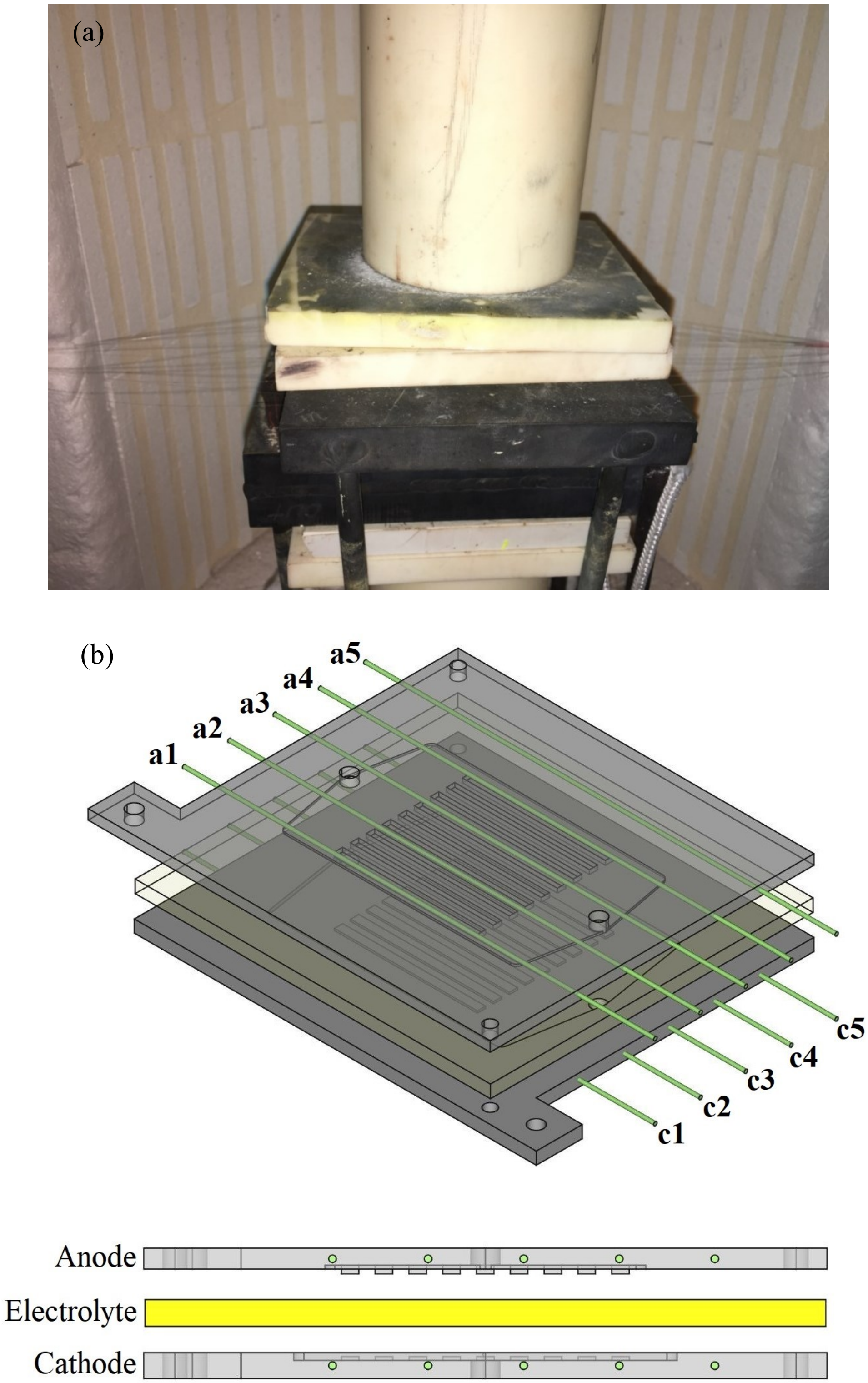

Figure 37 (a) A photograph of the SOFC assembly with inside the furnace, with 10 fiber sensors inserted into the electrodes. (b) Isometric and side views of the SOFC current-collectors and electrolyte stacked, with illustrations of labelled fiber sensors inserted into their respective microstructured channels.

First set of temperature measurements were taken at 800°C (furnace temperature), 250 sccm flow rate of 100% H_2, 100 sccm of air flow, and current of 2 A, where each fiber was separately interrogated. Then the current was varied from 0 to 2 A with steps of 0.5 A for the center anode sensor (a3) that exhibited the most pronounced temperature changes. After every measurement a reference was retaken at 0 A, to eliminate furnace temperature fluctuation effects. Figures 38(a-c) show the temperature distribution at different conditions measured by the fiber sensor in the middle channel of the anode (a3).

The figures 38(a-c) reveal that there is a systematic rise in temperature of 4°C through a formation of a "hump" in the temperature profile that was even clearer on the anode sensors than the cathode and on the sensors towards the center rather than the periphery of the active region. It was also evident that the hump width increases until steady state is reached at almost 60 seconds from driving the current from the fuel cell. This immediate observation was expected from prior knowledge that H_2 gas has a relatively higher conductivity than air, also because the reaction hot spot occurs very close to the fuel gas inlet at the anode side. The H_2 flow was lowered to 100 sccm and temperature measurements were retaken for all sensors while keeping the rest of the conditions constant.

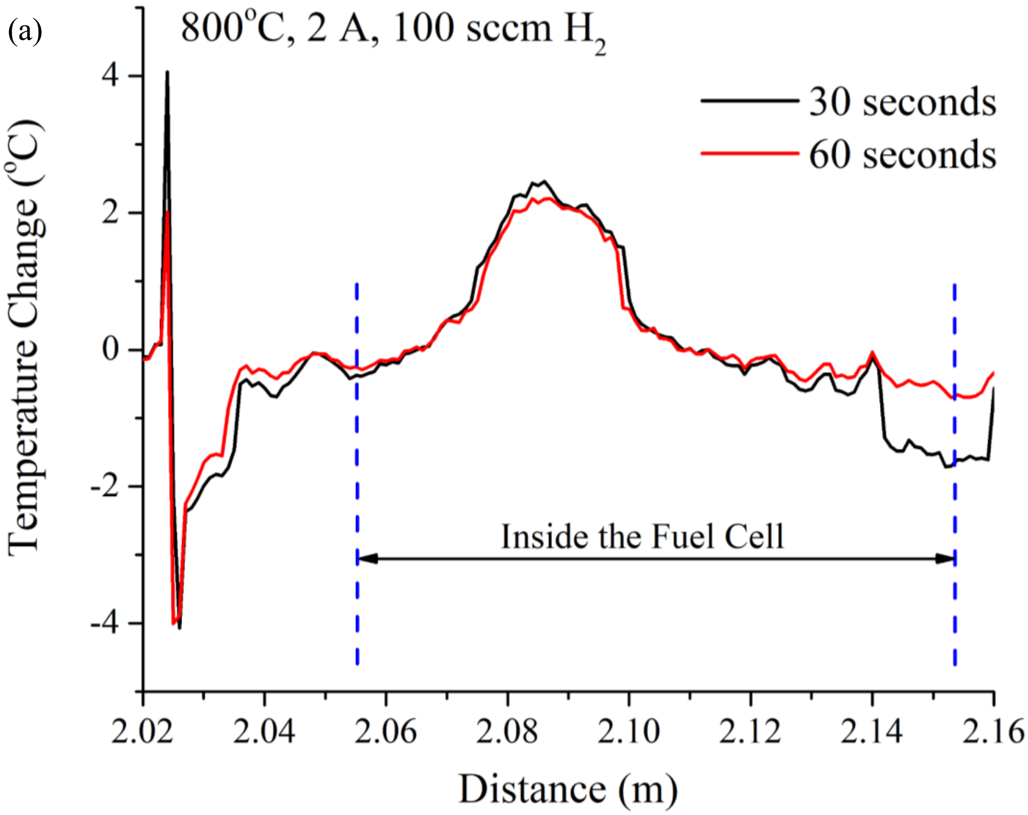
(a)
800°C, 2 A, 100 sccm H_2
30 seconds
60 seconds
Inside the Fuel Cell
Temperature Change (°C)
Distance (m)
4
2
0
-2
-4
2.02
2.04
2.06
2.08
2.10
2.12
2.14
2.16

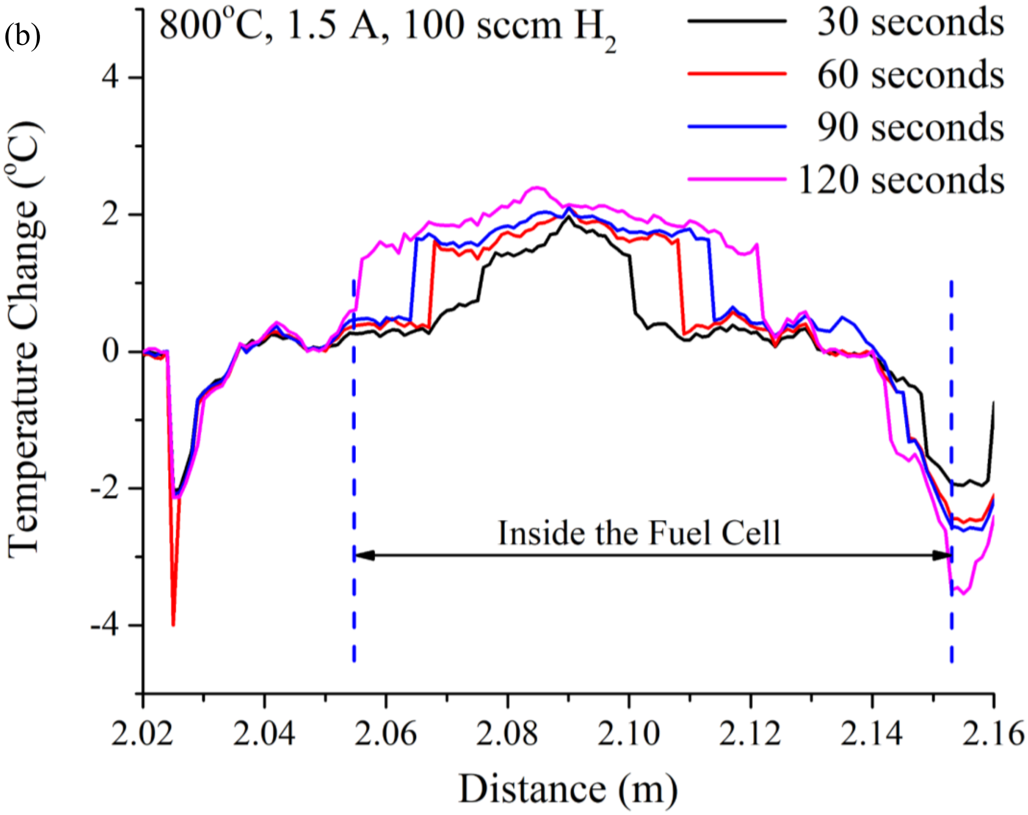
(b)
800°C, 1.5 A, 100 sccm H_2
30 seconds
60 seconds
90 seconds
120 seconds
Inside the Fuel Cell
Temperature Change (°C)
Distance (m)
4
2
0
-2
-4
2.02
2.04
2.06
2.08
2.10
2.12
2.14
2.16

(c)

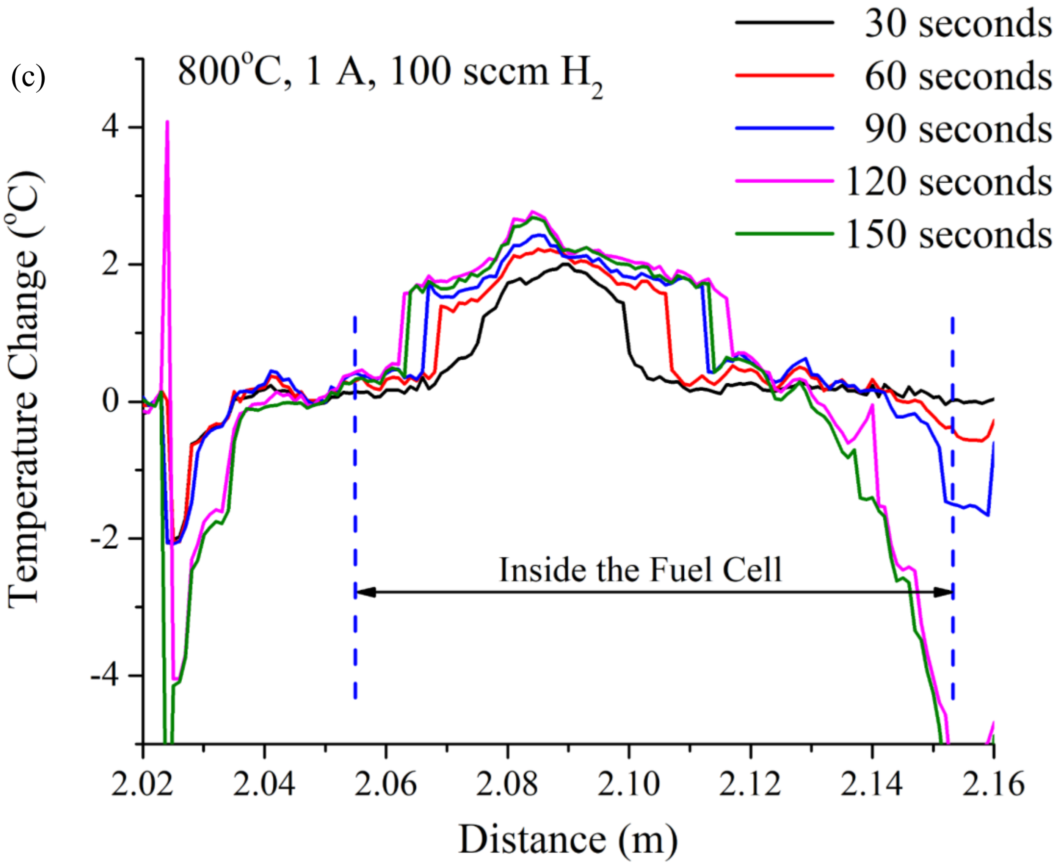

Figure 38 Temperature distribution obtained by the distributed optical fiber sensor at the middle of the anode (a3) plotted every 30 seconds at 800°C, 100% H_2 concentration inside the cell environment, and a current value of (a) 2 A, (b) 1.5 A, and (c) 1 A.

During the cell operation, some small amount of drift in the furnace temperature, or ambient temperature with respect to the cell, results in external heating or cooling of the cell. This is observable as a systematic rise or fall in the temperature of the ends of each sensor section as the cell heats or cools from the outside – in. This occurrence is evident in figures 38(a-c), shown as temperature fluctuations on the right side of the region labelled “inside the fuel cell” apparently caused from outside the fuel cell and not related to the fuel cell reaction. On the other hand, internal temperature changes induced by the cell current are easily distinguishable as they occur inside the cell section, and are not necessarily symmetric.

The temperature distributions for all 10 sensors obtained at 800°C and at 2 A of current collected are plotted in figures 39(a-b). The temperature profiles obtained from each sensor make sense, but since each plot is based on a different reference, not all plots can make sense when plotted together. It became obvious that order to obtain the 3D temperature distribution for each electrode, using all five sensors at each side, at certain cell operation conditions, the sensors must be interrogated simultaneously to reduce problems from re-referencing each sensor on its own. In addition, to eliminate the furnace temperature fluctuation effects that will make it difficult to obtain the 3D temperature profile interrogating each sensor separately.

To overcome this hurdle, the anode sensors were fusion-spliced into a single fiber string, as were the five cathode fiber samples, to allow for simultaneous interrogation for more accurate reconstruction of a two-dimensional temperature profile of each electrode at the set fuel cell conditions. Figure 40 shows the backscattered Rayleigh spectra for the anode and cathode sensor strings. The problem with cascading several Rayleigh enhanced sections is that each enhanced section would contribute to the optical signal loss such that the SNR is worsened on every addition of a laser-enhanced section. Therein, we note that the optical signal attenuation, introduced by each sensor here, is low enough to permit at least five sensors to be cascaded on the same fiber. The SNR of the fifth sensor downstream in the cascade had experienced ~25 dB deterioration in signal power. As long as a reasonable optical power is maintained for all downstream sensors, additional sensors can be cascaded. In other words, more sensors on the same fiber may require increased light-source power or a reduction in the artificial backscattering intensity using a faster laser writing speed.

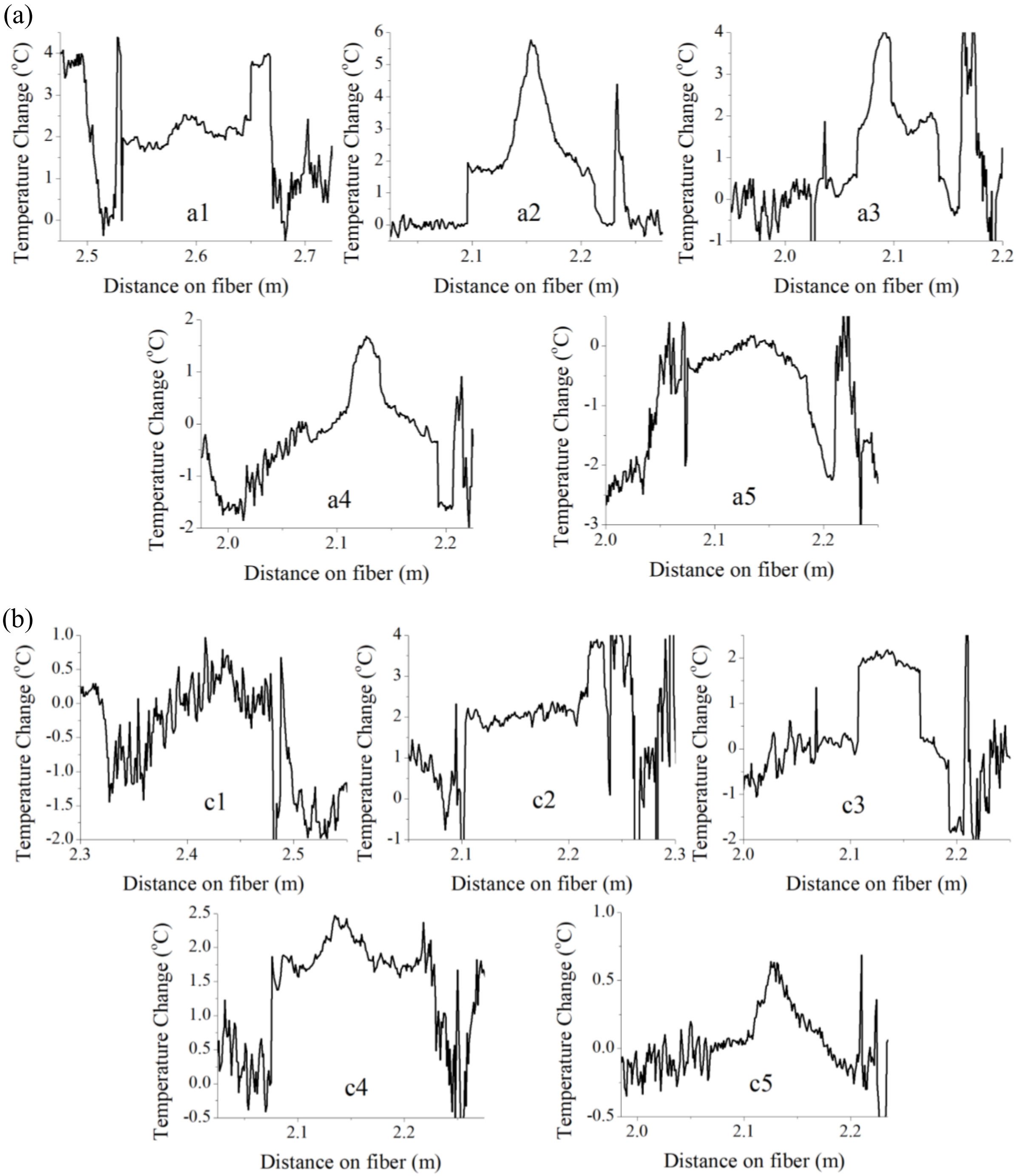

Figure 39 The temperature distributions obtained separately from each fiber sensor at the (a) anode side (a1 to a5), and at the (b) cathode side (c1 to c5). For these plots, the furnace temperature was set to 800°C, and the current drawn from the cell was 2A.

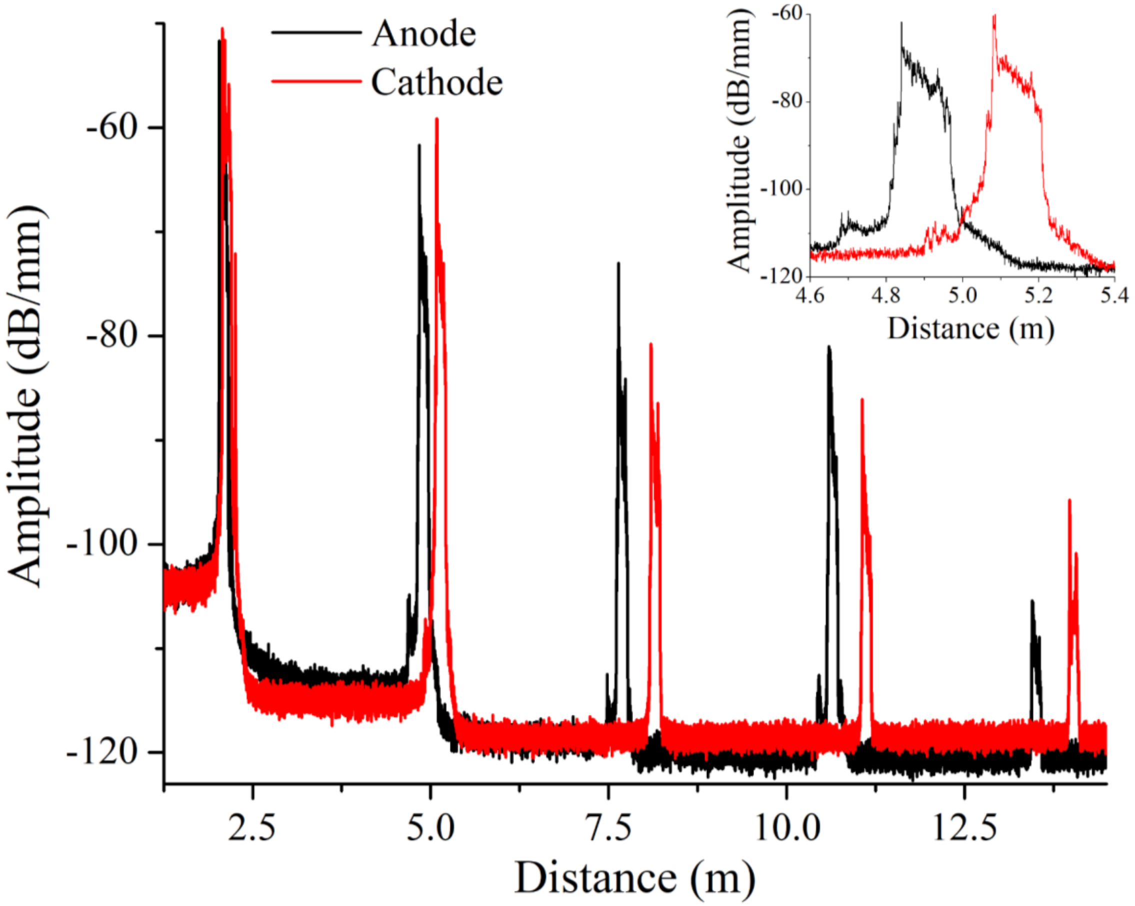

Figure 40 The Rayleigh backscattered distributions of the sensors at the anode (cathode) side connected to one fiber strand for simultaneous temperature monitoring of several spatial locations at the anode (cathode) plate. The inset illustrates the Rayleigh backscattered signals from two laser-enhanced fiber sections, one located at the anode side (black); the other located in the cathode side (red).

Temperature measurements were resumed at varying fuel flow rates at 800°C, 100 sccm airflow, at 2 A. The tested H_2 flow rates were 100, 50, and 10 sccm balanced with N_2 to reach a total flow rate of fuel and N_2 of 100 sccm. Three measurements were taken at each flow rate condition at 30, 60 and 90 seconds from driving the current, with one reference taken at 0 A at each flow rate condition. Is has been noted that the 30 and 60 seconds measurements capture the transient effect inside the fuel cell, while the 90 second measurement is long enough to capture the steady state reaction inside the fuel cell, but still short enough to avoid external furnace temperature fluctuations to affect the sensors readings. It is interesting to note that at fuel starvation conditions, i.e. at flow rate 10 sccm of H_2, the current was lowered to 1 A to raise the voltage above 0.4 V to avoid the damage of the fuel cells plates at this harsh setting. This set of measurements was with varying fuel flow was also repeated at 750°C (±5°C furnace temperature fluctuation).

5.5.4 Results of distributed temperature testing in SOFC system

The temperature change measurements recorded at various fuel cell conditions were plotted against distance on fiber sensor with respect to the reference temperature profile measured at open circuit. The transient effects, shown in plots of figure 38 are also distinctly shown in figure 41(a). The temperature profile clearly varies at different times measured from the start of driving the current. The section of the fiber inside the fuel cell electrode is marked in figure 41, as well as the section of the sensor inside the furnace. The hump appears first at the first one third on the fiber, very close to the fuel gas inlet, then spreads out to both sides until steady state is achieved at approximately 90 seconds. The figure also shows the sensors capturing the ±5°C temperature fluctuation inside the furnace, and how it affects the longer duration measurements (>90 seconds) as the furnace temperature drop spreads from the outside of the fuel cell to the inside.

The results after over 72 hours of exposure to high temperatures are both very consistent and repeatable. Moreover, the results are intuitive as the peak of the hump appears closer to the H_2 gas inlet, and shifts closer to the inlet when the H_2 flow rate is reduced (see figure 41(a)). This shift in temperature peak matches the fuel utilization trend that was calculated as 15.2% for 100 sccm of H_2, 30.4% for 50 sccm of H_2, and 76.0% at H_2 starvation conditions of 10 sccm of H_2

flow. That is to say, at lower H_2 concentration, the probability for it to react becomes higher, so more H_2 molecules react sooner on entry to the cell, and rather closer to the H_2 gas inlet.

The "humps" in the temperature distribution in figures 41(a) and (b) indicate the reaction hot spots. It is interesting to note, the locations of the hottest points does not change with time, only with H_2 concentration, corroborating the previous conclusions proposed. Comparing the temperature distribution in figures 41(a) and (b), the temperature rises are at the anode (cathode) reach 4.03°C (2.04°C) after 90 seconds of drawing current from the SOFC. The reaction at the anode side is as twice as hot than it is at the cathode side. It is also noted that the temperature is higher at 50 sccm H_2 flow rate than is it at 100 sccm of H_2 flow rate. Hence, the reaction is higher at 50 sccm of fuel flow rate conditions.

Simultaneous measurements were made by each set of five sensors, and were used to reconstruct the 3D temperature distribution using a MATLAB® code, and plotted in figure 42. The temperature readings were obtained from both sets of cascaded sensors then plotted in color scale in 2D geometry to achieve the 3D temperature plot. Figure 42 reveals the reconstruction of the 3D temperature profile from each sensing point of the 0.5 cm distributed sensor, mapped to their respective locations on the schematics of the fuel cell current-collector electrodes. The 3D temperature profile plots better depict where the reactions occur at anode and cathode sides of the electrolyte. They show also multiple hot spots; one large reaction hot spot at the anode side and two reaction hot spots at the cathode side.

Reaction hot spots appear close to the H_2 (air) inlet at the anode (cathode) side, if a little lateral displacement. The second cathode hot spot appears near the air outlet, with a large displacement to the periphery of the active area. The anode hot spot appears to be affecting the cathode side in the location vertically allocated close to the anode reaction hot spot. It was also noted that the temperature profile rise due the reaction spreads faster at the cathode side than the anode. This experiment configuration enabled the observation of reaction hot spots, those did not appear in the two fiber sensor experiment [88].

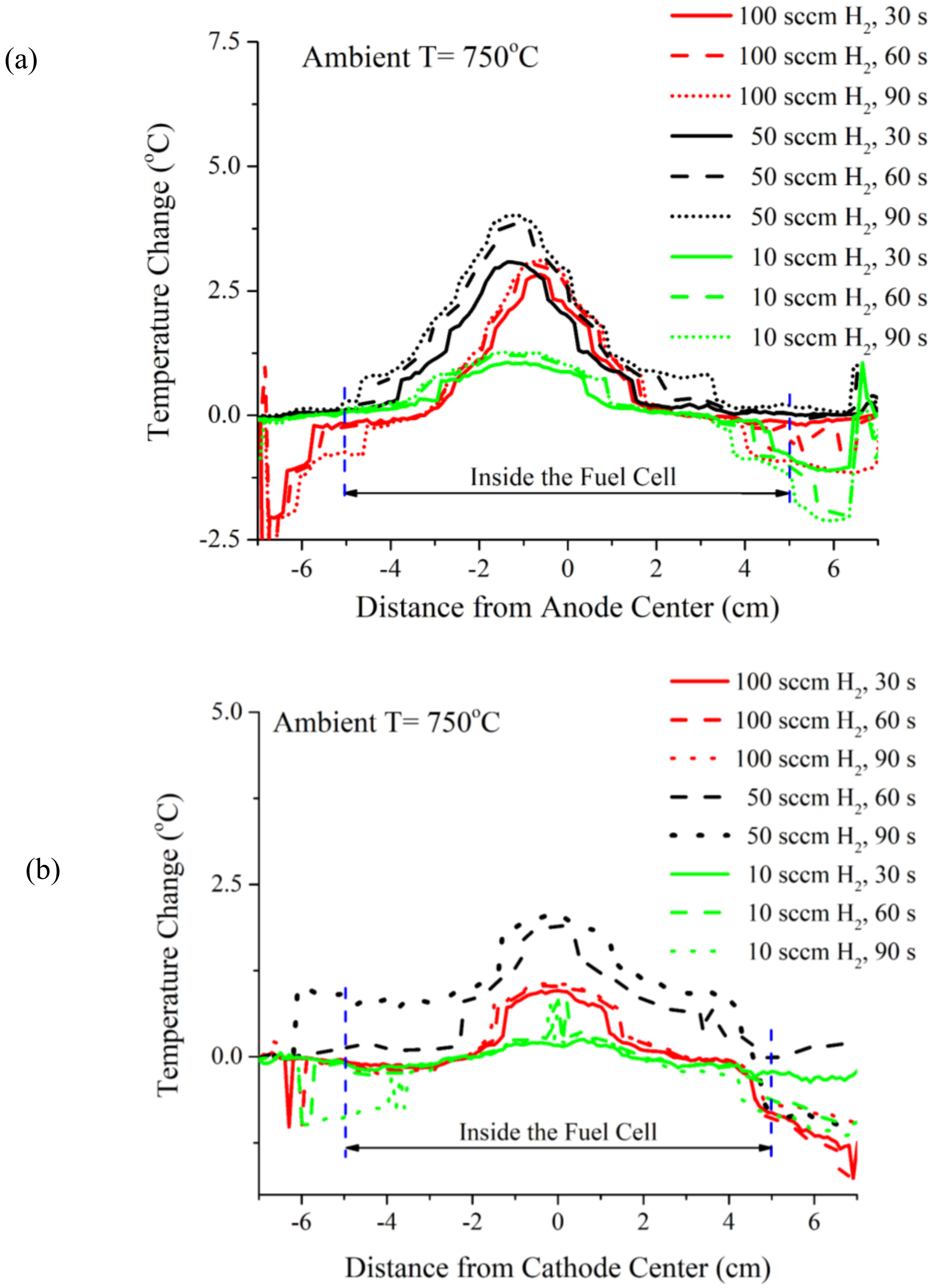

Figure 41 Transient temperature effects visible from internal cell reactions and externall from furnace temperature fluctuations at the (a) anode, and (b) cathode centers. The reaction hottest locations at different H_2 concentrations are the peaks of the temperature distributions. The hottest reaction loactions are static at constant H_2 concentrations. The peaks shift to the left (closer to the H_2 inlet) at the anode side at lower H_2 flow rates. The peaks locations are the same for the temperature distributions at the cathode side, at different H_2 fuel flow rate conditions.

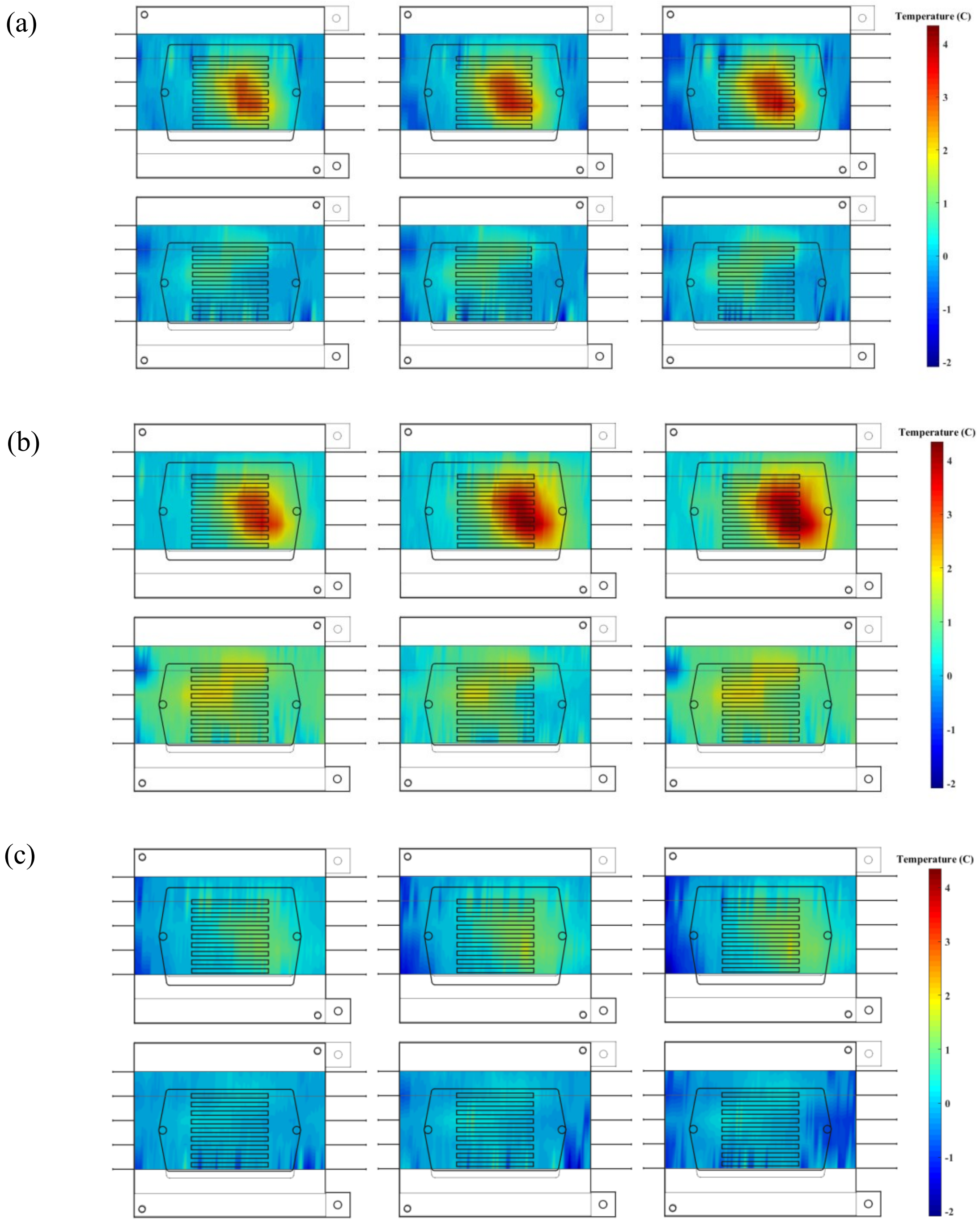

Figure 42 The temperature profile plotted in 3D for the fuel cell operating at 750°C, 1 A, (a) 100, (b) 50, and (c) 10 sccm of H_2 from fuel inlet. At each reaction condition the profiles at the anode (top) and cathode (bottom) at are plotted at 30, 60, and 90 seconds (from left to right). Quick observations: anode is hotter than cathode, at lower H2 concentration the reaction hottest spot is closer to H2 gas inlet (right hole at anode), and there are two hot spots in the cathode profile; one of which is vertically below the anode's hottest point.

5.6 Ultrafast Laser-Enhanced Distributed Sensors Conclusion

The ultrafast laser-fabricated distributed-sensors on SMF-28e+® and Vascade® optical fibers, proved thermally stable for temperatures up to 800°C. The ultrafast laser-inscribed nanostructures were highly affected by the ionizing effects of nuclear irradiation, namely RII changes, as the process of nanostructure inscription and the exposure to neutron fluxes have the same effect of altering the refractive index of glass. Nevertheless, the sensors Rayleigh profile drift was slow and fiber samples with both types of sensors withstood neutron fluxes at an excess of 10^{14} n/cm^2/s for over 188 days providing valuable information about the reactor core environment. Continuously inscribed nanostructures on F-doped cores of Vascade® fibers produces relatively stable distributed temperature sensors, capable of monitoring in-pile experiments, in situ.

A viable real-time system for mapping the temperature distribution inside an operating high-temperature SOFC was demonstrated for the first time. This novel technique resulted as a combination of optical frequency domain reflectometry with the ultrafast Rayleigh enhancement of standard optical fiber for compatibility with high-temperature operation. Although this technique does not eliminate the drift in Rayleigh scattering exhibited in fused silica in harsh environments, it does provide a means of increasing scattering intensity and stability such that high-value measurements can be made for a longer period of time.

Because researchers have struggled to make these types of measurements for a long time, we believe that the value added in even short-term measurements is high. As we have noted, these measurements correlate well with appropriately featured simulations, and the technique can be used by SOFC designers and engineers to verify new designs, or validate multi-physics cell models. Since a new level of measurement detail is provided by our technique, we believe that designers can now take the next step in design complexity, and use measurement data to mitigate the occurrence of current-induced hot spots in new cells. This can be accomplished through a careful combination of current and fuel control without modifying existing geometries. In another long-desired process improvement, cell designers can modify the channel geometry in order to offset current-induced temperature increases with varying channel sizes. This may further increase the longevity of SOFCs, which will aid their adoption in the energy generation market.

Finally, ultrafast laser-enhancement of optical fibers technique together with the incorporation of AM may be useful in development of "smart" sensing structures for a number of other harsh-environment applications including nuclear reactors, gas turbines, and gassifiers. Because optical fiber is immune to electrical interference, it is possible to obtain measurements where regular electrical sensors traditionally fail. Finally, we note that in addition to electrical interference immunity and high-temperature operation, the cost of optical fiber is extremely low, and a large quantity of fiber can be cheaply implemented to realize many thousands of sensing points at very low cost. Even when considering the generally large cost of an interrogation system, the price per sensing point can still be extremely low.

6.0 Distributed Fiber Sensor Fused Additive Manufacturing for Smart Component Manufacturing

Optical fibers are mechanically versatile and offer low intrusiveness to the system they monitor. One unique trait of the optical fiber is their abilities to perform distributed measurement while an unmodified fiber can be used to perform continuous measurement along the fiber with high spatial resolutions. The distributed fiber sensors that can withstand harsh environments are particularly useful for energy applications from fossil fuel, to renewable energy, and to nuclear energy. The high spatial resolution information harnessed by the distributed sensors can be used to improve reactor structures, to optimize control algorithm, and to monitor structure integrity [39].

The implementation of optical fiber in energy systems have been a major challenge for their functional realization and longevity. In the past, fiber optical sensors are implemented after the construction of energy production systems (e.g. reactors or turbine). These practices incur significant limitation in term of sensor deployment and their function realization due to constrains on spaces and accessibility. Hence, direct embedding of optical fibers in metal components designed for energy application before their final assembly becomes a viable and potentially important solution.

Successful embedding of optical fibers inside metallic parts has proven to be extremely challenging. Different host structure materials like composites, polymers, metals, and ceramics, can accommodate optical fibers as demonstrated in various literature using different techniques [40]. The critical issue when embedding optical fiber into metals is that the metals have very high melting temperatures, such that during embedding, the fibers would need protection from the excessive thermal loading and intrinsic stresses that can distort the spectral envelope of FBGs and induce cracking [1]. Furthermore, structural anisotropies, voids between the fiber and the host, and reduced densities compared to bulk materials are among other concerns [38].

Additive manufacturing (AM) offers a solution to the fiber embedding problem. AM covers different technologies in which structural components are built from the ground up [38], layer by layer, undergoing a series of fabrication processes. This means that each severe process can be broken into less severe steps [1] allowing the fiber to survive the harsh embedding conditions.

Various manufacturing techniques have been established for the embedding process. It involves two steps; fiber encapsulation with a metal then embedding of the coated fiber in a metallic part. The first step aims to protect the fiber from severe embedding conditions have been proposed in various published articles and using metals like Ni, Cr, Al and Cu [37-41, 94-99]. In literature, the insertion of the coated fiber into metallic parts have been reported using various techniques like using Au coating then arc spraying Ti [37], using casting of Al [96], and using selective laser melting (SLM) to embed fibers in U-shaped grooves in [38, 94]. In addition, metalizing fiber with Cr is reported in [39] using RF sputtering then electro-coating with Ni then finally embedding in SS using SLM. Upon completion of the embedding process the distributed or point fiber sensor is characterized to measure its function realization, dynamic range, residual strains from the embedding process, repeatability, delamination or slippage point, and failure/breaking point.

A major challenge for operation of a silica-based optical fiber embedded in metal is delamination. It merely arises from the significant difference between the coefficients of thermal expansion (CTE) of both the metal material (~10 ppm/K) and glass (~0.5 ppm/K) that would cause axial stress build-up on the interface between the two materials. For a given temperature change, metals expand (or contract) at a larger extent than glass, causing extreme shear stresses on the glass in the vicinity of the metal/glass interface, that could eventually break the glass fiber, or detach the glass fiber from the encapsulating metal part. While slippage may not be entirely disruptive for a temperature sensor, a strain sensor would require proper adhesion of the embedded silica glass fiber, at all points, to the encapsulating metallic part. Also, while providing for better adhesion, by choosing a suitable keying layer and perfecting the fabrication processes in cleaner environments may defer delamination to greater temperature changes, nevertheless, delamination is inevitable owing to the order of magnitude difference in thermal expansion coefficients between glass and metal that will cause axial stresses to overcome the adhesion at some point. Still, research is being conducted to defer delamination of sensors to a later stage, at higher temperatures, thus achieving larger dynamic/operational range of the fiber sensor [38-40, 94, 95].

In this last chapter, we review previous studies and propose our own efforts aiming for safe embedding of optical fibers into metallic structures using AM techniques. Finite element (FE) computational tools are utilized to study the effect(s) of varying composite material parameters, before carrying out the embedding experiment.

6.1 Previous Efforts for Embedding Optical Fibers into Metallic Structures

In an embedding process where optical fibers were embedded in titanium matrix composites (TMC), Baldini et al [37] broke down the composite material fabrication and processing into less severe steps. TMC are metal matrix composites comprised of silicon carbide fibers and titanium alloys. Gold coated optical fibers were first arc sprayed with titanium for protection and then sandwiched between two previously prepared half laminates, and linked altogether using diffusion bonding. They have reported a distortion in the coating and the cladding of the fiber, and also a deterioration of sensing above 750°C.

Later, Lee et al [96] have reported the use of casting to embed optical fibers and F-P interferometers into aluminum. Lin et al [97] in 1998, reported the use of lead cladding before embedding into aluminum, to enhance the sensitivity of FBG sensor by nearly five times that of a bare fiber and up to an operating temperature of 300°C. The lead (solder) cladding was melted and poured into a U groove with aluminum foil lining, then left to solidify with the FBG fiber sensor placed inside. The metal cladding simply enhances the thermal sensitivity of the FBG sensor as metals have higher CTE that would cause the metal to react (expand or contract) more dramatically for a given change in temperature, compared to bare or polymer coated silica based fiber, which causes greater, or in other words, more responsive shifts in Brillouin frequency. An effort that featured the use of the CTE mismatch in favor of the optical sensor. Something that was made possible at low temperature operation.

In 2001 X. Li et al [40, 95], have demonstrated the embedding of metallic coated FBG sensors into nickel structures. They have reported its accuracy to be 2°C, and a 100% boost in temperature sensitivity above that of a bare FBG. They have also demonstrated and for the first time, the embedding of FBG in stainless steel structures. Nickel was deposited on stainless steel using electrolysis and then the optical fibers with the sputtered thin metal layer were placed on the substrate to be electroplated with layer of nickel, and finally covered with deposits of stainless steel. The interface between the lastly deposited stainless steel and nickel was layered and uneven; an evidence of diffusion. They recorded an improvement in embedding quality after the optimization of cleaning the optical fibers and substrates. The electrolytically deposited nickel was extremely thick, in excess of 2 mm in diameter, causing the formation of uneven grains that become larger and more irregular towards the interior of the sample. The extent that thermal stress and residual stresses from laser cladding will impair the bonding between the interfaces; nickel layer to stainless steel substrate, the optical fiber to nickel layer interface, and nickel layer to laser cladded stainless steel, was not known, and delamination was not observed post processing.

In 2011, an implementation of embedded FBG sensor in machining tools was reported Alemohammad et al [98], featuring the use of low temperature laser micro-deposition of silver on fiber then nickel electroplating. Silver deposition with achieved by laser-assisted mask-less micro-deposition (LAMM), then subsequent to nickel electroplating tungsten carbide-cobalt (WC-Co) was deposited on the steel structure using laser solid freeform fabrication (LSFF).

Y. Li et al [99] have investigated the feasibility of embedding metal coated FBG in metal foils using ultrasonic spot welding. Their study featured the use of chemical plating and chemical electroplating protection methods in spot welding with copper and aluminum foils of 250 μm and 450 μm thicknesses, respectively. They have observed the difficulty of embedding fiber in copper because of its high hardness that causes the fiber to be destroyed, and as for the embedding in aluminum using ultrasonic spot welding; chemical plated protection was ineffective but successful embedding using chemical- electroplating was achieved and the sensitivity of the FBG was doubly enhanced compared to bare fiber.

In 2014, Maier et al [39] reported the embedding of FBG based and in fiber F-P optical fiber sensors in two stainless steel structures using the AM process of SLM, maintaining their basic sensing capabilities. They applied a chromium keying layer to allow for strong adhesion between glass and nickel. Nevertheless, delamination and slippage occurred at temperatures above 435°C.

Havermann et al [38, 94] have reported the use of direct or selective laser melting (SLM) to manufacture 316-stainless steel components, where thinly nickel-coated optical fibers (thicknesses ~350 µm) with FBGs were placed in U-shaped grooves on stainless steel parts, then the powder is melted on top to cover the fiber. Figure 43 shows a photograph of a stainless steel embedded FBG sensor by Havermann et al [38]. They have reported successful embedding of optical fiber when the protective coating exceeds 330 µm (see figure 44(a)). They have tested their successful embedding of the temperature and strain sensors by measuring the Bragg frequency shift, and analyzed their samples using cross-sectional microscopy. In situ measurements were reported for temperatures less than 400°C. Delamination occurred at 350°C, with reported gaps of above 300 nm at 500°C owing to differences in CTE (figure 44(b)).

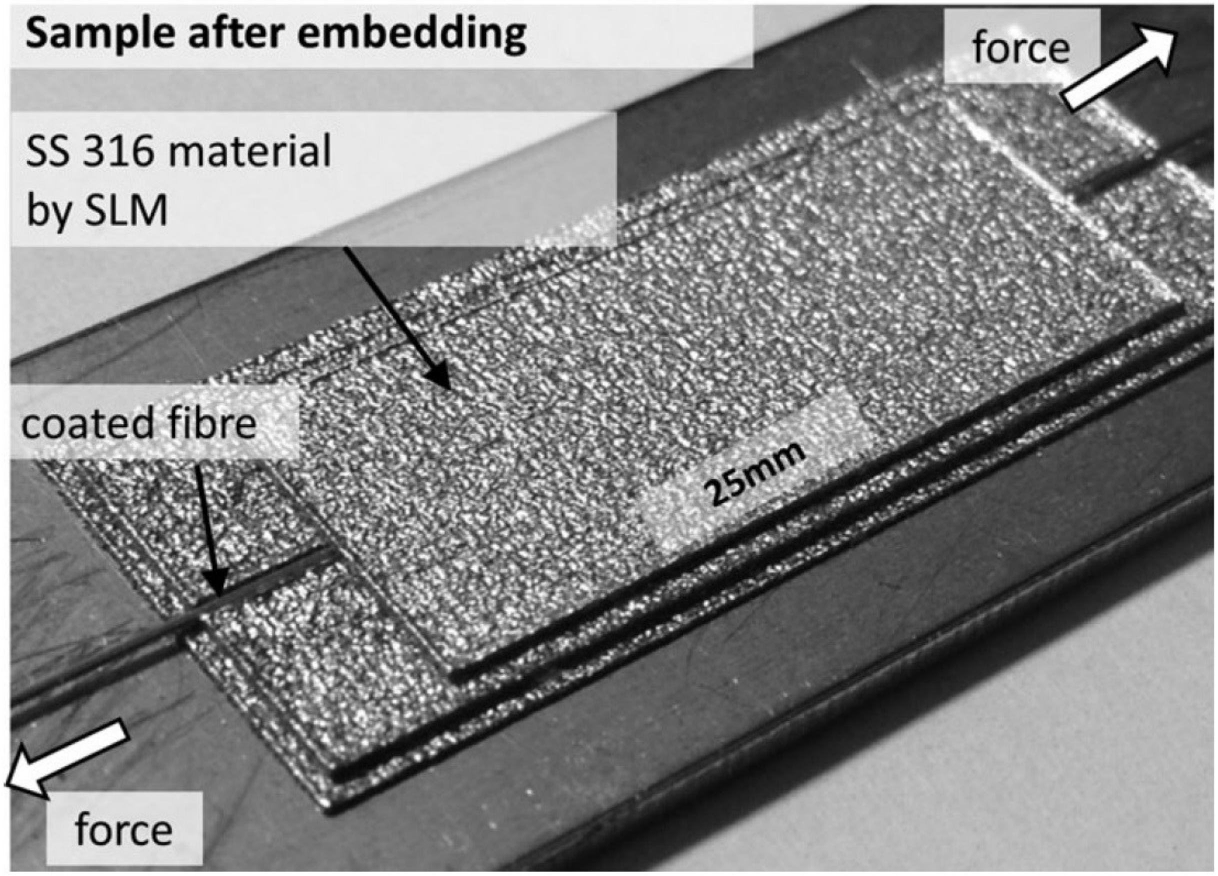

Figure 43 The nickel plated FBG optical fiber sensor after embedding in 316-stainless steel constituting a strain sensor [38] © 2015 IEEE.

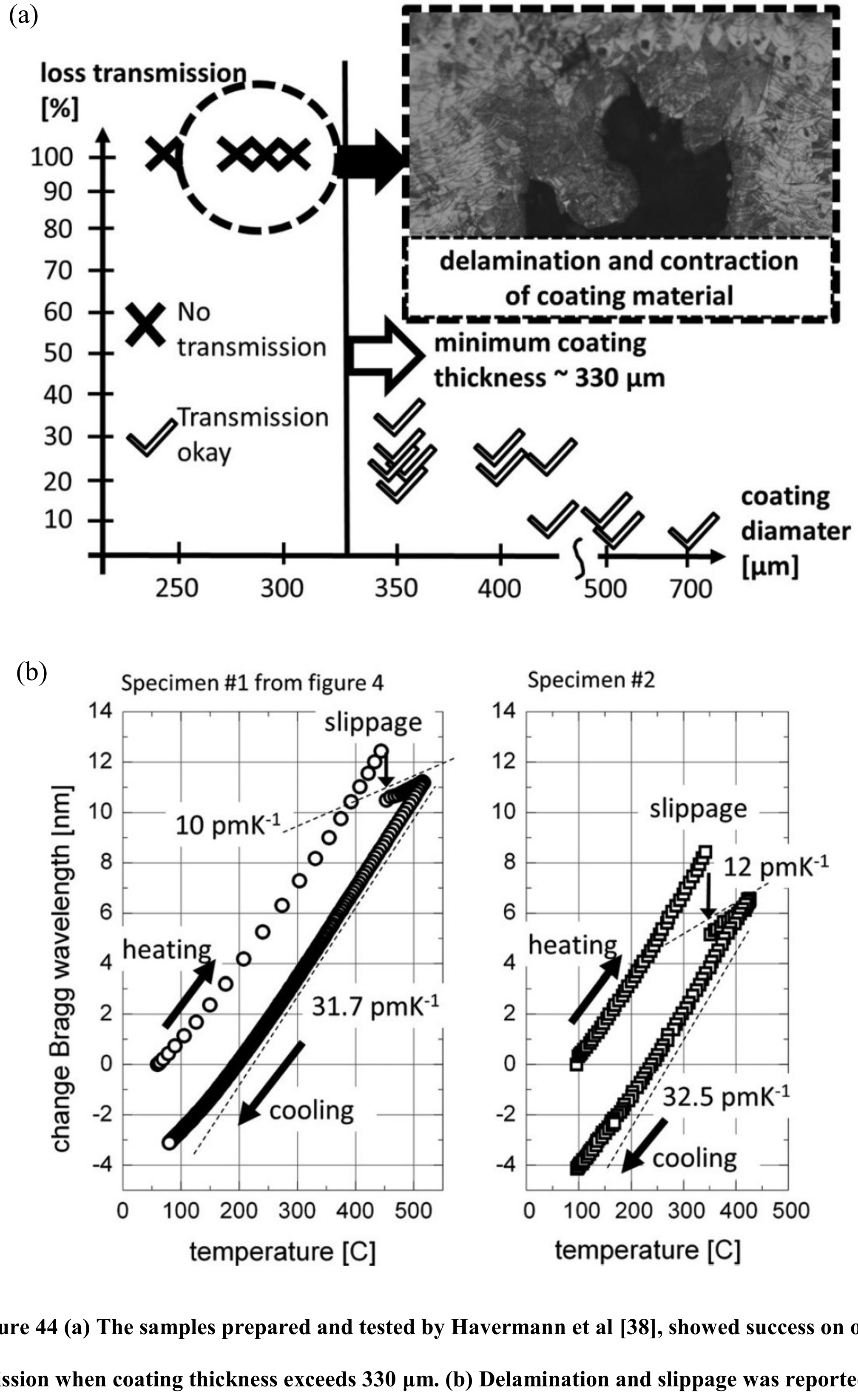

Figure 44 (a) The samples prepared and tested by Havermann et al [38], showed success on optical transmission when coating thickness exceeds 330 µm. (b) Delamination and slippage was reported between silica fiber and nickel coating for two samples above 350°C [38] © 2015 IEEE.

6.2 Sensor Interrogation Setup

The optical fiber sensor is connected to a commercial OBR unit (Luna Innovations® OBR4600) described in section 2.1.1. In a Rayleigh OFDR configuration, the spatial distance is mapped to the frequency domain through FFT. The frequency domain is swept using a tunable laser and the distributed Rayleigh profile is obtained from the backscattered signals. This profile information is the signature of the fiber under test, at constant test conditions like temperature and strain. If the test condition is perturbed the Rayleigh spectrum shifts accordingly, and the amount of shift is obtained through autocorrelation between the new profile and the reference profile. This spectral shift can be converted to temperature (or any physical quantity affecting the Rayleigh profile) change by scaling using the proper coefficient. The OBR instrument measures the accumulated losses, temperature, and strain on all locations on the fiber up to a limiting spatial resolution (as low as 0.1 mm).

6.3 Sensor Fabrication

The sensor fabrication undergoes two crucial steps, namely fiber coating, and embedding. Firstly, the fiber is coated with a protective metal jacket. Most metal hosts for embedding such as stainless steel, nickel, iron and titanium have high melting points that would cause damage of the fiber on processing [94]. The protective metal coating helps alleviate the thermal loading on the fiber [38], and increases the likelihood of the glass fiber surviving the harsh embedding conditions. The tradeoff remains; as it is ideally desired to carry out embedding in a high temperature built structure that would not constrain the range of applications in which the sensing component may be deployed. But high temperature processing is severe for the optical fiber to endure, so a thick protective coating must be applied, which in turn compromises the final physical, mechanical and structural properties of the structure. The metal(s) used for the coating purpose should be carefully selected to be unreactive and stable at the structure's operating temperature. The metal(s) used for coating the fiber should also bond strongly to the silica-based optical fiber, from one side, and to the host material from the other [38].

For stainless steel parts, nickel has been widely used for coating purposes; for nickel is a constituent of corrosion resistant stainless steel and has a melting temperature of 1455°C, close to that of 316-stainless steel (1371-1399°C), and considerably below that of silica (1723°C). Moreover, nickel coating can be easily applied using electroplating. However, the order of magnitude mismatch in CTE between Ni and glass will always cause residual strains during embedding, and eventually delamination on temperature variation.

Invar, a nickel-iron alloy, combines merits of nickel deposition with the prospect of glass-metal interface problems deterred to higher temperatures. The CTE of Invar is a function of its constituting Ni: Fe ratio. Invar can reach a CTE as low as 1.2 ppm/K that is nearly 2 times that of glass at a composition ratio of 36% Ni: 64% Fe. At this composition the alloy is denoted Invar-36. With this cut down in CTE mismatch between the two materials, metal and glass, more stable interfaces can be formed with less residual strains, and prolonged adhesion. Perfecting the alloy composition is adamant to achieve the minimal CTE that is closest to glass [100]. The only problem is depositing alloys is much more complicated than depositing metals. In the following sections, the steps of attempted embedding of optical fibers into Invar-36 are presented.

6.3.1 Fiber metallization

Twelve centimeters of optical fiber is mechanically stripped from its polymer (acrylic) jacket and fixed on the substrate inside of an e-beam chemical vapor deposition (e-beam CVD) chamber. Deposition was carried out at 4 Å/sec then the fiber was taken out, rotated 180° then placed back in the vacuum chamber to deposit on the rest of the fiber. Metallization was attempted using Cr and W. Tungsten provided a better coating material for its higher conductivity and very low affinity to react with air upon removal from the deposition chamber. In this stage, 50 nm of tungsten was deposited on silica glass to achieve electrical conductivity necessary to the following stage. It is worth to note, most commercial deposition tools use W filament to heat the target metal in e-beam, and plasma evaporators, or in sputtering instruments. Therefore, using W as a target metal is very undesirable, as the deposition tool will be operating at extreme conditions.

6.3.2 Fiber coating using electroplating

Metalized fiber from the previous stage is sufficiently electrically conductive to be used in a reverse galvanic cell setup, where the coating metal (Invar-36 alloy bar from Ed Fagan® Inc.) is the anode and the cathode is the specimen to be coated. The composition of the electrolyte for coating is obtained from [101]. The electrolyte composition is given in table 7 (chemicals from Sigma Aldrich® and Thermal Fisher Scientific®). This coats Ni: Fe roughly at a ratio 36%: 64% at 43°C and a current density 30 mA/cm^2 to achieve a low coefficient of thermal expansion of 6.3 ppm/K, half of that of Ni, and closer to that of silica glass.

Table 7 Invar-36 electrolyte composition.

Chemical	Concentration
Nickel Sulfamate (M/l)	0.9
Nickel (II) Bromide (M/l)	0.1
Iron (II) Sulfate (M/l)	0.15
Boric Acid (g/l)	25
Sodium Saccharin(g/l)	5
Wetting Agent (g/l)	0.01
Ascorbic Acid (g/l)	1

Metalized optical fibers (commercial fibers from IVG fiber®, Ontario, Canada) with 1300 nm of Cu coating were used for these tests, to finesse the right formulation and conditions for deposition of Invar optimal composition. The coated samples were characterized using energy dispersive x-ray spectroscopy (EDS) to confirm the correct compositions of the Ni: Fe alloy with a 4.4% composition variation (figure 45(a)).

Other samples with W metallization were electroplated with Invar-36. The fiber sensor was monitored in real-time using the OBR to measure the residual strains during Invar deposition. The results in figure 45(b) show compressive strains building up as the thickness of the electrodeposited layer increases. The Invar-36 coated samples suffered irregularities that made it hard to further embed them into SS parts.

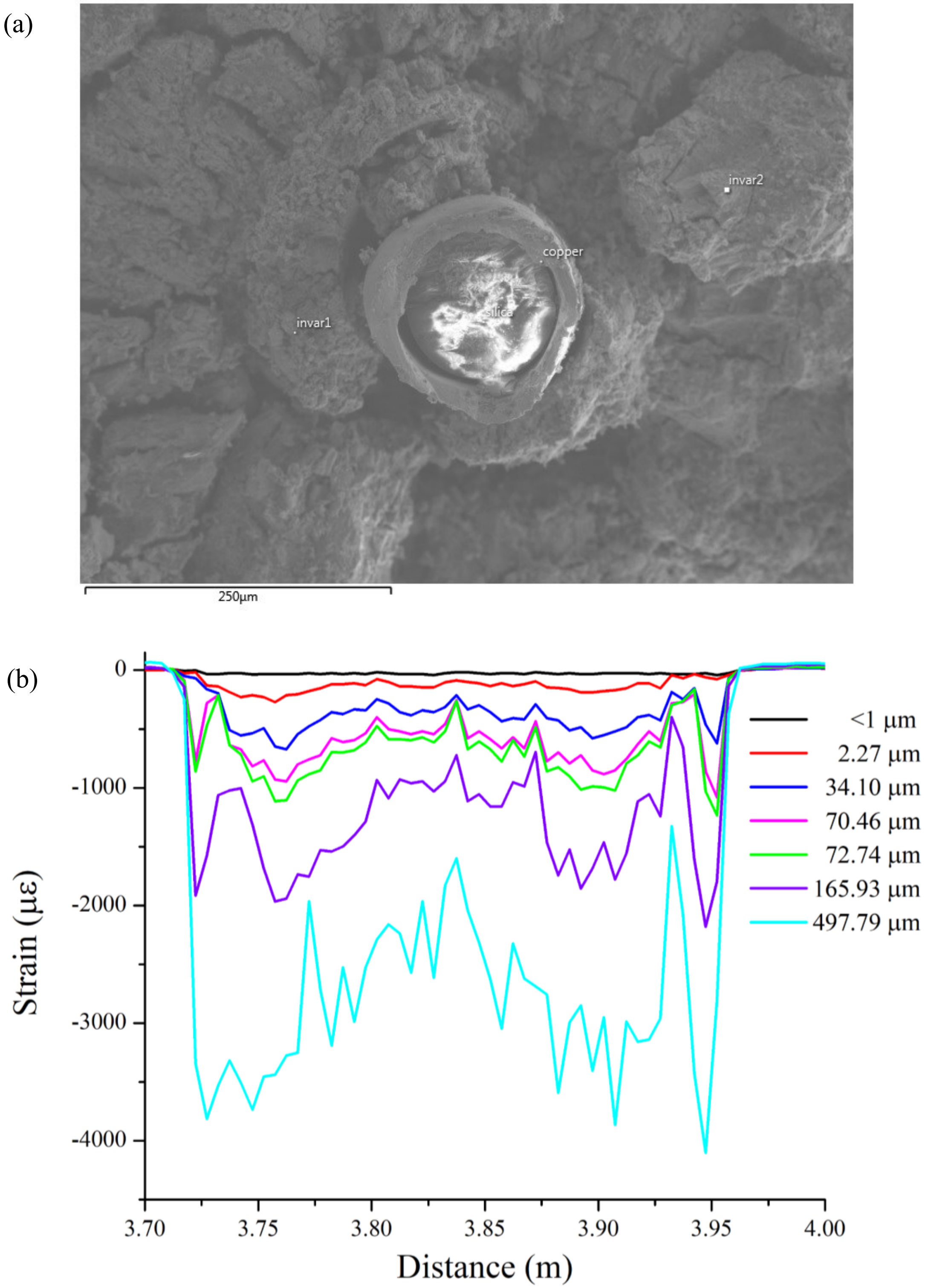

Figure 45 A microscopic image of an optical fiber sample, metalized with Cu, and electro-embedded in Invar-36. The Ni: Fe ratio was perfected with 4.4% accuracy using electroplating.

6.3.3 Coated fiber embedding

Fiber samples coated with metals can undergo either Laser Engineered Net Shaping (LENS) embedding process or 3D printing (EOS®) into metallic parts. Our LENS trials featured burial of the Cu coated fiber under 4 mm layer of Ti. It was apparent from the residual stresses induced from embedding stage that the materials for embedding must be finessed to alleviate the stresses. Not much progress can be reported here, and embedding of Invar-36 coated fibers into SS has not been attempted.

6.4 Experimental Testing of the Sensor

Embedded fiber sensors were fabricated. The fiber sensors were metalized with 50 nm of tungsten, and electro-coated with an Invar-36 layer. The coating layer thickness was varied from 400-800 μm in diameters. The fabricated samples were tested in a tube furnace. The furnace's temperature was monitored by a thermocouple with accuracy of 0.1°C. This test was devised to gauge the functional realization of the embedded sensors and to characterize the delamination conditions. It was also devised to examine the reversibility of operation of the fabricated sensors, and determine the dynamic range of their operation.

The first sensor (photographed in figure 46(a)) was coated with 800 μm of Invar-36. The sensor was placed in the tube furnace in N_2 ambient then heated up to 300°C, and cooled down to room temperature, then heated up to 800°C. The oven temperature was stepped up gradually, 5°C at a time, and left for 20 minutes at each temperature step. The Rayleigh profile was recorded at every temperature step after stabilization. The shift in Rayleigh profile of the sensor at various temperature steps is shown in figure 46(b). Following the spectral profiles in figure 46(b), it can be inferred that both tips of the sample suffer the highest strains that continue to build-up at higher temperatures.

Delamination was evident between 425°C and 509.5°C. Figure 47(a) illustrates the change in trend of the sensor's Rayleigh spectral shift as temperature was raised to 800°C. Heating beyond 509.5°C resulted in a spectral shift that is hardly different than before delamination. The curve in figure 47(a) was linearly fitted for the regions before and after delamination to assess the effect of delamination in the sensor's Rayleigh thermos-optic coefficient. Figure 47(b) reveal that the slope had changed from -2.52 GHz/°C (R-squared 0.998) to -2.48GHz/°C (R-squared value of 0.971), with a factor of 21.6%. This can be interpreted as the Invar-36 coating of 800 μm diameter (~337.5 μm thick layer) generated very little stresses on the glass-Invar interface, due to the significant cut-down in CTE mismatch. In other words, the distributed temperature sensor operation has been affected by ~21.6%. The fact that the sensor survived delamination and resumed function beyond 509.5°C, and up to 800°C, makes it a very good temperature sensor; for it had realized its functionality with a controllable error. It can also be used as strain sensor for operations <425°C.

The sensor was kept at 800°C for two days, then the temperature was ramped down to room temperature. The fiber sensor broken on the ramp down. Post thermal treatment was was carried out, which revealed that the glass fiber broke at both tips of the sample, where glass exited the coated section. The sample showed no signs of corrosion, and EDS microanalysis revealed the sample composition remained unchanged from thermal treatment. Heating in N_2 ambient has done its cause.

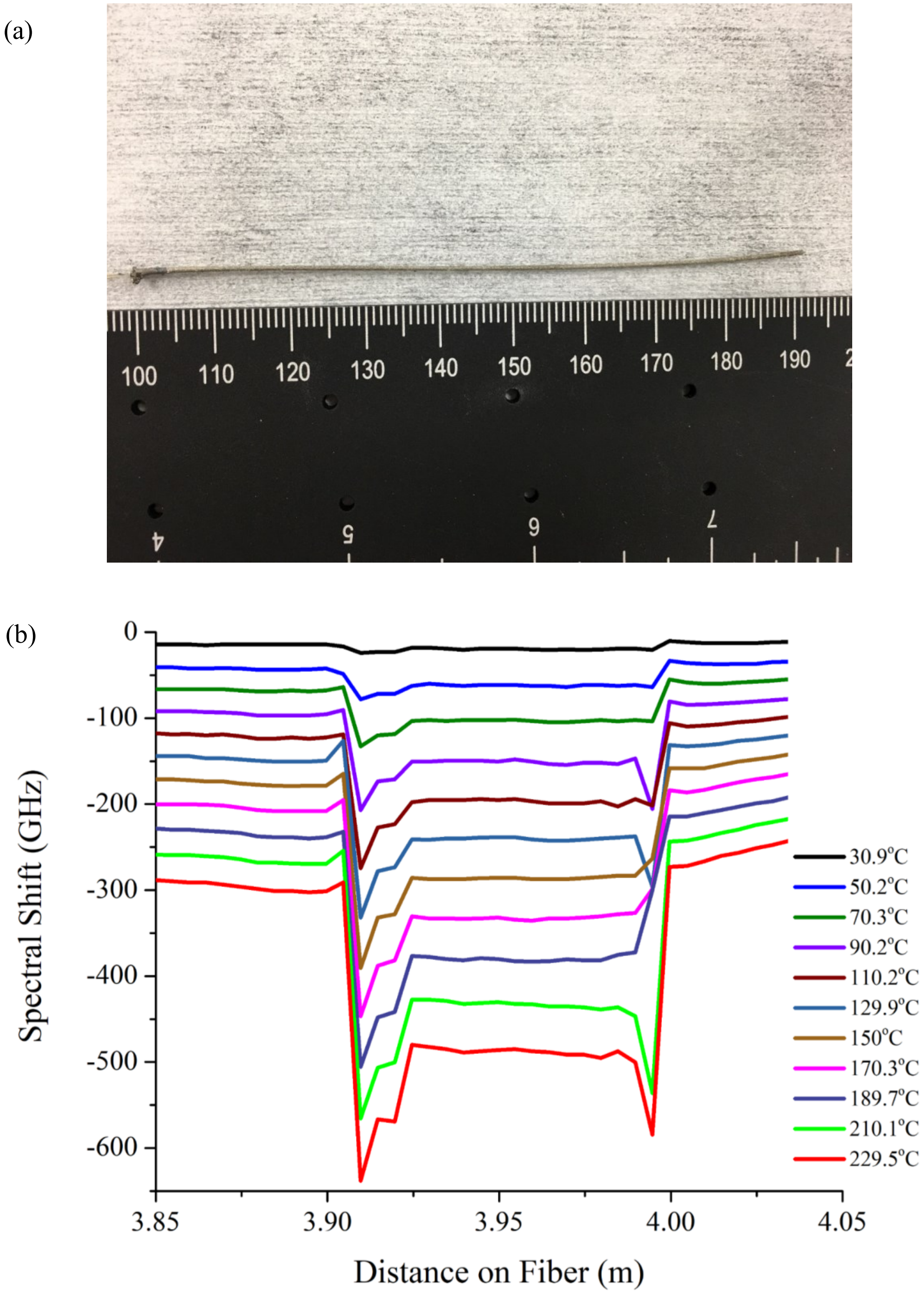

Figure 46 (a) Photograph of the 800 μm diameter, Invar-coated optical fiber. (b) Some Rayleigh spectral shift distributions recorded for the Invar-coated fiber sample, on the furnace temperature ramp up to 300°C.

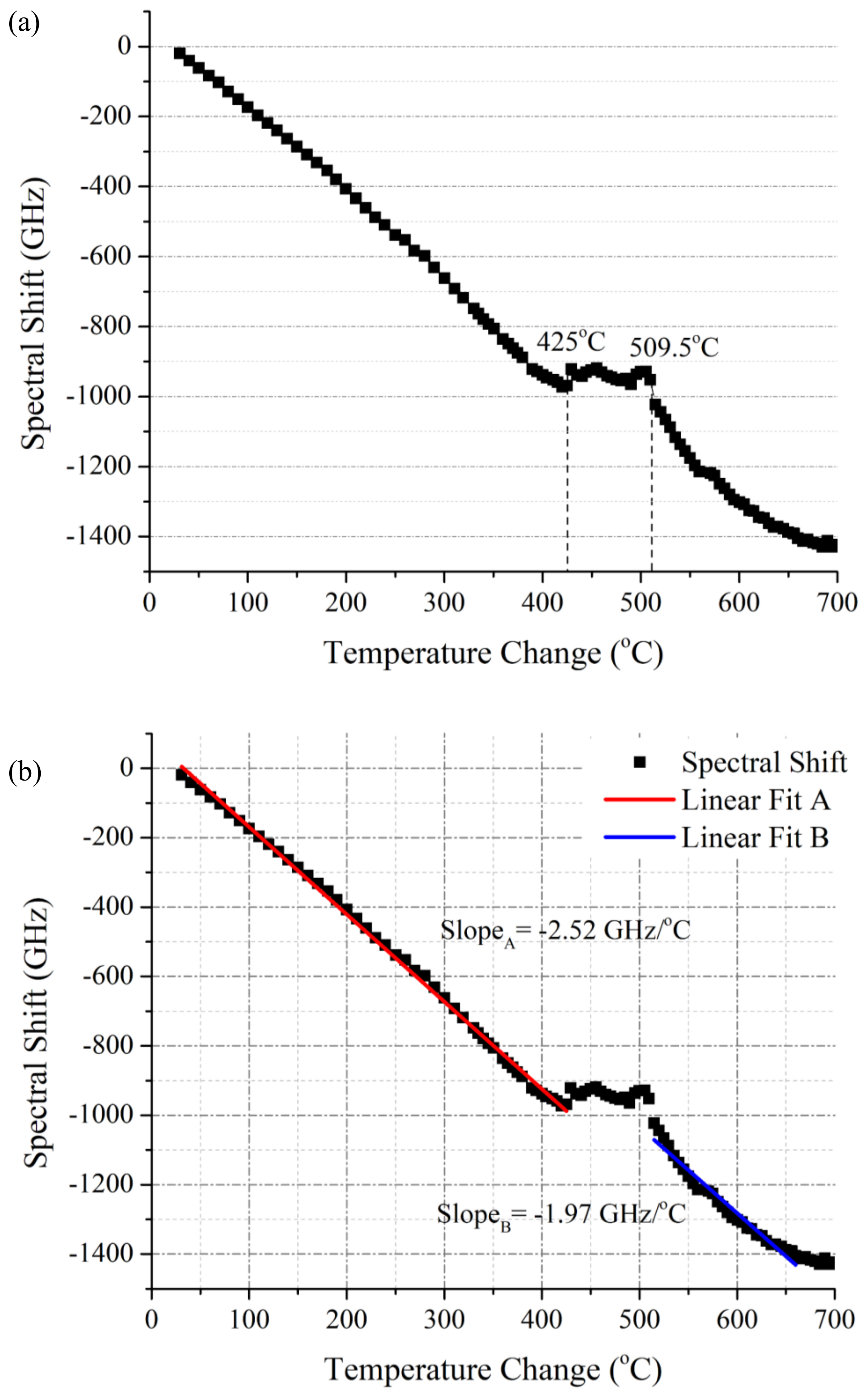

Figure 47 (a) Rayleigh spectral shift measured at different temperatures for the 800 µm diameter, Invar-coated optical fiber. Delamination is marked between 425°C and 509.5°C (b) The spectral shift regions before and after delamination linearly fitted.

A 400 μm Invar-plated fiber sample was tested afterwards. The furnace temperature was raised from room temperature to 125°C, in steps of 5°C, with a heating rate of 1°C/min. The furnace was stabilized at each temperature step for 15 minutes before heating up to the next step. Again, at each step the fiber sensor was interrogated using the commercial OBR, and the Rayleigh backscattered profile recorded. The furnace was then cooled back to room temperature following a similar cooling down process. The second heating cycle resumed the next day, this time heat was ramped up to 280°C, following the same heating procedure. The furnace was gradually cooled down to room temperature for the second time, before the third heating cycle commenced. In the third heating cycle the furnace temperature was stepped up to 800°C, gradually, 5°C at a time.

A bare fiber, stripped of the polymer jacket, was kept with the Invar-plated sample at all conditions, and its Rayleigh spectral shifts were recorded at every step of the test. Figure 48 shows the results from the heat cycling tests inside the tube furnace for the Invar-36 coated sample, as well as the bare fiber control sample. The inset in figure 48 shows the linear fits of the experimentally obtained spectral shifts at different temperatures. The results from linear fitting are presented in table 8.

The slopes of the spectral shift points indicate how the distributed sensor reacts to changes in temperatures. A coated sample will have both rising temperatures and induced thermal strains factored into its spectral shift changes. A spectral shift change from a bare fiber will mainly be due to temperature cycling. Nevertheless, the bare fiber section's slope had changed as intrinsic silica naturally reacts to thermal processes. These changes understandably diminish in magnitude every heat treatment, for the silica structure will anneal and thermal processes will be of reduced effect.

On other hand, the Invar-plated silica will react differently with heat cycles, due the effect of the metallic encapsulation of silica. Although, the change in slope started with a smaller magnitude than that of bare fiber, it was increased with heat treatments, especially after the third heat ramp-up. The spectral shift slope changes due to the first heat cycle was less than that of the bare fiber, due to the fact that the metal coated fiber sample had been through several heating treatments during e-beam CVD metallization and electroplating stages before getting to the point of the first thermal treatment in the furnace test. However, the changes afterwards are of significantly larger magnitude as the glass-metallic alloy interface experiences higher temperatures for the first time.

For this sample spectral shift irregularity appeared around 350°C indicating the onset of delamination. At 400°C, the glass had completely detached itself, yet again safely, from the metallic encapsulation, then resumed regular spectral shift with a slope that is 19.43% deviated than before delamination. The fiber behavior is now close to that of a bare fiber, if for a 38.73% mismatch in spectral shift slopes. Because the encapsulated fiber was not simply free of the metallic-alloy, thermally induced stresses remained affecting the fiber sensor. It is plausible to state that these stresses are in the radial and axial direction, as metallic-alloy coating expands with heat pressing inwards on the fiber, and stretching the fiber upon elongation. The sample was kept at 800°C for two days as well, before the furnace’s temperature was ramped down. Yet again the sample broke at the tips upon cooling.

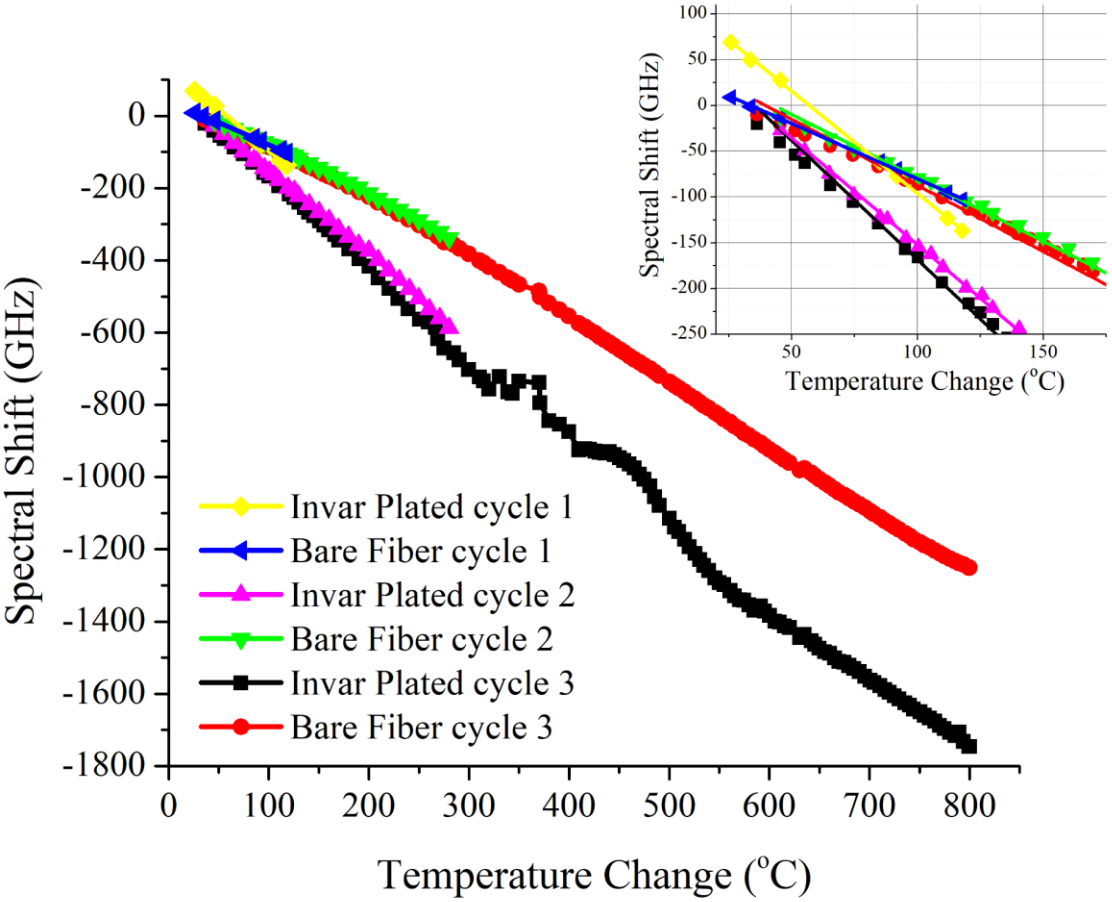

Figure 48 Rayleigh spectral shift measurements at temperature ramp-ups for three heating cycles. The spectral shifts were recorded for the 400 µm Invar-coated fiber, and for a bare-fiber control experiment. The inset is a close-up view of the spectral shifts, linearly fitted for comparison.

Table 8 Results of thermal cycling tests on Invar-36 plated fiber samples. Bare fiber was used as control for the thermal testing.

	Thermal treatment	Slope (GHz/°C)	Standard error in slope (GHz/°C)	% Change in slope from previous stage
Invar plated sample	Heating from 25°C to 125°C	-2.23577	0.01693	N/A
	Heating from 25°C to 280°C	-2.25493	0.01170	0.85698
	Heating from 25°C to 800°C before delamination	-2.42794	0.01502	7.67252
	Heating from 25°C to 800°C after delamination	-1.95603	0.03067	19.43664
Bare fiber sample	Heating from 25°C to 125°C	-1.21105	0.01278	N/A
	Heating from 25°C to 280°C	-1.38586	0.01278	14.43458
	Heating from 25°C to 800°C	-1.42483	0.01385	2.81197

A comparison of the performance of the two samples with 400 µm and 800 µm diameter Invar-36 coatings was drawn. The Rayleigh spectral shift changes for both samples are quite similar. The spectral changes after delamination is quite similar; 21.6% and 19.4% of their respective trends before delamination. Delamination started ~75°C sooner for the thinner sample, but this can be written off to imperfection in the sensor fabrication. However, both sensors survived delamination, and were capable of carrying out measurements post-delamination. Both sensors were capable of withstanding multiple heat cycles, but not when temperatures dropped down from 800°C. Both Invar-36 coated samples had shown the same vulnerability at the tips where bare silica glass protruded at both sides of the coated section.

Varying the thickness of the Invar-coating does not affect the operation of the distributed sensor. Figure 49 illustrates the identical behavior of two samples with various coating thicknesses. Apart from the onset and completion of slippage, both samples exhibited almost the same spectral shift changes with temperature variation. The primary function of the coating layer is to protect the optical fiber during later stages of AM embedding. Hence, it would be beneficial to embed in thicker Invar coating to better protect the fiber at later stages, without the fear of compromise of the sensor operation.

More samples were fabricated and used to devise the tests explained above. Experimental efforts reported here, were carried out in conjunction with finite element simulations, that gave insight about the attempted sensor designs, choice of materials and tests to be conducted. In the following section, the computational studies for this experiment is presented.

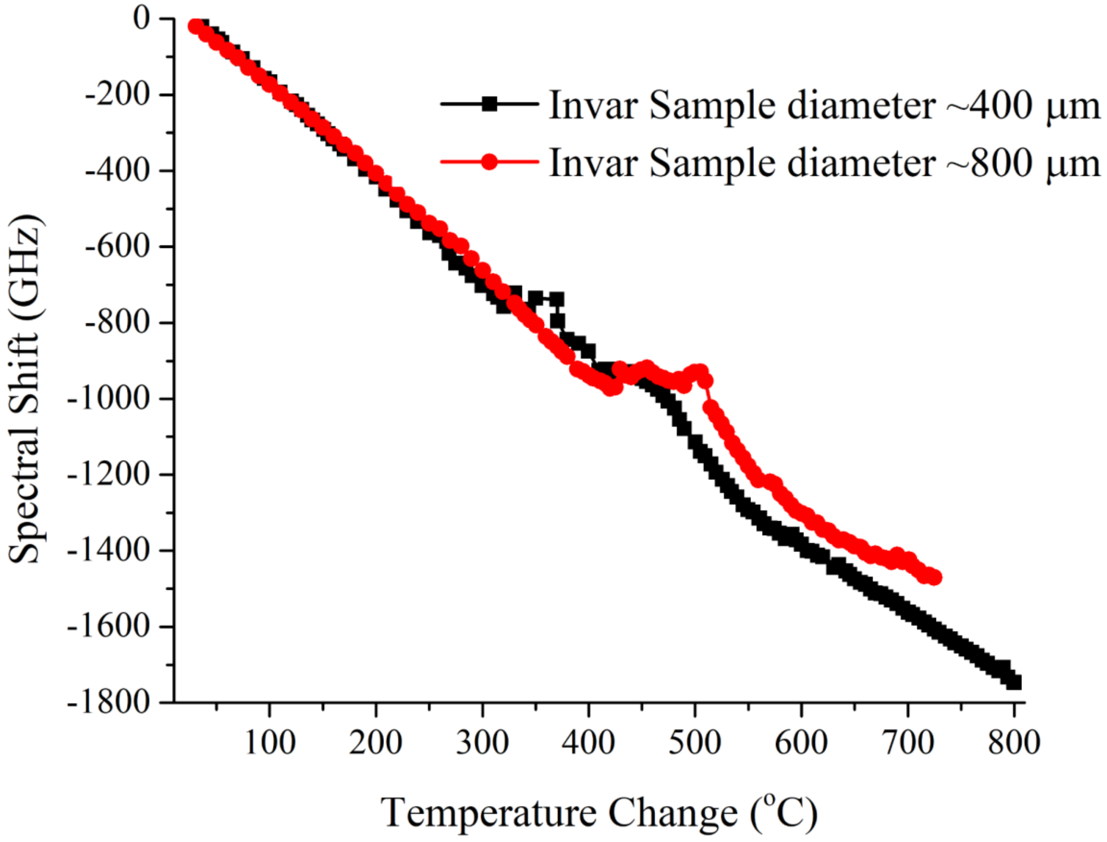

Figure 49 Rayleigh spectral shifts at different temperatures for two Invar-36 plated samples of different coating thicknesses. The two samples behaved in a similar way, if for a tiny mismatch.

6.5 Finite Element Simulation

Computational models were constructed to study the effect of increasing the temperature on the interface between silica glass and metal in designs where silica is embedded in metallic structures. This study utilized COMSOL Multiphysics® to develop a hypothetical understanding of the "perfect intermediate layer" properties through modeling, so a reasonable experimental system can be devised. The structure design shown in figure 50(a), illustrates the chosen model where 5 mm of silica glass cylinder of 125 um in diameter is encapsulated by Invar-36 alloy, and 430-stainless steel. The design parameters and material specifications are given in table 9. Simulating silica glass coated with Invar (built in material in COMSOL®), heating was applied as fixed temperature surface on the outer surface of the metallic cylinder then finite element calculations were carried out at steady state. Figure 50(b) shows the convection heating used to properly mimic the heating process inside the tube oven used for experiments.

Table 9 Design and material specification for embedding fiber FE model.

	Silica Core	Invar Alloy Coating	Stainless Steel Substrate
Diameter (μm)	125	300	>600
CTE (ppm/K)	0.5	Built-in function of T	11.4

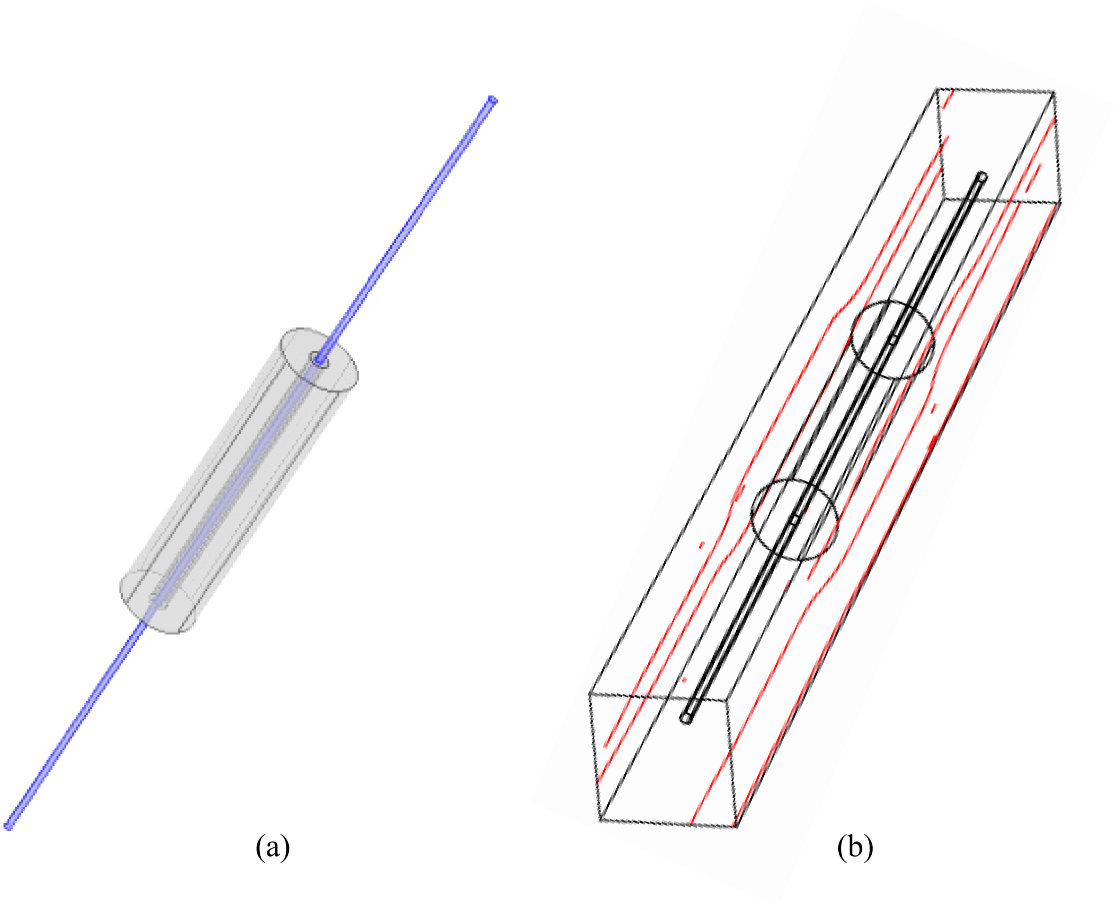

(a) (b)

Figure 50 (a) A schematic of the embedded silica fiber coated with metallic layer. (b) The heating simulation method chosen to mimic the heating process inside the experimental tube furnace.

6.5.1 Effects of varying temperatures on strains at the glass-invar interface

Firstly, a three-layer model (figure 51 illustrates) was used to simulate the strains components at the glass-metal 1, and metal 1-metal 2 interfaces, at a 100 K temperature rise. The simulated element comprised three layers, namely the glass fiber, the protective coating metal, and the embedding metal (table 10).

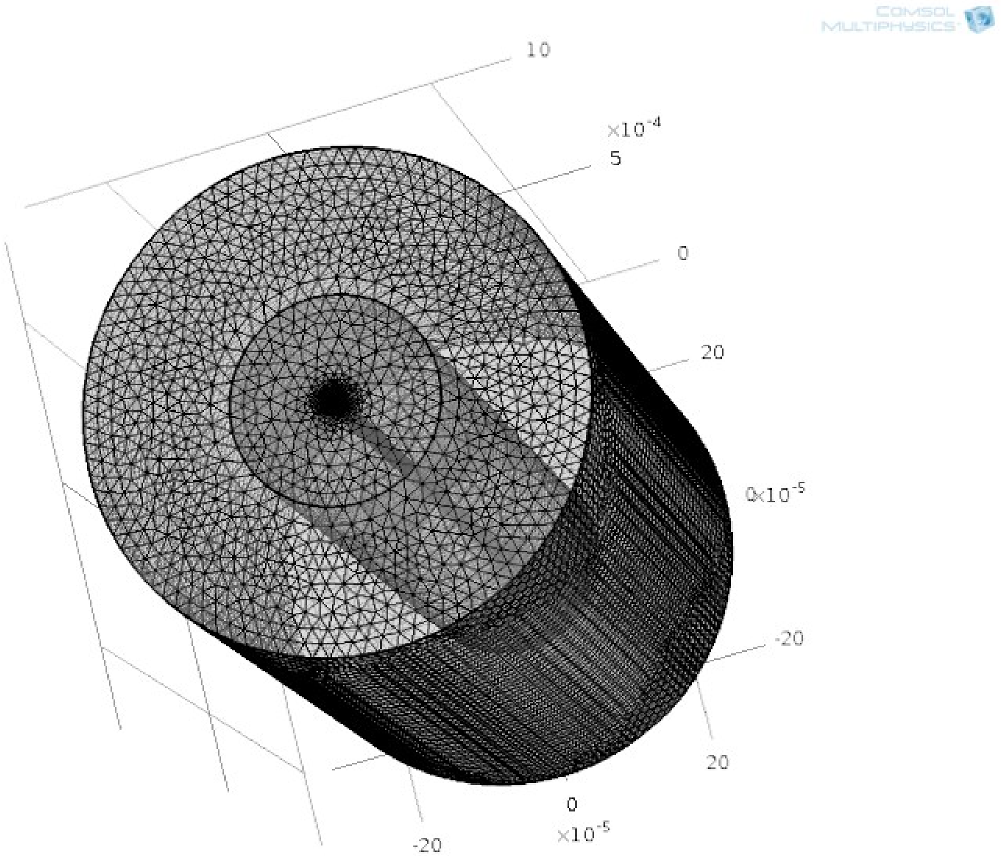

Figure 51 Finite element mesh for the three layer model. The inner layer is silica glass. The intermediate and outer layers are metals.

Table 10 Coefficients of thermal expansion for materials used in investigating the effects of increasing temperature on the strain distributions at the glass-metal 1 interface, and metal 1-metal 2 interface.

Material	Coefficient of Thermal Expansion α (ppm/K)
Silica glass	0.55
Metal 1 (Ni)	12.3
Metal 2 (AISI-SS)	17

The results from this simulation show that the first principal strains are dominantly in the azimuthal (circumferential) direction as shown in figures 52(a-b). Figures 53(a-b) and 54 (a-b) show that the second and third principal strains are predominantly in the axial (longitudinal) and radial directions, respectively. The azimuthal component is responsible for torsion stresses, while the axial and radial components are responsible for tensile and compressive stresses, in their respective directions.

It is important to note that while the both azimuthal and axial components contribute to slippage, and eventually delamination, is it understood that only the axial and radial strain components can affect the fiber sensor measurements. That is to say, the axial component at the glass-metal 1 interface will have a tensile effect on the fiber sensor, while the radial strain component will press on the fiber inwards, both straining the fiber sensor. This is a desirable effect for strain sensors, but not on temperature sensors.

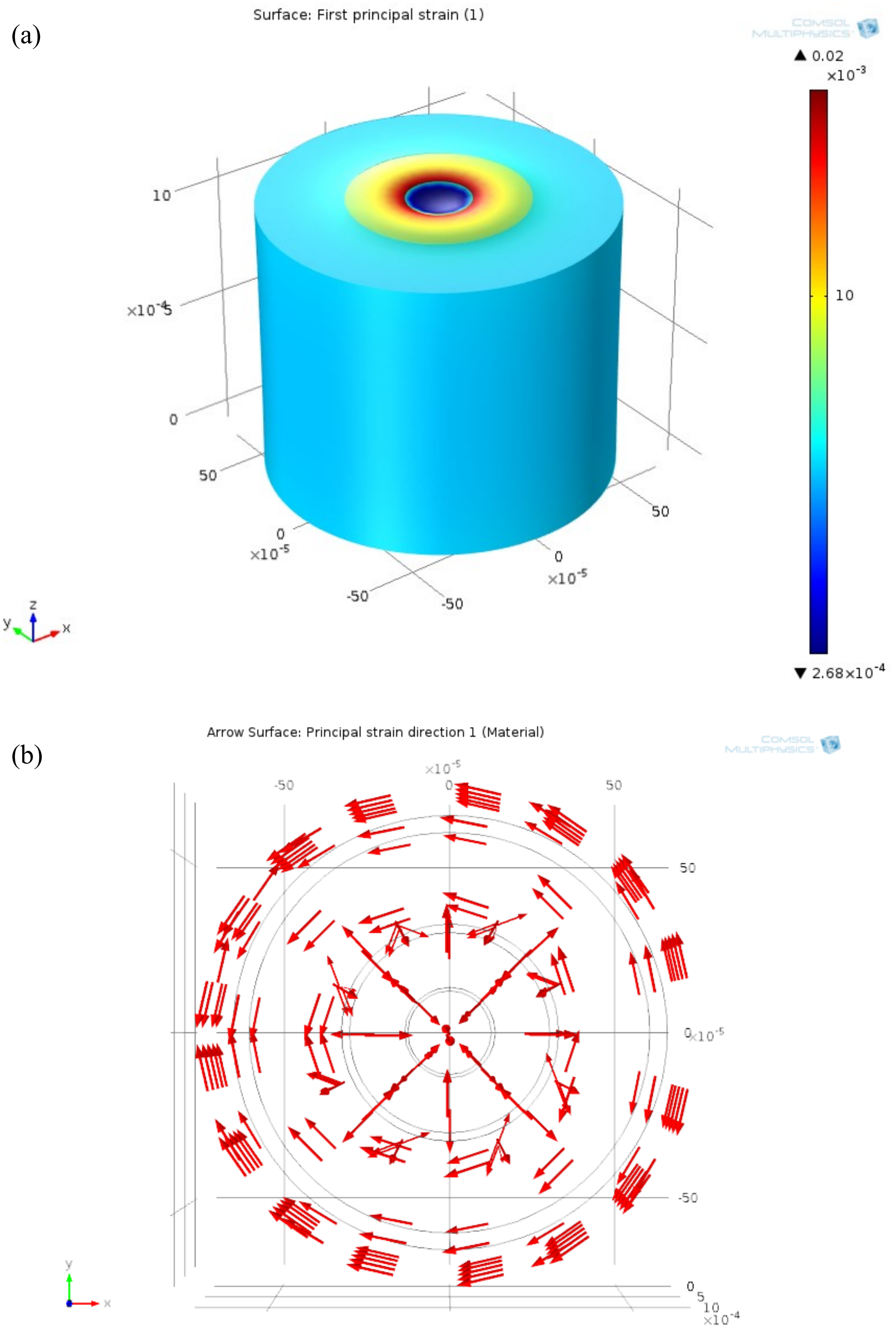

Figure 52 (a) First principal strain distribution simulated at constant temperature rise. (b) Vector representation of the azimuthally (circumferentially) dominant first principal strain.

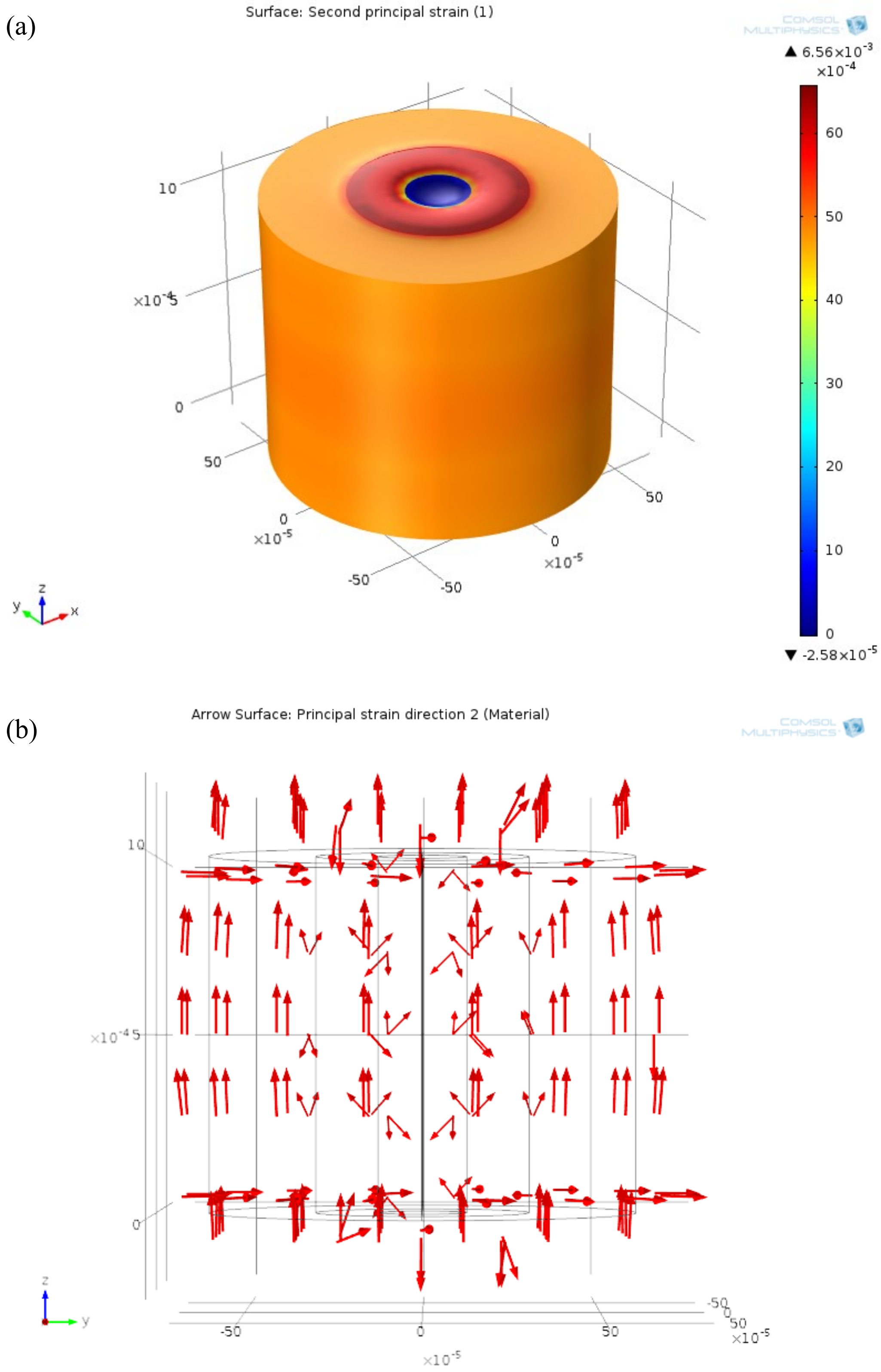

Figure 53 (a) Second principal strain distribution simulated at constant temperature rise. (b) Vector representation of the axially dominant second principal strain.

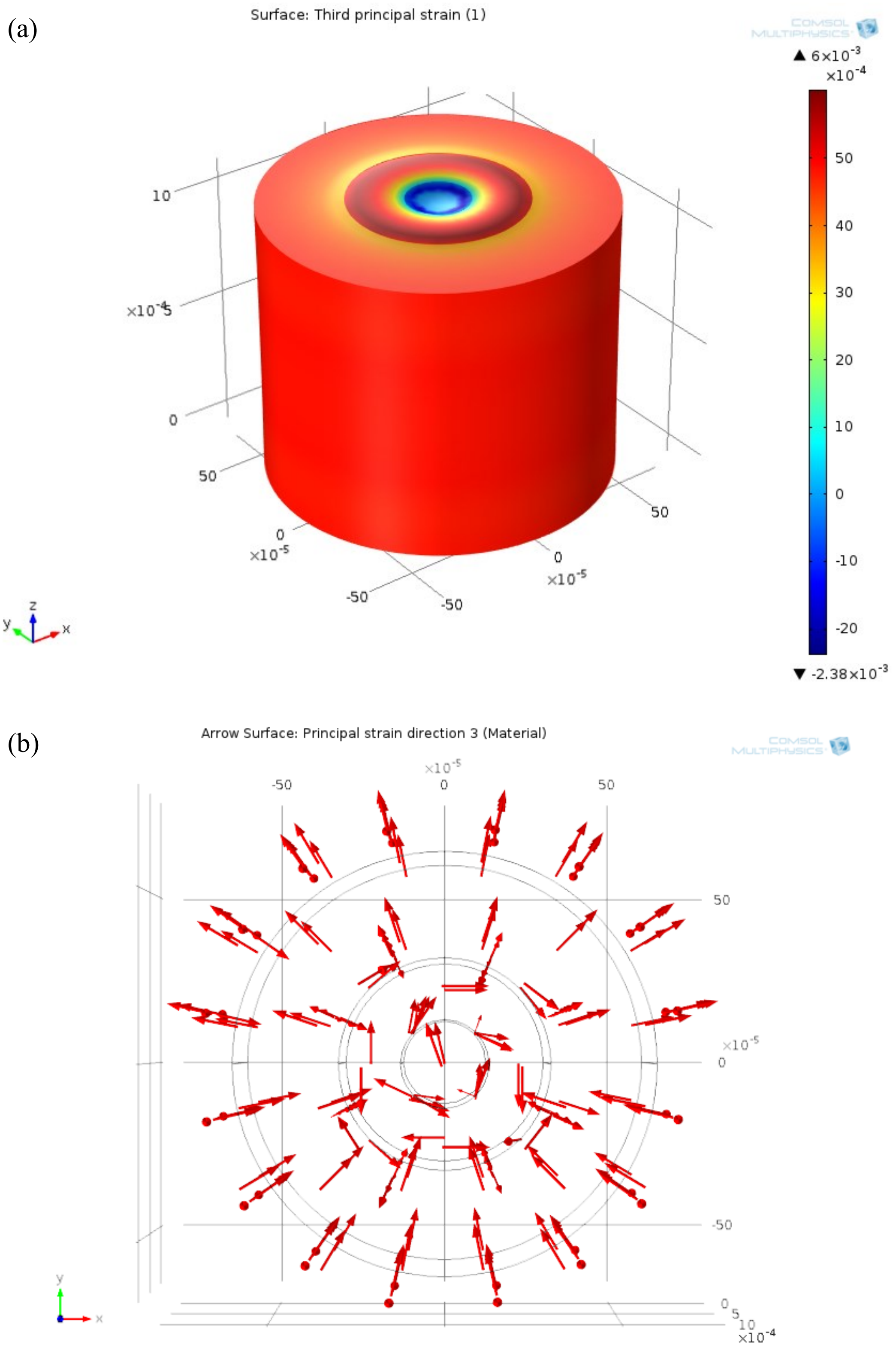

Figure 54 (a) Third principal strain distribution simulated at constant temperature rise. (b) Vector representation of the radially dominant third principal strain.

To test this understanding, the three-layer model was then used to calculate strains at the glass-metal 1 interface at different temperature elevations. The strain component in a general direction shown in figure 55(a) was resolved to the three principal directions; the azimuthal, axial, and radial directions. The first, second, and third principal strains are plotted in figures 55(b-d) at different temperature elevations with respect to room temperature (293.15 K). It is evident that the first principal strain in the azimuthal direction is approximately >2.44 times the axial and radial strain components. Moreover, the profile of the strain component in a general direction, and the dominant azimuthal strain peak from both tips where the glass fiber exits the metal-coated region. These profiles' shapes are completely identical to the profiles of the experimental testing on Invar-coated samples in figure 46(b).

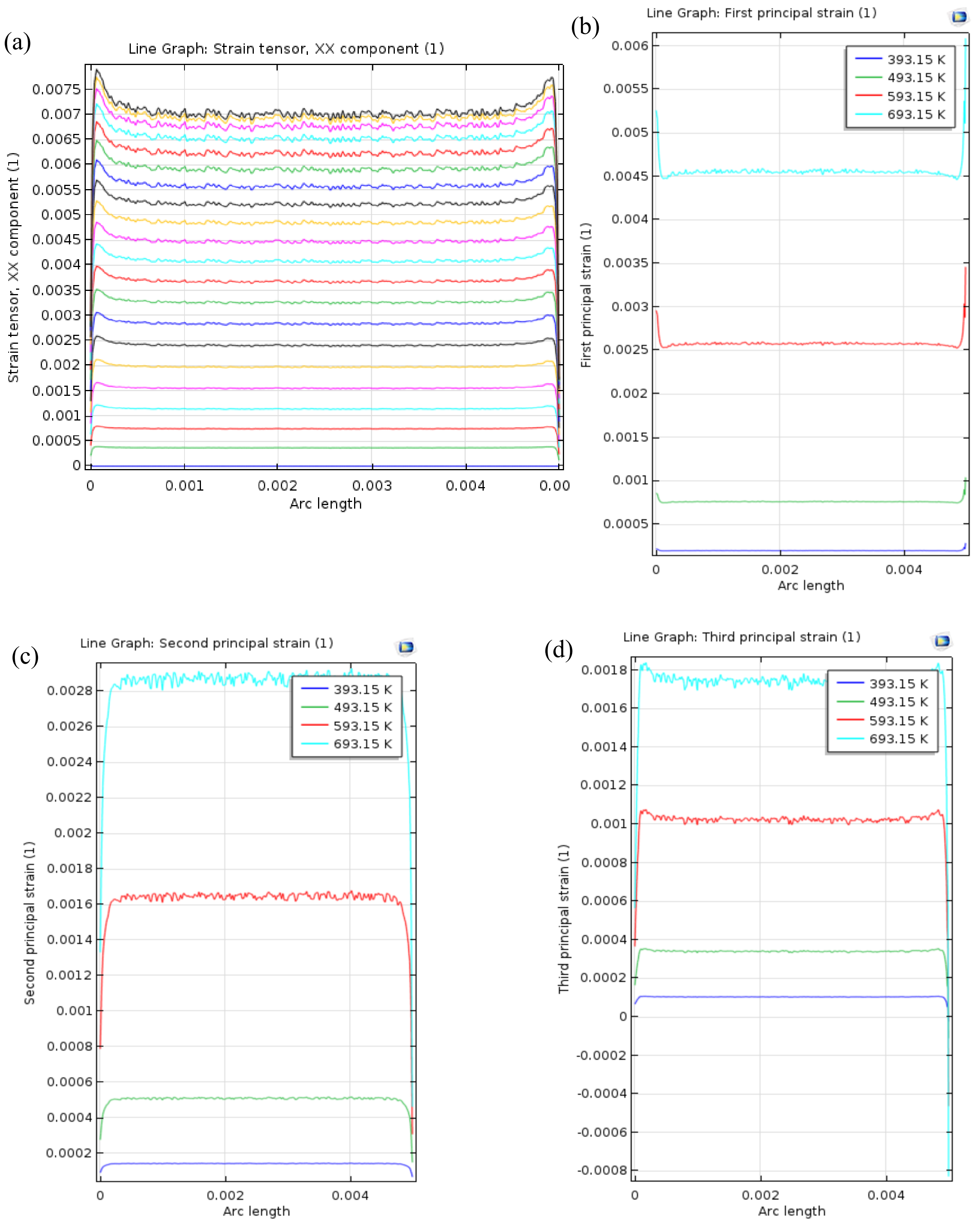

Figure 55 Strain components at a (a) general, (b) azimuthal, (c) axial, and (d) radial directions with respect to the glass-metal 1 interface simulated at different temperatures.

6.5.2 Effects of varying the CTE of the metallic coating layers

Using the simple three-layers of coaxial cylinders model, different permutations of CTE of the metallic coating layers were simulated, to determine the induced strain effects of varying the CTE of the both the intermediate and outer metallic encapsulations on the inner glass fiber. First, a parametric sweep was used to vary the CTE of the intermediate layer while keeping the CTE constant for both the inner (glass) and outer (stainless steel) layers. The results are shown in figure 56(a-c) for the first, second and third principal strains, respectively, at both interfaces between inner glass to intermediate metal 1 layers, and the intermediate metal 1 to outer metal 2 layers.

Figure 56(d) illustrates the first principal strain distributions on the glass-metal 1 and metal 1-metal 2 interfaces as the CTE for metal 1 was varied from 0.55 ppm/K (glass) to 17 ppm/K (metal 2). While the first principal strains are intuitively understood, where strains are minimal at an interface when the CTE of both layers are matched, the results for the second and third principal strains show that strains at both interfaces rise systematically by raising the coefficient of thermal expansion of the intermediate layer. The resolution from this is to minimize mismatch in the CTE between the inner and intermediate layers, that is designing an experiment that produces Ni:Fe concentration such that the CTE is minimized. However, there seems to be a residual strain that appears at the inner-intermediate interface even at zero mismatch in CTE of both materials.

(a) Predominantly in azimuthal direction

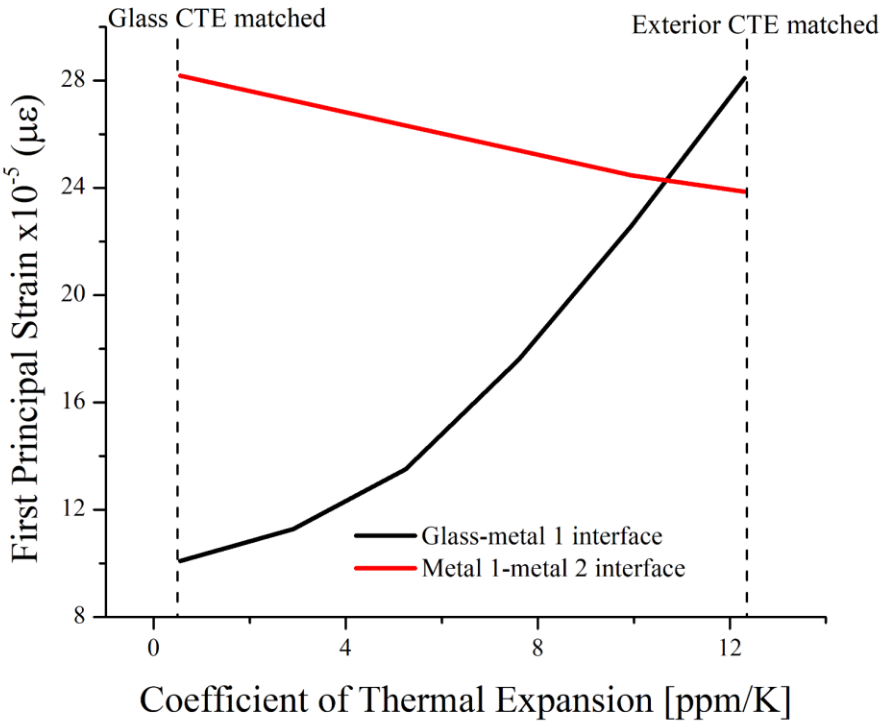

(b) Predominantly in axial direction

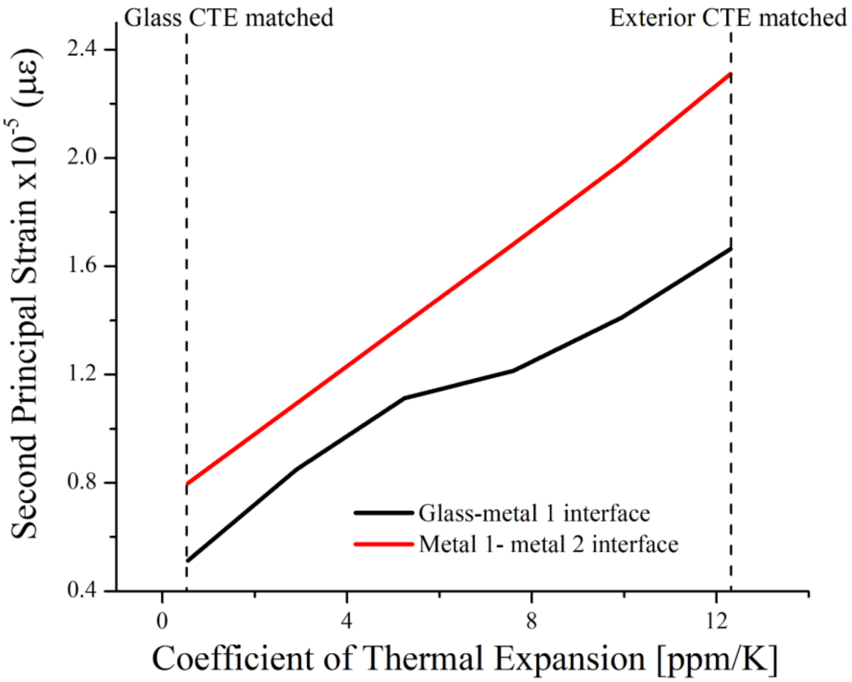

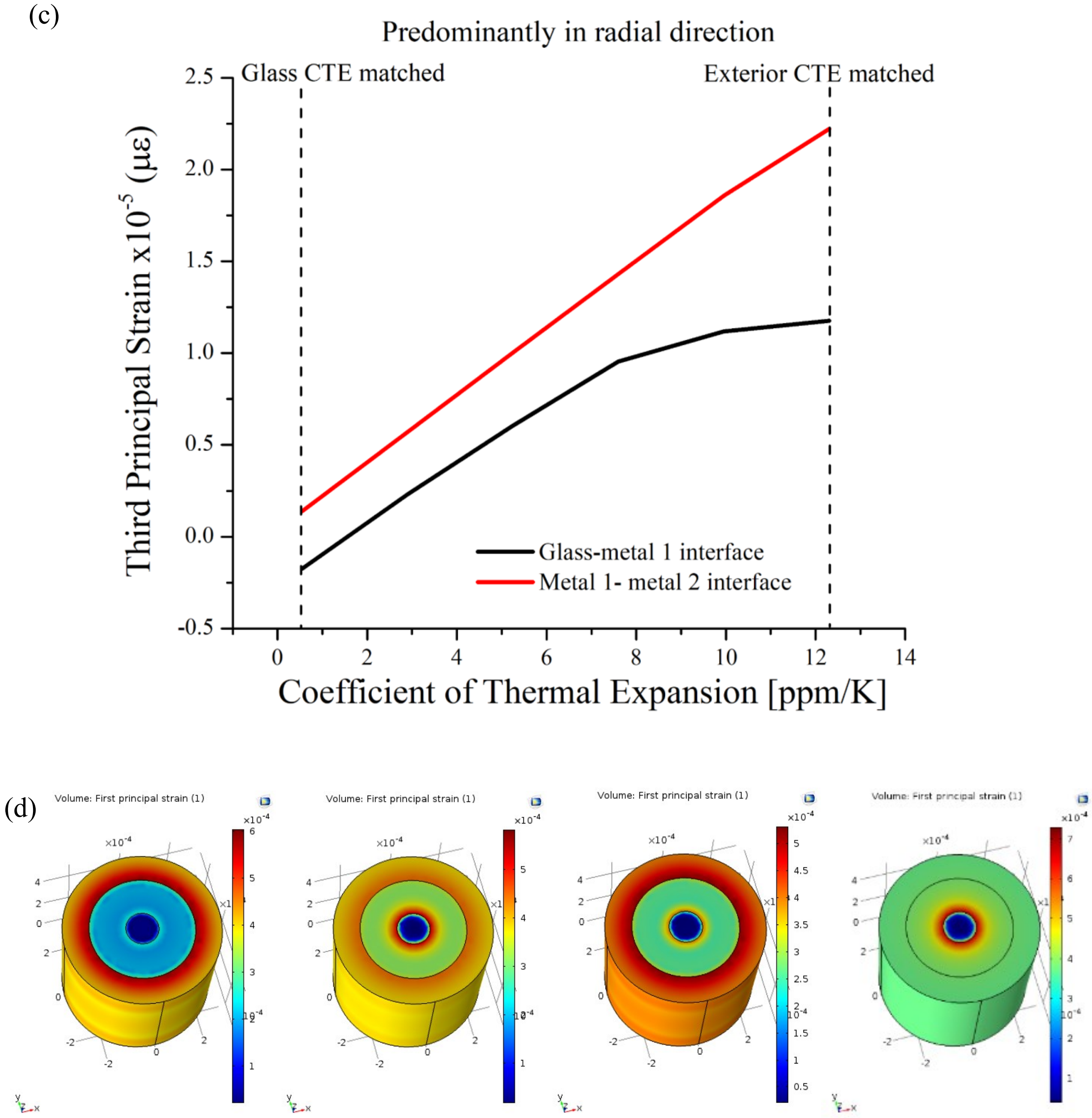

Figure 56 Effect of varying the CTE of the intermediate layer from glass value to stainless steel on the (a) first (azimuthal), (b) second (axial), and (c) third (radial) principal strains. The figures in (d) show how strain distribution gradually changes from low (high) strains at the inner (outer) interface at CTE match (mismatch), to from high (low) strains at the outer (inner) interface at CTE mismatch (match).

The parametric sweep simulations were extended to vary the CTE of the outer material to further study the strains induced at the two interfaces. The CTE was varied from 0.55 (that of the inner material) to 12.3 ppm/K with steps of ~1.95 ppm/K. For each value of the outer layer CTE, the CTE of the intermediate layer is similarly swept from 0.55 to 12.3 ppm/K. The azimuthal component of strains at the two interfaces is shown in figure 57(a), where each colored family of curves resemble a constant CTE of the outer layer. The plots shown assert that the magnitude of mismatch in CTE at an interface in proportional to the strains induced at the interface. These curves reveal further insight that the residual strains in the inner material are mostly dependent on the mismatch in CTE between the inner and outer materials, while the intermediate layer has almost no significance on such strains. The axial strains shown in figure 57(b) reveal low dependence on mismatch between inner and intermediate layers (lines within a band of one color) and high dependence on the mismatch between the outer and inner material's CTE (different colored bands).

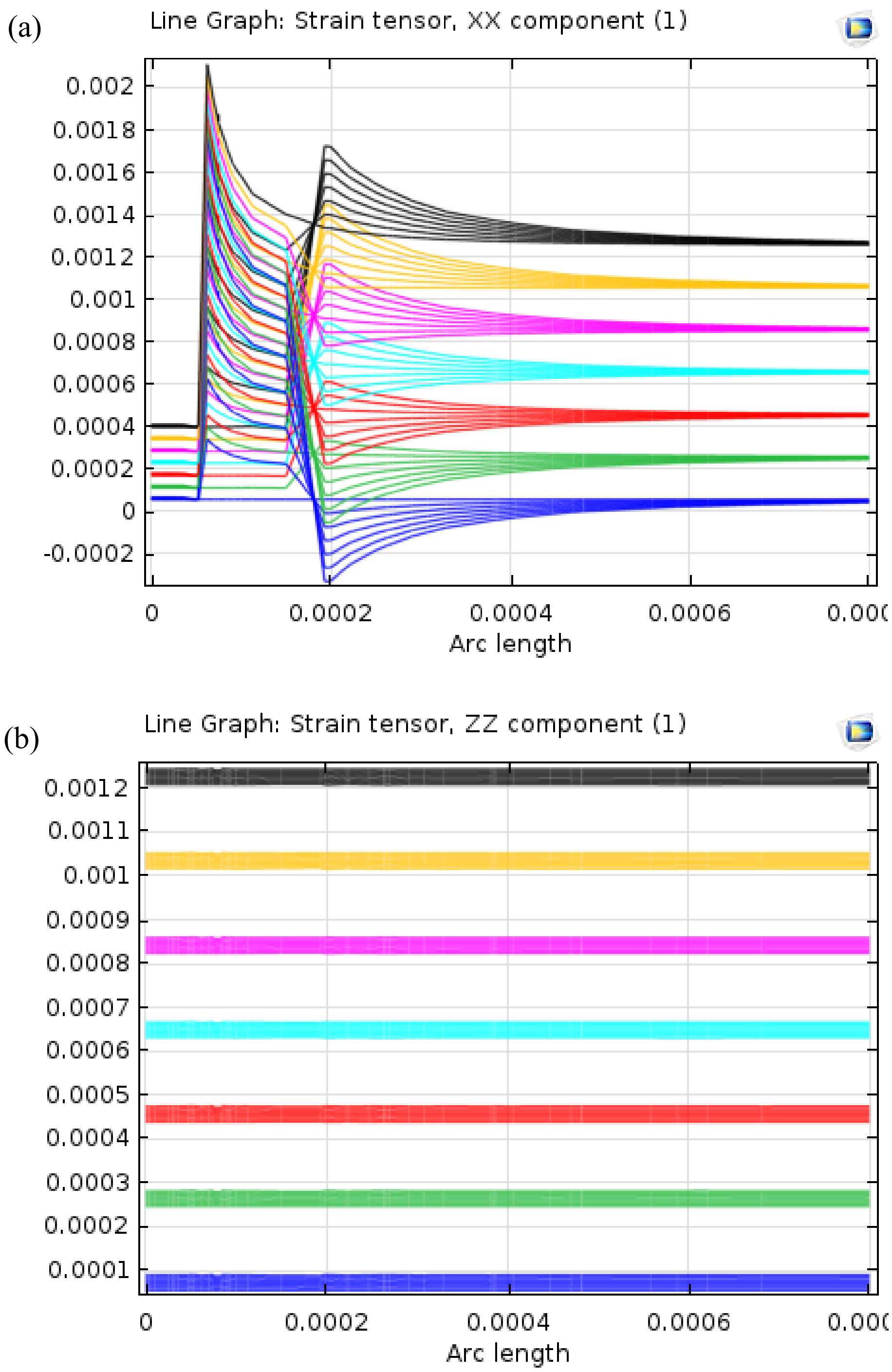

Figure 57 The effect of varying the CTE of both the intermediate and outer layers on the strain components in the (a) azimuthal, and (b) axial directions. Each color represents a CTE of the outer layer varied from 0.55 ppm/K (blue) to 12.3 ppm/K (black). Within a colored band, the CTE of the intermediate layer is varied similarly from 0.55 to 12.3 ppm/K.

6.5.3 Effects of varying the coating material

Three different materials; Invar, Ni, and Cu were attempted as coating materials for glass. The materials' CTE used for this run are shown in table 11. Strains on the glass-coating interface where obtained at different temperature elevations. The results in figure 58(a) reveal that invar is the best choice for coating glass, as it induces the least strains on glass compared to Ni and Cu. Upon adding a second encapsulating layer, to simulate stainless steel embedding, the results where changed to reveal that mismatch between stainless steel and the coating material can highly influence the choice of the coating material.

Upon embedding copper produced the best results (minimal strains), for there is no mismatch in CTE between copper and the chosen AISI stainless steel. Figure 58(b) illustrates, for embedding coated glass in stainless steel, Cu has bested Invar and Ni. Cu even induced less strains that coating with invar without embedding in stainless steel above ~300°C. The change in CTE of Invar around its Curie temperature explains the changes in the plot as the CTE of the Ni-Fe alloy is a function of temperature.

Table 11 Coefficients of thermal expansion for the materials used in investigating the effects of varying the coating material on the thermally induced strains at the glass-metal coating interface.

Material	Coefficient of Thermal Expansion α (ppm/K)
Silica glass	0.55
Ni	12.3
Cu and AISI-SS	17

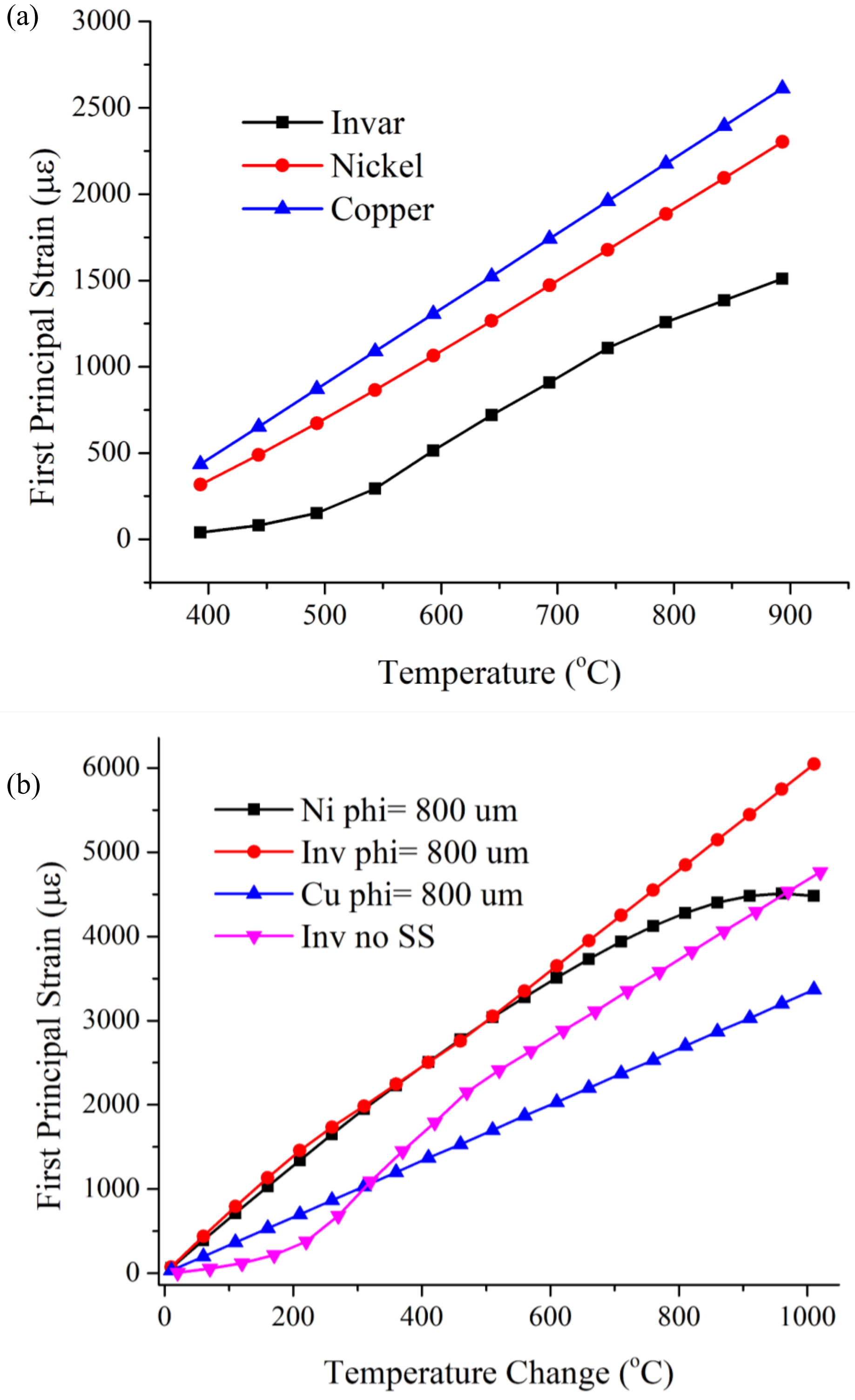

Figure 58 Simulated first principal strains induced at the glass/metal interface due to ramping up temperature both (a) before, and (b) after embedding in stainless steel.

6.5.4 Effects of varying the Young’s moduli of the surrounding metals

The three layer model was further used to run a parametric sweep where the Young’s (elastic) moduli of the intermediate and outer materials were varied. The thermally induced strains at the two interfaces were measured for a certain temperature rise. The results are shown in figures 59(a-b) following the same color depiction in the previous section with when CTE was swept. The amount of mismatch of Young’s moduli at both interfaces hardly affects the azimuthal and axial component of the induced strains at both interfaces, if for a mild perturbation at the outer layer. Hence, the elastic modulus is rather insignificant for the delamination problem.

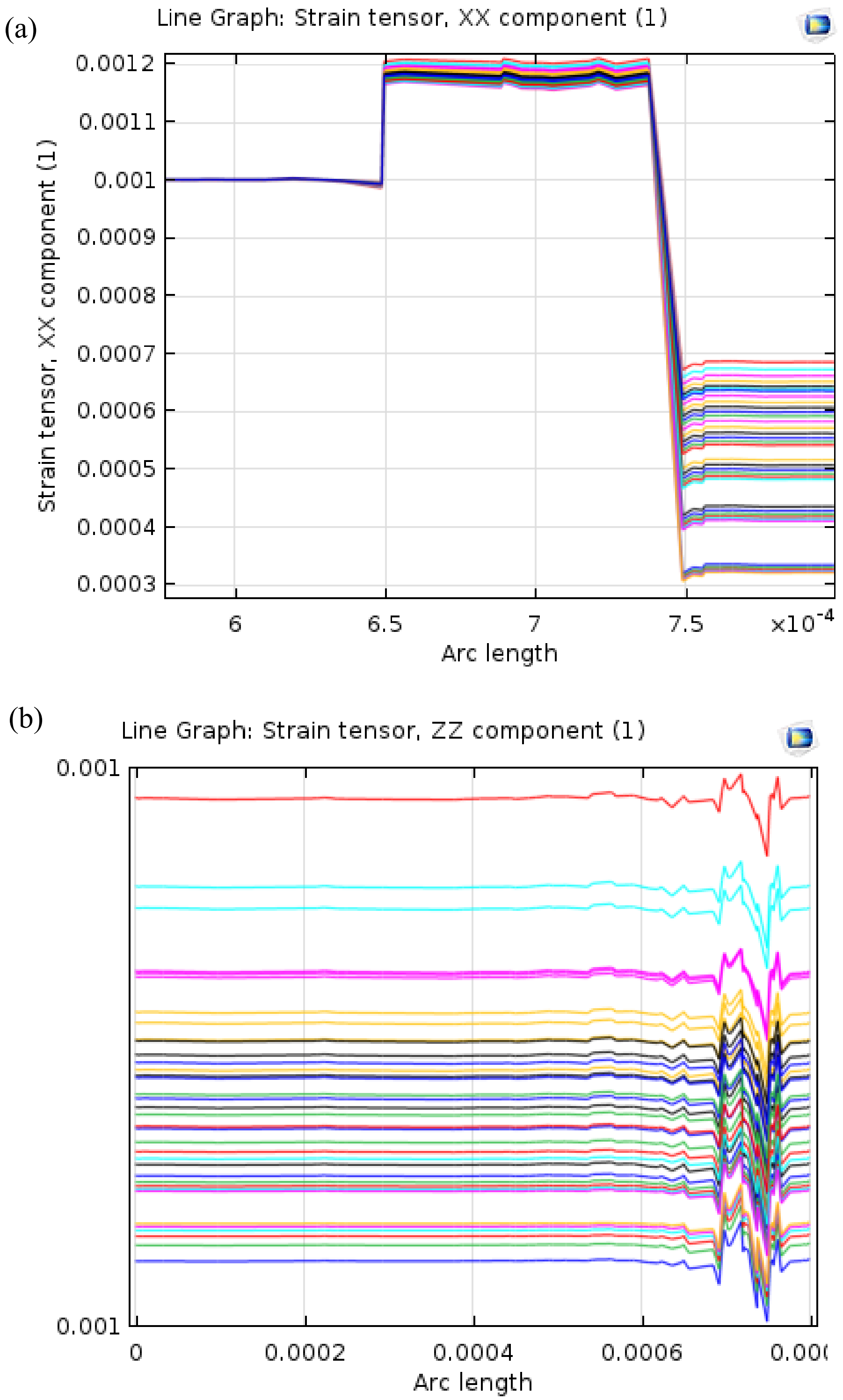

Figure 59 The induced strain effects of varying the modulus of elasticity of the intermediate and outer layers on the interfaces between glass and metal 1, and metal 1 and metal 2. The induced strains are plotted in the (a) azimuthal, and (b) axial components.

6.5.5 Effects of varying the thickness of the intermediate protective layer

Here a model where glass, 125 µm in diameter, is encapsulated by an Invar coating layer whose thickness was varied from 200 to 500 microns, with a 50 micron step. Different temperature elevations were swept while calculating the strains induced at the glass- metal interface. The results are given in figures 60(a-b). Increasing the coating thickness would slightly increase the principal strains induced at the glass-metal coating interface. This simulation was repeated using Cu coating, and although the strains induced are relatively higher in Cu, the behavior upon varying the thickness is somewhat the same.

While thicker metal coatings would better protect the fiber during embedding in a subsequent LENS or 3D printing process, the thickness must be optimized to minimize the residual strains induced on the sensor and for the fiber to survive embedding. Figures 61(a) and (b) show that increasing the thickness of the coating layer, at a constant rise in temperature, has a negligible effect on the azimuthal component of strain. This meant that the coating thickness was of less significance to the delamination problem than the CTE. Consequently, it was needed to sweep the CTE of the coating material at various coating thicknesses.

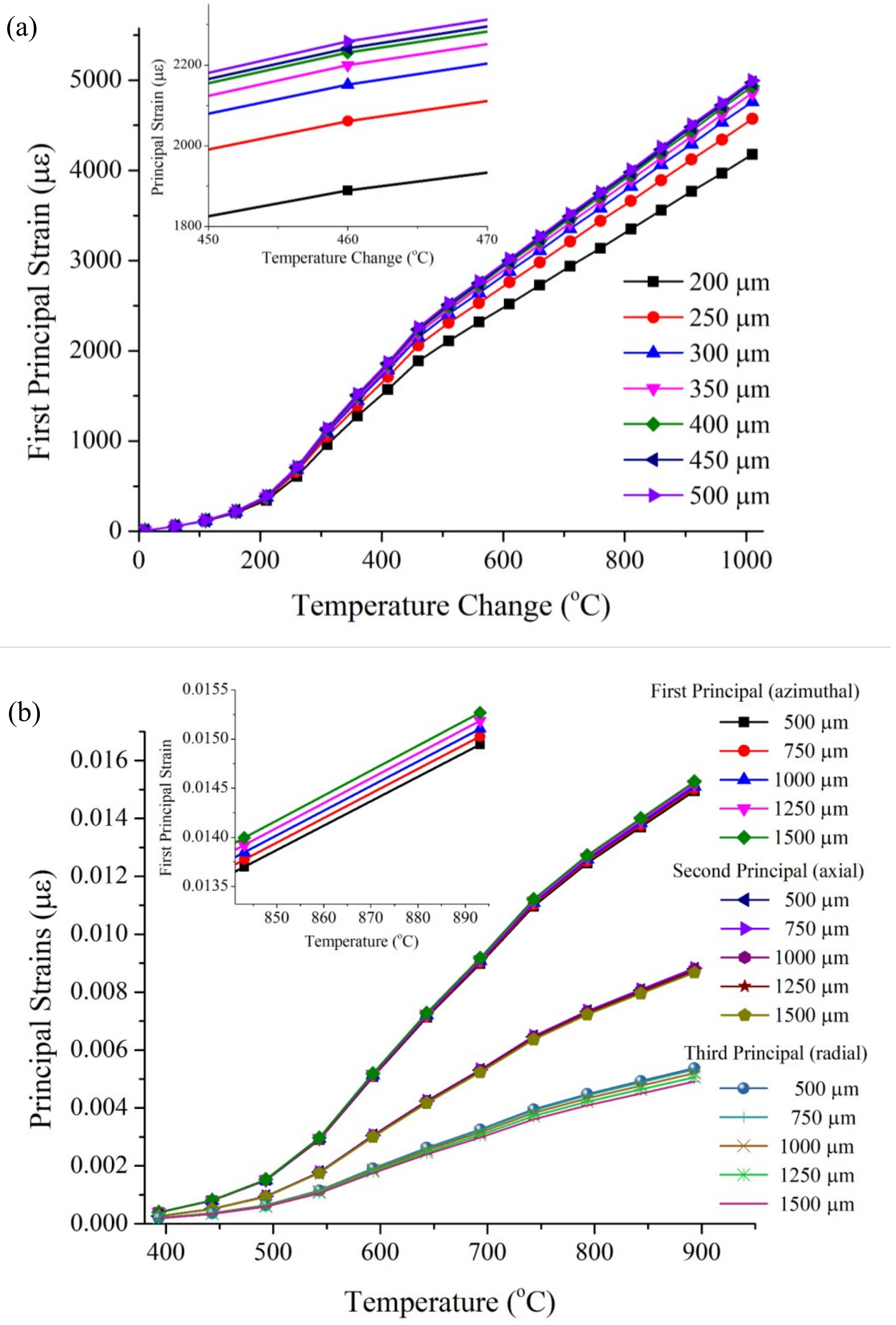

Figure 60 The induced first principal strains at the glass-metal interface at several thicknesses of Invar coating. (b) All three principal strains induced as Invar coating thickness was swept from 500 to 1500 μm. The insets in both figures are enlargements of the first principal strains.

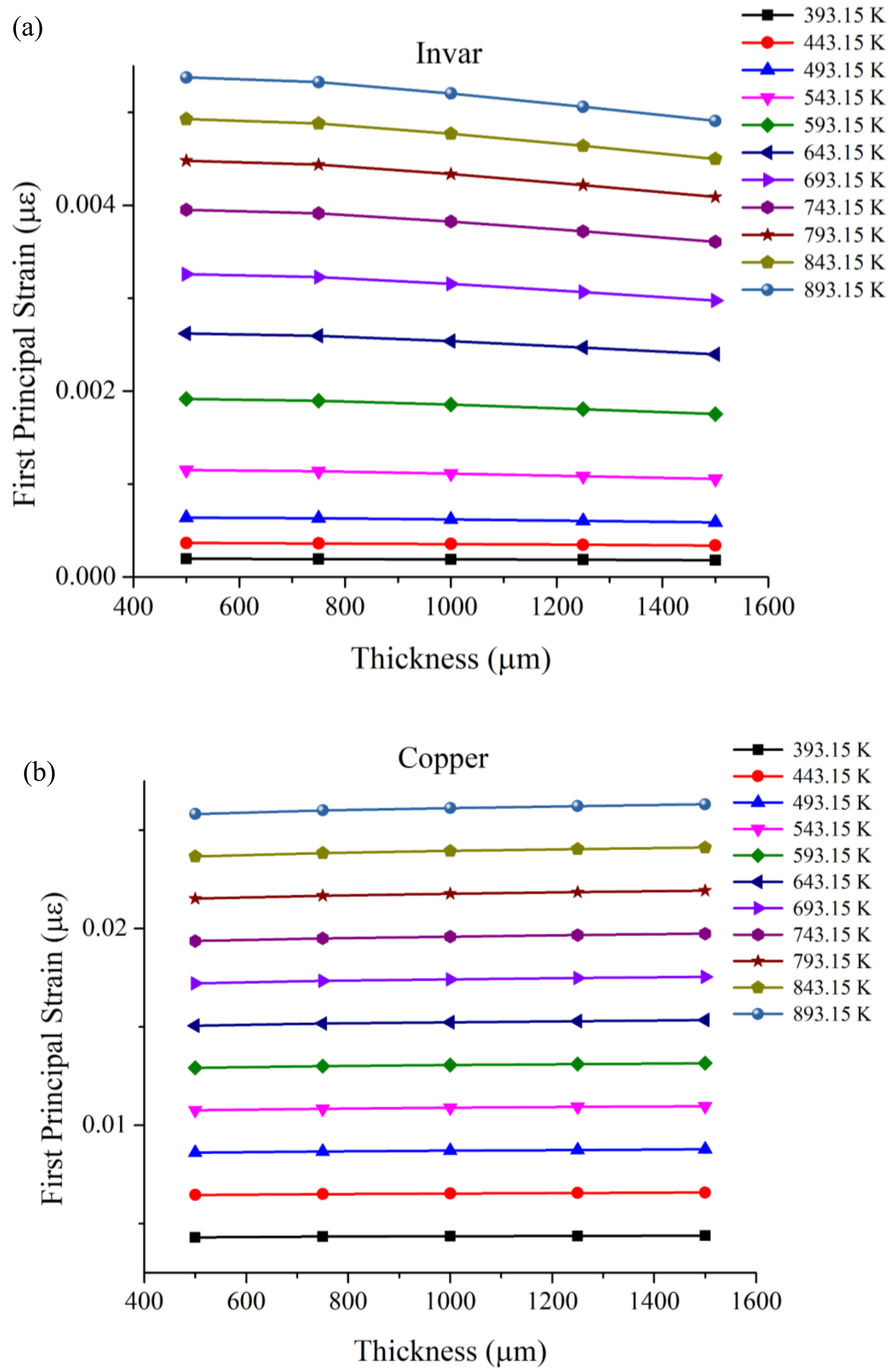

Figure 61 The effect of varying the thickness of the coating layer, at constant temperature rise, on the first principal strain induced at the glass- metal interface for (a) Invar-36, and (b) Cu coating materials.

In order to investigate the significance of varying the coating thickness with respect to varying the CTE, the embedded fiber was simulated at various intermediate layer thicknesses while also sweeping the CTE of both the intermediate and outer layers. The intermediate layer thickness was swept from 650 to 1100 µm, using steps of 50 µm. The intermediate layer's CTE was swept from 0.55 ppm/K to 12.3 ppm/K at each intermediate layer thick and each CTE of the outer layer. The latter's CTE was swept from 0.55 to 12.3 ppm/K, with steps of 1.95 ppm/K, as well. Figure 62(a) illustrates that varying the thickness intermediate coating layer would only result in shifted versions of the curves in figure 57(a).

The same can be observed about the curves in 62(b), which are not significantly different than the curves in figure 57(b). That is to say that the azimuthal and axial components of strain, which are the major cause for delamination, are hardly affected by the intermediate layer thickness compared to CTE mismatch at the glass-metal 1 and metal 1-metal 2 interfaces. The effect of varying the intermediate layer thickness seems to fade in comparison with varying the CTE, i.e., the CTE mismatch controls the amount of strain on glass-invar interface. Thickness of invar affects that too, but to a lesser extent.

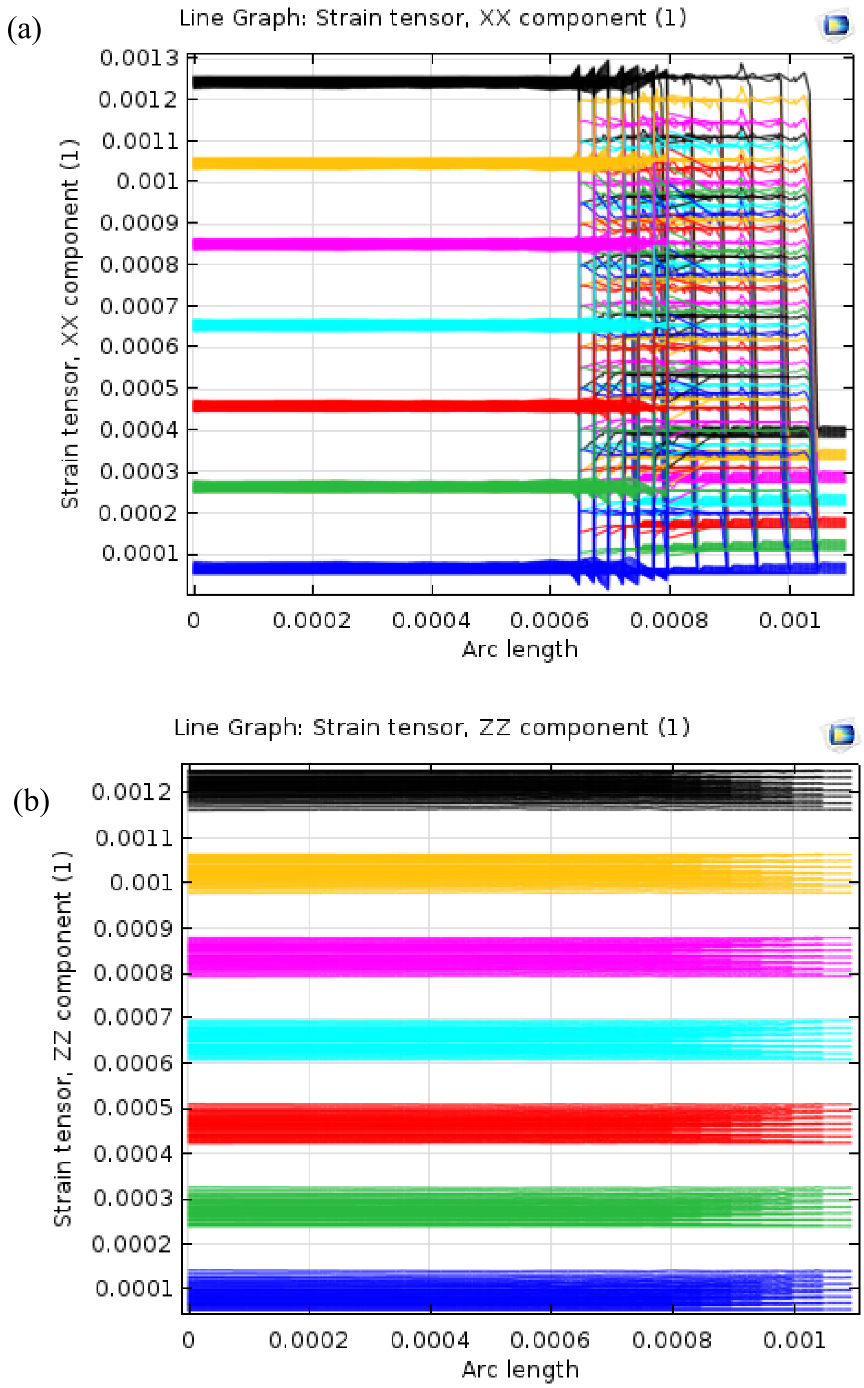

Figure 62 The (a) azimuthal, and (b) axial components of strains induced at the two interfaces between glass and metal 1, and metal 1 and metal 2. Each color represents a CTE of the outer layer varied from 0.55 ppm/K (blue) to 12.3 ppm/K (black). Within a colored band, the CTE of the intermediate layer was varied similarly from 0.55 to 12.3 ppm/K, and the thickness of the intermediate layer was varied from 650 to 1100 µm.

6.5.6 Effects of varying embedding layer thickness

Embedded glass fiber in AISI stainless steel was modelled. The glass cylinder was coated with 300 μm diameter of invar, then an external second layer of coating was used to simulate the SS embedding. Temperatures were varied at different outer layer thicknesses, sweeping the thickness parameter from 1 μm to 1200 μm. The induced strains on the inner-intermediate interface are plotted in figure 63. The plots show the elaborate difference between the case of no embedding and various embedding thicknesses. Also significantly higher strains are induced on the fiber-intermediate layer interface as thickness of the embedding layer is increased.

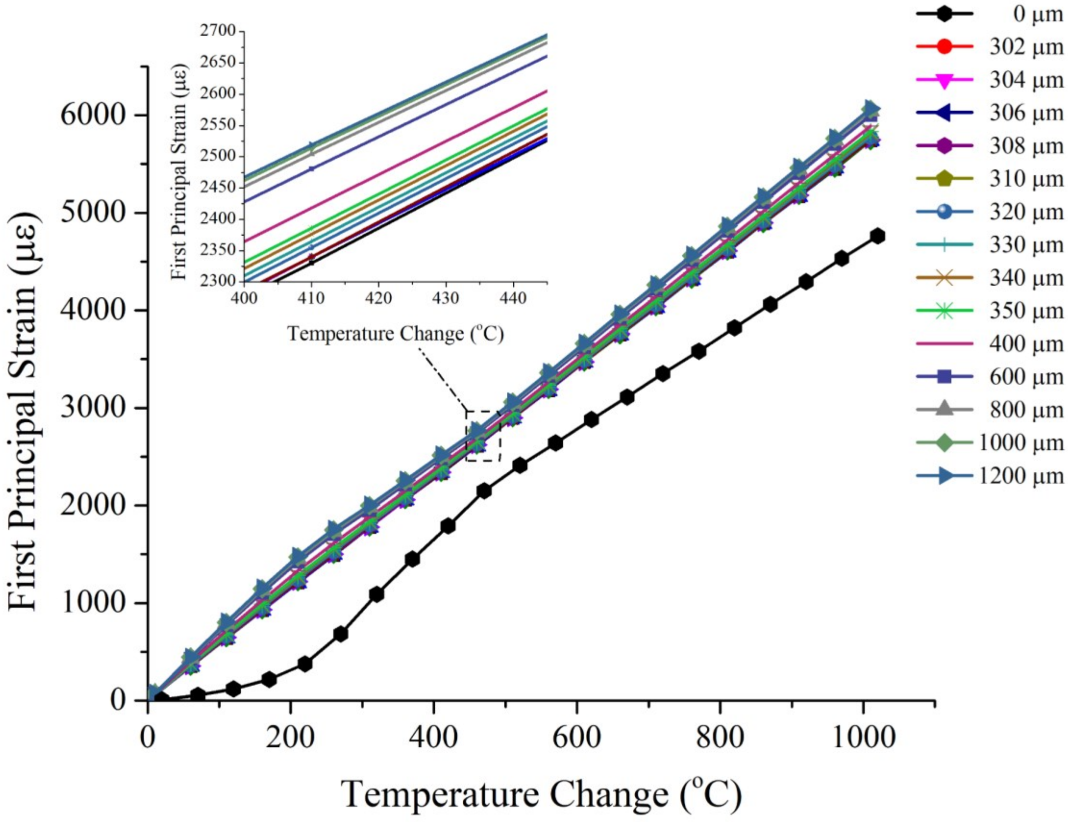

Figure 63 The azimuthal strains induced at the glass-intermediate layer interface increases upon increasing the thickness of the embedding SS layer. The inset is an enlarged view of the strains induced by the embedding SS layer.

6.5.7 Effects of varying the keying layer

Various simulations of very thin coatings were attempted to demonstrate the effect of different choices of keying layers that are primarily used to make the coating layer adhere to silica glass. In experiment, W and Cr were elements of choice. The problem simulating adhesion is three-fold. The keying layer is very thin compared to the coating and embedding layers. The keying layer is typically <50 nm in thickness, whereas the coating is layer is usually >300 μm according to [38]. This complicates the simulation as it is very difficult to simulate a mesh that has a part that is an order of magnitude greater than another part of the same mesh. The computational power for such calculation is still to exist. Secondly, the computational tool used utilizes classical physics equations for macro-scaled systems, and would not account for the small-scale effects. Thirdly, adhesion, or delamination for that matter, can not be simulated in such multi-physics packages. For the multi-physics packages do not recognize sub-atomic interactions. They only recognize mesh points and geometries, and use those along with material parameters and boundary conditions to calculate for the field at all mesh points using finite element approximated calculations. So, no matter what temperature rise is inflicted upon an interface with a mismatched CTE, the FE simulator will solve for the strains at the interface. Something that, in real experiment, would easily delaminate the interface. Unless, the researchers were able to formulate or come up with figures for the limits of adhesion between different material, this kind research will remain provisional, and tentative.

6.6 Conclusion of Fiber Embedding in Invar-36

Embedding of silica-based fiber have been attempted into metallic parts. Invar-36 has been chosen as protective coating material to mitigate the thermal strains induced upon the glass-metal interface upon rise in temperatures. If the strains are mitigated at said interface; slippage, delamination, or even breakage; can be deterred to more drastic temperature variations. FE computational tools has been utilized to simulate strains induced at the interfaces, specifically the glass-metal interface, to gain perspective and to help optimize the embedded sensor designs. Several parameters were swept at different temperature rises, to compute the strains at the interfaces of the embedded designs. Computations revealed that induced strains are highly affected by the choice of intermediate material, i.e., CTE of the coating layer.

Several implementations of fibers embedded into Invar-36 were tested in the tube furnaces reaching temperatures up to 800°C. The sensors showed signs of delamination at 350°C. Compared to previous work from Havermann et al [38], this sample had undergone delamination and slippage at a similar range of temperatures. Although the Invar-36 did not much deter delamination, the samples have survived and continued to function properly during post-delamination heat cycling. Furthermore, Invar-coated samples have proven repeatability and stable operation before delamination.

The mismatch in spectral shifts between Invar-coated and uncoated glass is an indication of the CTE mismatch between Invar-36 and glass. The electroplating procedure of the Invar alloy needed better finessing to engineer the optimal CTE according to the Ni: Fe composition in the deposited alloy. Nevertheless, the spectral deviation (38.73%) of both Invar-coated and uncoated optical fiber indicate that the CTE mismatch is less than an order of magnitude. This definitely is an improvement, compared to other embedding studies that involved embedding glass into other metals like copper and nickel. Other effects like the behavior of the sensor below, at, and above Curie temperature, need further investigation through careful experimental inspection and additional simulations.

The FE studies have provided deeper understanding of the embedding problem. Varying the thicknesses of the Invar-coating has shown very little effect on the induced strains at the glass-metal alloy interface. Both experimental and computational studies have agreed on that diminished effect. However, until interface strains are empirically characterized at the point of delamination, and the limits of adhesion be quantitated, computational studies cannot help further with studies of adhesion and delamination.

Bibliography

[1] S. Girard, J. Kuhnhenn, A. Gusarov, B. Brichard, M. Van Uffelen, Y. Ouerdane, A. Boukenter, and C. Marcandella, “Radiation effects on silica-based optical fibers: Recent advances and future challenges,” *IEEE Transactions on Nuclear Science,* vol. 60, no. 3, pp. 2015-2036, 2013.

[2] A. Yan, S. Huang, S. Li, R. Chen, Y. Huang, and K. Chen, "Ultrafast Laser Enhanced Rayleigh Scattering Characteristics in D-Shaped Fibers for High-Temperature Distributed Chemical Sensing," *OSA Technical Digest (online).* p. BTh4B.4.

[3] F. Berghmans, B. Brichard, A. F. Fernandez, A. Gusarov, M. Van Uffelen, and S. Girard, "An introduction to radiation effects on optical components and fiber optic sensors," *Optical waveguide sensing and imaging*, pp. 127-165: Springer, 2008.

[4] E. Friebele, “Optical fiber waveguides in radiation environments,” *Optical Engineering,* vol. 18, no. 6, pp. 186552, 1979.

[5] E. Friebele, C. Askins, M. Gingerich, and K. Long, “Optical fiber waveguides in radiation environments, II,” *Nuclear Instruments and Methods in Physics Research Section B: Beam Interactions with Materials and Atoms,* vol. 1, no. 2, pp. 355-369, 1984.

[6] T. Wijnands, L. K. De Jonge, J. Kuhnhenn, S. K. Hoeffgen, and U. Weinand, “Optical absorption in commercial single mode optical fibers in a high energy physics radiation field,” *IEEE Transactions on Nuclear Science,* vol. 55, no. 4, pp. 2216-2222, 2008.

[7] D. L. Griscom, “Radiation hardening of pure-silica-core optical fibers by ultra-high-dose γ-ray pre-irradiation,” *Journal of applied physics,* vol. 77, no. 10, pp. 5008-5013, 1995.

[8] B. Brichard, P. Borgermans, A. F. Fernandez, K. Lammens, and A. Decreton, “Radiation effect in silica optical fiber exposed to intense mixed neutron-gamma radiation field,” *IEEE Transactions on Nuclear Science,* vol. 48, no. 6, pp. 2069-2073, 2001.

[9] G. Berruti, M. Consales, M. Giordano, L. Sansone, P. Petagna, S. Buontempo, G. Breglio, and A. Cusano, “Radiation hard humidity sensors for high energy physics applications using polyimide-coated fiber Bragg gratings sensors,” *Sensors and Actuators B: Chemical,* vol. 177, pp. 94-102, 2013.

[10] F. Berghmans, A. F. Fernandez, B. Brichard, F. Vos, M. C. Decreton, A. I. Gusarov, O. Deparis, P. Megret, M. Blondel, and S. Caron, "Radiation hardness of fiber optic sensors for monitoring and remote handling applications in nuclear environments." pp. 28-40.

[11] A. Faustov, A. Gusarov, M. Wuilpart, A. Fotiadi, L. Liokumovich, I. Zolotovskiy, A. Tomashuk, T. de Schoutheete, and P. Megret, "Comparison of gamma-radiation induced attenuation in Al-doped, P-doped and Ge-doped fibres for dosimetry," *IEEE Transactions on Nuclear Science,* vol. 60, no. 4, pp. 2511-2517, 2013.

[12] D. K. Gifford, B. J. Soller, M. S. Wolfe, and M. E. Froggatt, "Distributed fiber-optic temperature sensing using Rayleigh backscatter." pp. 511-512.

[13] X. Bao, and L. Chen, "Recent progress in Brillouin scattering based fiber sensors," *Sensors,* vol. 11, no. 4, pp. 4152-4187, 2011.

[14] A. Motil, A. Bergman, and M. Tur, "State of the art of Brillouin fiber-optic distributed sensing," *Optics & Laser Technology,* vol. 78, pp. 81-103, 2016.

[15] T. Parker, M. Farhadiroushan, V. Handerek, and A. Rogers, "Temperature and strain dependence of the power level and frequency of spontaneous Brillouin scattering in optical fibers," *Optics letters,* vol. 22, no. 11, pp. 787-789, 1997.

[16] C. Lee, P. Chiang, and S. Chi, "Utilization of a dispersion-shifted fiber for simultaneous measurement of distributed strain and temperature through Brillouin frequency shift," *IEEE Photonics Technology Letters,* vol. 13, no. 10, pp. 1094-1096, 2001.

[17] M. Alahbabi, Y. Cho, and T. Newson, "Simultaneous temperature and strain measurement with combined spontaneous Raman and Brillouin scattering," *Optics letters,* vol. 30, no. 11, pp. 1276-1278, 2005.

[18] L. Zou, and O. M. Sezerman, "Method and system for simultaneous measurement of strain and temperature," Google Patents, 2009.

[19] Y. Weng, E. Ip, Z. Pan, and T. Wang, "Single-end simultaneous temperature and strain sensing techniques based on Brillouin optical time domain reflectometry in few-mode fibers," *Optics express,* vol. 23, no. 7, pp. 9024-9039, 2015.

[20] A. Li, Y. Wang, J. Fang, M.-J. Li, B. Y. Kim, and W. Shieh, “Few-mode fiber multi-parameter sensor with distributed temperature and strain discrimination,” *Optics letters,* vol. 40, no. 7, pp. 1488-1491, 2015.

[21] Y. Xu, M. Ren, Y. Lu, P. Lu, X. Bao, L. Wang, Y. Messaddeq, and S. LaRochelle, “Multi-parameter sensor based on stimulated Brillouin scattering in inverse-parabolic graded-index fiber,” *Optics letters,* vol. 41, no. 6, pp. 1138-1141, 2016.

[22] Y. Mizuno, N. Hayashi, H. Tanaka, Y. Wada, and K. Nakamura, “Brillouin scattering in multi-core optical fibers for sensing applications,” *Scientific reports,* vol. 5, 2015.

[23] Z. Zhao, Y. Dang, M. Tang, B. Li, L. Gan, S. Fu, H. Wei, W. Tong, P. Shum, and D. Liu, “Spatial-division multiplexed Brillouin distributed sensing based on a heterogeneous multicore fiber,” *Optics letters,* vol. 42, no. 1, pp. 171-174, 2017.

[24] W. Jin, W. C. Michie, G. Thursby, M. Konstantaki, and B. Culshaw, “Simultaneous measurement of strain and temperature: error analysis,” *Optical Engineering,* vol. 36, no. 2, pp. 598-610, 1997.

[25] P. Ferdinand, S. Magne, V. Dewynter-Marty, C. Martinez, S. Rougeault, and M. Bugaud, "Applications of Bragg grating sensors in Europe." p. OTuB1.

[26] S. J. Mihailov, “Fiber Bragg grating sensors for harsh environments,” *Sensors,* vol. 12, no. 2, pp. 1898-1918, 2012.

[27] A. Gusarov, and S. K. Hoeffgen, “Radiation effects on fiber gratings,” *IEEE Transactions on Nuclear Science,* vol. 60, no. 3, pp. 2037-2053, 2013.

[28] A. F. Fernandez, A. I. Gusarov, S. Bodart, K. Lammens, F. Berghmans, M. Decre, P. Me, M. Blondel, and A. Delchambre, “Temperature monitoring of nuclear reactor cores with multiplexed fiber Bragg grating sensors,” *Optical Engineering,* vol. 41, no. 6, pp. 1246-1254, 2002.

[29] A. Gusarov, A. F. Fernandez, S. Vasiliev, O. Medvedkov, M. Blondel, and F. Berghmans, “Effect of gamma–neutron nuclear reactor radiation on the properties of Bragg gratings written in photosensitive Ge-doped optical fiber,” *Nuclear Instruments and Methods in Physics Research Section B: Beam Interactions with Materials and Atoms,* vol. 187, no. 1, pp. 79-86, 2002.

[30] A. Gusarov, “Long-term exposure of fiber Bragg gratings in the BR1 low-flux nuclear reactor,” *IEEE Transactions on Nuclear Science,* vol. 57, no. 4, pp. 2044-2048, 2010.

[31] A. F. Fernandez, A. Gusarov, B. Brichard, M. Decréton, F. Berghmans, P. Mégret, and A. Delchambre, “Long-term radiation effects on fibre Bragg grating temperature sensors in a low flux nuclear reactor,” *Measurement Science and Technology,* vol. 15, no. 8, pp. 1506, 2004.

[32] A. F. Fernandez, B. Brichard, F. Berghmans, and M. Decreton, “Dose-rate dependencies in gamma-irradiated fiber Bragg grating filters,” *IEEE Transactions on Nuclear Science,* vol. 49, no. 6, pp. 2874-2878, 2002.

[33] A. Gusarov, F. Berghmans, A. F. Fernandez, O. Deparis, Y. Defosse, D. Starodubov, M. Decreton, P. Mégret, and M. Bondel, “Behavior of fibre Bragg gratings under high total dose gamma radiation,” *IEEE Transactions on Nuclear Science,* vol. 47, no. 3, pp. 688-692, 2000.

[34] A. Gusarov, F. Berghmans, O. Deparis, A. F. Fernandez, Y. Defosse, P. Mégret, M. Decréton, and M. Blondel, “High total dose radiation effects on temperature sensing fiber Bragg gratings,” *IEEE Photonics technology letters,* vol. 11, no. 9, pp. 1159-1161, 1999.

[35] R. S. Fielder, D. Klemer, and K. L. Stinson-Bagby, "High neutron fluence survivability testing of advanced fiber Bragg grating sensors." pp. 650-657.

[36] L. Remy, G. Cheymol, A. Gusarov, A. Morana, E. Marin, and S. Girard, “Compaction in optical fibres and fibre Bragg gratings under nuclear reactor high neutron and gamma fluence,” *IEEE Transactions on Nuclear Science,* vol. 63, no. 4, pp. 2317-2322, 2016.

[37] S. E. Baldini, D. J. Tubbs, and W. A. Stange, "Embedding fiber optic sensors in titanium matrix composites." pp. 162-169.

[38] D. Havermann, J. Mathew, W. N. MacPherson, R. R. Maier, and D. P. Hand, “Temperature and strain measurements with fiber Bragg gratings embedded in stainless steel 316,” *Journal of Lightwave Technology,* vol. 33, no. 12, pp. 2474-2479, 2015.

[39] R. Maier, D. Havermann, O. Schneller, J. Mathew, D. Polyzos, W. MacPherson, and D. Hand, "Optical fibre sensing in metals by embedment in 3D printed metallic structures." p. 915707.

[40] X. C. Li, F. Prinz, and J. Seim, “Thermal behavior of a metal embedded fiber Bragg grating sensor,” *Smart materials and structures,* vol. 10, no. 4, pp. 575, 2001.

[41] V. Guilbaud-Massereau, A. Celerier, and J. Machet, “Study and improvement of the adhesion of chromium thin films deposited by magnetron sputtering,” *Thin Solid Films,* vol. 258, no. 1-2, pp. 185-193, 1995.

[42] M. Lezius, K. Predehl, W. Stower, A. Turler, M. Greiter, C. Hoeschen, P. Thirolf, W. Assmann, D. Habs, and A. Prokofiev, “Radiation induced absorption in rare earth doped optical fibers,” *IEEE Transactions on Nuclear Science,* vol. 59, no. 2, pp. 425-433, 2012.

[43] K. W. Bennett, and J. Koh, "Aluminum doped optical fiber," Google Patents, 2010.

[44] S. Girard, B. Tortech, E. Regnier, M. Van Uffelen, A. Gusarov, Y. Ouerdane, J. Baggio, P. Paillet, V. Ferlet-Cavrois, and A. Boukenter, “Proton-and gamma-induced effects on erbium-doped optical fibers,” *IEEE transactions on nuclear science,* vol. 54, no. 6, pp. 2426-2434, 2007.

[45] B. Brichard, A. Fernandez Fernandez, H. Ooms, and F. Berghmans, "Study of the radiation-induced optical sensitivity in erbium and aluminium doped fibres." p. 35.

[46] T.-S. Peng, Y.-C. Hsieh, L. A. Wang, W.-C. Chiou, and R.-Y. Liu, "Effects of aluminum doping concentrations on radiation sensitivity of erbium-doped fibers." pp. 77534K-77534K-4.

[47] J. Wang, M.-j. Li, and D. A. Nolan, "The Lowest-loss of 0.35 dB/km in an Aluminum-doped SM Optical Fiber." p. 3 pp.

[48] M. E. Froggatt, D. K. Gifford, S. Kreger, M. Wolfe, and B. J. Soller, “Characterization of polarization-maintaining fiber using high-sensitivity optical-frequency-domain reflectometry,” *Journal of lightwave technology,* vol. 24, no. 11, pp. 4149-4154, 2006.

[49] M. A. Zaghloul, A. Yan, R. Chen, M.-J. Li, R. Flammang, M. Heibel, and K. P. Chen, “High Spatial Resolution Radiation Detection Using Distributed Fiber Sensing Technique,” *IEEE Transactions on Nuclear Science,* vol. 64, no. 9, pp. 2569-2577, 2017.

[50] A. Ramsey, W. Tighe, J. Bartolick, and P. Morgan, “Radiation effects on heated optical fibers,” *Review of scientific instruments,* vol. 68, no. 1, pp. 632-635, 1997.

[51] D. P. Hawn, C. M. Petrie, T. E. Blue, and W. Windl, “In-situ gamma radiation induced attenuation in silica optical fibers heated up to 600 C,” *Journal of Non-Crystalline Solids,* vol. 379, pp. 192-200, 2013.

[52] M. Van Uffelen, “Modelisation de systemes d'acquisition et de transmission a fibres optiques destines a fonctionner en environnement nuclaire,” Paris 11, 2001.

[53] S. Girard, J. Keurinck, Y. Ouerdane, J.-P. Meunier, and A. Boukenter, “Gamma-rays and pulsed X-ray radiation responses of germanosilicate single-mode optical fibers: influence of cladding codopants,” *Journal of Lightwave Technology,* vol. 22, no. 8, pp. 1915, 2004.

[54] B. J. Hoover, M.-J. Li, and S. Li, "Two-core optical fibers for distributed fiber sensors and systems," Google Patents, 2017.

[55] M.-J. Li, S. Li, J. A. Derick, J. S. Stone, B. C. Chow, K. W. Bennett, and D. M. Sutherlin, "Dual core optical fiber for distributed Brillouin fiber sensors." p. AW4I. 3.

[56] K. P. Chen, M. Zaghloul, and M.-J. Li, "Dual-Core Fiber Characterizations for Distributed Simultaneous Temperature and Strain Measurements Using Brillouin Optical Time Domain Analysis." p. W4A. 32.

[57] M. A. Zaghloul, M. Wang, G. Milione, M.-J. Li, S. Li, Y.-K. Huang, T. Wang, and K. P. Chen, “Discrimination of Temperature and Strain in Brillouin Optical Time Domain Analysis Using a Multicore Optical Fiber,” *Sensors,* vol. 18, no. 4, pp. 1176, 2018.

[58] E. Ip, G. Milione, M.-J. Li, N. Cvijetic, K. Kanonakis, J. Stone, G. Peng, X. Prieto, C. Montero, and V. Moreno, “SDM transmission of real-time 10GbE traffic using commercial SFP+ transceivers over 0.5 km elliptical-core few-mode fiber,” *Optics express,* vol. 23, no. 13, pp. 17120-17126, 2015.

[59] G. Milione, E. Ip, Y.-K. Huang, P. Ji, T. Wang, M.-J. Li, J. Stone, and G. Peng, "1.2-Tb/s MIMO-less transmission over 1 km of four-core elliptical-core few-mode fiber with 125-μm diameter cladding." pp. 1-3.

[60] G. Milione, E. Ip, M.-J. Li, J. Stone, G. Peng, and T. Wang, “Mode crosstalk matrix measurement of a 1 km elliptical core few-mode optical fiber,” *Optics letters,* vol. 41, no. 12, pp. 2755-2758, 2016.

[61] G. Milione, P. Ji, E. Ip, M.-J. Li, J. Stone, and G. Peng, "Real-time Bi-directional 10GbE Transmission using MIMO-less Space-division-multiplexing with Spatial Modes." pp. 1-3.

[62] A. Morana, S. Girard, E. Marin, C. Marcandella, S. Rizzolo, J. Périsse, J.-R. Macé, A. Taouri, A. Boukenter, and M. Cannas, “Radiation vulnerability of fiber Bragg gratings in harsh environments,” *Journal of Lightwave Technology,* vol. 33, no. 12, pp. 2646-2651, 2015.

[63] A. Cusano, A. Cutolo, and J. Albert, *Fiber Bragg grating sensors: recent advancements, industrial applications and market exploitation*: Bentham Science Publishers, 2011.

[64] H. Henschel, J. Kuhnhenn, and U. Weinand, "High radiation hardness of a hollow core photonic bandgap fiber." pp. LN4-1-LN4-4.

[65] M. A. Zaghloul, M. Wang, S. Huang, C. Hnatovsky, D. Grobnic, S. Mihailov, M.-J. Li, D. Carpenter, L.-W. Hu, and J. Daw, “Radiation resistant fiber Bragg grating in random air-line fibers for sensing applications in nuclear reactor cores,” *Optics express,* vol. 26, no. 9, pp. 11775-11786, 2018.

[66] S. J. Mihailov, C. Hnatovsky, D. Grobnic, K. Chen, and M.-J. Li, “Fabrication of Bragg Gratings in Random Air-Line Clad Microstructured Optical Fiber,” *IEEE Photonics Technology Letters,* vol. 30, no. 2, pp. 209-212, 2018.

[67] S. J. Mihailov, D. Grobnic, H. Ding, C. W. Smelser, and J. Broeng, “Femtosecond IR laser fabrication of Bragg gratings in photonic crystal fibers and tapers,” *IEEE Photonics Technology Letters,* vol. 18, no. 17, pp. 1837-1839, 2006.

[68] S. J. Mihailov, C. W. Smelser, D. Grobnic, R. B. Walker, P. Lu, H. Ding, and J. Unruh, “Bragg gratings written in all-SiO2 and Ge-doped core fibers with 800-nm femtosecond radiation and a phase mask,” *Journal of Lightwave Technology,* vol. 22, no. 1, pp. 94, 2004.

[69] C. W. Smelser, S. J. Mihailov, and D. Grobnic, “Formation of Type I-IR and Type II-IR gratings with an ultrafast IR laser and a phase mask,” *Optics express,* vol. 13, no. 14, pp. 5377-5386, 2005.

[70] C. Hnatovsky, R. Taylor, P. Rajeev, E. Simova, V. Bhardwaj, D. Rayner, and P. Corkum, “Pulse duration dependence of femtosecond-laser-fabricated nanogratings in fused silica,” *Applied Physics Letters,* vol. 87, no. 1, pp. 014104, 2005.

[71] P. Lu, S. J. Mihailov, H. Ding, D. Grobnic, R. B. Walker, D. Coulas, C. Hnatovsky, and A. Y. Naumov, “Plane-by-plane inscription of grating structures in optical fibers,” *Journal of Lightwave Technology,* vol. 36, no. 4, pp. 926-931, 2018.

[72] P. Lu, S. Mihailov, H. Ding, D. Grobnic, R. Walker, D. Coulas, C. Hnatovsky, and A. Naumov, "Plane-by-plane inscription of grating structures in optical fibers." pp. 1-4.

[73] S. Hochreiter, and J. Schmidhuber, “Long short-term memory,” *Neural computation,* vol. 9, no. 8, pp. 1735-1780, 1997.

[74] E. Bricchi, and P. G. Kazansky, “Extraordinary stability of anisotropic femtosecond direct-written structures embedded in silica glass,” *Applied physics letters,* vol. 88, no. 11, pp. 111119, 2006.

[75] S. Richter, M. Heinrich, S. Döring, A. Tünnermann, S. Nolte, and U. Peschel, “Nanogratings in fused silica: Formation, control, and applications,” *Journal of Laser Applications,* vol. 24, no. 4, pp. 042008, 2012.

[76] J. Zhang, M. Gecevičius, M. Beresna, and P. G. Kazansky, “Seemingly unlimited lifetime data storage in nanostructured glass,” *Physical review letters,* vol. 112, no. 3, pp. 033901, 2014.

[77] Y. Xu, P. Lu, S. Gao, D. Xiang, P. Lu, S. Mihailov, and X. Bao, “Optical fiber random grating-based multiparameter sensor,” *Optics Letters,* vol. 40, no. 23, pp. 5514-5517, 2015/12/01, 2015.

[78] Y. Shimotsuma, P. G. Kazansky, J. Qiu, and K. Hirao, “Self-organized nanogratings in glass irradiated by ultrashort light pulses,” *Physical review letters,* vol. 91, no. 24, pp. 247405, 2003.

[79] Y. Liao, W. Pan, Y. Cui, L. Qiao, Y. Bellouard, K. Sugioka, and Y. Cheng, “Formation of in-volume nanogratings with sub-100-nm periods in glass by femtosecond laser irradiation,” *Optics Letters,* vol. 40, no. 15, pp. 3623-3626, 2015/08/01, 2015.

[80] Y. Liao, J. Ni, L. Qiao, M. Huang, Y. Bellouard, K. Sugioka, and Y. Cheng, “High-fidelity visualization of formation of volume nanogratings in porous glass by femtosecond laser irradiation,” *Optica,* vol. 2, no. 4, pp. 329-334, 2015/04/20, 2015.

[81] R. Taylor, C. Hnatovsky, and E. Simova, “Applications of femtosecond laser induced self-organized planar nanocracks inside fused silica glass,” *Laser & Photonics Reviews,* vol. 2, no. 1-2, pp. 26-46, 2008.

[82] A. Rudenko, J.-P. Colombier, and T. E. Itina, “From random inhomogeneities to periodic nanostructures induced in bulk silica by ultrashort laser,” *Physical Review B,* vol. 93, no. 7, pp. 075427, 2016.

[83] C. Hnatovsky, R. Taylor, E. Simova, P. Rajeev, D. Rayner, V. Bhardwaj, and P. Corkum, “Fabrication of microchannels in glass using focused femtosecond laser radiation and selective chemical etching,” *Applied Physics A,* vol. 84, no. 1-2, pp. 47-61, 2006.

[84] F. Liang, R. Vallée, and S. L. Chin, “Mechanism of nanograting formation on the surface of fused silica,” *Optics Express,* vol. 20, no. 4, pp. 4389-4396, 2012/02/13, 2012.

[85] C. Hnatovsky, D. Grobnic, D. Coulas, M. Barnes, and S. J. Mihailov, “Self-organized nanostructure formation during femtosecond-laser inscription of fiber Bragg gratings,” *Optics Letters,* vol. 42, no. 3, pp. 399-402, 2017/02/01, 2017.

[86] Y. Dai, A. Patel, J. Song, M. Beresna, and P. G. Kazansky, “Void-nanograting transition by ultrashort laser pulse irradiation in silica glass,” *Optics Express,* vol. 24, no. 17, pp. 19344-19353, 2016/08/22, 2016.

[87] M. Wang, M. A. Zaghloul, S. Huang, A. Yan, S. Li, R. Zou, P. Ohodnicki, M. Buric, M.-J. Li, and D. Carpenter, "Ultrafast Laser Enhanced Rayleigh Backscattering on Silica Fiber for Distributed Sensing under Harsh Environment." p. ATh3P. 4.

[88] A. Yan, S. Huang, S. Li, R. Chen, P. Ohodnicki, M. Buric, S. Lee, M.-J. Li, and K. P. Chen, “Distributed Optical Fiber Sensors with Ultrafast Laser Enhanced Rayleigh Backscattering Profiles for Real-Time Monitoring of Solid Oxide Fuel Cell Operations,” *Scientific reports,* vol. 7, no. 1, pp. 9360, 2017.

[89] “http://www.corning.com/media/worldwide/coc/documents/PI1463_07-14_English.pdf.”

[90] “https://www.corning.com/media/worldwide/coc/documents/Fiber/PI1445_3.17.pdf.”

[91] L. Technologies, "Optical Backscatter Reflectometer 4600," 2013.

[92] D. Tucker, M. Shelton, and A. Manivannan, “The role of solid oxide fuel cells in advanced hybrid power systems of the future,” *The Electrochemical Society Interface,* vol. 18, no. 3, pp. 45, 2009.

[93] S. Celik, B. Timurkutluk, and M. D. Mat, “Measurement of the temperature distribution in a large solid oxide fuel cell short stack,” *International Journal of Hydrogen Energy,* vol. 38, no. 25, pp. 10534-10541, 2013.

[94] D. Havermann, J. Mathew, W. N. MacPherson, R. R. Maier, and D. P. Hand, "In-situ measurements with fibre Bragg gratings embedded in stainless steel." pp. 9157A1-9157A1.

[95] X. Li, “Embedded sensors in layered manufacturing,” Stanford University Stanford, CA, 2001.

[96] C. E. Lee, J. J. Alcoz, W. Gibler, R. A. Atkins, and H. F. Taylor, "Method for embedding optical fibers and optical fiber sensors in metal parts and structures." p. 110.

[97] G.-C. Lin, L. Wang, C. Yang, M. Shih, and T. Chuang, “Thermal performance of metal-clad fiber Bragg grating sensors,” *IEEE photonics technology letters,* vol. 10, no. 3, pp. 406-408, 1998.

[98] H. Alemohammad, and E. Toyserkani, “Metal embedded optical fiber sensors: Laser-based layered manufacturing procedures,” *Journal of Manufacturing Science and Engineering,* vol. 133, no. 3, pp. 031015, 2011.

[99] Y. Li, W. Liu, Y. Feng, and H. Zhang, “Ultrasonic embedding of nickel-coated fiber Bragg grating in aluminum and associated sensing characteristics,” *Optical Fiber Technology,* vol. 18, no. 1, pp. 7-13, 2012.

[100] N. Mehanathan, V. Tavassoli, P. Shao, L. Sorenson, and F. Ayazi, "Invar-36 micro hemispherical shell resonators." pp. 40-43.

[101] T. Hirano, and L.-S. Fan, "Invar electrodeposition for MEMS application." pp. 252-259.